Durham E-Theses

On the growth of zinc oxide nanowires towards photoelectrochemical applications

ALEJANDRO GALAN-GONZALEZ

How to cite:

Use policy

On the growth of zinc oxide nanowires towards photoelectrochemical applications

Alejandro Galán González

A thesis presented for the Degree of

Doctor of Philosophy

Department of Engineering

Faculty of Science

Durham University

September 2020

Dedicated to family and their unrelenting support.

Y a mi tata.

Thank you.

"Ideas do not last long. Something must be done with them."

- Santiago Ramón y Cajal

On the growth of zinc oxide nanowires towards photoelectrochemical applications

Alejandro Galán-González

Abstract

Zinc oxide is regarded as an attractive semiconductor alternative to the most commonly used silicon and GaAs owing to its abundancy, thermodynamic stability and the large variety of morphologies it can be grown into. Among these morphologies, nanowires (NWs) have gathered vast attention as an ideal research platform for new and enhanced functionalities of ZnO. One of these functionalities is the integration of ZnO into the renewable production of hydrogen from water splitting. In this thesis, the growth of ZnO NWs, its doping and surface functionalization are studied with the aim of developing highly efficient photoelectrochemical (PEC) water splitting photoanodes.

Before delving in the functional application, a growth study of the ZnO NWs was necessary to understand the factors that control this growth. For this, a seed mediated chemical bath deposition (CBD) approached was explored in detail and adopted. Control over NW growth was obtained by tuning the seed layer deposition with two different techniques (atomic layer deposition and sol-gel processing) and by controlling the CBD parameters. This study demonstrated that NW diameter, length, growth orientation and crystallinity can be controlled by this approach.

To modulate the optoelectronic properties, ZnO NWs were doped with two different transition metals, copper and cobalt. A detailed study of the optoelectronic properties of these doped-ZnO NWs revealed that the introduction of cobalt into the ZnO lattice considerably improved the optoelectronic properties of ZnO. This enhancement was induced by the introduction of traps states in the bandgap of ZnO prompted by the interaction between the sp orbitals of ZnO and the d orbitals of Co. In particular, a 1% nominal doping yielded the most promising results of this study.

Further improvement of the ZnO properties towards PEC water splitting was achieved by functionalizing the surface of the NWs with iridium and a metal-organic framework the zeolitic imidazolate framework-8 (ZIF-8). The successful integration was demonstration by electron microscopic analysis that showed the control of this conformal surface functionalization. The integration of Co-doping and ZIF-8 functionalization resulted in a large enhancement of the PEC performance of the ZnO NWs, doubling the photogenerated current and the stability over time while also increasing the incident photon-to-current efficiency from 11% for ZnO NWs to 75% in the blue and ultraviolet region for ZnO:Co@ZIF-8 core-shell NWs.

Declaration of Authorship

The work in this thesis is based on research carried out in the Advanced Materials, Electronics and Communications Research Challenge, Department of Engineering, Durham University. The work of this thesis has not been submitted elsewhere for the obtention of a research degree.

The ZnO nanowires presented in this work were prepared by the author. The characterization with scanning and transmission electron microscopy and energy-dispersive x-ray spectroscopy was carried out by the author with help from Dr. Leon Bowen in the Department of Physics at Durham University. The atomic force microscopy analyses were performed by the author with the assistance of Dr. Chris Pearson at Durham University.

The x-ray diffraction measurements were made by Gary Oswald in the Department of Chemistry at Durham University. The x-ray reflectivity study was carried out by the author in the Department of Physics at Durham University.

Ultraviolet-visible spectroscopy analyses were performed by the author. The other optical-based characterizations, fast-transient absorption, photoluminescence and cathodoluminescence spectroscopy, were carried out by Aswathi K. Sivan in the Istituto per la Microelettronica e i Microsistemi (IMM), CNR in Rome, Italy. The analysis of the experimental data was collaboratively carried out by Aswathi, her supervisor Dr. Faustino Martelli and the author.

The photoelectrochemical characterization shown in this work was performed by Dr. Javier Hernández-Ferrer, with help from the author at the electrochemistry laboratory of the Instituto de Carboquímica (ICB-CSIC) in Zaragoza, Spain. The analysis of the experimental data was carried out by Javier and the author, in collaboration with Dr. Wolfgang Maser and Dr. Ana Benito.

v

Acknowledgements

I would first to express my deepest gratitude and appreciation to Prof Del Atkinson for his friendship, guidance and direction. The gruelling task that is a PhD was much easier thanks to the countless discussions and your meticulous scrutiny on every step of the road. I would like to also thank Prof Dagou Zeze and Dr Andrew Gallant for their guidance and help during my PhD. My sincere thanks to all three as well for giving me this opportunity as part of the INDEED ITN in the Horizon 2020 Framework.

Gracias a Lidia, Iñaki, Nacho, Aitana y mis dos soles, Hugo y Julia, mi familia. Gracias por vuestro apoyo incondicional, vuestro consejo y vuestro amor. Gracias por darme las alas para poder alcanzar mis sueños. Gracias también a Ariam y Maura por ser mi familia en Durham y por todas las experiencias que hemos compartido. Nada habría sido lo mismo sin estos tres años viviendo juntos. Gracias a Meri, por estar siempre ahí y por tu apoyo incondicional. Gracias a Víctor, porque, aunque los años sigan pasando, todo sigue igual, y eso es lo bonito. Gracias a Sergio y Ernesto por las incontables noches de charlas y juegos que ayudan a olvidarse de todo.

I would like to thank Dr Edgar Muñoz, for guiding me through my first baby steps in this world of research, and for doing so with your big smile and your immense kindness. A massive thank you to Dr Wolfgang Maser and Dr Ana Benito for their continuous support and help. Thank you for always listening to me and all my ideas and for your guidance in the work we have been sharing since I stated my endeavour in research. And of course, thanks to Javi, whose help has been essential to this work.

I am very grateful to Aswathi Sivan not only for the work we have achieved together, but for the amazing friendship we developed along with it. I would also like to appreciate Vanessa and Iman, for all the time shared in the office and the endless chats, discussions and time shared. I hope we can have another paper plane fight soon. A special thanks to Dr Leon Bowen for all the long discussions and sessions of microscopy we shared as well as your help, which made them much more enjoyable I would also like to thank everyone in room 142 in Physics, especially Charles and Ben, for their help and discussions throughout these years.

List of publications

- Galán-González, A. J. Gallant, D. A. Zeze and D. Atkinson. *Controlling the growth of single crystal ZnO nanowires by tuning the atomic layer deposition parameters of the ZnO seed layer*, **Nanotechnology**, 30(30):305602 (2019).

- Galán-González, A. K. Sivan, J. Hernández-Ferrer, L. Bowen, L. Di Mario, F. Martelli, A. M. Benito, W. K. Maser, M. U. Chaudhry, A. J. G., D. A. Zeze, D. Atkinson. *Metal-Organic Framework Functionalization of Doped Metal Oxide Semiconductors for Highly Efficient Water Splitting Photoanodes*, **ACS Applied Nano Materials**, 3, 8, 7781-7788 (2020).

- K. Sivan, A. Galán-González, L. Di Mario, N. Tappy, J. Hernández-Ferrer, D. Catone, S. Turchini, A. M. Benito, W. K. Maser, A. Fontcuberta i Morral, A. Gallant, D. A. Zeze, D. Atkinson, and F. Martelli. *Optical properties and carrier dynamics in Co-doped ZnO nanorods*, http://arxiv.org/abs/2006.16740. Submitted to **Nanoscale Advances**.

Contents

xi

Chapter 1

Introduction

1.1 Background

Semiconductor technology has revolutionized society in a way that very few discoveries can match. Since the discovery of the first semiconductor effect by Faraday[1] in the first half of the 19th century to the invention of the first transistor by Bardeen, Shockley and Brattain[2] in 1947 at Bell Labs to the current Information Era we live in, based on computers and telecommunications, semiconductors are one of the cornerstones upon which modern society is built. Gordon Moore predicted in 1965[3] (the well-known Moore's Law) that the advancement in semiconductor technology would lead to one of the most important technological feats of humanity: the miniaturization of semiconductor devices, particularly metal-oxide-semiconductor field-effect transistors (MOSFETs). This miniaturization has made it possible for all of us to have access to computers, mobile phones and an endless stream of other devices that, 50 years ago, would have only been part of science fiction. The principal building block of this semiconductor technology and one of the most precious resources to society nowadays is silicon, which can be thought as the paradigm in semiconductor technology.

Among the many contributions that semiconductors have made to the world, one of the most important is the development of renewable sources of energy and, in particular, solar energy[4]. The core concept of this technology is the absorption of solar energy and its transformation into electricity by a semiconductor. The most common semiconductor used in solar technology is silicon[5]. Research on photovoltaic solar cells has been ongoing for more than half a century, which has advanced the efficiencies with which a solar cell work from around 4% to the current day values reaching as high as 26%[6]. As attractive and beneficial as silicon-based solar technology is, it is not able to fulfil the ever-increasing global energy demands and, therefore, phase out fossil fuels (petrol, natural gas). In addition, due to the global demand for silicon and applications constraints, other semiconductors are currently being investigated to obtain competitive alternatives to silicon technology that can diversify the semiconductor market. The ideal alternative should be a material as abundant as silicon that can be easily processed and integrated in existing technology while, at the same time, challenging the performance obtained from silicon-based devices. Although this seems like an almost unattainable goal, researchers have found other semiconductors such as $GaAs$[7], Fe_2O_3[8], TiO_2[9] or ZnO[10] that can compete with silicon, be it because of their availability, performance or cost. Among these, ZnO has risen as one of the most attractive alternatives owing to its abundancy, thermodynamic stability and semiconducting properties. ZnO is a direct semiconductor with a wide bandgap and wurtzite crystal phase as its most stable crystal structure. In addition, ZnO has attracted the attention of researchers in the last two decades thanks to the variety of morphologies[11] it can be grown into. This, along with its base properties and the ease with which these can be modified, have made ZnO an attractive research material platform in the quest of finding alternatives to silicon[12].

The search for alternative renewable clean energies has resulted in researchers finding hydrogen as the potential solution to the global energy demand[13, 14]. Hydrogen is known as the element that powers stars[15] and harnessing this power is most certainly attractive. Not only is the combustion of hydrogen highly energetic (its combustion enthalpy has a value of -286 kJ/mol) but it is also very clean, generating only water vapour as by-product. However, there are two main hurdles

that hydrogen technology needs to overcome before being considered viable[16]. The first is controlling the combustion, as hydrogen is highly explosive. The second is the sustainable production of hydrogen[17].

Nowadays, the majority of hydrogen is produced from hydrocarbon reforming[18, 19], an industry directly dependent on fossil fuels. As such, alternative routes to the production of hydrogen must be developed to ensure a sustainable supply of hydrogen. One of these routes is known as photoelectrochemical water splitting. In short, this is a technology based on converting solar energy into chemical energy by using a semiconductor that can absorb light and use this energy to split the chemical bonds of a water molecule, yielding hydrogen and oxygen as a result of the process. The first report on such technology was provided by Fujishima[20] in 1972 and, since then, research has pushed towards the development of efficient photoelectrochemical water splitting cells[21]. This technology is, potentially, the cleanest possible form of energy as it only requires a light source and water to produce hydrogen, which would be subsequently burnt to produce water vapour, thus resulting in a cyclic process.

As photoelectrochemical water splitting is a process that requires a semiconductor subjected to a demanding combination of properties, research has thus focused on developing such a suitable semiconductor[22]. In this sense, the material should ideally have a low cost, be abundant and functionally should provide a large amount of photocurrent generated with high efficiency over a long lifetime. ZnO is one of the candidates for this application due to its low cost and common availability. However, ZnO suffers from some key drawbacks such as its wide bandgap, or poor photocurrent generation, and the performance stability over time, which currently limits the potential application of ZnO in photoelectrochemical water splitting.

1.2 Aims of the thesis

The aim of this thesis is the development of different functionalization strategies that can help boosting the performance of ZnO in photoelectrochemical water splitting by modifying some of the intrinsic properties of ZnO that are problematic in its application in water splitting. For this, a combinational nanotechnological approach

in the form of ZnO nanowires was selected due to its large potential. The properties of ZnO were modulated both from the inside and outside by means of internal doping of the crystal structure of ZnO and by functionalizing its external surface with a metal-organic framework. These three features (nanostructural approach, doping and surface functionalization) are shown to largely enhance the performance of ZnO in photoelectrochemical water splitting while providing a functional mechanism for this improvement. This is considered to be a significant step forward for the potentially widespread implementation of ZnO in photoelectrochemical water splitting.

ZnO nanowires were selected as the nanomorphology that could provide the best photoelectrochemical performance owing to their large surface-to-volume ratio and their small lateral charge transfer distance. ZnO nanowires were grown by a seed-mediated chemical bath deposition process under different growth conditions. The ensuing growth study, backed by electronic microscopy techniques, was utilised to determine the growth conditions that would be deemed best for the functional performance of these ZnO nanowires as water splitting photoanodes. To modify the properties of these nanowires, cobalt and copper doping and two different strategies of surface functionalization were explored in terms of growth and optoelectronic properties to determine which of the different enhancements proposed would have a greater impact on the water splitting performance of the ZnO nanowires.

The subsequent photoelectrochemical study of the functionalized ZnO nanowires provided deeper insight into the performance of these nanowires as water splitting photoanodes as well as the functional mechanism that governs the enhancement of the performance. This mechanism paves the way for the application of the strategies proposed in this thesis into other material systems, be it using different semiconductors or other possible functionalizations of ZnO.

1.3 Thesis outline

The initial chapters of the thesis, Chapters 2-4, provide the necessary background for the understanding of the concepts described in the results. These results are the core of this work and represent the scientific outcomes obtained in this thesis, gathered in Chapters 5-8. As such, the thesis starts with a description of the principal physical concepts that govern the properties of semiconductors as well as the basics of the

targeted application, photoelectrochemical water splitting, which provides the underpinning physics needed to understand and put into context the research presented in this thesis. For this, an introduction to semiconductor physics is provided, focusing first on the crystalline structure of semiconducting inorganic solids. This is followed by a brief description of what the electronic band structure is and how can it be formally obtained. Finally, a discussion of the processes involved in photonic excitation and subsequent recombination of charge carriers is provided. The introduction to the semiconductor physics is followed by a description of some of the most relevant morphologies that any inorganic semiconductor can adopt, with a particular emphasis on those at the nanoscale. Finally, the theoretical background required for the discussion of photoelectrochemical water splitting is provided, going from the basic theory that describes the process to the different efficiencies that govern it and how the most important metrics used to determine the performance of a photoanode were obtained in this work.

In Chapter 3, a detailed description of ZnO from a material science point of view is provided. Starting with a snapshot of its most significant structural and optoelectronic properties, the focus is then shifted to the multitude of different techniques used to grow ZnO, divided into gas phase and liquid phase growth techniques. This is followed by a discussion of the various nanomorphologies in which ZnO can be grown. This discussion is structured on the basis of the dimensionality of the morphology in question, i.e. depending on how many dimensions of the nanomorphology are in the nanoscale. This forms the general introductory section of the chapter. The second part of this chapter details the growth and functionalization of the ZnO morphology selected for this work, that is nanowires (NWs). As such, first the growth of textured seed layers by atomic layer deposition and sol-gel processing are described, followed by the growth of ZnO nanowires by chemical bath deposition. Finally, the doping during growth of the nanowires and post-growth surface functionalization are discussed.

The different ZnO nanowire growth and functionalization methodologies and the analytical techniques utilised throughout the thesis to study the properties and performance of the ZnO nanowires are described in Chapter 4. For this, the growth

of the ZnO seed layers, ZnO nanowires, doping and surface functionalization are consequently discussed. This is followed by an introduction to the different types of microscopy techniques used: atomic force microscopy, scanning electron microscopy and transmission electron microscopy. As a continuation, the x-ray related techniques, x-ray diffraction and x-ray reflectivity are presented, followed by the spectroscopic techniques used to analyse the chemical environment of the ZnO nanowires. These techniques are x-ray photoelectron spectroscopy and energy dispersive x-ray spectroscopy. The second to last part of the chapter is dedicated to the discussion of the optical analysis utilised in this thesis, namely ultraviolet-visible spectroscopy, fast transient absorption spectroscopy, photoluminescence and cathodoluminescence spectroscopy. Finally, the experimental conditions under which the photoelectrochemical characterization of the ZnO nanowires was carried out are provided.

The first results are shown in Chapter 5, in which a study of the controlled growth of ZnO nanowires is presented. This study shows the control over the growth of the ZnO nanowires depending on the deposition technique used for the seed layer (atomic layer deposition or sol-gel processing), the conditions under which these seed layers are deposited and the parametric influence of the chemical bath deposition conditions. This vast parameter space is explored and the results are demonstrated by means of electron microscopy and statistical studies extracted from these microscopy analyses. The crystallography of the ZnO nanowires is also studied, demonstrating their single crystal quality.

In Chapter 6, the doping of the ZnO nanowires with two transition metals, cobalt and copper, is explored, along with the influence that this doping has on the optoelectronic properties of the nanowires. Detailed optical analyses were carried out to understand the electronic structure of the doped nanowires and how the introduction of these dopants changed the electronic band structure and charge carrier dynamics of ZnO. Based on the results observed in this chapter and a thorough literature review, a theoretical model for the electronic band structure of the material is proposed.

The surface functionalization of ZnO is discussed in Chapter 7. This discussion is divided in two main sections, depending on the functionalizing material used. The

first part deals with the use of iridium as enhancer of the photoelectrochemical performance of the ZnO nanowires. For this, it is shown that self-assembled iridium nanoparticles can be deposited on the lateral faces of the ZnO nanowires, forming a functionalizing layer that shows promise for water splitting. The second part is focused on the surface functionalization of ZnO nanowires using a metal-organic framework (MOF), the zeolitic imidazolate framework-8. This MOF was shown to be integrated following two different solution based techniques, drop casting and spin coating. The structural and optical characteristics of these metal-organic framework functionalized nanowires were studied to understand their potential in water splitting.

The photoelectrochemical study of all the ZnO nanowire-related structures discussed in Chapters 5, 6 and 7 is provided in the final results chapter, Chapter 8. This shows a detailed study of the performance of undoped, doped, functionalized, and doped and functionalized ZnO nanowires in terms of their total photocurrent generated, on-off behaviour and photoconversion efficiency. The different performances observed for these groups of nanowires are discussed based on the results of the previous chapters. The photoelectrochemical study presented in this chapter shows the large potential that the integration of doping and surface functionalization of ZnO nanowires has on its performance photoelectrochemical water splitting photoanode. In addition, a theoretical model that includes doping, surface functionalization, electronic band structure and carrier dynamics is proposed in an effort to further push the understanding of these nanomaterials and enable the utilization of ZnO nanostructure in this functional application.

The final chapter of the thesis, Chapter 9, is the conclusion of the thesis. In this chapter, the principle findings and results extracted from the results chapters are summarised, showcasing their importance within the fields of material science and photoelectrochemistry. The final part of the chapter comprises the discussion on the new ideas and approaches that form the possible future work based on the results extracted from this thesis and that would serve as a steppingstone to further the knowledge and importance of the field.

Chapter 2

Theoretical background and photoelectrochemistry of semiconductors

2.1 Introduction

This chapter provides an overview of the main physical properties of semiconductors, their many morphologies and the necessary considerations and theoretical background for their application in photoelectrochemistry. First, a detailed introduction on what a semiconductor is and the physics that govern their key properties is provided. The discussion of these properties of semiconductors will serve as the theoretical basis for the results described in the later chapters of the thesis. In this sense, particular attention will be paid to the description of the structure of crystalline solids and how this is directly related to the intrinsic semiconducting characteristics of the material in question. This is followed by a discussion of the energy levels and band structure of semiconductor materials and the importance that these have on the functional application of semiconductors. Finally, the description of the processes of photoexcitation and subsequent

generation of carriers is provided, setting the basis for the later discussion on photoelectrochemistry.

Second, the multiple morphologies that semiconductors can adopt are described, starting from single crystal silicon to the different nanomorphologies that have been the focus of semiconductor research in the recent years. As third and final part of the chapter, an in-depth view of the photoelectrochemistry of semiconductors is presented. This describes what photoelectrochemistry and photoelectrochemical (PEC) water splitting are, analyses the underpinning physics of the PEC process, its requirements from a materials science point of view and covers how the different metrics that are used to describe the PEC performance of a semiconductor can be measured and compared. This last section of the chapter will be used as the basis for the discussion of the results presented in Chapter 8 that pertain to the PEC performance of all the ZnO-based functional devices developed in this thesis.

2.2 Basic physics of semiconductors: background theory and charge carrier photogeneration

Semiconductors are a type of material that have an electrical conductivity in between that of insulators and conductors due to either the presence of an impurity in its structure or induced by a change in temperature. Independently of the origin of the semiconducting character, semiconductors have revolutionized science and our day to day lives in previously unimaginable ways. From computers to televisions and communications, semiconductors have been at the core of the progress of humanity into the Information Era we currently live in. Therefore, understanding the underpinning physics that govern the properties of semiconductors is paramount from a scientific point of view. For this, it is necessary to first discuss the crystal structure and properties of solids, as these are the basis for any functional semiconductor device. It should be noted that the focus of this work from here onwards will be on inorganic crystalline solids. Other semiconductor materials such as amorphous semiconductors[23, 24] or organic semiconductors[25-27] will not be discussed here, please refer to the literature provided for further reading on these two other types of semiconductors. The description of the crystal structure of solids

will then be utilised to study one of the most important characteristics of semiconductors, i.e., their electronic band structure. Band theory is a key component in the description of the semiconducting properties of a material as it provides an explanation for the presence, formation and transport of charge carriers (electrons and holes) within a crystalline solid. These charge carriers can be generated by different types of excitations such as thermal, electromagnetic or photonic. The latter will be described in detail here since the focus of this thesis is the photoelectrochemical application of ZnO nanostructures, which is highly dependent of the photogeneration of charge carriers. The introduction to semiconductor physics provided here is also a snapshot of the field. Further information on the properties of inorganic semiconductors can be obtained in the works of Mishra[28] and Neamen[29].

2.2.1 Crystal structure of inorganic semiconductors

The crystal structure is the description of the ordered arrangement of atoms in a crystalline material. The quality of the crystal structure is key for the performance of any semiconductor device. In this sense, the best crystal quality of a solid corresponds to a single crystal, which means that the crystalline solid is formed by a single, continuous and uninterrupted crystal structure that has no defects in its structure. The most important and well-known single crystal semiconductor material is silicon, which will be described in a later section of this chapter. If the crystal structure of a solid has growth defects or impurities it cannot be considered a single crystal and, therefore, exerting control over these defects and impurities is key to ensure and tune the performance of any semiconductor device.

To describe the crystal structure of a solid, there are a set of concepts and parameters that must be detailed. The first of these concepts is the lattice of a crystal structure, which represents a set of ordered points that form a periodic structure. Therefore, the crystal structure of a single crystal material will be formed by a single lattice reproduced over space. Crystal lattices are formed by atoms and, thus, the concept of basis of a lattice needs to be introduced. The crystal basis is the building block of the crystal and it is usually defined by a single or a pair of atoms characteristic of the crystalline material. Therefore, a crystal will be the sum of a lattice and a basis[30] in such a way that the atom from the basis will occupy specific position on the lattice.

Any lattice is defined by a set of three vectors, labelled here as *a*, *b* and *c*, so that any point in the lattice, **R**, can be obtained by translation as follows,

$$\boldsymbol{R} = ma + nb + pc \qquad \text{[Eq. 2.1]}$$

where *m, n, p* are integers. In the case that the three vectors *a*, *b* and *c* form a cell of the lattice with the smallest possible volume, the vectors will be called primitive vectors and the volume cell they enclose is thus defined as the primitive cell[31]. The repetition by simple translation operations of this primitive cell in three-dimensional space will fill all the lattice space without leaving gaps. Due to the existence of this primitive cell that fills all the lattice space, the lattice of any crystal is demonstrated to have a periodicity that can help define the symmetry of the structure. This permits the description of symmetry groups that encompass lattices with the same structural properties. In total, there are 14 different types of three-dimensional lattices that are defined by their primitive vectors *a*, *b* and *c* and the angles α, β and γ between them. Among these, there are two families of lattices that comprise the crystal structure of the most common semiconductors: cubic and hexagonal[32].

The cubic crystal system is the simplest possible crystal structure that a solid can have as the unit cell is in the shape of a cube. This means that the three primitive vectors are equal and the three angles previously defined are 90°. There are three main varieties of this crystal system (see Figure 2.1), depending on the position of the atoms of the basis within the lattice:

- Primitive cubic, which has atoms only on the corners of the cube.
- Body-centered cubic (bcc), which has an atom in the centre of the cubic unit cell as well as on the corners of the cube.
- Face-centered cubic (fcc), which has an atom in the centre of the lateral faces of the cube along with the atoms on the corners.

One case of particular interest of cubic crystal structure is obtained when two fcc lattices are interpenetrated, with one displaced from the other by a factor of *a/4*, with *a* being the primitive vector. This type of structure has two atoms per basis, as shown in Figure 2.1d for the zinc blende structure of ZnO. Depending on the nature of these two atoms, the crystal structure will either be the diamond cubic structure, if both atoms are the same, or a zinc blende structure, if the
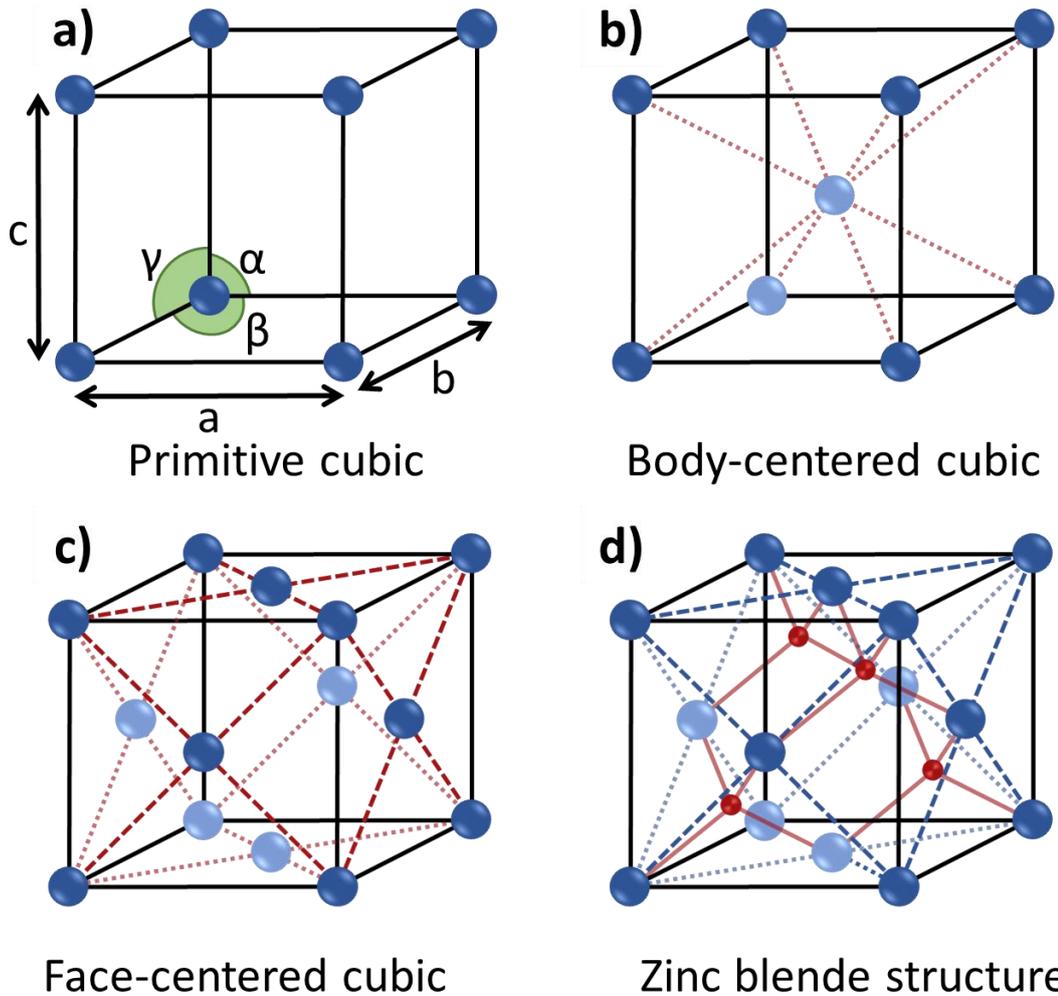
Figure 2.1. Three principal varieties of the cubic crystal system **a)** primitive, **b)** body-centered and **c)** face-centered, depending on the position of atoms in the lattice. The primitive vectors *a*, *b*, *c* and the angles α, β and γ between them have been included in the primitive cubic cell for clarity. **d)** Example of a zinc blende crystal structure, in particular that of ZnO. In this structure, blue atoms represent Zn and red atoms, oxygen.

atoms are different. These two structures are the most important in the semiconductor industry. The diamond structure is that found in elemental semiconductors like silicon or germanium, which are the most widely used semiconductors, particularly silicon. In contrast, the zinc blende structure is characteristic of materials such as GaAs or CdS, known as compound semiconductors. Compound semiconductors are commonly denoted by the position of the atoms that form them in the periodic table, i.e., III-V for GaAs or II-VI for CdS. Although compound semiconductors are less common in industry (albeit industrially viable) compared to the ubiquitous silicon, semiconductor research in the past couple of decades has been mostly focused on these due to their outstanding tunability and nanoscale morphologies that show great potential[33, 34].

The hexagonal crystal system is also very important in semiconductor technology. The most common structure within this system is the hexagonal close pack structure (hcp). One of the most common examples of an hcp structure is the wurtzite crystal structure, which has a considerable importance in semiconductor technology as it is the crystal structure of many compound III-V and II-VI semiconductors such as BN, GaN, SiC or ZnO[35, 36], the latter being the focus of this thesis. A schematic of the ZnO wurtzite structure is shown in Figure 2.2. The wurtzite crystal structure is formed by two sets of hcp structures, one for each type of atom of the compound semiconductor. In this way, each atom is tetrahedrally coordinated with four atoms from the other element. A key feature of the wurtzite structure is the lack of inversion symmetry, which confers piezoelectric[37] and pyroelectric[38] properties to semiconductor materials with this crystal structure.
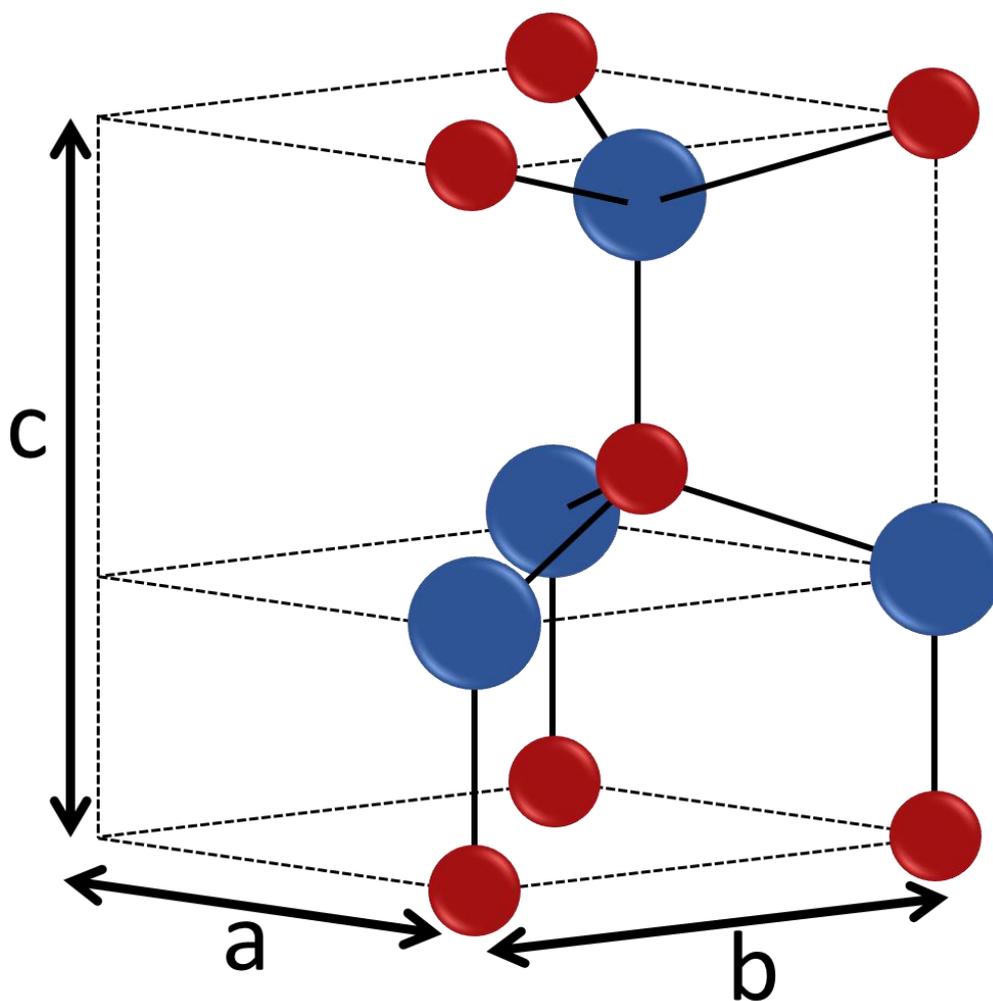
Figure 2.2. Schematic representation of the wurtzite crystal structure, in particular for ZnO. The blue spheres represent Zn atoms, while the red spheres indicate the position of O atoms. Only a slice of the hexagonal structure is presented here for clarity. The primitive vectors a and b are equal.

Once the most important semiconductor crystal structures have been introduced, it is necessary to describe the directions and planes within the crystalline material. The planes in a crystal are usually denoted by a series of integers called Miller indices, which are commonly used is the description of the crystal structure of semiconductors[39]. To obtain these Miller indices, first it is necessary to define a set of reciprocal lattice vectors, *a**, *b**, *c** such as,

$$a^* = 2\pi \frac{b \cdot c}{a \cdot b \cdot c}; \ b^* = 2\pi \frac{a \cdot c}{a \cdot b \cdot c}; \ c^* = 2\pi \frac{a \cdot b}{a \cdot b \cdot c} \qquad \text{[Eq. 2.2]}$$

where *a*, *b* and *c* are the primitive vectors. These reciprocal lattice vectors are such that,

$$a \cdot a^* = 2\pi; a \cdot b^* = 0 \qquad \text{[Eq. 2.3]}$$

thus resulting in a general reciprocal lattice vector **G**, akin to **R** described in Eq. 2.1, given by,

$$\boldsymbol{G} = ha^* + kb^* + lc^* \qquad \text{[Eq. 2.4]}$$

where *h*, *k*, *l* are the integers known as Miller indices. These Miller indices are determined by finding the intercepts of the plane with the basis axis in terms of lattice constants (*a*, *b*, *c*) and subsequently obtaining the reciprocals of these number as per Eq. 2.2. As a final step, these reciprocal vectors must be reduced to the smallest integer possible, while maintaining their ratio. These three smallest reciprocal numbers are the *h*, *k*, *l* Miller indices and are always presented between parenthesis as in (*h k l*). If a plane intercepts one of the axis in the negative side of the axis, then said Miller index will have a bar "‾" accent. For example, should the plane intercept the x axis on the negative side, then the Miller indices would be ($\bar{h} \ k \ l$).

Figure 2.3 shows three different planes in a cubic system with their corresponding Miller indices. In particular, the (1 0 0), (1 1 0) and (1 1 1) planes are shown for a primitive cubic crystal structure. The description of planes by Miller indices is of importance when describing the crystal structure of a semiconductor as this structure can determine some of the physical and surface properties of a semiconductor. These indices are also helpful in the identification of the different crystal phases that a semiconductor can grow in, thus providing a better understanding of the functionality of a material.
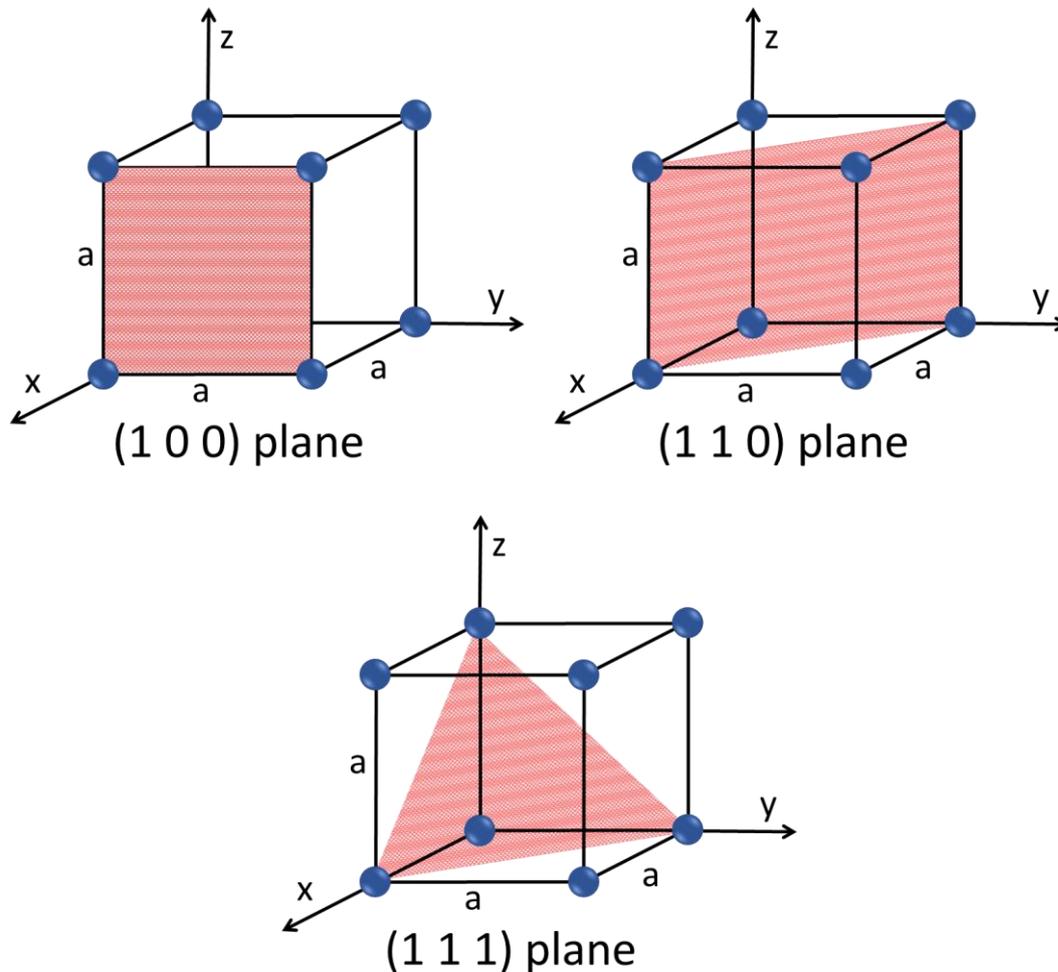
Figure 2.3. Schematic representation of three different planes with their corresponding Miller indices in a primitive cubic crystal lattice. The primitive vectors *a*, *b* and *c* are equal, hence the labelling as *a*.

2.2.2 Crystal defects

Up to now, the description of crystal structures has been done under the consideration of crystals being perfect, defectless, ordered arrangements of atoms. However, in reality, defects are present during crystal growth either due to thermodynamic considerations (such as a change of the conditions during the growth) or by the introduction of impurities.

Independently of whether these defects are introduced intentionally or unintentionally, their presence has to be considered and controlled to ensure that their introduction is not detrimental to the optical and electronic properties of the semiconductor. These defects can be characterized as single point defects, affecting individual atoms in the lattice, or more extended as planar and volume defects that

affect entire unit cells[40]. Point defects are particularly important in the semiconductor industry.

These defects can be present in many different forms (Figure 2.4)[41]:

- Vacancies, which correspond to an atom missing in the crystal lattice of the material. This is effectively a void in the lattice that strains it as the environment of the neighbouring atoms is different than normal.

- Interstitial defects, which are atoms that assume normally unoccupied positions in the crystal lattice. This creates a distortion in the lattice dependent on the nature of the interstitial atom, both its size and electronic structure. There are two types of interstitials, namely self and impurity interstitial species. The former is an interstitial of the same nature as the atoms that form the lattice of the materials while the latter is an interstitial atom of different nature than those that form the lattice.

- Substitutional defects occur when an atom of different nature to those that form the crystal lattice is introduced in a position in the lattice that is normally occupied by an atom. Therefore, a distortion in the lattice parameters will take place as the substitutional atom will be either smaller or larger than those of the original lattice. This can also induce changes in the optoelectronic properties of the semiconductor, depending on the nature of the substitutional atom.

These point defects (highlighted in Figure 2.4) are a result of doping the semiconductors, which is the process by which impurities are purposefully introduced into a semiconductor with the aim of modifying the electronic structure and optoelectronic properties[42]. A more in detail discussion on doping and its effect on the properties of semiconductors is provided in the next section. Other semiconductor lattice defects will not be discussed in this work as point defects are the most interesting for the goal of this thesis. More information on semiconductor defects can be found in the comprehensive work by Rockett[43].

2.2.3 Electronic band structure of semiconductors

The electronic band structure of a solid describes the energy levels that an electron may or may not have within the solid. Thus, the electronic band structure is formed by allowed and forbidden bands that electrons can and cannot occupy. A formal
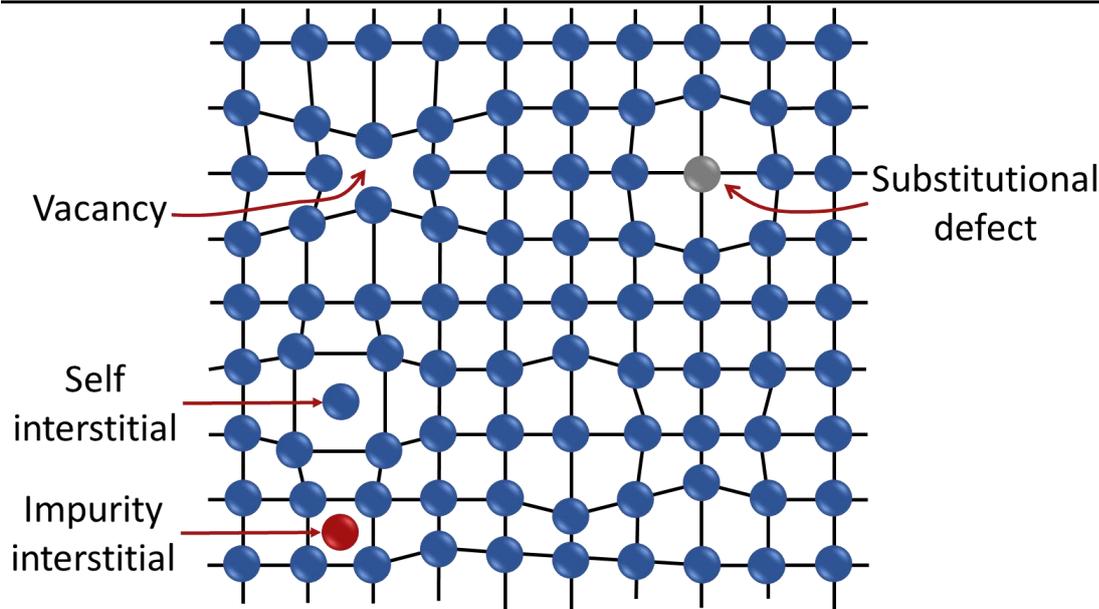
Figure 2.4. Schematic representation of an atomic lattice showing the principal types of point defects (vacancy, self and impurity interstitial and substitutional interstitials) discussed here. The red and grey atoms represent elements other than those of the lattice.

description of the band structure is required for the correct understanding of the concepts linked to it. For this, only a crystalline solid with a periodic structure is going to be considered. This formal description is based on quantum mechanical methods. The basis of this description is the time-dependent Schrödinger equation for electrons,

$$\left[-\frac{\hbar^2}{2m_0} \nabla^2 + V(r,t) \right] \psi(r,t) = E\psi(r,t) \qquad \text{[Eq. 2.5]}$$

where $\hbar$ is the reduced Planck's constant, corresponding to $\hbar=h/2\pi$; m_0 is the mass of an electron, E is the energy of the system and $V(r,t)$ is the potential energy of the electron, yielding ψ solutions, where ψ is the electron wave function[28]. These ψ solutions are a series of allowed energy values that represent the energy levels in which electrons can be found. Those values that are not part of the solution form the forbidden bands in which electrons cannot be found.

The ψ wave functions obtained as solutions to the Schrödinger equation in a periodic crystalline solid are considered independent of time. Hence, the Schrödinger equation is only dependent on the space component r as in,

$$\left[-\frac{\hbar^2}{2m_0} \nabla^2 + V(r) \right] \psi(r) = E\psi(r) \qquad \text{[Eq. 2.6]}$$

Assuming there is no potential energy on the electron, this can be further simplified to

$$-\frac{\hbar^2}{2m_0}\frac{d^2\psi(r)}{dr^2} = E\psi(r) \qquad \text{[Eq. 2.7]}$$

In a periodic crystal, the Schrödinger equation can be solved following Bloch's theorem, which states that the energy eigenstates for an electron in a crystal can be represented by a Bloch wave such as

$$\psi_k(r) = e^{ik\cdot r}u_k(r) \qquad \text{[Eq. 2.8]}$$

where ψ is the Bloch wave, k is the wave vector and $u(r)$ is a periodic function in r that is periodic with the periodicity of the lattice. Assuming a single unit cell of the crystal, then $\psi(r) = e^{ik\cdot r}$. Introducing this relation in Eq. 2.7,

$$\frac{d\psi(r)}{dr} = -ike^{ik\cdot r}; \frac{d^2\psi(r)}{dr^2} = i^2k^2e^{ik\cdot r} = -k^2e^{ik\cdot r} \qquad \text{[Eq. 2.9]}$$

And subsequently substituting Eq. 2.9 in Eq. 2.7 it is obtained that,

$$-\frac{\hbar^2}{2m_0}\cdot\left(-k^2e^{ik\cdot r}\right) = E\cdot e^{ik\cdot r} \Rightarrow E = \frac{\hbar^2}{2m_0}k^2 \qquad \text{[Eq. 2.10]}$$

indicating that there is a parabolic relation between the energy of the system and the k vector associated to the wave function. The same relation can be obtained by using the de Broglie relation that shows the wave-particle duality[44]. Considering the wavelength of an electron λ is related with its momentum p by

$$\lambda = \frac{h}{p} = \frac{h}{m_0v} \qquad \text{[Eq. 2.11]}$$

with h being Planck's constant, m_0 the electron mass and v the electron velocity. If the wave vector k is considered instead of the wavelength following the relation

$$k = \frac{2\pi}{\lambda} \qquad \text{[Eq. 2.12]}$$

then an electron in free space can also be describe by the wave vector k as

$$k = \frac{2\pi}{h}p = \frac{p}{\hbar} \Rightarrow p = \hbar k \qquad \text{[Eq. 2.13]}$$

Previously it was considered that the electron has no potential energy. Therefore, the energy of the system corresponds only to the kinetic energy of the electron

$$E = E_C = \frac{1}{2}m_0v^2 = \frac{p^2}{2m_0}, with\ p = m_0v \qquad \text{[Eq. 2.14]}$$

Introducing Eq. 2.13 in Eq. 2.14, it is obtained that

$$E = \frac{\hbar^2}{2m_0} k^2 \qquad\qquad \text{[Eq. 2.15]}$$

with Eq. 2.15 being the same as Eq. 2.10. These results mean that there is a parabolic relationship between the energy of the system and the wave vector k by which a specific series of bands will be obtained that satisfy Eq. 2.6. A total of N k-values can be obtained, with N being an integer that corresponds to the number of unit cells in the crystal, hence the periodicity shown in Eq. 2.8. Figure 2.5 shows a representation of the energy bands obtained by solving the Schrödinger equation for a crystalline material. In this schematic, the allowed energy bands are separated by the forbidden energy bands. As shown, the separation between the allowed energy bands is periodic and the size of these allowed bands diminishes until the core level of the atoms is reached. The forbidden energy bands are commonly labelled as bandgaps, E_g, and will be referred to as such from now on, especially in the discussion of the results in the later chapters.

This description of band theory shows that the allowed energy states of electrons are formed by a series of intercalated allowed and forbidden bands. A crucial consideration with these allowed bands is their level of occupation, i.e., whether they are completely or partially occupied by electrons. To analyse this consideration, first it is necessary to point out that thermodynamic effects directly
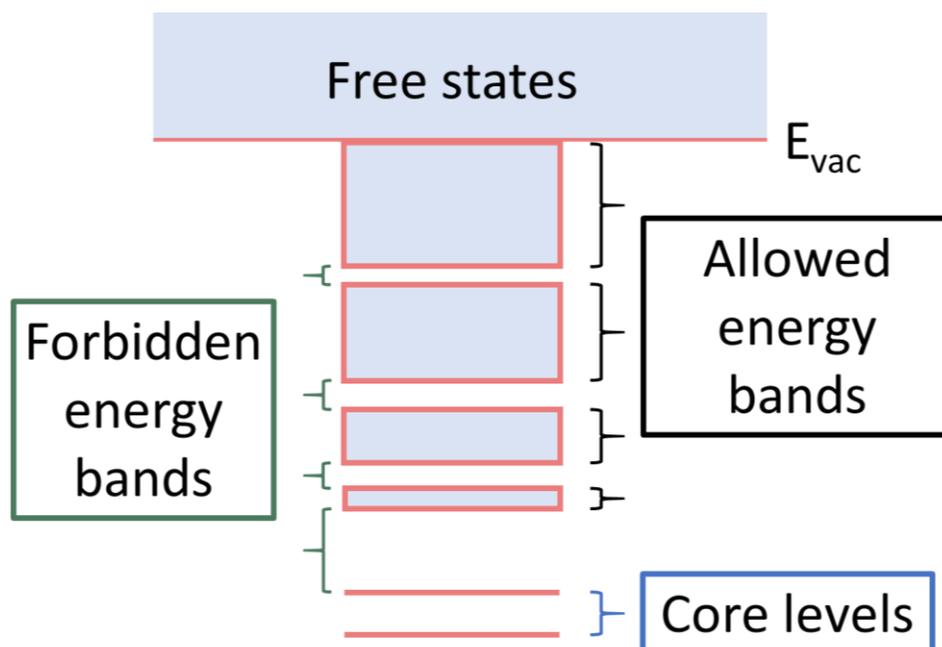
Figure 2.5. Schematic representation of the allowed and forbidden energy bands obtained from resolving the Schrödinger equation for different k wave numbers.

influence this occupancy[45]. Hence, the ideal case of 0 K is considered. At this temperature, if a band is completely occupied by electrons, the net charge will be zero as electrons are particles that can only move to empty states and, hence, carry no current in a filled band due to the unavailability of these empty states. This results in a situation by which there is a completely occupied energy band, followed by a bandgap and a completely empty band, resulting in an infinite effective resistivity. This is the case for semiconductors and insulators. If an energy band is only partially filled, then the presence of available empty states will allow electron conduction, i.e. a net current, which implies a lower resistivity, characteristic of metals. Following this considerations and for the particular case of semiconductors at 0 K, the highest occupied energy band is called valence band, whereas the next band after the bandgap that is unoccupied is named conduction band. There are multiple subsequent valence and conduction bands provided by the periodicity of the crystal but, for simplicity, only the first set is discussed here. If vacuum is considered as the reference point, the difference between the valence band and the vacuum level is called the electron affinity for semiconductors[46]. Similarly, the difference between the highest occupied electronic state of a metal and the vacuum level is known as work function. A schematic of this description is provided in Figure 2.6.

Following this description, it can be stated that, at 0 K, the valence band of a semiconductor is completely filled with electrons while the conduction band is empty. However, at finite temperatures T > 0 K, some of the electrons from the valence band will be thermally excited to the conduction band. These electrons in the conduction band can carry current as there are empty states available to which they can move. The electrons that are excited from the valence to the conduction band will thus leave unoccupied states in the valence band. These "missing" states are denoted as holes, which are quasiparticles with a positive mass equal to that of the electron and that act in an electric or magnetic field with a positive charge, thus being a balance to the electrons. Holes represent the absence of an electron and, hence, are not a particle per se, thus the quasiparticle definition. Therefore, any process that involves the movement of an electron (from the valence to the conduction band, for example) will have, as a result, the presence of a hole.
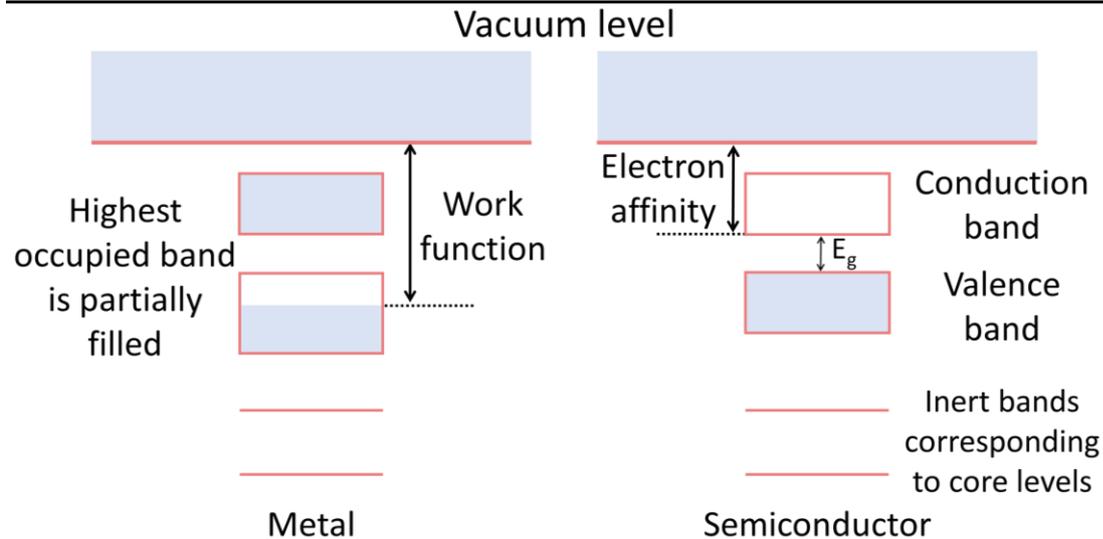
Figure 2.6. Schematic representation of the band structure of a metal and a semiconductor. The highest occupied energy band of the former is partially filled while that of the latter is completely filled. The energy differences with respect to the vacuum level used as reference have been included.

2.2.4 Direct and indirect bandgaps

Up to now, the electron-hole pair has been described and the theoretical background for the electronic band structure of crystalline solids has been provided. Nonetheless, there is still an additional concept that is required while discussing the electronic band structure of a semiconductor. This is related to whether the semiconductor in question has a direct or indirect bandgap. A direct bandgap semiconductor is such that the valence and conduction bands have the same wave vector k. Otherwise, the bandgap of the semiconductor is considered indirect. This consideration for the bandgap of semiconductors has implications in the interaction of photons and electrons in the semiconductor, a process of utmost importance for the semiconductor industry that will be described later in this chapter. An example of the band structures of two of the most important semiconductors, silicon and GaAs, are shown in Figure 2.7a,b, respectively. With regards to pure silicon, it has an indirect bandgap with a value of 1.1 eV, which is considered to be a very small bandgap. However, its direct bandgap is much larger, having a value of 3.4 eV. In contrast, GaAs only has a direct bandgap of 1.43 eV at room temperature. This difference between direct and indirect bandgap for GaAs and Si plays, as previously mentioned, a critical role in the optical properties of these materials. Independently of whether the bandgap is direct or indirect, electrons and holes in semiconductors have a certain

mobility under an electric field. This means that, for example, electrons can move from the valence band to the conduction band either by thermal or other external excitation such as an electric or magnetic field or light. Therefore it is necessary to analyse the density of these two types of charge carriers and the effect this has on the properties of the semiconductor. For this, the analysis will be carried out on pure semiconductors, also known as intrinsic semiconductors as their semiconducting properties come naturally from the material itself. Silicon or GaAs are examples of intrinsic semiconductors. For intrinsic semiconductors at temperatures above 0 K, there will be electrons that are excited from the valence to the conduction band. Therefore, there is an electron density *n* and a hole density *p* if the material is in thermodynamic equilibrium. As such, it is possible to define the density of states of an intrinsic semiconductor. The density of states is the number of available electronic states per unit volume per unit energy around an energy *E*, which can be defined as

$$N(E) = \frac{\sqrt{2}(m^*_{dos})^{\frac{3}{2}}(E - E_C)^{\frac{1}{2}}}{\pi^2 \hbar^3} \qquad \text{[Eq. 2.16]}$$

where *N(E)* is the energy dependent density of states, m^*_{dos} is the density of states mass and E_c is the energy value of the edge of the conduction band. An analogous
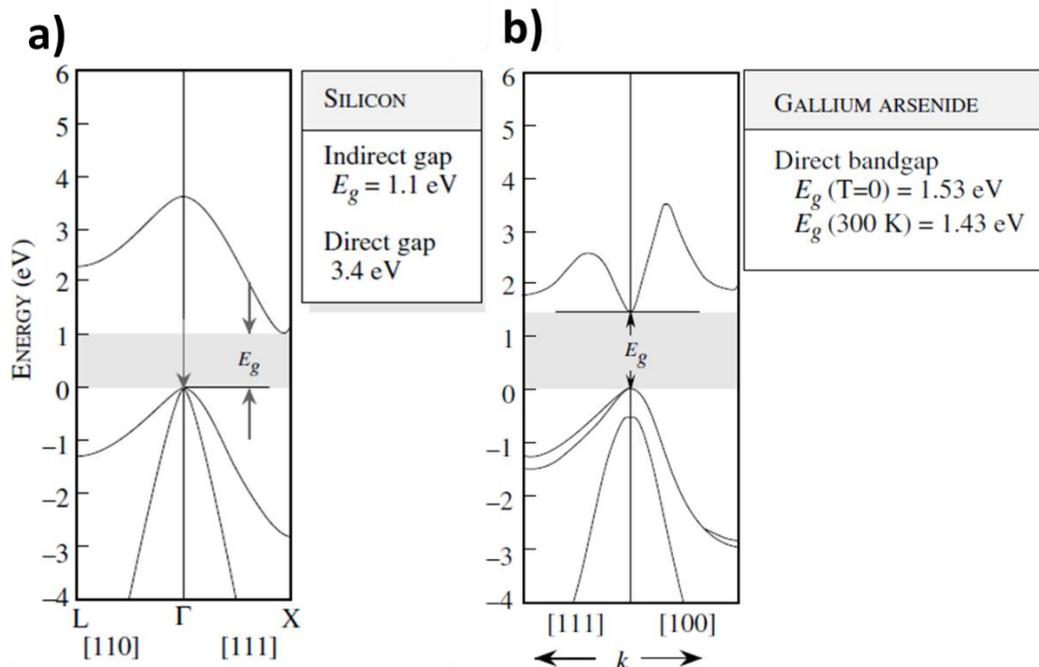
Figure 2.7. Band structure of **a)** silicon and **b)** gallium arsenide, showing the direct and indirect bandgap as well as the energy of this gap[28].

expression exists for the valence band, replacing the energy term for $(E_v - E)^{1/2}$ with E_v the energy of valence band edge. For intrinsic semiconductors, as previously stated, the electrons in the conductions band come from the valence band. Thus, $n = p = n_i = p_i$, with n_i and p_i being the intrinsic electron and hole concentrations, characteristic of each semiconductor. As this concentration is characteristic of each semiconductor, it is necessary to estimate it to understand the properties of the semiconductor. In this regard, the electron density can be estimated from the density of states and the distribution function. The former was described in Eq. 2.16. The distribution function is an estimation of the occupation number of any of the energy levels of the studied system, as long as this system is in equilibrium. For this, the free energy of the system is minimized. In the particular case of electrons[28], the distribution function $f(E)$ is,

$$f(E) = \frac{1}{\exp\left[\frac{E - E_F}{k_B T}\right] + 1} \qquad \text{[Eq. 2.17]}$$

where E is the energy of the system, k_B is Boltzmann constant, T is the temperature and E_F is the Fermi level[47]. The Fermi level is an energy level at which, in thermodynamic equilibrium, there is a 50% probability that this level is occupied. Putting these two concepts together (density of states and distribution function), the electron density in the conduction band can be estimated by

$$n = \int_{E_c}^{\infty} N_e(E) f(E) dE = \frac{1}{2\pi^2}\left(\frac{2m_e^*}{\hbar^2}\right)^{3/2} \int_{E_c}^{\infty} \frac{(E - E_c)^{1/2}}{\exp\left[\frac{E - E_F}{k_B T}\right] + 1} dE \qquad \text{[Eq. 2.18]}$$

which for small values of n, when the unity in the distribution function can be disregarded, results in

$$n = N_c \exp\left(\frac{E_F - E_c}{k_B T}\right), with\ N_c = 2\left(\frac{m_e^* k_B T}{2\pi\hbar^2}\right)^{3/2} \qquad \text{[Eq. 2.19]}$$

with N_c being the effective density of states in the conduction band and m_e^* the effective mass of electrons. If an analogous derivation is carried out for holes, then the hole concentration p obtained is

$$p = N_v \exp\left(\frac{E_v - E_F}{k_B T}\right), with\ N_v = 2\left(\frac{m_h^* k_B T}{2\pi\hbar^2}\right)^{3/2} \qquad \text{[Eq. 2.20]}$$

Therefore, if the product np is calculated, the expression obtained is such as,

$$np = 4\left(\frac{k_B T}{2\pi\hbar^2}\right)^3 (m_e^* m_h^*)^{3/2} exp\left(\frac{-E_g}{k_B T}\right) \qquad \text{[Eq. 2.21]}$$

which indicates that the product *np* is independent of the Fermi level, being only dependent on the temperature and the intrinsic properties of the semiconductor in question. As such, the concentration of electrons and holes are inversely proportional for an intrinsic semiconductor in such a way that if one increases, the other must decrease. Moreover, the relation $n = p = n_i = p_i$ is true for intrinsic semiconductors and, thus, Eq. 2.21 can be expressed for the concentration of the individual charge carriers as

$$n_i = p_i = 2\left(\frac{k_B T}{2\pi\hbar^2}\right)^{3/2} (m_e^* m_h^*)^{3/4} exp\left(\frac{-E_g}{2k_B T}\right) \qquad \text{[Eq. 2.22]}$$

From Eq. 2.22, the actual Fermi level energy can be approximated[28] as a value dependent on the energy of the conduction and valence band as well as the effective masses of the electrons and holes as

$$E_{Fi} = \frac{E_c + E_v}{2} + \frac{3}{4}k_B T \ln\left(\frac{m_h^*}{m_e^*}\right) \qquad \text{[Eq. 2.23]}$$

Thus, for an ideal approximation in which $m_e^* = m_h^*$, the Fermi level of an intrinsic semiconductor will lie exactly in the middle of the bandgap. In real semiconductors, this equality is not true and the Fermi level will be slightly shifted towards the valence or the conduction band. From this discussion, it is observed that the carrier concentration in intrinsic semiconductors is highly dependent on the temperature. This, is turn, is problematic for the application of these materials to devices as the flow of a current will induce heating that will increase the carrier concentration. If this concentration is high enough ($\sim 10^{15}$ cm^{-3}), the leakage current during operation will be too high, disrupting the efficient functionality of the device. Therefore, it is necessary to control the carrier density of a semiconductor to ensure an efficient performance. This is achieved by a process known as doping[48], which was briefly mentioned previously in the discussion of the point defects of a crystalline solid. Doping in semiconductor technology refers to the controlled introduction of impurities in the lattice of a semiconductor to modulate its optoelectronic properties[49]. This can be achieved during the growth of the semiconductor or in post-growth processing by means of diffusion or ion implantation. The introduction of the

impurities (dopants) aims to provide additional electrons or holes to the semiconductor, allowing the tunability of properties of the semiconductor such as its conductivity or response to light.

To exemplify doping, the case of silicon is discussed here. Silicon is an element that has four valence electrons. When a dopant is introduced into silicon, it will substitute for one of the silicon atoms. In order to obtain a significant change in the semiconducting properties of silicon, the electronic structure of the dopant must be different to that of the silicon, meaning that the number of valence electrons cannot equal four. Therefore, the most common doping agents used with silicon are elements from Group V and Group III of the periodic table. Using a Group V element (N, P, As or Sb) as a dopant will induce an excess of electrons into the electronic structure, as these elements have five valence electrons. Therefore, doping with Group V elements is known as donor doping[50], as additional electrons are provided to the electronic structure of the semiconductor, turning silicon into an n-type semiconductor. In contrast, Group III elements (B, Al, Ga or In) have three valence electrons. As such, the introduction of one of these elements as a dopant will induce a deficit of electrons, i.e. an excess of holes. Thus, Group III dopants are known as acceptors[51] and their introduction leads to silicon becoming a p-type semiconductor. From a band structure point of view, these doping agents introduce new energy levels in the bandgap, in close proximity to the valence and conduction bands, that directly affect the dynamics of the charge carriers in the semiconductor. Figure 2.8a,b shows a schematic of the atomic and band structure of silicon doped with Group V and Group III elements, respectively. The excess charge carriers (electrons or holes) introduced by the doping (n-type or p-type) are mobile within the structure of the semiconductor and, hence, the new energy levels appear in the bandgap. These levels are placed in proximity of the corresponding band, depending on the type of charge carrier: conduction band for electrons and valence band for holes.

The "type of semiconductor" has now been briefly introduced and it refers to the majority type of carrier, i.e. the type of charge carrier that has a higher concentration in the semiconductor compared to its intrinsic form. In this sense, n-type semiconductors have electrons as the majority charge carriers, while p-type
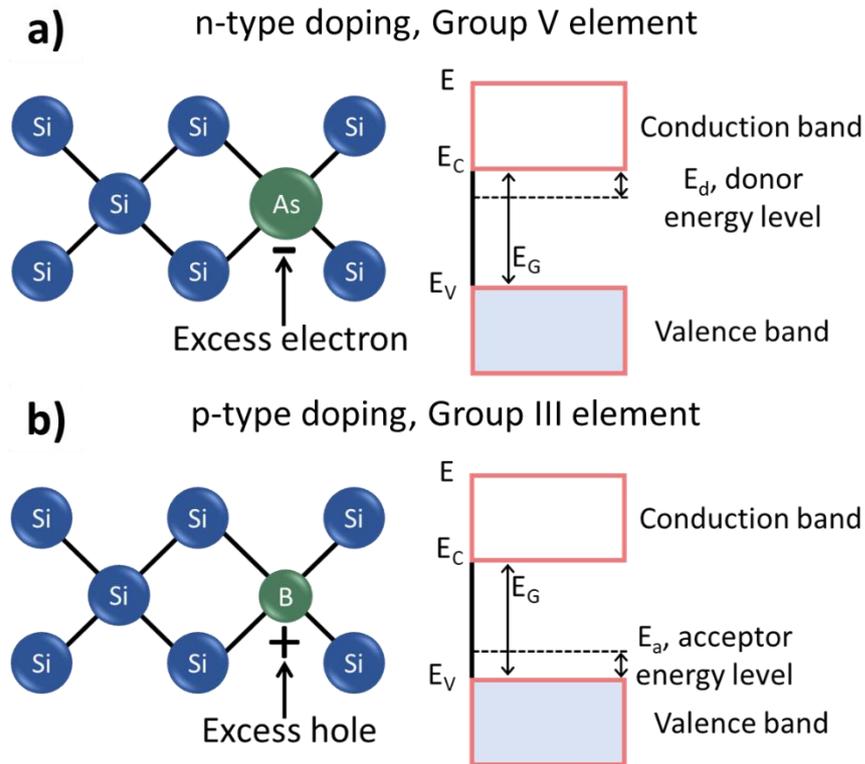
Figure 2.8. Schematic of the atomic and band structure of silicon doped with **a)** Group V and **b)** Group III elements. The excess electrons and holes are mobile charge carriers introduced in the semiconductor structure as a result of the doping with an element that has a different number of valence electrons compared to silicon, inducing the presence of new energy levels in the band structure.

semiconductors have holes as the majority carrier. Doping can also be utilized in semiconductors that have an intrinsic n or p-type character to modulate their optoelectronic properties. This is of interest from a technological point of view as it can help tune the optical character of a semiconductor, its semiconducting properties or can confer it with properties otherwise unattainable such as chemical sensitivity or photoresponsivity. As ZnO is the focal point of this thesis, doping of ZnO and its influence on the optoelectronic properties of the material for functional applications will be thoroughly discussed, with a theoretical introduction provided in Chapter 3 and the results obtained from a doping study shown in Chapter 6.

2.2.5 Excitation of charge carriers

So far, the description of the charge carriers in a semiconductor has been made considering the equilibrium state. However, most processes in which semiconductors are used involve some form of excitation. The most basic type of excitation is thermal excitation. In this sense, the influence of shifting from 0 K to a finite positive temperature was described. This is the simplest form of excitation. Other possibilities

are electric or light-based (photonic) excitations. Independently of the source of the excitation, its effect is the same: the extraction of an electron from the valence band. Since the aim of this thesis is to demonstrate the functional application of ZnO-based nanostructures on photoelectrochemical water splitting, the discussion of the excitation of charge carriers and its consequences will be based around photonic excitations, i.e. excitation from a light source.

Photonic excitation takes place when a photon reaches the semiconductor and excites an electron. The excitation will directly depend on the energy of the incoming photon, which is dependent on the wavelength of the photon. Therefore, the energy of the photon E_{ph} is

$$E_{ph} = \frac{hc}{\lambda} = h\nu \qquad\qquad \text{[Eq. 2.24]}$$

with h being Planck's constant, c the speed of light in vacuum, λ the wavelength of the photon and ν the frequency of the photon. When the photon reaches an electron in the valence band, the energy of this photon is transferred to the electron, exciting it and removing it from the valence band. This removal leads to the creation of a hole, thus the photonic excitation is said to generate electron-hole pairs. This excitation process[45] is schematically represented in Figure 2.9a. When a photon with energy E_{ph} reaches an electron in the valence band with energy E_i, it will be excited to a final position with energy E_f, represented here in the conduction band. Thus, this interband transition can be represented through the conservation of energy as

$$E_f = E_i + E_{ph} = E_i + \frac{hc}{\lambda} \qquad\qquad \text{[Eq. 2.25]}$$

As such, the final position of the excited electron will be dependent on the wavelength of the incoming photon. Moreover, for this transition to take place, the sum of the energies, E_f, has to be such that $E_f > E_G$, i.e., the energy of the photon has to be enough to excite the electron from the valence to the conduction band. This is a critically important concept for any photonic-based application such as solar cells as it marks the possible range of functional application of a semiconducting material. In this sense, photoelectrochemical applications or solar cells should ideally work in the visible region of the electromagnetic spectrum, which implies a range of wavelengths between 380 nm (violet) and 750 nm (red). This wavelength range
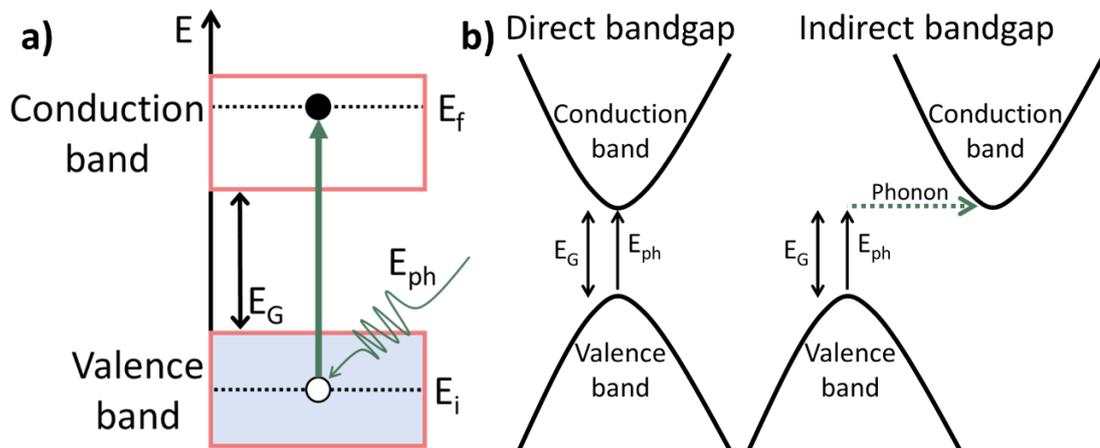
Figure 2.9. a) Schematic representation of the photonic excitation of an electron from the valence to the conduction band, dependent on the energy of the photon. **b)** Representation of the photonic excitation of an electron from semiconductors with a direct or indirect bandgap and the consequent necessity of a phonon for the latter case.

corresponds to an energy band between 3.3 eV and 1.65 eV. Therefore, depending on the bandgap (E_G) of the semiconductor, it should be able to absorb and utilize different portions of the visible electromagnetic spectrum. In this sense, lower bandgaps such as that of GaAs are typically more desirable as these allow the use of a broader region of the visible spectrum.

Another important feature of the photonic excitation of a semiconductor is the relationship between this excitation and the type of bandgap that the semiconductor in question has. Previously, it was discussed that semiconductors can have a direct or indirect bandgap, depending on the relative position of the top of the valence band and the bottom of the conduction band. These two cases are presented in Figure 2.9b. The case of a direct bandgap was detailed in Figure 2.8a, in which the energy of the photon is sufficient to excite an electron from the valence band to the conduction band. In the case of indirect bandgap semiconductors, the energy of the incoming photon is not enough to excite an electron to the conduction band, due to the displacement of the bottom of the conduction band with respect to the top of the valence band, as depicted in Figure 2.8b. Therefore, the presence of a phonon is required for the excitation of an electron from the valence to the conduction. Otherwise, the energy of the photon will not suffice to excite the electron to the conduction band.

Once an electron has been excited, the system will tend to return to its equilibrium state. This means that the photogenerated charge carriers will undergo

a process known as recombination, with the system returning to a relaxed state once the excitation source is no longer present. This recombination process is of considerable importance in semiconductor technology. In general terms, the recombination process describes the relaxation of an electron in the conduction band by which it loses energy and re-occupies an available site in the valence band. There are two main types of recombination processes, i.e. radiative and non-radiative. To understand and distinguish between the two, there is a parameter for the charge carriers that must be studied: the carrier lifetime. This parameter is a measure of the average time it takes for a minority charge carrier to recombine. In this sense, the carrier lifetime has two components, i.e. the radiative and non-radiative lifetimes. Whichever is shorter will determine the most likely outcome of the recombination process. Therefore, the charge carrier lifetime can be expressed[28] as,

$$\frac{1}{\tau} = \frac{1}{\tau_r} + \frac{1}{\tau_{nr}}$$
[Eq. 2.26]

where τ, τ_r, τ_{nr} are the average, radiative and non-radiative carrier lifetimes.

Radiative recombination, or more specifically band-to-band radiative recombination, is a process by which an electron from the conduction band relaxes into the valence band. This process involves a form of spontaneous emission, typically a photon. Due to the difference between direct and indirect semiconductors explained previously, the radiative recombination of carriers is only meaningful in direct bandgap semiconductors as the requirement of a phonon for indirect materials makes it less significant[45]. Non-radiative recombination is a relaxation process akin to the radiative one, but involves a phonon instead of a photon, which heats the semiconductor. This is detrimental for photonics applications of semiconductors and, thus, is an undesired process. There are three main pathways for non-radiative recombination[52] of charge carriers:

- Trap-assisted recombination, which occurs when an electron is captured by a trap state in the bandgap. Trap states are interband states that form in a semiconductor due to the presence of a foreign atom (dopant) or defect. Their presence may be unintentional, as an impurity, or intentionally inserted in the semiconductor. Trap states capture electrons and, once filled, they cannot accept

any more charge carriers. It is possible that, in a secondary step, the electron will further relax to the valence band to occupy an empty state, finishing the recombination process. This trap assisted recombination is commonly known as Shockley-Read-Hall (SHR) recombination[53].

- Auger recombination is another relaxation process by which the energy released during the electron-hole recombination is transmitted to a tertiary charge carrier, exciting it to a higher energy level. This excitation is not enough to move the tertiary carrier to a new energy band and, hence, it will lose its excess energy by thermal vibration.

- Surface recombination is a process similar to the trap-assisted recombination, but takes place at the surface of the semiconductor. This is possible due to the presence of surface defects, i.e. trap states, on the surface of the material due to defects in the crystalline structure. This type of recombination is of special interest in the ZnO field, as will be discussed in Chapter 3 and shown in Chapter 6 in the transition metal doping of ZnO.

For more information on non-radiative recombination of charge carriers in semiconductors, please refer to the work of Abakumov[54]. The concepts of photogeneration and recombination of charge carriers will be used throughout this thesis to understand the optoelectronic properties of ZnO, how these can be tuned and their influence on the functional performance of ZnO-based nanostructures.

The aim of this section was to provide a summarized introduction to the most important concepts and ideas required for the understanding of the semiconductor technology and physics that will be further developed for the particular case of ZnO, which is the focus of this work. As noted at the beginning of the section, there are other works that develop a deeper insight into semiconductor technology, physics and applications and the reader is referred to those. From the discussion in this section, there are some key concepts that will be of particular interest for this work in the later chapters of this thesis, namely the crystalline and electronic structure of semiconductors, doping, point defects and the photogeneration and recombination of charge carriers. It should be noted that the main purpose of this section was to briefly present the notions of semiconductor physics using the most common semiconductor, i.e., silicon, before introducing ZnO NWs in Chapter 3. This is because

ZnO NW is more complex, but the main semiconductor investigated in this research. Using Si concepts such as electronic band structure, energy bandgap, impurity doping will help understand better the properties of ZnO NWs. For illustration, it helps understand better how the doping of ZnO is exploited to modify and control the energy bandgap of ZnO for various applications, including in photoanodes.

2.3 Semiconductor morphologies

In the previous section, the properties of a semiconductor were described at an atomic level, discussing the theoretical background that makes this type of material such an important piece of modern society. However, the design of semiconductor devices, from small circuits to computers or solar cells cannot be done at such a miniscule level. It is thus necessary to study and understand the different shapes that a semiconductor can take, i.e. the morphologies of a semiconductor. These morphologies will be discussed in this work in terms of their size, going from macroscale morphologies such as thin films or single crystal silicon to nanomorphologies of few nanometres in size, like quantum dots. Note that this section only consists of a brief description of different morphologies and their main applications. A more thorough discussion on this topic lies outside the scope of this work.

As discussed in the introductory chapter, silicon is the most important semiconductor element and has been the driving force of the current Information Era we live in. As a consequence, the first morphology to be discussed is silicon itself. Silicon is utilised in the semiconductor industry as a pure element (or doped to tune its properties) and, for this, there are three main allotropic morphologies used: amorphous silicon, monocrystalline silicon and polycrystalline silicon[55]. All three are formed of pure silicon and their only difference lies in the ordering of their crystalline structure, going from having no crystal structure (amorphous) to having a multi grains or single crystal structure. Each of these allotropes have different applications due to their properties:

- Amorphous silicon has been mostly utilised in photovoltaic and display technologies. Its application in photovoltaics is due to its low-cost, although it exhibits a low efficiency compared to its crystalline allotropes. In display

technologies, amorphous silicon has been widely utilised as the active layer in thin-film transistor (TFT) liquid crystal displays (LCDs). More information on this morphology can be found on the detailed work of Street[56].

- Polycrystalline silicon is formed by small Si crystallites that have different crystalline orientations. This silicon allotrope is widely utilised in integrated circuits, mostly as a gate material in different transistor technologies[57]. However, its widest application is in photovoltaics, where polycrystalline silicon solar cells are and have been the most widespread solar technology in the world[58]. Although their efficiency is lower than monocrystalline silicon solar cells, their lower price and availability to be deposited onto a variety of substrates has made this morphology the most attractive for the photovoltaics industry[55].

- Monocrystalline silicon is the single crystal form of silicon. Its primary application is in the fabrication of integrated circuits and discrete components that are the base of the semiconductor device fabrication industry. The single crystal character of this morphology makes it the most expensive and most efficient allotrope of silicon. Hence, its use in photovoltaics is generally more limited to applications where the efficiency is prime over the cost. At the same time, being single crystal means that it is possible to build billions of transistor-based devices in a single chip as there will be no defects that can hinder the functionality of these devices. This has led the electronics industry to the development of a large single-crystal silicon processing facilities.

The second most important morphology to be discussed is thin films. A thin film is a layer of material mainly characterized by its thickness. Thin films can be used as flat films of a material or as a conformal coating of a different morphology. Independently of this, the controlled deposition of thin films is fundamental for a wide variety of semiconductor applications. Advances in thin film technology have been necessary for the development of technological breakthroughs such as light-emitting diodes[59] (LEDs), magnetic storage[60, 61], photovoltaics or coatings[62] (antireflective or hydrophobic coatings, for example). Depending on the application, the thickness of the thin film can vary, ranging from hundreds of micrometres in solar cells to few nanometres in magnetic storage. Semiconductor thin films can be deposited with virtually any semiconductor available, from the aforementioned

polycrystalline silicon in photovoltaics to GaAs or GaN in LEDs. More information of thin films can be found in the work of Frey[63]. Thin films and the allotropic morphologies of silicon represent the two largest semiconductor morphologies in the world and in the electronics industry. However, other semiconductor morphologies have been one of the focal points of researchers in the last two decades owing to the incredible potential that these morphologies display for new and improved applications and functionalities[64-66]: nanoscale morphologies (nanomorphology) or nanostructures. These morphologies are characterized by having at least one of their dimensions in the nanometre scale. Therefore, these morphologies are classified on this basis in this work as three-dimensional (3D), when all the dimensions are below 100 nm, two-dimensional (2D) if one dimension is above 100 nm and one-dimensional (1D) if two are above 100 nm.

The first and possibly most extended example of a nanomorphology is the nanoparticle. Nanoparticles (NPs) are 3D nanomaterials that can take many different forms (stars, spheres, rods, fibres, cages) as long as their dimensions remain within the constraints mentioned previously. Due to their extremely small size, NPs are, in most cases, subjected to quantum effects that would otherwise not be significant in bulk materials[67]. As such, semiconducting NPs have gathered significant attention from researchers as the possibilities of these nanostructures seem limitless due to the possible exploitation of features such as quantum confinement[68]. These NPs can also be used as photosensitizers for other materials and morphologies, granting them a higher sensitivity towards light[69]. Semiconductor materials such as Si, TiO_2, CdSe or Fe_2O_3 have been widely investigated as NPs[70]. A particular case of NPs is quantum dots (QDs), which are characterized for their extremely small size in the order of a few nanometres. The miniscule size of QDs means that, from a semiconductor point of view, their properties are in between a bulk semiconductor and the constituent atoms, to the point where they can have discrete electronic states that can be quantized. Furthermore, their optoelectronic properties are directly dependent on their size. This can be exploited, for example, to control the wavelength of an emitted photon from a semiconducting QD[71], meaning that it is possible to control the colour of the light emitted from a QD. Due to these features, QDs have been widely studied in light emitting applications (LEDs, lasers), photovoltaics or as photodetectors.

Two-dimensional nanomaterials can take a large variety of shapes such as nanoribbons, nanobelts, nanorods (NRs), nanowires (NWs) or nanotubes (NTs). Out of these, the last two are the most important and most studied of these nanomorphologies. NTs are elongated rod-like hollow nanostructures. Their diameter is in the nanometre scale, while their length is usually unconstrained. These tubes are typically cylindrical in shape and their inner diameter can vary. The most well-known type of nanotube are carbon nanotubes (CNTs), which consist of one or more cylindrical layers of hexagonally bonded carbon. One important feature of NTs (and of 2D nanomorphologies in general) is their aspect ratio, which is the relationship between their length and their diameter. Semiconducting NTs (except for CNTs) have not been the subject a research as widespread as other 2D counterparts have shown more promise.

In contrast, semiconductor NWs (and to a lesser extent NRs), have been thoroughly studied due to their attractive properties and control over their growth. NWs and NRs are similar structures (rod-like prismatic nanostructures) that differ in one key facet: their aspect ratio. A NR is considered to have an aspect ratio below 10, while NWs have an unconstrained but larger aspect ratio. In both cases, the diameter of these nanostructures is expected to be in the nanometre or tens of nanometres range. Similarly to NPs, those NWs of a sufficiently small diameter will feature quantum confinement provided the short lateral charge transfer in these morphologies. Hence, the energy levels observed in NWs can differ from those observed for bulk materials. Semiconductors such as ZnO, Si, GaAs, InGaAs, Fe_2O_3, SnO_2 or TiO_2, to name a few, have been grown in NW or NR morphology for their functional application towards electronic devices such as transistors, solar cells, gas sensors, photodetectors or quantum computing.

Regarding 1D nanomorphologies, there is a large variety of different shapes and structures that nanomaterials can adopt, from nanoflowers to nanorings or nanocages. These morphologies have only one dimension in the nanometre scale (the thickness of a nanoring, for example). These morphologies are characterized by being considerably more complex than NPs or NWs, making their integration in industry-scale applications remarkably complicated. Nonetheless, they have been

introduced in applications such as sensing[72] or bio-immobilization[73], albeit with less success than their 2D and 3D counterparts.

This brief mention of semiconductor morphologies has been provided as an overview of how vast and complex the field of semiconductor research has become. In this work, attention is directed towards ZnO nanowires as the semiconductor and morphology of choice. A thorough description of ZnO from a material science point of view, its properties, morphologies, applications, tunability and growth is provided in Chapter 3 as the backbone for the discussion of the results obtained in this work, which are shown in Chapters 5-8.

2.4 Photoelectrochemical water splitting of semiconductors

In Chapter 1, it was outlined how this thesis targets the study and development of new avenues to enhance the functional performance of ZnO NWs as photoanodes in the photoelectrochemical (PEC) water splitting. This process is based on photoelectrochemistry, the interaction between light and a semiconductor submerged in an aqueous bath. The working principle of this process is based on using a semiconductor that can absorb photons when under illumination (following the concepts described in the previous sections) in such a way that the energy coming from these photons will be transformed into chemical energy, which comes from the bonds between oxygen and hydrogen in the water molecules of the aqueous solution. Therefore, in this section, an introduction and theoretical background to the core concepts that govern photoelectrochemical water splitting will be provided, establishing its origins, the potential of this technique, its main shortcomings and the hurdles that research is trying to overcome. Following this, details of the principal metrics that determine the PEC performance of a semiconductor, especially with regards to the different efficiencies will be subsequently discussed. Finally, a summary on how these metrics were experimentally obtained in this work, including their constraints and requirements, will be presented.

2.4.1 Theoretical background of photoelectrochemical water splitting

In general terms, photoelectrochemistry is the part of physical chemistry that deals with interaction of light and electrochemical systems. Photoelectrochemical water splitting is a particular strand of photoelectrochemistry that investigates the

production of hydrogen from water and solar energy. This strand was initiated in 1972 with the work of Fujishima and Honda[20], in which they described the photolysis of water molecules using TiO_2 photoanodes. Photolysis is the process by which a molecule is decomposed as result of its interaction with photons. Since this work was published, PEC water splitting has garnered large amounts of attention from researchers as it could potentially solve the one of the everlasting problems of modern society: finding an energy source that is reliable, renewable and that could cope with the increasing demands of energy. This was described in Chapter 1.

The working mechanism of photoelectrochemical water splitting is, in its basic form, rather simple. A semiconductor material (ZnO in this work, acting as photoanode) is introduced in an aqueous solution (denominated from now on as electrolyte) and it is exposed to light. This light can come from a solar simulator if it is a laboratory scale experiment or, in the ideal and real case, the light source would be the sun. The semiconducting photoanode will absorb photons from the light source with sufficient energy to overcome its bandgap (as explained in the previous section) that will consequently generate electron-hole pairs. These are then transferred to the photoanode-electrolyte interface, where the charge carriers will initiate a redox reaction with water, resulting in the oxidation of water to yield oxygen and hydrogen gas. Although this process may seem straightforward, there are a multitude of parameters and considerations to successfully achieve a PEC water splitting process that is both efficient and durable at the same time. The discussion in this section regarding PEC water splitting is provided at a basic level and centered around an n-type semiconductor photoanode to accurately represent ZnO in a PEC water splitting system. This describes the most important topics as well as those of concern to the results developed in the later chapters of this thesis. For more information, please refer to the work of Memming[45] for general concepts of electrochemistry and the works of Walter[22] and Chen[74] for photoelectrochemistry.

Before delving in the details of the water splitting process and all the considerations it entails, it is necessary to describe where the water splitting reaction is carried out. No matter if the process is studied at laboratory scale or at larger, industrial scale, the water splitting process takes places in a photoelectrochemical cell. A schematic of this cell is presented in Figure 2.10. This figure is the cornerstone
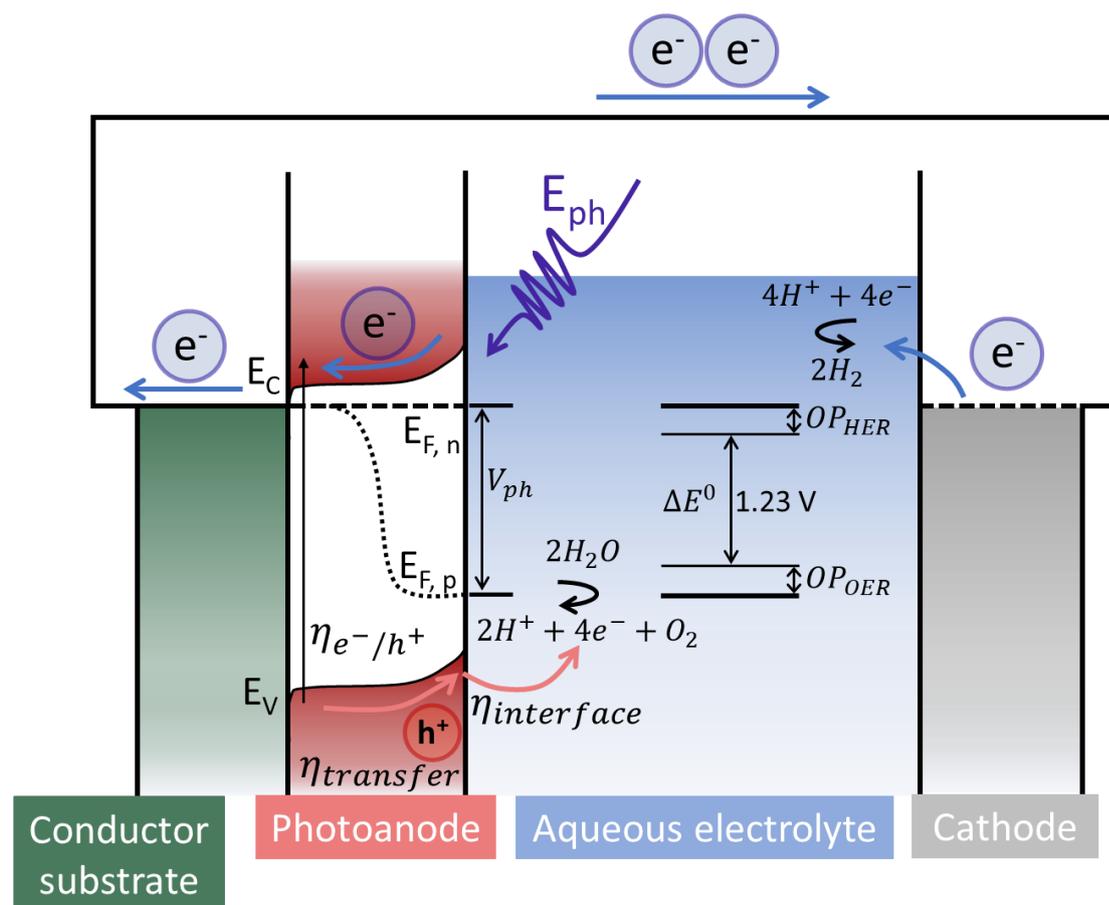
Figure 2.10. Schematic band structure and working mechanism of a photoelectrochemical cell based on an n-type semiconductor photoanode, illustrating the photogeneration of electron-hole pairs, the transport of this charge carriers, the energies required for the water splitting process to take place and the main water splitting reactions.

of this section as the most important features of the water splitting process will be explained from it. The basic parts of the cell are the two electrodes and the aqueous electrolyte. For the particular case of n-type semiconductor PEC cells, the photoanode is a semiconductor (ZnO in this thesis) while the cathode (also referred to as counter electrode) will be made of a well-studied and stable material (platinum here) that ensures that any effect observed during the PEC study can be directly attributed to the photoanode, which is the electrode of interest. In between the two there is an aqueous electrolyte. In an ideal case, this electrolyte would be normal, unaltered water. However, in the work carried out in this thesis, the electrolyte was an aqueous solution of KOH, used to set the pH of the solution to a value of 13 to ensure a better charge transfer in the electrolyte. The final structural part of the cell is the substrate on which the photoanode is deposited. This substrate has to fulfil two conditions: to be transparent and to have high conductivity to efficiently transfer

electrons. Thus, indium-tin oxide films on glass (ITO/glass or ITO for simplicity) substrates were selected. As stated earlier, the key component of this PEC cell is the semiconducting photoanode and, as such, it will be the focal point in the discussion.

Under illumination (marked in Figure 2.10 by E_{ph}), the semiconducting photoanode generates electron-hole pairs. The position of the valence and conduction bands are represented by E_v and E_c, respectively. The charge-carriers are generated and separated with an efficiency labelled as η_{e^-/h^+}. This will be discussed in more detail in a later part of this section. Once separated, the charge carriers are required for two different parts of the water splitting process and, for this, they are transferred to the electrolyte (holes) and to the counter electrode (electrons) with a transfer efficiency, $\eta_{transfer}$, associated to them.

For the PEC setup discussed here, holes play the most important part as they are the ones that initiate the water splitting process. Moreover, as this cell is based on an n-type semiconductor, holes will also be the minority charge carriers, meaning that the better the charge separation process is, the higher the number of available holes will be, boosting the PEC performance of the cell. This is particularly important as research has shown that the water splitting process typically involves two water molecules and, therefore, four holes[75, 76], meaning that a high number of holes is required to obtain significant amounts of hydrogen. The water splitting process can be divided into two sub-reactions, namely the oxygen evolution reaction (OER) and the hydrogen evolution reaction (HER). The names of these two reactions are self-explanatory in the sense that the OER governs the production of oxygen from water and the HER, the production of hydrogen from the H^+ produced during the OER. Both sub-reactions are presented in Figure 2.10 next to the electrode in which they take place, i.e. the photoanode for the OER and the cathode for the HER.

Holes are the driving force of the OER as these supply the energy required to split the O-H bond of water and thus start the water splitting process. Once the water splitting process has been initiated and H^+ produced in solution, these will migrate in the electrolyte towards the cathode, where they will react with the photogenerated electrons, thus forming hydrogen as a final product. Therefore, the efficient transfer of photogenerated electrons and holes from the respective electrodes to the

electrolyte is paramount for a competitive water splitting material, determined by the $\eta_{interface}$ efficiency.

Regarding the energy required for the water splitting process to be started, there is a base requirement of 1.23 V associated with the minimum thermodynamic work that the needs to be supplied to water to break the O-H bonds. This minimum thermodynamic work is represented in Figure 2.10 by ΔE^0. However, this energy requirement is only for an ideal case and, in reality, the energy required for the water splitting process will be larger due to the presence of kinetic overpotentials, represented as OP_{OER} and OP_{HER} for the respective half-reactions[74]. A kinetic overpotential is the energy difference between the theoretical potential difference required and the real, which is obtained experimentally. These overpotentials are associated with the energy required to drive the kinetics of the OER and HER half-reactions at the surface of the electrodes. Accounting for these additional energy requirements, the total driving force required for the water splitting process was represented as a photovoltage V_{ph}, which is always lower that the bandgap of the semiconductor used as the photoanode, as a result of losses related to the recombination (mostly trapping) of charge carriers. In this sense, the photovoltage V_{ph} can be understood as the potential difference between the quasi-Fermi levels of the holes ($E_{F,p}$) and the electrons ($E_{F,n}$). These quasi-Fermi levels represent the Fermi level for the corresponding charge carrier, once the carriers have been displaced from the equilibrium, i.e., once the semiconductor is excited by light. In more general terms, efficient and unassisted water splitting will take place when the quasi-Fermi levels of both carriers are such that the photovoltage required for the process is constrained within these two energy levels.

Providing this snapshot of the water splitting process, it is necessary to specify the most important technological factors to be considered in order to design an efficient, sustainable and unassisted photoelectrochemical water splitting system which could be considered as the ideal system:

- Under illumination, the semiconductor must be able to generate enough energy to surmount the thermodynamic requirements and overpotentials characteristic of the water splitting process.

- The bandgap of the semiconductor has to straddle the redox potentials of the OER and HER reactions at the surfaces of the electrodes. In addition to this, the bandgap should be minimized in order to absorb photons from the largest possible portion of the electromagnetic visible spectrum.

- Charge transfer at the surface of the electrodes should be facilitated to minimize the corresponding kinetic overpotential. This is especially true for the semiconductor photoanode as it is where the holes (minority charge carriers) are transferred to the electrolyte.

- The PEC performance of the photoanode must be stable over long periods of time. For this, the semiconductor material selected has to be resistant to photocorrosion, the degradation of the surface of the photoanode due to the photogenerated charge carriers. This particular topic is discussed in more detail in Chapter 8.8.

Finding a material that satisfies these basic requirements has been a very challenging task to which researchers have dedicated the last four decades as the potential of the water splitting process is considerably appealing[22]. An additional consideration should also be made to these requirements. The water splitting process should be as efficient as possible, meaning that as much of the solar energy received by the PEC cell should be utilised in the conversion of water into hydrogen. It is therefore necessary to describe these different efficiencies and other related metrics that are used to describe the PEC performance of a material.

2.4.2 Descriptive metrics of the photoelectrochemical water splitting process

The different efficiencies that characterize a photoelectrochemical system are the most important metric to describe its performance. However, and for comparative purposes in the quest to determine the best performing semiconductor, there are two concepts that need to be defined. The first one is the photocurrent of the PEC cell, defined as the current generated by the photoanode when it is exposed to a light source. In this sense, the photocurrent of an ideal PEC system will be the current generated under solar radiation. Typically, this photocurrent is provided as the current density normalized to the size of the photoanode measured, although the

physical property that is measured is the generated photocurrent. The second one is the applied bias or applied potential. In the previous section, considerations were made for an ideal water splitting cell that only uses photonic excitation to produce hydrogen. However, in most cases, a bias is applied to the PEC cell during operation and testing, which increases the current drawn from the device. However, this applied bias should never overcome the water hydrolysis potential (1.23 V) or, otherwise, the production of hydrogen would shift to a hybrid between photoelectrolysis and conventional electrolysis, meaning that it would not be possible to attribute how much each of the two processes is contributing to the water splitting process. These two metrics will be used throughout the discussion of the most common efficiencies that help describe the performance of a PEC system.

The most important efficiency (and metric) of a PEC system is the solar-to-hydrogen (STH) efficiency. The STH efficiency measures the overall effectiveness of the PEC system in transforming solar energy into hydrogen. As such, it is a direct measure of how good the functional performance of a semiconductor in water splitting is. In its most pure form, the STH efficiency is measured at zero-bias, meaning that there is no bias applied to the system, and the amount of hydrogen generated is directly measured as a rate of mmol over time. Thus, the formal definition of the STH efficiency is the ratio between the chemical energy of the hydrogen produced and the amount of solar energy that reaches the system. Following this definition, there are two necessary remarks. First, the chemical energy of the hydrogen produced is defined as the hydrogen generation ratio multiplied by the change in Gibbs free energy for hydrogen, which has a value of $\Delta G_{H_2}^0 = 237$ kJ/mol at 298 K. Second, for PEC experiments in which an artificial light source was used instead of direct solar radiation, a standard common reference for the light intensity was developed to streamline the research efforts in solar-based research. As such, the American Society for Testing and Materials G-173 standard was formulated[77]. This standard is based on a concept known as the air mass coefficient, which defines the direct optical length of a path going through the Earth's atmosphere divided by the path length vertically upwards. This means that the air mass coefficient determines the length that light travels before reaching the Earth's surface as a ratio over the atmospheric length, i.e. at the zenith. Based on the latitude

41

at which most people in the world live, which is at mid-latitudes, it was decided in the G-173 standard to use a solar zenith of 48.2°, which equates to approximately 1.5 times the thickness of the atmosphere. As such, and from now on, all the artificial illumination considered will be denominated as AM 1.5 G based on the 1.5 air mass ratio determined by the G-173 standard of the ASTM. After detailing these two concepts, the STH[74] can be formally defined as

$$STH = \left[\frac{H_{2,prod} \cdot \Delta G_{H_2}^0}{P_{total} \cdot A} \right]_{AM\ 1.5\ G}$$ [Eq. 2.27]

where $H_{2,\ prod}$ is the production rate of hydrogen in mol s^{-1}, $\Delta G_{H_2}^0$ is the Gibbs free energy of hydrogen, P_{total} is the power density of the illumination used in W/cm^2 and A is the area of the photoanode. This representation of the STH is its more formal definition, but it depends on the direct measurement of the amount of hydrogen produced (by gas chromatography, for example), which can be costly. As such, the STH can also be defined from a photoelectrochemical point of view as

$$STH = \left[\frac{j_{SC} \cdot 1.23\ V \cdot \eta_F}{P_{total}} \right]_{AM\ 1.5\ G}$$ [Eq. 2.28]

where j_{SC} is the photocurrent normalized to the area of the photoanode, hence a current density, typically given in mA cm^{-2}, and measured in short circuit conditions, 1.23 V is the potential of the photolysis of water and η_F is the Faradaic efficiency for the HER. The Faradaic efficiency is a measure of how efficiently the electrons transferred to the electrolyte take part in the hydrogen production, instead of being utilised in other parasitic reactions, such as the formation of hydrogen peroxide. The Faradaic efficiency can be obtained as the ratio of the total amount of hydrogen produced and the theoretical amount that would be produced in an ideal system. The description of the STH provided in Eq. 2.27 and Eq. 2.28 is only valid for systems where the stoichiometry between hydrogen and oxygen production is maintained. Although this is a difficult condition to perfectly ensure, it means that there are some constraints on the experimental method followed. One of the most important consequences of this consideration is the fact that the aqueous electrolyte used cannot contain any type of sacrificial molecules such as hole or electron scavengers. In these cases, the STH cannot be measured as the true production rate of hydrogen is unknown due to the accelerants that are introduced. In addition, a measurement

cannot be considered correct if the two electrodes of the cell are in separate compartments with different electrolytes (either different pH or one of the two compartments has a carrier scavenger).

Prior to the definition of the STH, it was discussed how, in most cases, a bias is applied to the water splitting cell to boost its performance. As such, measurements carried out with this condition do not fit in the STH definition as the 1.23 V from the photolysis of water is no longer true. Thus, a new concept known as applied bias photon-to-current efficiency[78] (ABPE) needs to be introduced to account for this applied potential. As stated earlier, only applied potentials lower than the thermodynamic potential required for the photolysis of water can be considered. Taking this into account, the ABPE is defined as

$$ABPE = \left[\frac{j_{ph} \cdot (1.23 - V_{bias}) \cdot \eta_F}{P_{total}} \right]_{AM\ 1.5\ G} \qquad \text{[Eq. 2.29]}$$

where j_{ph} is the photocurrent density and V_{bias} is the applied potential during the measurement, in V. In this case, the applied bias must be based on a standardised known quantity. For this, a reference electrode is introduced in the PEC cell when an applied bias is required. As this is the case for the work presented in this thesis, the next section will discuss the details on this reference electrode and the experimental setup used. Similarly to the STH case, this efficiency can only be correct if the two electrodes are submerged in the same electrolyte (even if they are compartmentalized) and no charge carrier scavenger[79] is included.

The final efficiency to be defined is perhaps the most utilized of those defined here, the incident photon-to-current efficiency (IPCE). This efficiency is a measure of the ratio between photocurrent generated and the photon flux as a function of the wavelength of the photons utilised. The IPCE takes into account the three efficiencies defined in Figure 2.10 as it considers the amount of charges generated per incident photon (η_{e^-/h^+}) and the efficiency of the charge transfer to the electrode-electrolyte interface ($\eta_{transfer}$) and in the interface of the electrode ($\eta_{interface}$). Therefore, the theoretical definition of the IPCE[74] is

$$IPCE = \eta_{e^-/h^+} \cdot \eta_{transfer} \cdot \eta_{interface} \qquad \text{[Eq. 2.30]}$$

where the IPCE is presented as the product of the three aforementioned efficiencies. Similar to the STH, this is a formalism that is complicated to measure in a PEC cell. As such, a different definition of this efficiency in photoelectrochemical terms is required. With this in mind, the IPCE can be defined as a function of the photocurrent measured at each wavelength as

$$IPCE = \frac{j_{ph} \cdot 1240}{P_{mono} \cdot \lambda}$$

[Eq. 2.31]

where j_{ph} is the measured photocurrent normalized to the area of the photoanode, 1240 is a constant obtained from multiplying Planck's constant and the speed of light, P_{mono} is the power density of the monochromatic light at each of the measured wavelengths and λ is the wavelength of the incident illumination. More information on the experimental considerations of the IPCE measurement and what it entails for P_{mono} is provided in the next section. The IPCE can be measured in a cell in which an external bias is applied, as long as this is stated, as the presence of this bias will modify the IPCE compared to the short circuit one. The IPCE is a very useful tool for the design of a PEC system as it allows the spectral analysis of a semiconductor. This means that, from an IPCE measurement, it is possible to determine the range of wavelengths that will provide the highest efficiency, which can be important in the design of multi-material PEC cells in which materials with different bandgaps can be utilised to maximize the absorption of light.

The metrics described in this section form the basis of any PEC analysis, although there are several others that could be considered. Nonetheless, these metrics provide a sufficient background to help understand the theoretical considerations that were discussed previously.

2.4.3 Experimental considerations of a photoelectrochemical cell

In the previous sections, the theoretical background of photoelectrochemical water splitting and its requirements were detailed, along with most significant metrics that govern the behaviour of this process and serve as comparative tools to assess the functional performance of a semiconductor. However, the experimental conditions under which the PEC is carried out also play an important role in the results obtained from these measurements. In this work, a three-electrode PEC cell was utilised, with basic water (pH 13) as the electrolyte used to enhance the change transfer within the

electrolyte, which improved the kinetics of the water splitting process. A schematic of this cell is presented in Figure 2.11. The exact experimental details of the potential and spectral ranges utilised in this work are described in Chapter 4.11, along with the same schematic here presented. The PEC used in this work consisted of three electrodes and a nitrogen gas inlet used to degasify the electrolyte during working conditions, in order to ensure that all the experiments were carried out under the same conditions. The electrolyte used, as previously stated, was a KOH aqueous solution with the pH fixed at 13.

In the previous section, while describing the ABPE, it was mentioned that, in the case where a PEC experiment was to be carried out under an applied potential, a reference electrode is necessary. This reference electrode (RE), along with the photoanode or working electrode (WE) and the platinum counter electrode (CE) forms the three-electrode setup of the PEC cell. A reference electrode is a PEC electrode that has a stable and known potential. The RE is therefore the standard to which the applied bias in the cell is referred. In this work, the reference electrode was a Hg/HgO electrode. The stability of the RE is ensured by encapsulating it in a salt bridge, which is typically formed by a porous membrane. The salt bridge is a device consisting typically of said membrane filled with water and with the reference electrode inside. The mission of the salt bridge is to ensure that the reference
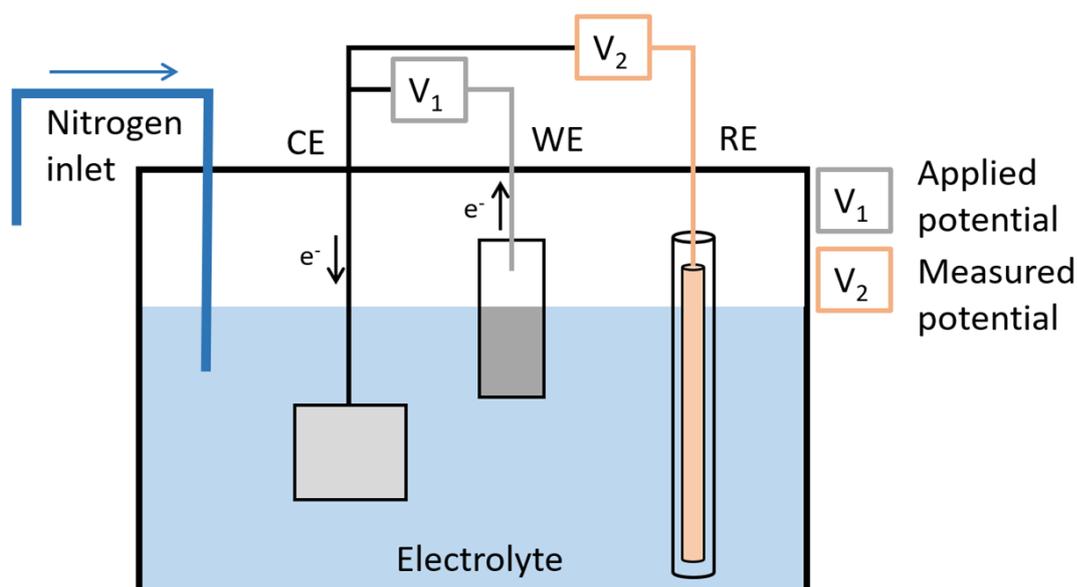
Figure 2.11. Schematic of the photoelectrochemical cell used to measure the water splitting performance of the different ZnO nanowire-based photoanodes developed in this thesis. The cell used consisted of a three-electrode setup along with a nitrogen inlet for the degasification of the electrolyte.

electrode is protected from any drastic transfer of charges of species that could significantly deplete it. In this way, the RE with its salt bridge represents a durable standard that ensures the consistency of the measurements. Although the presence of the salt bridge ensures the durability of the RE, there is an experimental consideration of importance to be considered when carrying out any measurement with such a RE. As the membrane of the salt bridge is filled with water, there is a possibility that, when the RE is put in the electrolyte, a liquid junction potential is formed. A liquid junction potential occurs when two electrolytes of different concentrations or nature are put in contact. In this case, the pH 13 electrolyte is put in contact with the water from the salt bridge. As a result, a diffusion of ions from the electrolyte with a higher concentration will take place, creating a charge dipole between the two electrolytes. This charge dipole will induce a potential difference in this liquid junction that can be measured. As such, before any measurement is carried out, it is essential to ensure that the two electrolytes are in equilibrium as the liquid junction potential can be detected, which would provide a result that does not match the reality. This issue is discussed in Chapter 8.3.

One final consideration regarding the RE is related with the way the photogenerated currents are reported. There is a wide variety of reference electrodes and, hence, obtaining comparative values of the photogenerated currents in a PEC study can be problematic. To solve this issue, all the photocurrent values obtained should be referred to the reversible hydrogen electrode (RHE), which was set as the standard for any PEC analysis. This is achieved by transforming the applied potentials (referenced to the RE used in the measurement) to the RHE by means of the Nernst equation. This equation relates the reduction potential of an electrochemical reaction to the standard electrode potential. Therefore, it is possible to convert the applied bias referenced to the RE, as if it were referred to the RHE using following the expression

$$E_{RHE} = V_{bias} + E_{RE}^0 + 0.059 * pH \qquad \text{[Eq. 2.32]}$$

where E_{RHE} is the resulting applied bias referenced to the RHE, V_{bias} is the applied potential, E_{RE}^0 is the potential of the RE with respect to the standard electrode

potential, 0.059 is a constant in the Nernst equation at standard temperature and *pH* is the pH of the electrolyte of the cell.

In a typical PEC experiment using a three-electrode setup and an applied bias, the desired potential difference is applied between the WE and the CE. At the same time, the potential difference between the WE and the RE is measured. In this way, the potential difference between the WE and the CE is regulated, so that the potential difference between the WE and the RE is equal to the one specified in the software associated with the measurement. These represent the input signals. This applied potential, along with the illumination, will generate a current in the WE (the output), which is measured and sent to the measuring computer. Depending on the type of measurement carried out, the conditions of this applied bias will vary. At any point during the PEC measurements, the light source will be directed at the semiconducting photoanode as this is the only part of the cell that is photosensitive.

Provided the considerations here described for the three-electrode cell, it is necessary to discuss the different PEC measurements that will be utilised in this thesis. The first of these analyses is the I-V curves, otherwise known as sweeping voltammetry. A voltammetry consists of an applied potential sweep in which the current is measured as a function of the applied potential. This analysis can be carried with or without illumination. Both are useful, as they provide information on the dynamics of the PEC process, as well as providing a key parameter that was mentioned during the discussion of the different efficiencies: the photocurrent generated (at an applied potential). In addition, this type of analysis can be done linearly or cyclically, meaning that the applied bias can either be swept from one value to another or it can continuously move from the starting to the final value. An example of cyclic sweeping voltammetry with and without illumination is presented in Figure 2.12. As it can be observed in this example, the photocurrent is reported as a current density, meaning that the photocurrent has been normalised to the area of the photoanode. In addition, the applied bias is referenced to the RHE (instead of being referred to the RE), to enable comparisons with other material systems. In this work, cyclic sweeping voltammetry was selected as the type of voltammetry used for the analysis of the PEC performance, with more details on the results from this analytical technique being shown in Chapter 8.
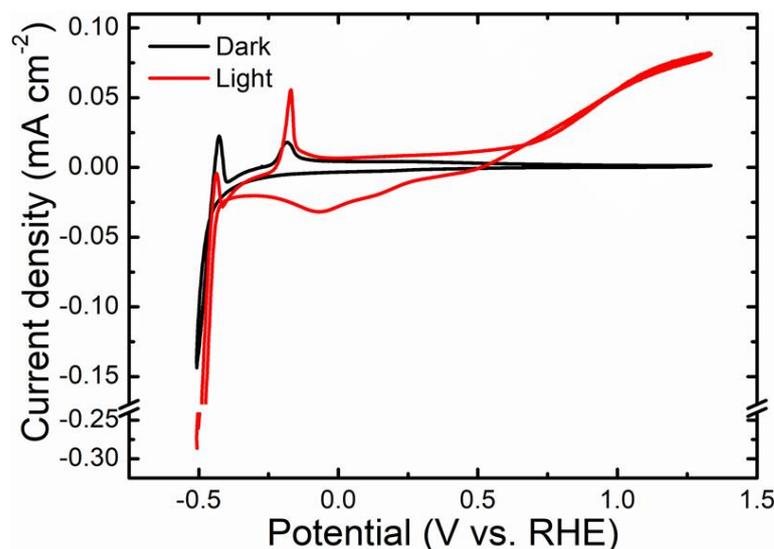
Figure 2.12. Example of a cyclic sweeping voltammetry carried out with no illumination (labelled as dark, in black) and under illumination (labelled as light, in red).

Another analysis of interest to understand the PEC performance of a semiconductor is amperometric analysis, or *I-t* curves. This type of analysis is carried out at a set applied bias, which in this work was set to 1.33 V vs RHE. The photocurrent is measured over time at this applied potential. This experiment is carried out under time-chopped illumination, meaning that every set amount of time (15 second approximately in this work), the illumination was switched from on to off or vice versa. In this way it is possible to study the dynamic response of the PEC system to light and the stability in short periods of time. An example of this type of analysis is provided in Figure 2.13a. The light chopping in this thesis was carried out manually as the monochromator did not incorporate an automatic chopper and, as a result, there is some variation on or off cycles. This was considered to have no significant effect on the information extracted from the amperometric curves.

The final analysis that was carried out for all of the studied samples is the measurement of the IPCE. These were also carried out at 1.33 V vs RHE. As detailed in the previous section (Chapter 2.3.2), the IPCE is a reflection of the amount of photocurrent generated per photon flux on the photoanode as a function of the wavelength of the monochromatic illumination. It consists, therefore, of a wavelength sweep that, in this work, was from 300 nm (ultraviolet region) to 750 nm (red region). An example of an IPCE sweep is shown in Figure 2.13b. As the semiconductor selected in this work was ZnO, which has a large bandgap of 3.3 eV
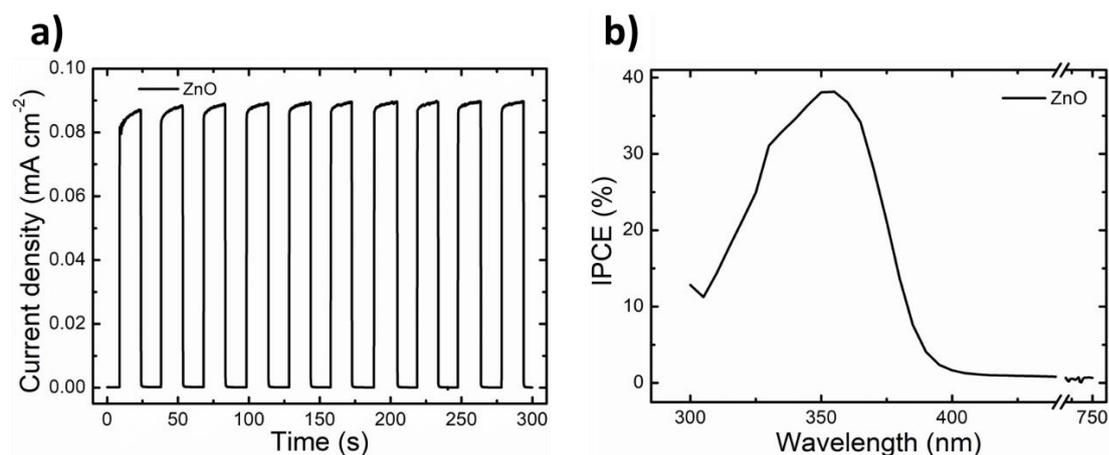
Figure 2.13. Example of an **a)** amperometric *I-t* curve with time chopped illumination and an **b)** IPCE measurement for ZnO.

(around 375 nm), it was expected that no meaningful IPCE would be obtained below 425 nm, hence the plot is cut from 450 nm to almost 750 nm. The IPCE measurements have a direct relationship with the bandgap of the semiconductor studied and any changes in this bandgap can be consequently observed in the IPCE measurement.

In Chapter 2.3.1, it was mentioned that the stability of the photoanode was a key parameter to obtain a competitive PEC water splitting cell. Therefore, functional stability measurements are paramount to understand the longer performance of the semiconductor used as a photoanode. These measurements are based on the measurement of the photocurrent generated at an applied bias (1.33 vs RHE) over a long period of time (5000 seconds in this thesis). The results obtained from these measurements are shown in Chapter 8.8.

The final PEC analyses carried out in this work were Mott-Schottky measurements. These measurements exploit the capacitance that forms at the interface between the photoanode and the electrolyte to measure certain properties of the semiconducting photoanode. To carry out this measurement, an alternate potential is applied to the PEC cell and the frequency of the alternate potential is varied. This gives rise to a plot in which the capacitance of the electrolyte-photoanode interphase is represented against the applied alternate potential (see Figure 2.14). This way, a sequence of points at different applied potentials are obtained. Two crucial characteristics of the PEC can be extracted from this plot, i.e. the flatband potential and the carrier density. The flatband potential, represented by the intercept of the linear best fits, is a potential that allows the establishing of the
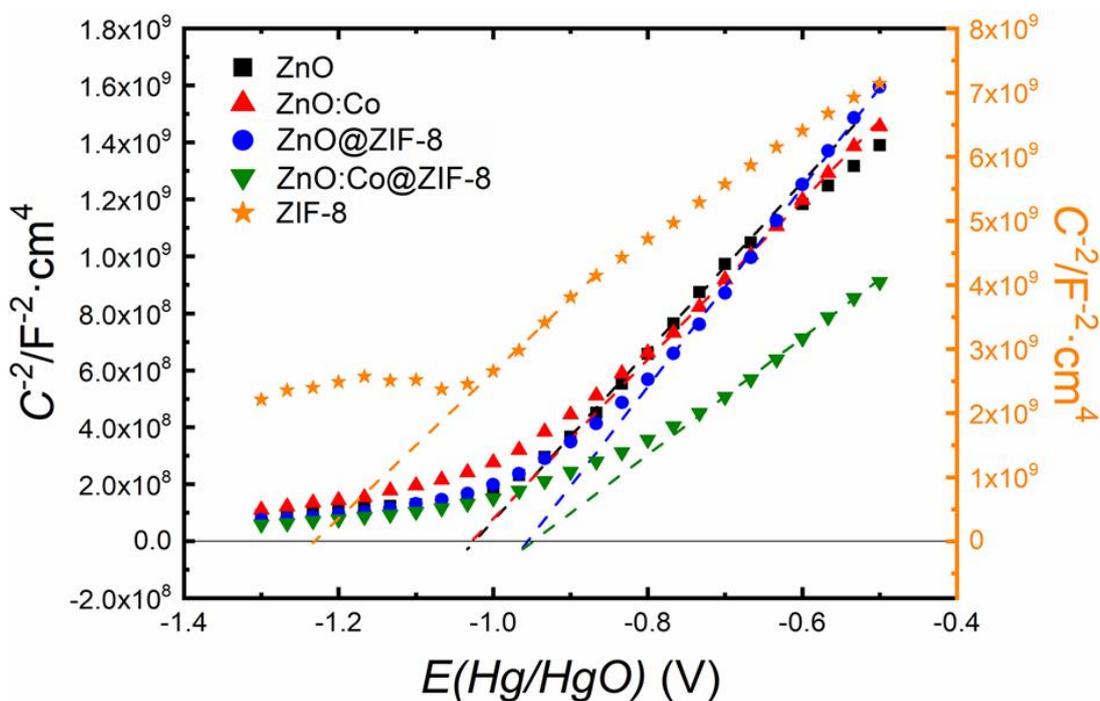
Figure 2.14. Example of a Mott-Schottky plot, in which the data points include dashed lines that represent the best linear fits that are used to study the slope of this plots (and hence the charge carrier density, in a qualitative way) and the flatband potential, which is obtained by the intercept of these best linear fits with the zero capacitance line. The orange coloured axis corresponds only to the ZIF-8 signal (orange coloured data).

relative position of the conduction band of the semiconductor with respect to a reference of potential, which in this case is the RHE. The carrier density can be estimated from Mott-Schottky measurements by analysing the slopes of the best linear fits. In this sense, if two slopes are compared, the larger the slope is, the smaller the density of charge carriers will be for that photoanode. Mott-Schottky measurements are extremely important in the development and design of enhanced photoanodes as they can provide information about the electronic band structure and charge carrier concentrations in a comparative basis, allowing the study and selection of those materials that would fit best the PEC cell requirements set in Chapter 2.3.1.

This section has provided a comprehensive yet basic snapshot of the background and most important considerations to be taken into account in the development and design of new and enhanced photoelectrochemical water splitting photoanodes. With this goal in mind, the later chapters detail into how the performance of ZnO, in this particular case, was improved by designing strategies to overcome some of the characteristic problems of ZnO. This improvement was

evidenced by the efficiencies and characterization metrics described in this section, which are utilised on a comparative basis to obtain the best performing photoanode material combination.

2.4.4 State of the art in semiconducting photoanodes for water splitting

As previously described, ZnO is the material used in this work to develop a PEC water splitting photoanode. Thus, it is necessary to contextualize the current state of the field with respect to the different commonly used semiconductor options available and the current performance of other ZnO-based systems. ZnO has been widely used as a semiconductor material to prepare water splitting photoanodes. Different approaches for the enhancement of ZnO, such as thin film doping[80] or quantum dot sensitization of ZnO NWs[81], have been explored in an effort to obtain the best possible photoanode performance. Other possible routes include the use of plasmonic nanoparticles in ZnO NWs[82], the integration of ZnO NWs and carbon nanomaterials[83] or careful engineering of the interface of ZnO[84] to provide the best possible reaction platform upon which the water splitting process is initiated. These reports focus on enhancing different properties of ZnO photoanodes such as STH or IPCE efficiencies, the overall current density photogenerated, or the average lifetime of the devices. Not only these contributions clearly illustrate the current focus of the state-of-the-art, but they also showcase the wide range of possible parameters that may be adjusted to enhance performance in the field.

It should be noted that there is a significant amount of literature regarding ZnO and photoelectrochemical water splitting, which cannot be covered exhaustively in this thesis. Therefore, the focus here is on some of the published data that are the most relevant developments to this thesis, which are summarised in Table 2.1. This allows the comparison of the performance of our findings with various results reported in the literature, which highlights the contextual significance of this research. Although the list is not exhaustive, the material systems shown in Table 2.1 are considered the most representative to this work, including different ZnO morphologies and other semiconducting metal oxides[85-90]. They provide a realistic benchmark to contrast the results reported in this work against the state-of-the art in the field. Table 2.1 also clarifies the details of the electrolytes used for the

measurement since they may influence the performance of the photoanodes as discussed previously. All the applied potential values given are referenced to the reversible hydrogen electrode (RHE), apart from the N-doped ZnO NRs[88], which is reference to a saturated calomel electrode (SCE) since this information is provided in the corresponding reference. The potential values presented in Table 2.1 are those at which the IPCE values were extracted. The comparison between the different material systems was carried out with respect to the IPCE because this is considered the metric that would better reflect the performance of the photoanodes. Other possibilities, such as the photogenerated current density, were not compared since these are highly dependent on the nature of the material, which, in turn, makes comparisons between materials rather unreliable.

Regarding the unfunctionalized semiconducting metal oxides highlighted in Table 2.1, it is clear that TiO_2 NRs shows a much higher IPCE[85] than any other base material. Hematite NWs[86] (Fe_2O_3) yield a poor IPCE of 4%, four times lower than that of the ZnO NPs[87] (16%). Nonetheless, an adequate engineering of the hematite by coupling it with titanium and a CoFe outer layer[86] results in a vast improvement in the IPCE, increasing it by more than four times, thus resulting in a competitive photoanode in this regard.

Focusing on ZnO, it is shown that thin films[87] yield a poor performance in terms of IPCE. However, as soon as a third dimension is introduced in the material in form of NPs, this IPCE increases. Nitrogen doping of ZnO nanorods[88] (NRs), another combinatorial nanotechnological approach, has been proven to increase this efficiency up to 25%, far above from the 16% obtained for the NPs[87]. Further, a core-shell structure based on ZnO NRs with a $Ni(OH)_2$ catalyst decoration[89] proves to soar the IPCE to 40%. However, comparing these two results with those of the core-shell engineered NWs of this thesis[90], it can be seen that the efficiency at 350 nm is five and two times higher, respectively, rising up to 75% at 350 nm. In terms of efficiency of ZnO material systems, this clearly underlines the importance of this work compared to the most competitive data reported in the literature[85-89].

Table 2.1. Comparison of the electrochemical conditions and performance of different semiconductors and morphologies with the work from this thesis.

Material	Electrolyte	Applied potential vs RHE (V)	IPCE
TiO$_2$ NRs[85]	Na$_2$SO$_4$	1.23	45% @ 380 nm
Fe$_2$O$_3$ NWs[86]	NaNO$_3$ + HNO$_3$	1.23	4% @ 350 nm
Fe$_2$O$_3$/Fe$_2$TiO$_5$/CoFe-PBA NWs[86]	NaNO$_3$ + HNO$_3$	1.23	17% @ 350 nm
ZnO thin film[87]	NaClO$_4$	1	10% @ 360 nm
ZnO nanoparticles[87]	NaClO$_4$	1	16% @ 350 nm
N-doped ZnO NRs[88]	Na$_2$SO$_4$	1.1 vs SCE	25% @ 380 nm
Ni(OH)$_2$/ZIF-8/ZnO/Ni NRs[89]	KOH	1.23	40% @ 350 nm
This work - ZnO:Co@ZIF-8[90]	**KOH**	**1.33**	**75% @ 350 nm**

Figure 2.15 provides a graphic representation of the IPCE values of the different material systems discussed, showing the large enhancement of the ZnO:Co@ZIF-8 doped core-shell approach taken in this work. Similar materials systems, such as the one reported by Li[89], show an IPCE almost half of the one reported in this thesis. Other ZnO-based material systems demonstrate a much poorer performance in terms of IPCE, which can be compared with some of the early results shown in Chapter 8.
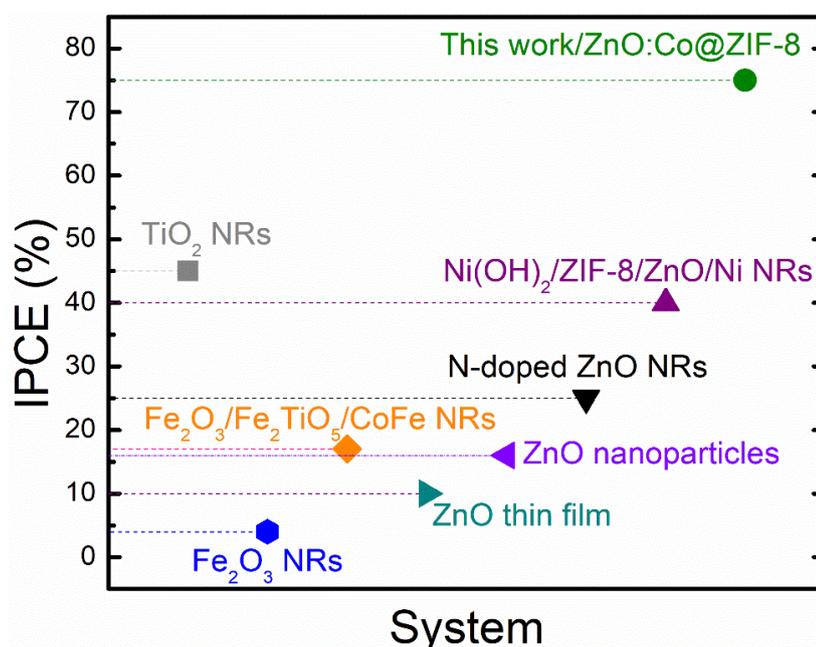
Figure 2.15. Graphical summary of the comparison of the performance of different semiconductor metal oxide water splitting photoanode material systems. The comparison is carried out in terms of their respective incident photon-to-current efficiency.

Moreover, different works envision the enhancement of different properties (those described previously in this chapter) of the ZnO-based photoanodes. Thus, the importance of the careful tuning of the properties of the ZnO NWs in their functional performance as water splitting is highlighted. This section has provided a snapshot of the current state of the art in photoelectrochemical water splitting. Further details on the field beyond the scope of this thesis can be found on the works of Walter[22] and Chen[74]. A more detailed description of the results and working mechanism of the photoanodes developed in this work is provided in Chapter 8.

2.5 Summary

In this chapter, the introductory background required to understand the developments and work presented in this thesis was detailed. For this, first, the concept of a semiconductor and its properties were introduced. This was followed by a description of the structure of crystalline inorganic solids and how any crystalline structure can be described. As a final point, the different point defects that can be appear in any crystalline structure during growth were briefly discussed, along with the repercussions that their presence has on the crystal lattice. Following the crystalline structure of inorganic solids, and using it as a basis, the electronic band structure of semiconductors was formally described. Starting with the Schrödinger equation and its application to a periodic crystalline lattice, the concept of allowed and forbidden bands was introduced and explained. Based on this concept, the idea of conduction and valence band, separated by a bandgap or forbidden band was discussed, along with the two different types of bandgaps that a semiconductor may present, direct or indirect. After defining the electronic band structure of a semiconductor, the concepts of density of states and charge carrier (electron and hole) were described, which resulted in the definition of what an intrinsic semiconductor and the Fermi level are. Finally, the doping of semiconductors was detailed as a route to modulate the optoelectronic properties of a semiconductor, giving rise to the concept of n and p-type semiconductors, depending on which the majority charge carrier is, electrons or holes. The introduction to the physics of semiconductors was finalised with the excitation (and more particularly, photoexcitation) of charge carriers and their subsequent radiative or non-radiative

recombination process. These two concepts will represent one of the cores on which a large part of the results presented in this thesis are based.

After the semiconductor physics background, a brief discussion on some of the most common semiconductor morphologies was presented. The first and most important morphology discussed were the allotropes of silicon: amorphous, polycrystalline and monocrystalline silicon. Their importance has been crucial in the development of the semiconductor technology that has boosted civilization into the current era, as it was highlighted. This was followed by the description of thin films and their multiple applications. Finally, the most important semiconductor nanomorphologies were described and their applications outlined. This discussion was carried out in terms of the dimensions of these nanomorphologies (one, two or three dimensions) dependant on how many of these were in the nanometre scale (below 100 nm). Thus, morphologies including nanoparticles, nanowires, nanotubes and nanoflowers were discussed.

The final part of the chapter focused on photoelectrochemical applications and, more specifically, photoelectrochemical water splitting. First, a theoretical description of the core concepts and processes that govern photoelectrochemical water splitting was provided. This was followed by a discussion of on the most important considerations to be taken into account when designing and developing new and enhanced semiconductor photoanodes for water splitting. The description of photoelectrochemical water splitting was followed by a summary of the principal efficiencies used to quantify and compare the performance of water splitting systems and how these are calculated. In particular, the concepts of solar-to-hydrogen efficiency, applied bias photon-to-current efficiency and incident photon-to-current efficiency concepts were explored. The necessary experimental considerations needed to help understand the results discussed in Chapter 8 were provided, with the photoelectrochemical water splitting cell utilised in this work as the focus upon which the discussion was centered. The details of how the metrics used to describe the photoelectrochemical performance of the ZnO nanowire-based photoanodes are also provided. These metrics are sweeping cyclic voltammetry, amperometric *I-t* curves, incident photon-to-current efficiency, stability and Mott-Schottky measurements. Finally, a revision of the state of the art of photoelectrochemical

water splitting was presented for comparison with results obtained in this thesis. This introductory chapter, along with Chapter 3 in which the properties and background for ZnO are provided, set the background and theoretical basis for all the concepts, ideas and results that are developed in Chapters 5-8.

Chapter 3

Zinc oxide nanowires: growth, doping and surface functionalization

3.1 Zinc oxide introduction

This chapter provides a general overview of ZnO from a material science point of view, discussing from its main physical properties to its applications, including the different growth and functionalization processes of ZnO. It begins with a description of the main properties of ZnO as a metal oxide and the many applications it has been used for throughout history. This is followed by a detailed account of the most important morphological, electronic and optical properties of ZnO, with a special focus on the properties relevant to the results and applications shown in the later chapters of the thesis. The, the different growth methodologies are discussed, with emphasis on chemical bath deposition (CBD) of ZnO nanomorphologies. These different morphologies are subsequently described, providing details of their main applications. In particular, nanowires (NWs) are described in more detail as this is the nanomorphology on which this work is focused. The CBD growth of ZnO NWs is then described in detail, especially with regards to why a seed layer is necessary and how the seed layer properties and the chemical growth conditions influence the

morphological properties of the NWs. This is followed by an account of the doping of ZnO NWs, how it can be achieved and why is it necessary, focusing on doping during CBD with metallic cations such as Co^{2+} or Cu^{2+}. Finally, the surface functionalization of ZnO NWs by the addition of a shell, or decoration with either iridium or a metal-organic framework is discussed, with an overview of their contribution towards improving the optical and electronic properties of the ZnO NWs for enhanced performance in photoelectrochemical applications. The ZnO basics detailed here are used to support the discussion of the growth and application results shown in Chapters 5, 6, 7 and 8.

3.2 Overview of ZnO: properties and applications

Zinc oxide is an inorganic metal oxide that in its usual state in nature is a white powder. It is insoluble in water. The global industry of ZnO is worth around USD 4.5 billion, and its principal application in industry is in the vulcanization of rubber, with almost half of the world's production being dedicated to this industry. Other applications include ceramics, paints (as pigment), agriculture, textile, cosmetics or pharmaceutical products (as a ultraviolet, UV, absorber)[91]. A detailed account of the industrial applications of ZnO can be found in the topical review of Kołodziejczak-Radzimska[92], which clearly indicates that the ZnO industry is a juggernaut with a critical role in important industries for our day-to-day lives. From a research point of view, ZnO has been implemented in a multitude of different devices, among which the most prominent are optical devices[12] (lasers, photodetectors, light-emitting diodes, LEDs), solar cells[93], gas sensors[94], anti-bacterial applications[95], energy harvesting[96] and water treatment[97] or water splitting[98] cells. The vast array of ZnO applications is enabled by its outstanding properties and by having one the largest varieties of nanomorphologies available of any semiconductor. An overview of these is provided here, with an in-depth description being provided by Özgür[10].

- From a structural point of view, ZnO in the nano scale is an optically transparent material that has three crystal structures: hexagonal wurtzite, zinc blende and cubic rock salt, as depicted in Figure 3.1. Out of the three, hexagonal wurtzite is the most thermodynamically stable in ambient conditions, while the other two require epitaxial growth from substrates (zinc blende) and extreme pressure
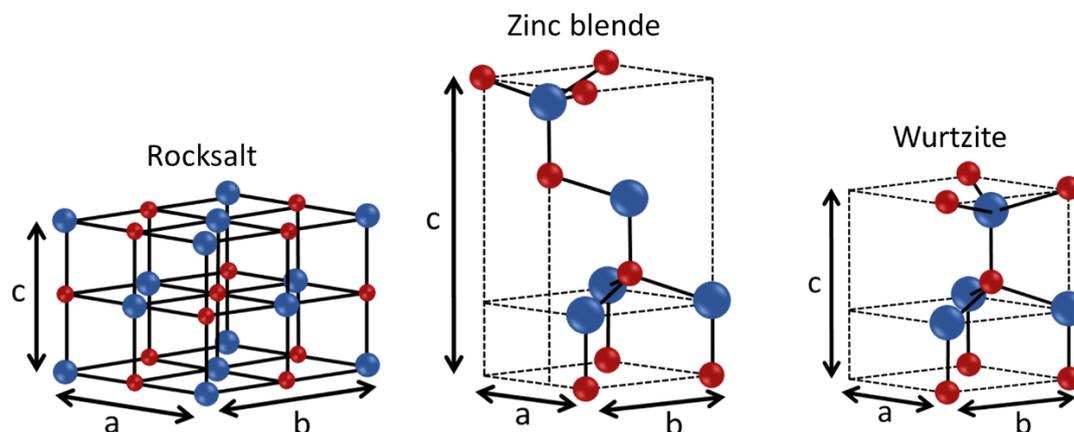
Figure 3.16. Schematic representation of the three crystal structures of ZnO. Only wurtzite is thermodynamically stable at room temperature. Blue spheres represent zinc while red spheres represent oxygen.

conditions (rock salt) to be stable. For the wurtzite structure, the coordination is a sp^3 tetrahedral structure in which a cation is surrounded by four anions and vice versa[10], see Figure 3.1. This crystal structure has three lattice parameters, a, b and c, with values of a = b = 3.3 Å and c = 5.2 Å and is a non-centric symmetry (no inversion symmetry), which is the source of the piezoelectric and pyroelectric properties of ZnO. The conjugation of these properties of the wurtzite crystal structure make it the desired phase of any ZnO nanomorphology growth due to the many applications it enables. Due to its bonding structure, ZnO has bonding characteristics intermediate between ionic and covalent bonding.

- Mechanically, ZnO is characterised by its low hardness[99], ranking it as a soft material in hardness tests, due to its low Young modulus. It has a high heat capacity, thermal conductivity and stability, with a melting point above 1900°C. The elastic properties of ZnO are worse when compared with other III-V semiconductors[100] such as GaN, as the elastic constants of ZnO are smaller than those of other III-V semiconductors.

- From an electrical point of view, ZnO is a II-VI semiconducting metal oxide with a wide direct bandgap of 3.3 eV. This wide bandgap permits the use of ZnO in a variety of optical-based devices centered in the UV-blue region of the electromagnetic spectrum. ZnO also has a large exciton binding energy of 60 meV, indicating that the excitonic emission of ZnO persists at room temperature, which is key for light emitting devices such as lasers. ZnO typically has

unintentional n-type doping attributed to native defects in its crystalline lattice[101], namely oxygen vacancies (missing oxygen atoms at regular lattice positions) and zinc interstitials (additional Zn atoms that occupy interstitial positions in the lattice). These defects also form atomic or molecular adsorption centres, prompting the use of ZnO in chemoresistive gas sensors. This unintentional doping due to native defects makes achieving p-type doping of ZnO one of the longest standing challenges[51, 102] in ZnO nanoengineering. This challenge has limited the number of available applications for ZnO in the semiconductor world. Nonetheless, n-type ZnO exhibits excellent electron mobility and strong luminescence, which combined with its abundance and ease of manufacturing make of ZnO one of the most researched semiconducting materials in the electronics industry. For a more detailed report on the semiconducting properties of ZnO and its applications, please refer to the work of Janotti[103]. The theoretical basis of the electronic concepts described here was provided in detail in Chapter 2.2.

Although the wide bandgap and unintentional n-type doping enable the use of ZnO is wide variety of applications, it also hinders it applicability in other type of devices. In particular, the wide bandgap hinders its use in light absorption-based applications, while the defects that cause the n-type doping may greatly decrease the stability and lifetime of ZnO-based photoelectrochemical devices. These are the main shortcomings that have to be tackled to improve the overall performance of ZnO. Nonetheless, the properties described previously, along with its low-cost, non-toxicity and ease of preparation, make of ZnO one of the most attractive semiconductors for large-scale production of devices. The most important characteristics of ZnO presented in this section form the basis for the upcoming discussion of ZnO growth, morphologies and the need for the material modifications implemented in this work to overcome the shortcomings described.

3.3 ZnO growth and nanomorphologies

Zinc oxide can be grown in a vast array of nanomorphologies using a wide range of techniques, from solution-based to vapour-liquid-solid (VLS) methods. Here, the use of these deposition techniques towards the growth of different ZnO

nanomorphologies is detailed. Depending on the desired morphology and application, different techniques will be optimal. In this regard, the chemical bath deposition (CBD) of ZnO nanostructures is the most attractive owing to its extreme process flexibility, low-cost, low-complexity and the excellent quality of the resulting material. As such, this technique will be the focus of this chapter. The main criteria used here to describe the different morphologies is their dimensionality. Taking this into account, ZnO nanowires (NWs) have become one of the most studied ZnO nanomorphology, along with nanoparticles. Thus, a more in detail account of the CBD growth of ZnO NWs and all the pertinent process considerations are provided in the Chapter 3.4.

3.3.1 Gas phase ZnO growth methodologies

A wide variety of techniques have been used throughout history to deposit ZnO with nano and macro scale dimensions. Most of these techniques are focused on the deposition of ZnO thin films, while others offer a larger variety of morphologies. For now, only the different techniques and their conditions will be detailed, with the morphologies being discussed in the following section. In general, a very simple classification of the ZnO deposition techniques can be made based on the working phase, i.e. gas or liquid phase growth. Gas phase techniques are mostly used for two-dimensional (2D) materials (thin films) while liquid phase methods are typically used for the growth of any dimension (3D, 2D or 1D) nanomaterials.

Gas phase techniques for the deposition of ZnO have been utilised for decades to produce high quality materials with a high throughput. In general, gas phase techniques entail that the zinc precursor is in gas phase before deposition. An example of a gas phase technique is pulsed laser deposition (PLD), which is a type of physical vapour deposition (PVD). ZnO thin film deposition using PLD is based on the ablation of a ZnO target[104] or a precursor such as dimethylzinc[105] inside a vacuum chamber that contains an inert gas (argon or nitrogen) and a reactive background gas (oxygen or a gas phase oxide) that acts as an oxygen donor. For the ablation of the target, a high energy pulsed laser is used. The properties of the as-deposited films can be controlled by tuning the laser energy and wavelength, the pulse repetition rate, the number of pulses and the substrate temperature, among others. The

deposition of ZnO thin films with PLD provides highly directional films with a preferential (0 0 2) crystalline orientation characteristic of the wurtzite crystal phase. Sputtering is another technique commonly used for the deposition of ZnO thin films. In short, an inert gas plasma (usually argon) is generated in a vacuum chamber in which a ZnO target is placed. This plasma, when close to the surface of the target, will have enough ionization energy to extract atoms from the target[106]. Another possibility is using a Zn target while generating a plasma that includes oxygen[107]. Independent of the process, sputtering is a thin film deposition technique with a very high throughput that does not require heating of the substrate to yield high quality film with large-scale homogeneity.

A different type of PVD technique is molecular beam epitaxy (MBE). MBE is an ultrahigh vacuum technique that is based on the controlled evaporation of zinc and the formation of ZnO by its interaction with oxygen gas introduced in the chamber. MBE provides a method for controlled deposition of high quality epitaxial ZnO thin films[108]. MBE also provides an easy pathway for the doping of ZnO[109], which is crucial for the implementation of ZnO in enhanced electronic devices. It has two main drawbacks, namely the requirement of expensive substrates for the epitaxial deposition of the material (typically sapphire) and the low deposition rate, which hinders the applicability of MBE-grown ZnO in industry. However, it still is a highly valuable research tool for studies on high quality epitaxial ZnO films.

Gas phase techniques based on chemical vapour deposition (CVD) have been thoroughly studied for the deposition of ZnO. A CVD process is based on exposing a substrate to a volatile precursor that either reacts or decomposes on the surface of the substrate, resulting in the deposition of the target material. CVD precursors are introduced in a deposition chamber using an inert carrier gas (nitrogen) in which the deposition substrate is kept at high temperatures (typically 450°C to 900°C depending on the process).

The traditional CVD process can be modified in a variety of ways. For example, instead of using a ZnO precursor, metal-organic (MO) precursors like diethylzinc[110] or zinc acetate[111] can be used in a process known as MOCVD, where these precursors are introduced into the reactor chamber along with an oxygen source (water, for example). As these precursors reach the surface of the substrate at high

temperature, they react to form ZnO and the by-products are exhausted by the carrier gas flow. Another example is the use of an aerosol to introduce the ZnO precursors in the reactor chamber[112]. This way, a zinc-based solution along with an oxygen source are bubbled in the chamber, were they are deposited on the substrate and react to form ZnO. One of the biggest benefits of CVD is that it can be used to grow 2D morphologies such as NWs. This type of CVD process requires gold-catalysed growth, in which gold droplets are systematically placed on the substrate to act as seeds for the NWs growth. After the deposition of the gold catalytic structures on the surface, ZnO vapour is introduced in the deposition chamber while keeping the substrate at a high temperature (above 850°C). This ZnO interacts with the gold droplet seeds, forming zinc complexes that are the basis for the growth of ZnO NWs[113]. CVD is proven to be a very versatile tool that can deposit high quality thin films and highly ordered, high quality, single crystal ZnO NWs depending on how the CVD process is carried out. Figure 3.2 shows schematics of typical MBE and MOCVD deposition systems.

Atomic layer deposition (ALD) is a particular type of CVD technique based on the sequential pulsing and purging of the zinc oxide precursors. This technique can be used for both thin films[114] and 2D nanostructures[115] growth. A thorough description of the use of ALD to deposit ZnO thin films, its mechanism, benefits and shortcomings is provided in Chapter 3.4.1.
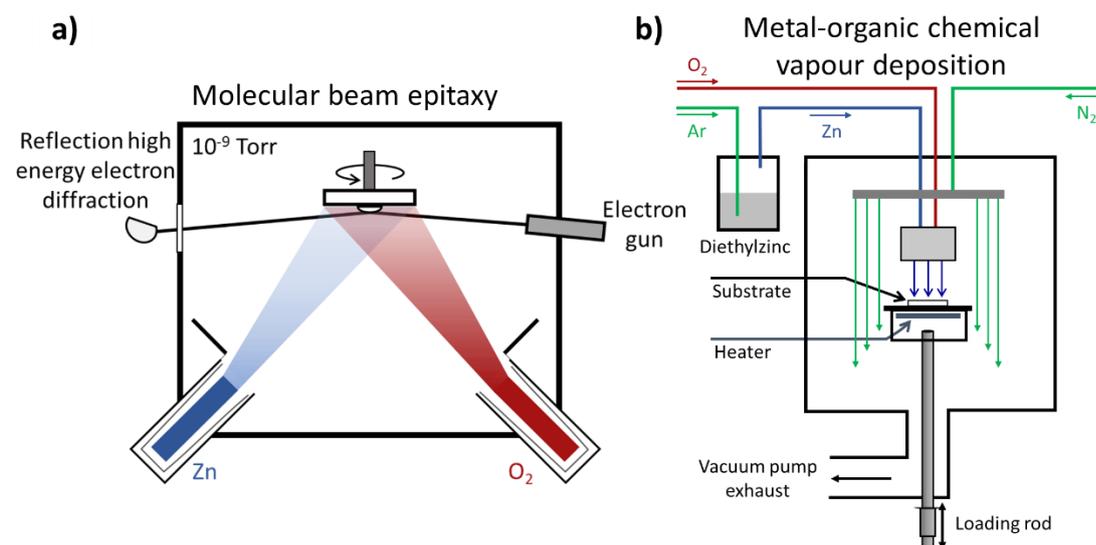
Figure 3.2. Schematic representation of **a)** molecular beam epitaxy and **b)** metal-organic chemical vapour deposition systems for the growth of ZnO nanostructures.

3.3.2 Liquid phase ZnO growth methodologies

Liquid phase techniques are an attractive alternative to gas phase methods, particularly due to their scaling-up possibilities, while obtaining high quality crystalline ZnO. One of the best-known liquid phase techniques is sol-gel deposition. This technique is used for the deposition of thickness-controlled ZnO thin films. It is based on the preparation of a solution containing a zinc precursor that is then deposited on a substrate by techniques such as dip coating or spin coating. As this is one of the techniques used here to deposit ZnO seed layers for the ZnO NW growth, a more detailed description is provided in Chapter 3.3.4.

One of the most widespread liquid phase techniques for the deposition of ZnO nanomaterials is the electrophoretic deposition (EPD) and, more specifically for ZnO, cathodic electrodeposition. EPD is a process commonly used in the industry in a wide range of applications, among which its use in the coating industry[116] is the most important owing to the high throughput with which it can coat complex and large structures. This process is based on the migration of colloidal particles in an electrolyte due to an applied electric field, depositing them in the cathode. Typically, experiments are carried out in a three-electrode cell setup, similar to the one described in Chapter 2.4, in which the cathode is the target substrate on which the ZnO nanomaterial will be deposited. For cathodic electrodeposition to be successful, the colloidal particles that form the electrolyte have to create a stable suspension that is able to carry a charge under the influence of an electric field. In the case of ZnO, this is achieved by preparing aqueous electrolytes containing either zinc nitrate[117] or zinc chloride[118], both of which form stable suspensions in water that carry charge and can be deposited on the cathode. Cathodic electrodeposition is used to grown a variety of ZnO nanomorphologies, from thin films to NWs[119] or nanotubes[120]. Moreover, this process can be applied to any substrate that is stable in the electrolyte and is conductive without the need of a seed layer, this opens the possibility of using a wider variety of substrates for the deposition of different ZnO nanomorphologies. Along with this range of possible substrates and morphologies, the ZnO nanomorphologies deposited all show a single crystal wurtzite phase,

demonstrating that cathodic electrodeposition is a high throughput growth technique for high quality ZnO.

Nonetheless, the most important and widespread liquid phase zinc oxide growth method is the solvothermal synthesis. Solvothermal growth involves any technique in which a substance is crystallized within a liquid solution (most commonly water for ZnO, hence hydrothermal synthesis from now on) at high temperature (anywhere between 70°C up to 300 °C) and high pressure. The growth solution contains the precursors required to grow the desired material. To achieve the high temperature and required high pressure, an autoclave, which is a Teflon-lined stainless-steel pressure vessel (see Figure 3.3), is used.

This way, as the growth solution is heated, the liquid will expand until it either fills the autoclave or starts evaporating. The filling of the autoclave is defined as,

$$Filling\ (\%) = \frac{V_S}{V_T} \qquad \text{[Eq. 3.1]}$$

where V_S is the volume occupied by the growth solution and V_T the total volume of the autoclave, then the pressure inside the autoclave can be obtained by correlating the filling, temperature and density of the solvent. The pressure inside the autoclave is known as autogenous pressure as it is generated from the solution without the application of any external pressure. By controlling the temperature, filling, pressure and concentration of the precursors in the growth solution, a large degree of control

Figure 3.3. Photograph of a Teflon lined stainless steel autoclave with its corresponding seals. Product of Toptionlab[121].

is attainable for the growth of the desired material. More details on the growth mechanisms and theoretical background of hydrothermal growth are provided in the detail account provided by Byrappa and Yoshimura[122].

Hydrothermal growth has been traditionally used as a high throughput, high quality and reproducible technique to grow bulk crystals of a vast variety of materials. The material obtained from this growth will either be a powder or large crystals. In the case of nanometric ZnO, hydrothermal growth has been used to grow a wide array of different nanomorphologies such as NWs[123], hollow spheres[124] or nanoparticles[125]. An example of these nanomorphologies is shown in Figure 3.4.

In this work, the ZnO NWs were all grown on seeded substrates using a technique derived from hydrothermal growth, known as chemical bath deposition (CBD). CBD is a liquid phase technique based on immersing a substrate in the growth solution containing the precursors so the growth takes place on the substrate[126]. In contrast to hydrothermal growth, the equipment required for a CBD process is reduced to a solution container (a glass beaker, for example) and a substrate mounting device. This means that CBD does not need an autoclave as it operates at atmospheric pressure. Furthermore, CBD allows the controlled growth of nanomaterials and thin films strictly restricted onto a nucleated substrate, providing a better control for the implementation of these nanomaterials in functional devices.
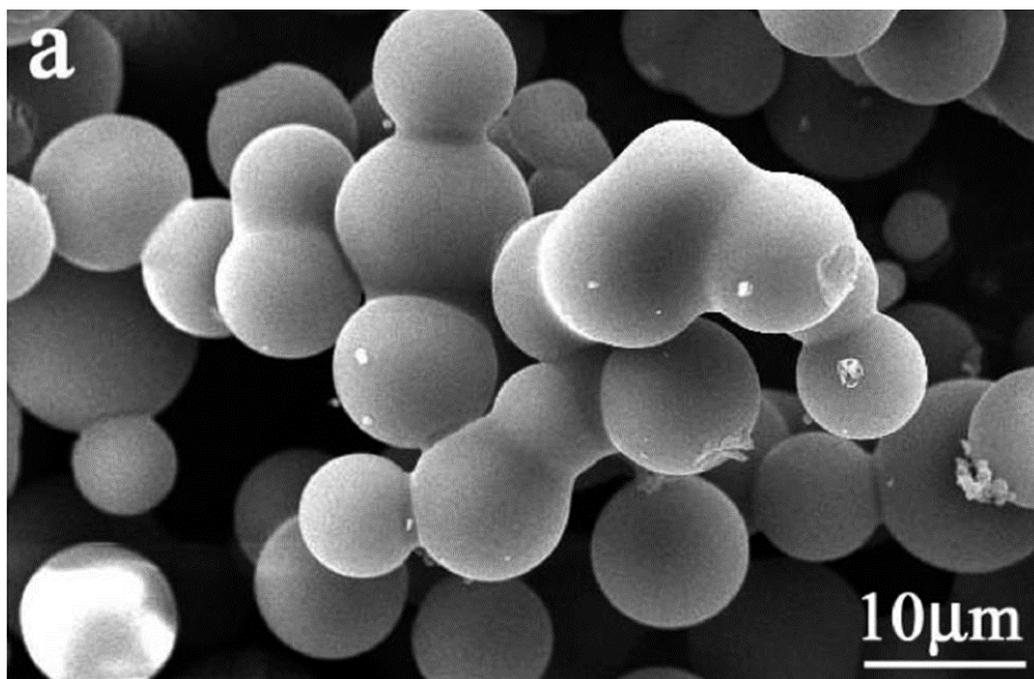
Figure 3.4. Zinc oxide hollow nanospheres grown through hydrothermal synthesis[124].

A detailed description of the use of CBD to grow ZnO NWs, the growth mechanism, its conditions, applications, advantages and shortcomings are provided in Chapter 3.3.5.

3.3.3 Growth of ZnO nanomorphologies

This section discusses the growth of different ZnO nanomorphologies. The characteristic used to sort these morphologies in this work is their dimensionality, defined as the number of dimensions that are below 100 nm length. In short, a morphology will be three-dimensional (3D) if all its dimensions are measured within the nanoscale. Likewise, 2D morphologies will have one dimension outside of the nanoscale with 1D morphologies having two dimensions above 100 nm[127]. An introduction to these morphologies was provided in Chapter 2.

ZnO nanoparticles (NPs) are the prime example of 3D ZnO. Other 3D morphologies include nanospheres and quantum dots (QDs), which are particular cases of NPs. NPs have been the most widely studied and implemented out the three discussed here, with a large variety of different applications. ZnO NPs are largely grown using liquid phase techniques, mainly hydrothermal synthesis and sol-gel processing[128]. The size of these NPs typically ranges from some nanometres to a few tens of nanometres. Owing to the size and the outstanding properties of ZnO, previously outlined (especially the non-toxicity), NPs have been used in a host of applications such as food packaging[129], in textiles as UV absorbers[130], solar cells[131], anti-bacterial[132] or biomedicine[133]. Figure 3.5 shows a typical TEM image of ZnO NPs, in which their 3D characteristic can be appreciated. For more information on ZnO NPs, please refer to the citations provided here in which reviews on the different growth methodologies and the specific properties for each application are provided in more detail.

ZnO nanospheres can be considered a particular case of ZnO NPs in which the shape of the NP is spherical. These are typically produced by hydrothermal synthesis and have been applied to various applications such as photocatalytic[134] and anti-bacterial[135] owing to their optical and chemical properties. ZnO QDs[136] have also been studied, although not as thoroughly as NPs. Similarly to NPs, ZnO QDs are synthesized by a chemical liquid phase route, solvothermal synthesis and they have
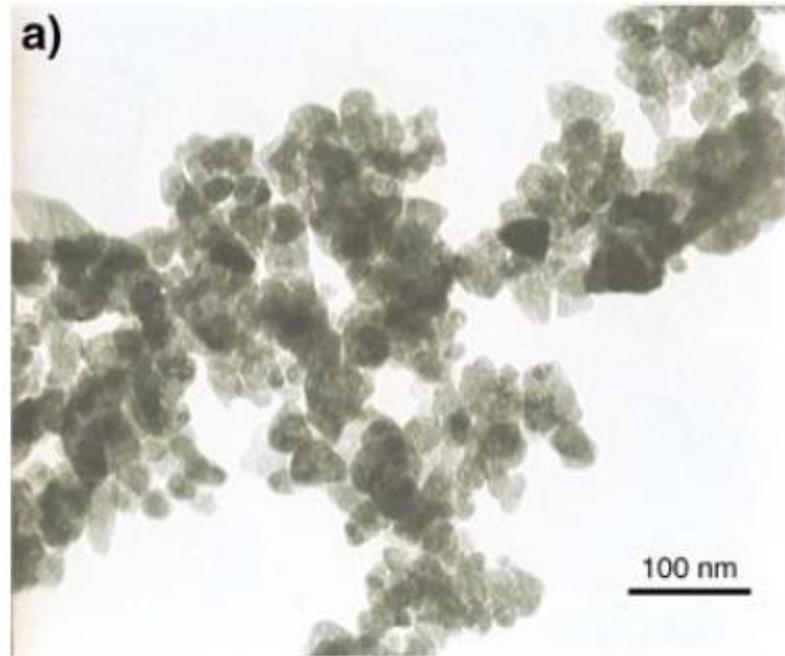
Figure 3.5. Typical TEM micrograph of ZnO nanoparticles[130].

been traditionally used as sensitizers by loading them on a matrix for gas[137] and mercury[138] sensing. However, QDs have also seen applications of their own such as in imaging of biomaterials[139] or as antimicrobial agents[136].

2D ZnO morphologies include structures like NWs, nanotubes (NTs) or nanobelts. This group corresponds to the most studied group in the last decades due to the outstanding properties that these morphologies have, opening up a vast array of applications. These 2D ZnO structures are characterized as being single crystal, easy to grow, having a high electron conductivity and being reproducible and tuneable in dimensions and optical and electronic properties. Owing to their small lateral dimensions, these morphologies have a lateral charge transfer that is shorter that the average lifetime of carriers, which has applications in sensing and photocatalysis[140]. Furthermore, these materials still absorb light in the characteristic range of ZnO within the electromagnetic spectrum while also having the large aspect ratio that characterizes them, which makes them attractive for UV-blue absorption, photodetectors and solar cells. Typically, ZnO NWs[141] and NTs[142] are solid or hollow hexagonal prisms, respectively, a shape that is characteristic of the hexagonal wurtzite crystal structure, while nanobelts[143] are rectangular prisms of the same crystalline structure. Figure 3.6 shows the three different morphologies in works representative of the results observed in the literature.

All three 2D structures are traditionally grown through solvothermal synthesis and, as detailed before, if they are grown on a substrate, in some cases it will be done by CBD, with a prior seed layer present as will be discussed in the next section. Independently of the growth method used, the characteristic single crystal wurtzite structure of these materials provides them with a morphological, optical and electronic structure that can be applied in a multitude of different fields, especially in the case of ZnO NWs. For example, ZnO NTs have been used as pH sensors[144] while nanobelts have seen use as ethanol sensors[145]. ZnO NWs have been utilised for applications ranging from gas sensing to LEDs, water treatment or electrocatalysis. Some of these applications are detailed in the descriptive works of Cui[146] and Zhou[147].

One-dimensional ZnO nanostructures include morphologies such as tetrapods, nanodisks or nanoflowers, to name a few. The main common characteristic of these 1D structures is that they are considerably larger than other nanomorphologies. In general, their applications are akin to those of the 3D and 2D structures, although their performance may be worse due to their increased lateral charge transfer distance. Nonetheless, these structures have been used in applications such as tetrapods in therapeutic applications[148],
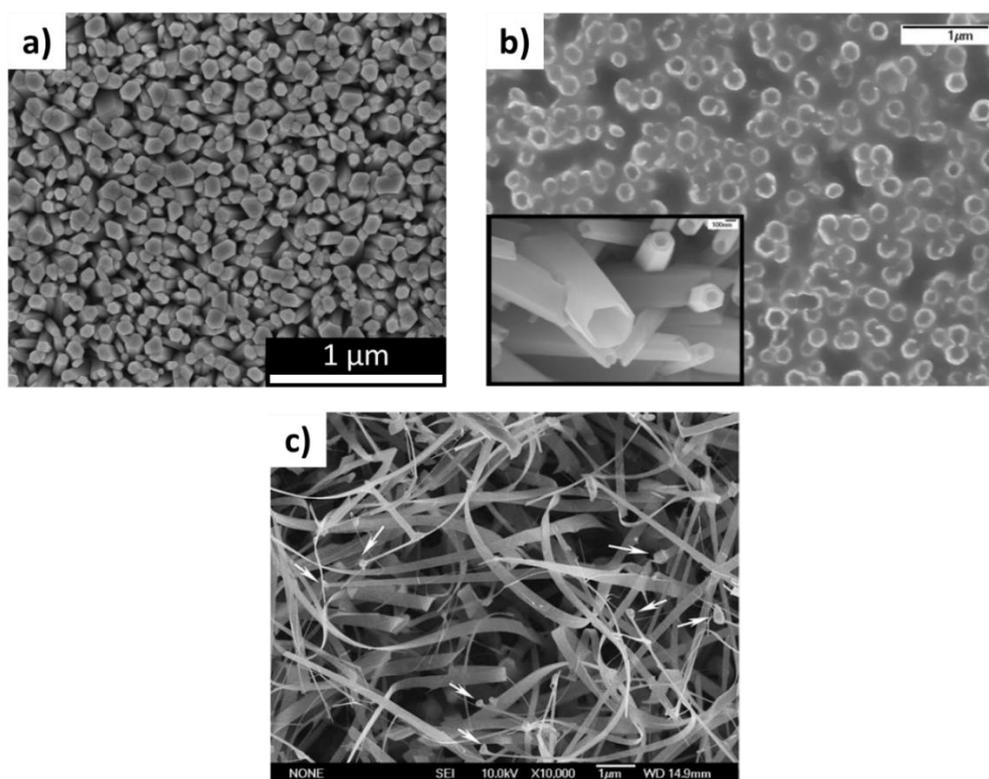
Figure 3.6. Scanning electron micrographs of **a)** ZnO nanowires, as-grown in this work, **b)** ZnO nanotubes[144] and **c)** ZnO nanobelts[143].

69

nanodisks in photocatalysis[149] or nanoflowers as biomedical scaffolding[150], with microscopy images of the first two shown in Figure 3.7.

3.4 ZnO seed layer deposition for nanowire growth

The growth of ZnO NWs using CBD is the focus of this work. Before the CBD growth of the NWs, it is necessary to deposit a ZnO seed layer that will provide the nucleation centres that promote the growth of single crystal wurtzite ZnO NWs with controllable morphology and orientation. To deposit the seed layer, techniques that provide control over the structural and morphological characteristics of the ZnO seed layer are required.

Thus, two different approaches were chosen for the deposition of ZnO seed layers for the CBD of ZnO NWs: atomic layer deposition (ALD) and sol-gel processing. ALD was used to study the influence of the seed layer properties on the NW growth while the sol-gel process was used for the preparation of devices on indium tin oxide (ITO) substrates for photocatalytic applications.

3.4.1 Atomic layer deposition of the ZnO seed layers

Atomic layer deposition is a CVD thin film deposition technique based on the sequential use of gas phase chemical reactants[114]. In a typical binary ALD process, an organometallic precursor and a co-reactant are sequentially introduced in the reaction chamber using an inert gas (N, Ar) as carrier. In between the sequential pulsing of the gas phase reactants, a purge time is allowed in which only the carrier gas is flowing in the chamber in order to remove any unreacted precursors and by-
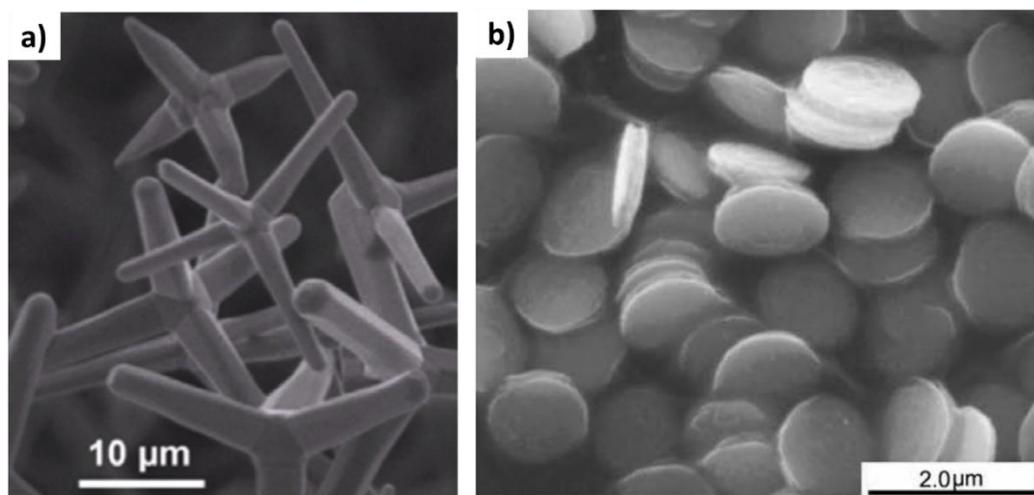
Figure 3.7. a) ZnO tetrapods grown for therapeutic applications[148]. **b)** ZnO nanodisks with enhances photocatalytic properties[149].

products. Thus, an ALD cycle consists of the sequential pulse and purge of both reactants, as illustrated in Figure 3.8. Along with these pulse and purge times, which regulate the amount of reactants introduced in the reaction chamber, the deposition temperature and total number of cycles can be controlled, opening a space parameter of up to six degrees of tunability. In an ideal ALD process, the pulse and purge times will be such that after every pulse, only a monolayer of the reactant will be deposited on the substrate. As such, when the next reactant is introduced in the chamber, the chemical reaction with the layer deposited on the substrate will be self-limiting, leading to the growth of an atomic layer of the target material. Depending on the target materials (metals, carbides, nitrides, metal oxides), the precursors and co-reactants used will be different. The most common materials deposited with ALD are metal oxides. For these, the precursor is an organometallic compound that reacts with an oxidant, typically water, to form the target material.

For ZnO, the most commonly zinc precursor used is diethylzinc (DEZ), and the co-reactant is water, that acts as an oxidant. Both precursors are separately introduced in a nitrogen or argon stream, which acts as both the inert gas utilised as carrier and purge. Using these precursors and with no dependence on the ALD parameters, the ideal reaction pathway for the controlled growth of ZnO seed layers from these precursors[151] is shown in the following equations,

$$\| - OH + Zn(CH_2CH_3)_2 \rightarrow \| - O - Zn(CH_2CH_3) + CH_3CH_3 \qquad \text{[Eq. 3.2]}$$

$$\| - OH + Zn(CH_2CH_3)_2 \rightarrow \| - O - Zn(CH_2CH_3) + CH_3CH_3 \qquad \text{[Eq. 3.3]}$$

$$\| - O - Zn(CH_2CH_3) + \| - OH \rightarrow (\| - O)_2 - Zn + CH_3CH_3 \qquad \text{[Eq. 3.4]}$$
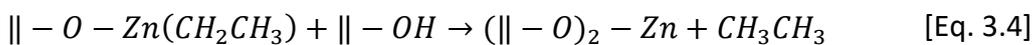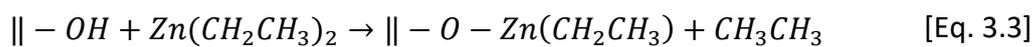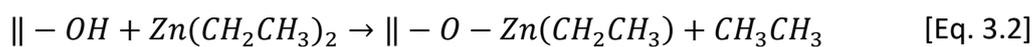
where $\| - X$ represents the top layer of the ZnO film and *X* is a compound bonded to it. Considering the top layer of a ZnO film during ALD deposition, the ZnO surface will have two different oxygen binding sites, a hydroxyl coming from the molecular water ($\| - OH$) and the other from dissociated water, with the former being more energetically favoured for binding. As such, when DEZ is pulsed under these conditions, the Zn atom in DEZ will bond to the hydroxyl bonding site of molecular water. Thus, one of the ethyl ligand groups of DEZ is removed by a simple ligand-exchange reaction, which consists in the substitution of a ligand in the original
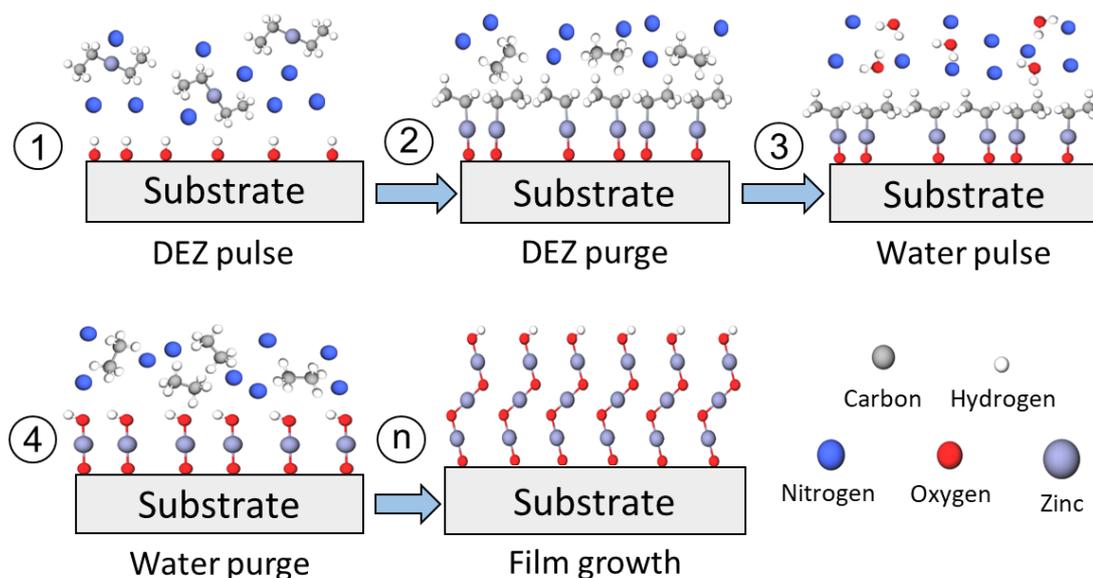
Figure 3.8. Schematic of the sequential pulsing and purging of the precursors used for the ALD ZnO seed layer deposition, where DEZ is diethylzinc, the zinc precursor.

molecule for another. In this case, the ethyl ligand that is removed is substituted by the hydroxyl group on the surface of the ZnO film. This process is represented in steps 1 and 2 of Figure 3.4 and by Eq. 3.2, which shows the pulse of DEZ and the ligand-exchange reaction that takes place, leaving monoethylzinc bonded to the surface of the film. Subsequently, water is pulsed in the chamber, which prompts another ligand-exchange reaction that dissociates the ethyl of the surface monoethylzinc, leaving once again a hydroxylated zinc surface, as at the beginning of the process. This is represented by steps 3 and 4 in Figure 3.4 and by Eq. 3.3. As an additional step (Eq. 3.4), a hydroxylated zinc ($\parallel$—$ZnOH$) can react with a bonded monoethylzinc, resulting in bonded zinc oxide to the surface of the film. This is a simple explanation of one possible growth model for the ALD deposition of ZnO. More information can be found in the thorough work of Weckman[151].

One crucial consideration for the ALD process is the saturation of the precursors, which is controlled by the pulse time of each reactant. The saturation of the precursors is defined as the amount of ZnO precursors adsorbed on the existing surface of the substrate. In an ideal ALD process, only one atomic layer will grow per ALD cycle as detailed earlier, leading to an almost flat and conformal surface with no additional roughness. For this to be true and considering all the other process parameters as constant (temperature, base pressure, gas flow of the carrier gas), the pulse time has to be such that it ensures only a monolayer is formed onto the existing

surface of the substrate, saturating the surface with the precursors. If the pulse time is too short, an incomplete heterogeneous film will be deposited; likewise, if the pulse time is too long, more than one monolayer of DEZ will deposit, over-saturating the surface with precursors, which would shift the deposition regime from ideal ALD closer to a more general CVD process. This means that longer pulse times may not yield an ideal ALD deposition with atomic control of the thickness and roughness or their properties may not be suitable for a ZnO seed layer. Moreover, these pulse times may need to be different if they are for DEZ or water. Regarding the purge times, it is also important to fine tune them to obtain a ZnO seed layer with the desired characteristics. If the purge times are too long, it may lead to the desorption of the previously adsorbed or deposited materials, which would cause a heterogeneous growth; on the other hand, if they are too short, not all the by-products and excess reagents will be exhausted, which may lead to an unwanted parasitic growth due to gas phase reactions and the possible deposition of by-products or excess reactants on the existing surface. Thus, tuning the pulse and purge times is necessary to obtain a seed layer using an atomic layer deposition system according to the requirements of the NW growth.

The deposition temperature is the other major parameter that controls the quality and regime of the ALD ZnO seed layer. Hence, the concept of temperature window must be introduced. The ALD temperature window[152] indicates the temperature range in which the deposition can be considered in ALD conditions as, at this temperature, the balance between the chemical reactivity and the desorption of the precursors will be ideal, leading to the self-limiting reactions that characterize the ALD process. Low temperatures may not be enough for the reagents to react while high temperatures can induce the desorption of the reactants. For ZnO, the ALD window is typically reported between 120°C and 250°C, depending on the system and other experimental conditions used[114].

The final ALD parameter to consider is the number of deposition cycles. The concept is simple, the higher the number of cycles, the larger the thickness of the seed layer will be. However, the number of cycles also has a direct influence on the structural properties of the surface of the seed layer, which is crucial for the controlled growth of the ZnO NWs. In this sense, the higher the number of cycles, the

rougher the surface will be, which can influence the NW growth. This effect typically occurs in regimes that are not ideal ALD depositions, although it can also occur in ideal ALD depositions for substrates that have small defects on their surface. The parameter space here discussed allows for sensitive control of the deposition process and, hence, control of the deposited films. This control was used in this work to explore the role of the seed layer in the NW growth, as it will be detailed in the discussion of the results shown in Chapter 5.

3.4.2 Sol-gel deposition of the ZnO seed layer

A sol-gel deposition process is based on the conversion of monomers into a colloidal solution that acts as the precursor for a gel of particles. Once the gel is formed, a thermal treatment is required to remove the remaining liquid from the solution and allow the densification and grain growth of the material[153].

For ZnO, sol-gel processing represents a collection of techniques among which dip coating, spin coating or drop casting are the most widespread to obtain thin films of ZnO with controllable properties. Independently of the deposition technique used, the sol-gel process can be divided in three steps, with a schematic presentation being shown in Figure 3.9:

- Preparation of the precursor solution (sol), which involves the use of different zinc precursors, mainly zinc acetate dehydrate ($ZnC_4H_6O_4$) or zinc chloride anhydrous ($ZnCl_2$), and solvents such as ethanol (C_2H_5OH) or 2-methoxyethanol ($C_3H_8O_2$) for the aforementioned precursors. $ZnCl_2$ in $C_3H_8O_2$ was the combination used in this work. For more information on the different precursors, please refer to the work of Znaidi[154].

  Deposition of the sol on the desired substrate using any of the previously listed techniques. After this deposition, the solution turns into a xerogel, which is a type of gel formed by drying with unhindered shrinkage. In this work, spin coating was the technique used. Spin coating consists of casting a certain amount of the precursor solution onto a substrate that is subsequently rotated at high speed to create a homogeneous layer of material by centrifugal force, in this case the ZnO xerogel.

Solution of ZnO precursors

Spin coating

Formation of xerogel film

Thermal treatment

Resulting dense film
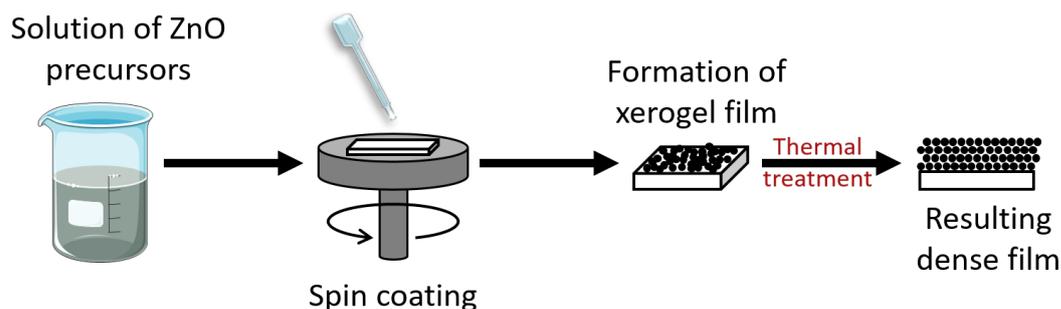
Figure 3.9. Schematic of the sol-gel deposition process of a ZnO seed layer using spin coating as the technique to deposit the sol on the substrate.

- Thermal treatment of the xerogel on the substrate on a hot plate, in an oven or in a furnace. The xerogel forms ZnO by evaporating the solvent, which induces viscous sintering, compacting the ZnO to generate a continuous and homogeneous seed layer. Viscous sintering is the process by which a gel is densified by a viscous flow of grain-liquid mixture once the volume fraction of liquid is sufficiently high[155].

Sol-gel deposition of ZnO offers a wide variety of options to control the properties of the seed layers. Here, only one set of conditions was used due to external factors related to the ALD system.

3.5 Chemical bath deposition of ZnO NWs

Chemical bath deposition (CBD) is a liquid phase technique derived from hydrothermal synthesis, as explained in Chapter 3.3.2. The technique was used in this work owing to its high process flexibility, tunability and high-quality production of ZnO NWs.

The CBD growth of ZnO NWs requires an underlying ZnO seed layer to promote the nucleation of the NWs, which increases the throughput and the quality of the as-grown NWs, while offering control over the morphology and orientation of the NWs. In this work, as-grown refers to NWs grown on a substrate not subjected to any further treatment or modification. The CBD growth of NWs offers a high degree of tunability owing to a variety of process parameters that can be controlled, namely the precursors used and their concentration, the synthesis time and temperature or the pH of the growth solution.

3.5.1 Precursor selection and growth mechanism of the CBD growth of ZnO nanowires

The CBD process consists of the preparation of an aqueous solution containing the Zn precursor and a reducing agent that supplies hydroxyl radicals to the growth solution. The general growth mechanism of the ZnO NWs, not considering the chemical precursors used, can be viewed in the following reactions, based on the works of Demianets[156, 157].

$$Zn^{2+} + 2OH^- \rightleftarrows Zn(OH)_2 \qquad \text{[Eq. 3.5]}$$

$$Zn(OH)_2 + 2OH^- \rightleftarrows [Zn(OH)_4]^{2-} \qquad \text{[Eq. 3.6]}$$

$$[Zn(OH)_4]^{2-} \rightleftarrows ZnO_2^{2-} + 2H_2O \qquad \text{[Eq. 3.7]}$$

$$ZnO_2^{2-} + H_2O \rightleftarrows ZnO + 2OH^- \qquad \text{[Eq. 3.8]}$$

$$ZnO + OH^- \rightleftarrows ZnOOH^- \qquad \text{[Eq. 3.9]}$$
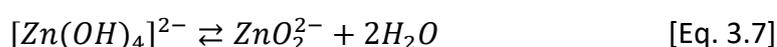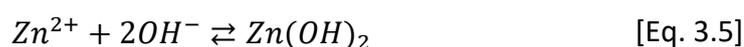
In short, the growth of ZnO NWs requires a Zn^{2+} precursor and a reducing agent. The reaction of these two ions in solution will produce zinc hydroxide and zinc hydroxide complexes. The hydroxide complexes will react with water to form ZnO and more hydroxide radicals that can then react again. Therefore, the two first factors to consider for the CBD growth of the ZnO NWs are the Zn^{2+} and OH$^-$ sources.

Regarding the zinc precursor, the most frequently used precursors are zinc nitrate hexahydrate[158] ($Zn(NO_3)_2 \cdot 6H_2O$), zinc acetate dihydrate[159] and zinc chloride[160], with zinc nitrate being the most commonly used of the three. Discussions in the literature regarding which of the three is best are inconclusive, as all three salts yield single crystal wurtzite phase ZnO NWs under similar growth conditions. In the work of Akgun[161], a direct comparison of the three zinc salts previously listed is made while all the seed layer deposition and NW growth conditions were kept constant. This work showed that zinc acetate provides higher aspect ratio NWs, followed by zinc nitrate and finally zinc chloride. Works like those of Yu Lin[160] and Abbasi[162] also discuss the growth of ZnO NWs using the different zinc salts. Nonetheless, a conclusive overall picture cannot be extracted from these works, mainly due to the vast variety of process parameters of the CBD growth of ZnO NWs. Differences in the seed layer deposition, growth temperature, solution pH and even the vessel in which the growth is done will directly influence the NW growth, making it almost impossible

to establish a thorough comparison of the influences that the zinc salts can have on the NW growth. Furthermore, there are no reports in the literature that discuss the use of different zinc salts for a specific application. There is not a definitive answer to which zinc salt is best for the NW growth and the photoelectrochemical applications discussed in this work. In view of this, it was decided to use zinc nitrate hexahydrate as the zinc salt in this work owing to its widespread use.

For the OH$^-$ source, there are different approaches to supply the required hydroxyl ions in the growth solution. The three main routes involve the use of different chemicals: a strong base such as NaOH or KOH, ammonia hydroxide or hexamethylenetetramine ($(CH_2)_6N_4$), HMTA). Of these three, the first one was discarded due to the disadvantage of using a strong base, especially for possible future scale-up. In order to support the application of the ZnO NWs in photoelectrochemical applications and their possible scale-up, it was decided to, if possible, avoid the use of harmful solvents or chemical that could hinder the introduction of this technology in industry. Comprehensive discussions of the use of either ammonia hydroxide or HMTA, such as the work of Jung[163], have shown the influences of both hydroxyl sources on the NW growth. In short, both hydroxyl sources can be used for the growth of NWs. However, their basicity is different, with that of ammonia hydroxide being higher, which will influence the NW growth due to the influence that the growth solution pH has on the growth of NWs, mainly due to the increased concentration of OH$^-$. Furthermore, the work of Strano[164] indicates that HMTA ensures better than other reducing agents that the single crystal wurtzite phase of the ZnO NWs will be obtained. Due to this, HMTA was used in this work.

After detailing the Zn^{2+} and OH$^-$ precursors used in this work, the growth mechanism established in Equations 3.5 to 3.9 can be reformulated and specified to zinc nitrate and HMTA[165] as follows,

$$Zn(NO_3)_2 \cdot 6H_2O \rightarrow Zn^{2+} + 2NO_3^- + 6H_2O \qquad \text{[Eq. 3.10]}$$

$$(CH_2)_6N_4 + 6H_2O \rightleftarrows 6HCHO + 4NH_3 \qquad \text{[Eq. 3.11]}$$

$$NH_3 + H_2O \rightleftarrows NH_4^+ + OH^- \qquad \text{[Eq. 3.12]}$$

$$(CH_2)_6N_4 + Zn^{2+} \rightarrow [Zn(CH_2)_6N_4]^{2+} \qquad \text{[Eq. 3.13]}$$

$$[Zn(CH_2)_6N_4]^{2+} + 2OH^- \rightarrow ZnO + H_2O + (CH_2)_6N_4 \qquad \text{[Eq. 3.14]}$$

$$Zn^{2+} + 4NH_3 \rightarrow [Zn(NH_3)_4]^{2+} \qquad \text{[Eq. 3.15]}$$

$$[Zn(NH_3)_4]^{2+} + 2OH^- \rightarrow ZnO + H_2O + 4NH_3 \qquad \text{[Eq. 3.16]}$$

$$Zn^{2+} + 4OH^- \rightarrow [Zn(OH)_4]^{2-} \qquad \text{[Eq. 3.17]}$$

$$[Zn(OH)_4]^{2-} \rightarrow ZnO + H_2O + 2OH^- \qquad \text{[Eq. 3.18]}$$
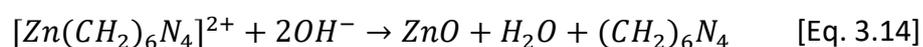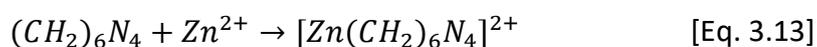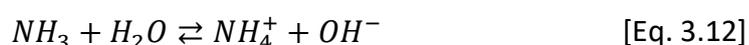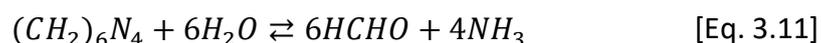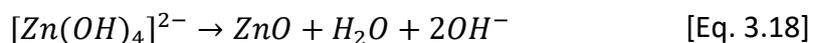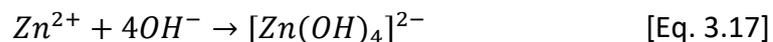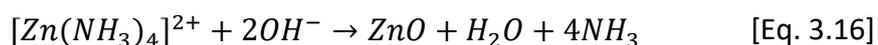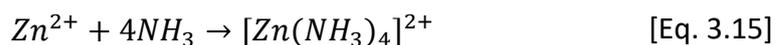
where the first two equations refer to the decomposition in water of zinc nitrate hexahydrate (Eq. 3.10) and HMTA (Eq. 3.11). The former provides the Zn^{2+} precursors that will form the ZnO NWs, while the latter decomposes into formaldehyde (HCHO) and ammonia (NH_3). This ammonia is subsequently hydrolysed (Eq. 3.12) into ammonium (NH_4^+) and hydroxyl (OH^-). From here on, there are three main reaction pathways for the formation of ZnO:

- Zn^{2+} and HMTA can form a complex ion (Eq. 3.13) that is then hydroxylated (Eq. 3.14) into water, ZnO and HMTA. As a result, the original HMTA is recovered while producing ZnO.

- Ammonia from HMTA forms a complex ion with Zn^{2+} (Eq. 3.15) that is subsequently hydroxylated into ZnO, water and ammonia (Eq. 3.16).

- Zn^{2+} forms a complex hydroxide (Eq. 3.17) as previously shown, $[Zn(OH)_4]^{2-}$, that will then decompose into ZnO, water and hydroxyl. This hydroxide complex is the building block of the ZnO NW structure as detailed later on.

As seen from this reaction mechanism, the critical step in the ZnO NW growth is the hydrolysis of ammonia into ammonium and hydroxyl ions in water solution under temperature. Thus, the role of HMTA in the growth of the NWs is key to fully understand the growth mechanism and how the concentration of HMTA will affect the growth. As the hydrolysis of HMTA is a reversible reaction, the release of OH^- to the growth solution is controlled.

3.5.2 Role of HMTA in the nanowire growth

To assess the role of HMTA in the NW growth, first it is necessary to provide a brief structural description of the growth of ZnO NWs. There are two possible growth directions for as-grown NWs: the axial growth (*c*-axis) along the [0 0 1] direction and the lateral or radial growth. Promoting axial growth leads to NWs with a higher aspect ratio (ratio between length and diameter), while the lateral growth will form NWs closer to a unitary aspect ratio. As seen from the reactions of the growth

mechanism, the growth of ZnO NWs takes place through complex cations. At the same time, the top (0 0 0 1) plane of the ZnO NWs is formed by a $[Zn(OH)_4]^{2-}$ complex, which has a high surface energy, indicating its readiness to react and stabilize into ZnO. Moreover, this hydroxide complex has a tetrahedral structure akin to that of the wurtzite ZnO, making it the ideal building block for the ZnO NWs. In addition, the side faces of the ZnO NWs are nonpolar, meaning that the positively charged complexes formed in the solution will preferentially react with the polar (0 0 0 1) plane.

Figure 3.10 shows a schematic describing this growth mechanism. Here, it can be seen that the highly reactive tetrahedral $[Zn(OH)_4]^{2-}$ complex directs the growth of the ZnO NWs along the [0 0 1] direction. This zinc complex is the one that grants the [0 0 1] growth direction of the ZnO NWs its reactive and polar characteristics.
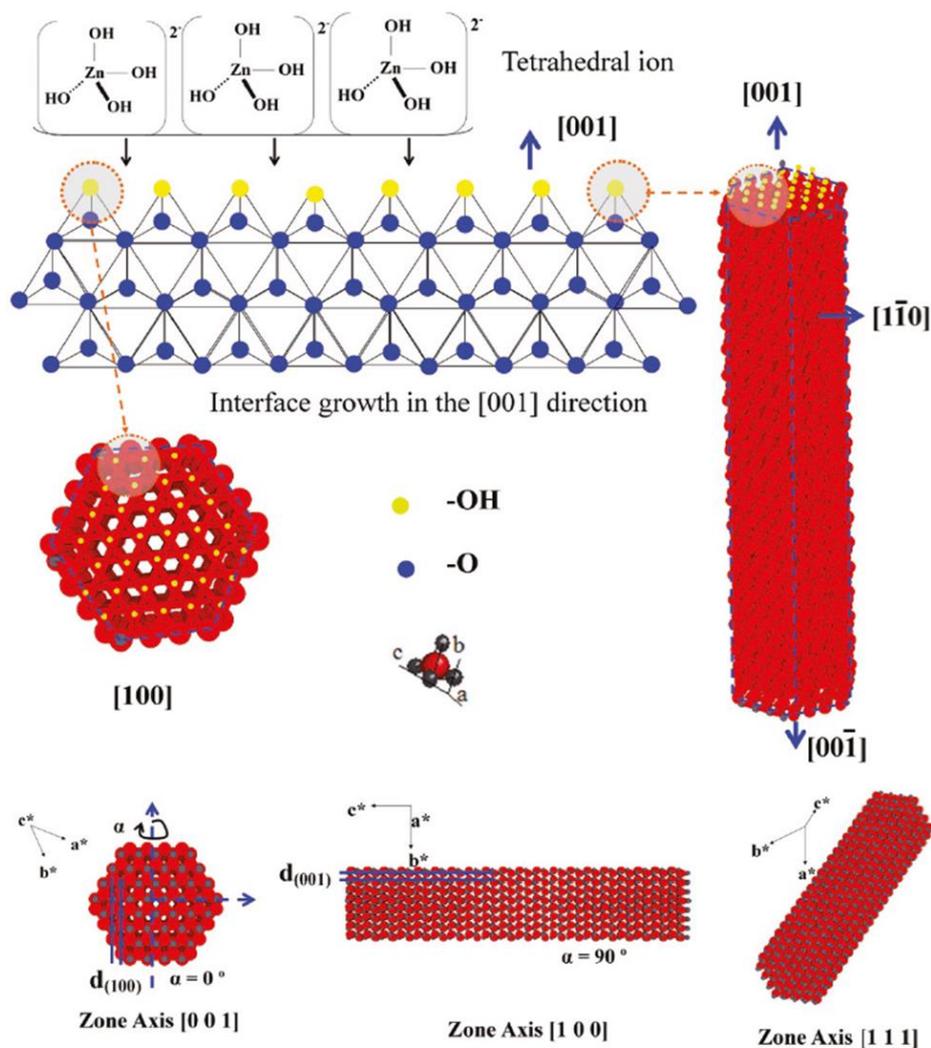
Figure 3.10. Schematic representation of the growth mechanism of ZnO nanowires, illustrating the polarity of the (0 0 0 1) plane and the non-polar lateral faces[165].

79

Considering the growth reactions and mechanisms, HMTA has two main roles in the ZnO NW growth. First, it acts as a pH modulator, supplying the required OH$^-$ ions in solution that drive the growth in a controlled manner, similarly to a pH buffer. Second, HMTA attaches to the non-polar lateral faces of the ZnO NWs, producing a steric hindrance that inhibits the lateral growth of the NWs as the zinc complexes generated in solution cannot access the nonpolar faces of the NWs, as reported by Strano[164] and Parize[166] separately. Nonetheless, this steric hindrance is dependent on the concentration of the precursors in the growth solution and the size of the crystallites of the underlying seed layer.

3.5.3 CBD control parameters and their influence on the nanowire growth

Zinc nitrate hexahydrate and HMTA were the precursors used in this work. It is crucial to accurately control the concentration used for each and the ratio between them, as this is key for the adequate growth of the ZnO NWs. One critical aspect of the CBD of ZnO NWs is that, at the same time that the NWs are growing on the seeded substrate, hydrothermal synthesis reactions take place in solution, forming ZnO nano and microstructures. The growth of these structures in solution depletes the growth precursors at a much faster rate than the growth on a substrate. Hence, it is necessary to ensure that the concentration of the precursors in the solution is high enough to continue the NW growth for the desired reaction time. As detailed earlier, HMTA inhibits the lateral growth of the NWs, promoting their axial growth and thus increasing their aspect ratio. However, if the HMTA concentration is too high, it may inhibit the growth of the NWs altogether, leading to the growth of other nanostructures such as nanoplatelets or nanodisks. For zinc nitrate, the concentration has to be such that it enables the controlled growth of the NWs. Should it be too high, an undesired compact ZnO layer will be formed; on the other, if the concentration is too low, the NWs will not fully form. Regarding the ratios between zinc nitrate and HMTA, it has been thoroughly discussed in the literature, with the consensus stating[163, 164] that higher densities of high quality and high aspect ratio NWs are obtained for equimolar ratios. Higher concentrations of HMTA than zinc nitrate provide a lower density of higher aspect ratio NWs. These considerations

clearly indicate that carefully selecting the concentration of both reagents is paramount to control the growth of ZnO NWs. As such, and based on these reports, a standard concentration value of 25 mM was used for both zinc nitrate and HMTA. For higher equimolar concentrations, the as-grown NWs have larger diameters and longer lengths owing to the richer growth solution. NWs grown under these and other conditions are discussed in Chapter 5.

There are three other CBD control parameters that directly influence the growth of the NWs, namely the pH of the growth solution and the time and temperature for the CBD growth (see Figure 3.11). Modifications of the pH values, by adding a base such as ammonia to the growth solution, for example, have considerable influence on the morphology and dimension of the as-grown ZnO NWs. The works of Baruah[167] and Verrier[168], among others, effectively show that for initial solution growth pH values in the neutral region (between 6.3 to 7.3), the CBD process yields hexagonal NWs with controllable dimensions. However, as this pH is increased to more basic,
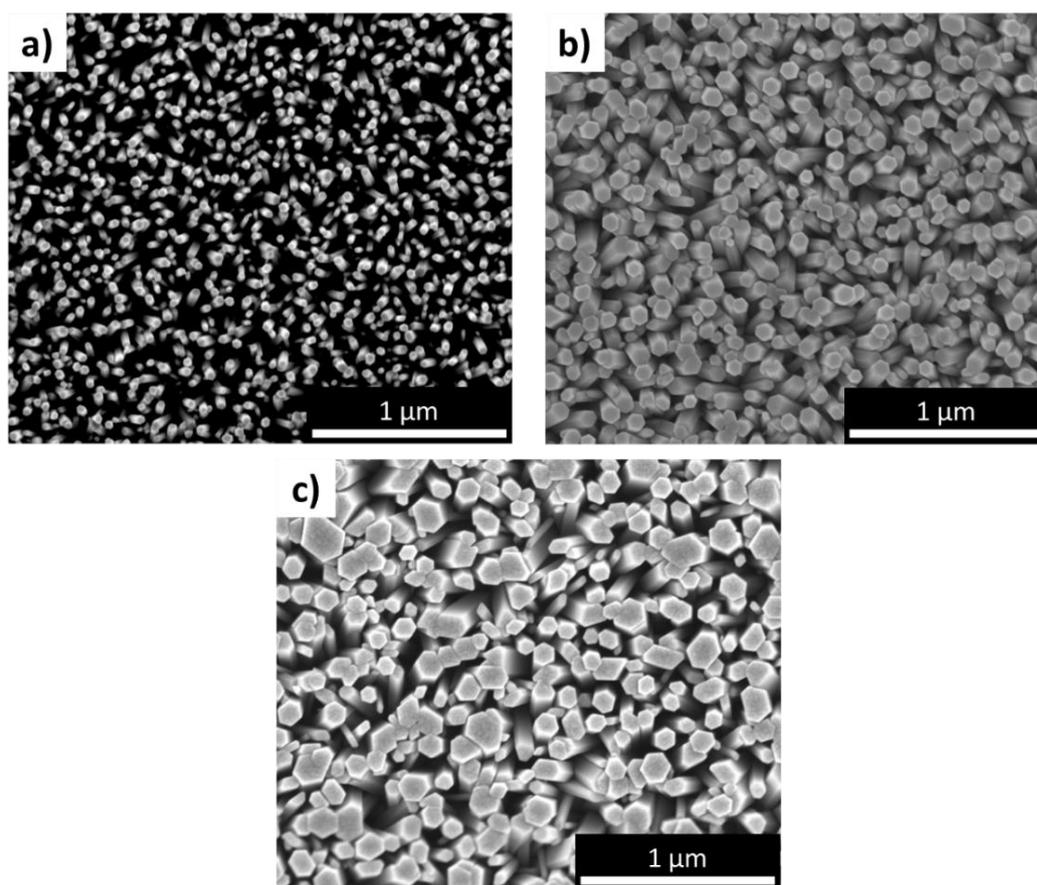
Figure 3.11. Scanning electron micrographs of ZnO NWs samples grown under different CBD conditions: **a)** 2 hours, 25 mM equimolar, **b)** 2 hours, 50 mM equimolar and **c)** 6 hours, 25 mM equimolar. The increase in both precursor concentration and synthesis time directly affect the NW diameter and density.

the ZnO nanomorphology changes from NWs to nanoneedles or flower-like structures, which are not desired for this work.

The temperature during growth has a large influence on the growth kinetics and, hence, on the growth rate of the NWs. In short, higher temperatures will improve the kinetics of the NW growth, increasing the growth rate of the NWs. However, increasing the temperature has its limitations. In the particular case of the CBD process, as the growth takes place in an unsealed processing unit (as opposed to an autoclave in hydrothermal synthesis), the temperature is limited by the boiling point of the solvent, in this case water. Therefore, the maximum working temperatures are in the range of 90°C to 95°C. Temperatures below 90°C, down to 50°C, will result in NW growth, although the growth rate will be much lower. Thus, in this work, 90°C was used for all the NW growth. No experiments were performed at other growth temperatures as the literature on this topic is extensive and comprehensive[163, 169] and this was considered outside of the scope of the work.

The synthesis growth time is the final CBD growth parameter discussed here. Its influence on the growth of the NWs is rather simple: the longer the growth time, the larger both the axial and lateral growth will be. Thus, the synthesis growth time is the prime control parameter to tune the dimensions of the NWs, along with the precursor concentration. In this work, 2 hours of growth time was established as the benchmark and other growth times used were compared to the 2 hours benchmark, as described in Chapter 5.

The final critical influence on the dimensions, crystallinity and orientation of the as-grown NWs comes from the seed layer. Regarding the crystallinity, provided that the preferential crystalline orientation of the as-grown wurtzite phase NWs is (0 0 2), a seed layer deposited with this crystalline orientation will yield in principle better quality NWs due to almost no lattice mismatch. Nonetheless, seed layers with other preferential crystalline orientations will also serve as adequate growth platforms for the NWs. The crystallite sizes within the seed layer, i.e., the size of the surface nanometric features, plays a key role in the starting diameter of the NWs. In essence, larger crystallite sizes will yield NWs of larger diameter, as detailed in Chapter 5. The last factor of considerable importance is the surface roughness of the seed layers. Indeed, seed layers with a larger surface roughness will induce random alignment of

the NWs during growth, while seed layers with a low roughness (typically below 1 nm) will yield vertically aligned NWs, as depicted in the schematic of Figure 3.12. The alignment of the NWs can play an important in certain applications, especially those with an emphasis on light absorption (solar cells) or those that take advantage of the large exposed surface to volume ratio of the NWs (gas sensing).

3.6 Doping of ZnO nanowires

Doping of ZnO is one of the most prominent areas of research in the field owing to the host of possible applications in which it can be implemented. The basics of semiconductor doping and why is it an interesting nanoengineering approach were discussed in Chapter 2. Doping of ZnO NWs, in particular, has been a subject of study for many years in the field thanks to the versatility of the NWs and the enhanced properties obtained after doping, which can further prompt the implementation of NWs in electronic devices. The doping of ZnO NWs has different aims depending on the material used as the dopant, although it is mostly focused on improving the optoelectronic properties of ZnO or changing the intrinsic type of semiconductor from n-type to p-type. The doping of ZnO NWs can be achieved through multiple methods. A critical feature of this doping is that the exact amount of dopants integrated in the ZnO NWs has to be carefully controlled, to ensure that the properties are tuned to the target application. Among the many available dopants, two in particular, cobalt and copper, have shown special promise in optoelectronic applications thanks to their ease of integration into ZnO and the control over the change induced in the NW properties[170, 171].
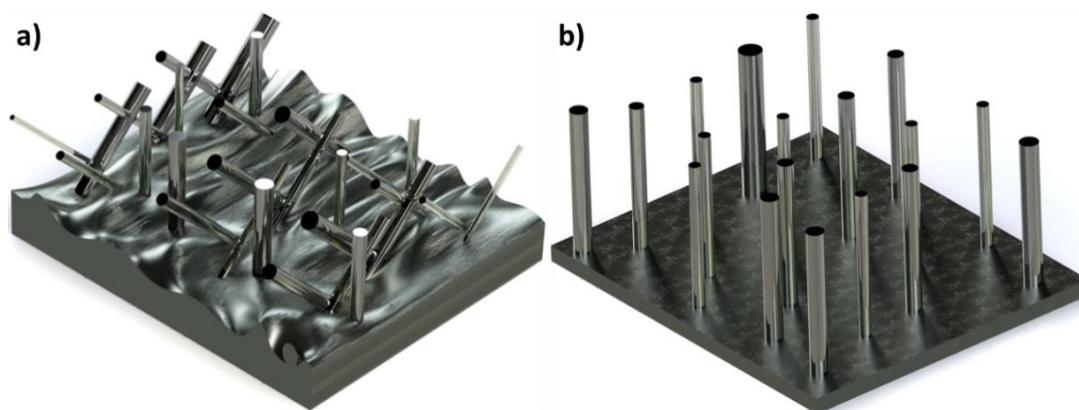
Figure 3.12. Schematic representation of the ZnO NW growth on **a)** rough or **b)** smooth seed layers, depicting the difference in the orientation of the as-grown NWs prompted by the texture and roughness of the seed layer.

ZnO can be doped with an almost limitless plethora of elements from the whole periodic table, from alkali metals to nitrogen or chalcogens. Independently of the ZnO growth technique used, the doping in most cases in done *in situ*, i.e., during the NW growth. In order to control the amount of dopants integrated during the NW growth, controlled quantities of the doping agent must be supplied during growth, either from the beginning or in an intermediate growth step. In general, the relation of Zn and dopant precursors before growth will not be a real quantitative reflection of the amount of dopants integrated into the NWs. The exact amount of integrated dopants has to be either quantitatively measured by techniques such as x-ray photoelectron spectroscopy (XPS) or, else, it can only be qualitatively compared with undoped NWs or NWs doped with a different amount of dopant.

The doping of ZnO NWs is based on the incorporation of the dopant agent taking place either as a defect[172] in the crystalline lattice of ZnO or as a substitutional atom taking the place of a Zn[173] or O[174] atom in the wurtzite lattice, see Figure 3.13. The selection of the dopant agent is typically linked with a target application. The main applications in which doping plays a role can be summarized as follows:

- ZnO is a photoactive material that absorbs light in the UV-blue regions of the spectra. Adding dopants to ZnO helps controlling the optical properties of the material, enabling light absorption in other regions of the visible spectrum. Dopants can also introduce electronic states that improve the photocatalytic properties of ZnO. For example, doping ZnO NWs with chromium[175] enhances the photocatalytic activity, while also providing a considerable boost to the light absorption across the whole visible range. Another example comes from the improved photocatalytic activity efficiency achieved by introducing lanthanum[176] into ZnO NWs.

- ZnO NWs have previously been described as ideal platforms for sensing applications owing to the excellent electronic properties of ZnO, the large surface to volume ratio and the availability of adsorption sites due to surface defects. The addition of dopants can greatly enhance the sensing properties of ZnO, giving rise to applications such as humidity sensing[177], by cadmium doping, ethanol sensing[178], by doping with gold, or efficiency enhanced UV sensing[179], by incorporating antimony in the ZnO lattice.

Pristine ZnO   Cobalt-doped ZnO
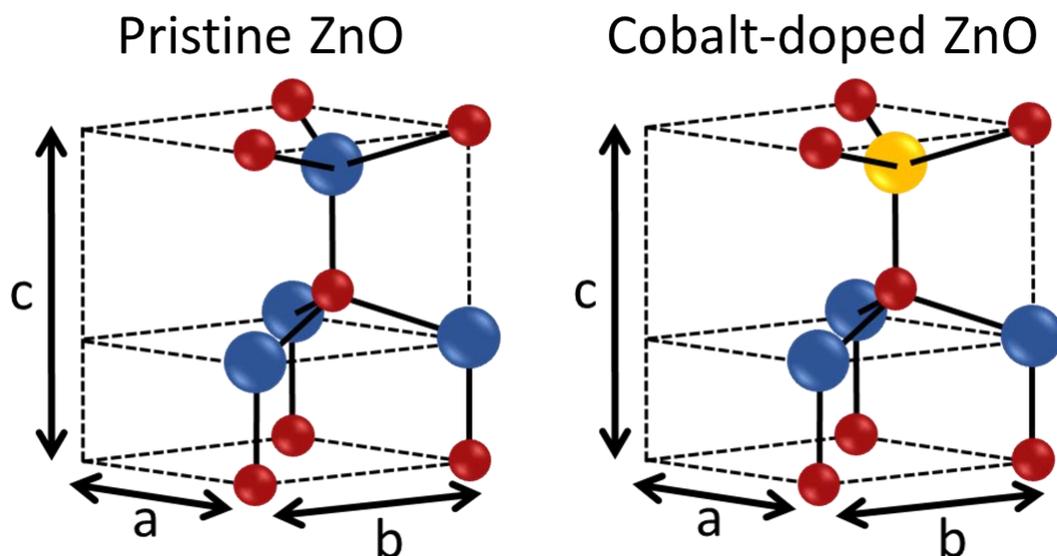
Figure 3.13. Schematic representing the change induced in the ZnO wurtzite lattice when substitutional cobalt doping in introduced. Zinc is represented in blue, oxygen in red and cobalt in yellow.

- New functionalities can be introduced in the ZnO NWs by the addition of specific dopants. In particular, introducing magnetic moieties has seen an exhaustive work in the literature as the low-cost, high quality and high throughput growth of ZnO NWs is interesting in spintronics. As such, the use of magnetic transition metals such as manganese[180] or cobalt[181] has shown promise for magnetic ZnO NWs.

- Changing the semiconducting type from n-type to p-type has been one of the most researched applications of ZnO doping as it would open the possibility of building p-n junction-based devices, which have a vast field of applications. Efforts to achieve this have been mostly focused on the use of lithium[182] as a dopant, although other elements such as silver or antimony have also shown promise, as shown in the detailed work Lu[183] about p-type doping of ZnO NWs.

As it can be seen in this brief overview of ZnO doping, a large variety of elements can be introduced into the ZnO lattice of the NWs to control their optoelectronic properties. More detailed information about the growth, enhancement and applications of doped ZnO NWs can be found in the thorough reviews of Samadi[170] and Hassanpour[171].

In this work, the ZnO NWs were grown and doped using CBD. Two different metals were selected as dopants, cobalt and copper. Both are known for providing

control over the optical properties of the NWs. In particular, they induce a red-shift in the absorption band edge of the ZnO NWs. This means that the bandgap of the NWs will be reduced, allowing the absorption of light at lower energies to enhance the performance of the photoelectrochemical applications in this work. Both dopants were integrated in the ZnO NWs *in situ* during the CBD growth of the NWs. For this, cobalt ($Co(NO_3)_2 \cdot 6H_2O$) or copper nitrate ($Cu(NO_3)_2 \cdot 3H_2O$) were used as the metal cation salt, which was dissolved along with the zinc nitrate and HMTA in the solution for the NW growth. These cations have a 2+ valence, the same as zinc, which prompts their integration into the ZnO lattice directly by substitution[184] of a Zn atom with a Co or Cu atom.

Substitutional doping induces changes in the structure of the ZnO NWs due to the difference in atomic radii between Zn and the doping agents. As these atomic radii differ by a few Angstroms, when a Zn atom is substituted, small changes in the lattice parameters will be induced, slightly distorting the wurtzite structure, while maintaining the crystalline structure of the NWs, meaning that the NWs are still single crystal wurtzite phase ZnO. Furthermore, Co and Cu doping induce structural changes in the NWs due to different growth kinetics that result in larger diameter NWs compared to the undoped ones. This effect of the doping is shown for Co-doped ZnO NWs in Figure 3.14. To control these structural changes and tune the effect on the optical properties, different concentrations of cobalt or copper nitrate were introduced into the growth solution so a comparative study was established. For this, the ratios between the dopant nitrate and zinc nitrate were varied to achieve a better
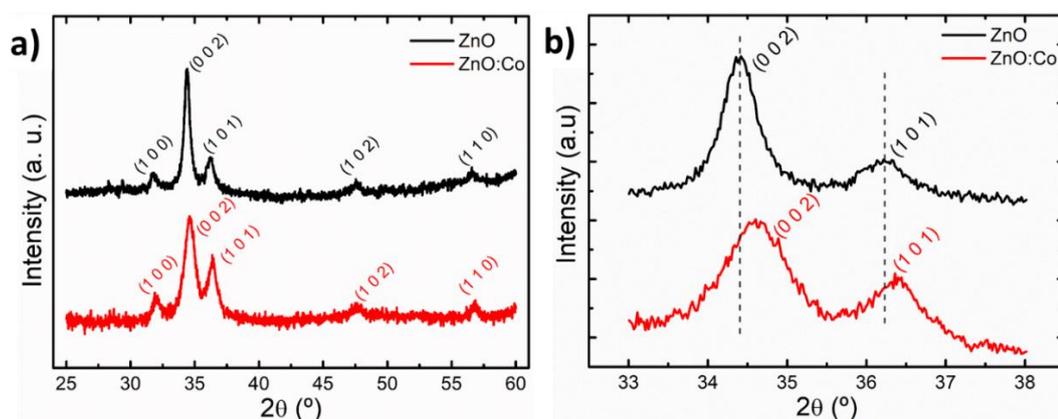
Figure 3.14. X-ray diffraction spectra of **a)** pristine and **b)** Co-doped ZnO NWs showing the characteristic peak main peaks of wurtzite phase ZnO. The shift in the (0 0 2) and (1 0 1) peaks towards higher diffraction angles after Co-doping is a clear indication of the substitutional character of the cobalt doping owing to the difference in atomic radii between Zn and Co atoms.

understanding and control of the influence that of two dopants upon the growth, properties and applications of the resulting doped-ZnO NWs. A detailed description of the different doping conditions and their influences on NW growth and optical properties is presented in Chapter 6, while their functional performance in photoelectrochemical water splitting is detailed in Chapter 8.

3.7 Surface functionalization of ZnO nanowires

The surface functionalization of ZnO NWs has been widely utilised to develop the properties of ZnO to better match the requirements of the target application. This, along with doping, opens a variety of tunability options that can tailor the properties of the ZnO NWs to specific applications. Furthermore, the NW morphology incentivises the use of surface functionalization thanks to its large surface to volume ratio, so any enhancement provided by the surface functionalization is further boosted by the original large surface area of high aspect ratio NWs. Surface functionalization of ZnO NWs can be used to sensitize the light absorption of the NWs, passivate surface defects to enhance the operational lifetime or add catalytic moieties. For this, different methods can be used. Here, three of these will be discussed, namely the core-shell structuring using the ZnO NWs as core, the integration of ZnO NW cores and metal-organic framework outer layers and the surface decoration of the NWs with precious metal and, in particular, iridium.

3.7.1 Core-shell structuring of ZnO nanowires

It is possible to take advantage of the NW morphology and its verticality to coat their surface with another material to add functionality. This can be achieved through different techniques that offer the possibility of depositing a thickness-controlled shell. There are two key features to successfully implement a core-shell structuring: first, the orientation of the NWs has to be as vertical as possible so shadow effects can be avoided, as showcased in Figure 3.7. Second, the thickness of the deposited shell should be homogeneous and of a controlled thickness to ensure an adequate integration of the shell and the ZnO core. Typically, the shell thickness is of the order of a few nanometres, which can be deposited using different techniques such as CVD or PLD. However, the most commonly used technique for the core-shell structuring is ALD. As detailed in Chapter 3.4.1, ALD allows atomic control of thin film deposition.

Moreover, ALD is a conformal coating technique, meaning that it can homogeneously and controllably coat nanostructures. This, combined with the large variety of available materials (especially semiconducting metal oxides) makes of ALD the most desirable technique for core-shell structuring.

The group of David Zhang has shown how materials such as HfO_2[185] or ZrO_2[186] can be integrated with NWs as a shell (see Figure 3.15) to tailor the optoelectronic properties of the ZnO NWs for enhanced performance in applications such as lasing or UV emitters. The performance of ZnO NWs as the electron transport layer in a solar cell can be boosted by the deposition of a thin TiO_2 layer[187] that acts as a recombination suppresser, improving some key solar cell parameters. Another example of the extreme versatility of ALD comes from the fabrication of nanocapacitors[188] using ZnO NWs as core and a multi-layered shell based on Al_2O_3 and aluminium-doped ZnO, both of which are deposited using ALD.

3.7.2 Metal-organic framework integration

Metal-organic frameworks (MOFs) are organometallic reticular compounds formed by coordination networks of organic linkers and metallic nuclei. The flexibility with which these two building units can be varied in geometry, size and functionality provides the unique properties of MOFs, with tens of thousands of different structures being reported[189]. MOFs are crystalline structures that, owing to their unique reticular architecture, have outstanding porosity and surface area, exceeding those of other porous materials such as zeolites or carbons[190]. Furthermore, the large
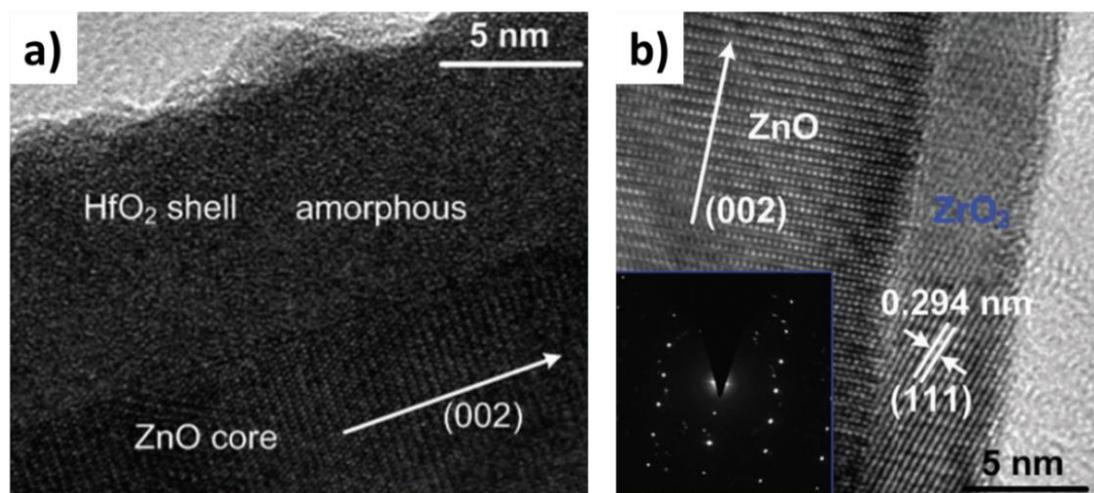
Figure 3.15. Transmission electron microscopy and selected area diffraction patterns of **a)** ZnO/HfO$_2$ core/shell nanowires[185] and **b)** ZnO/ZrO$_2$ core/shell nanowires[186], demonstrating the integration of ZnO cores and metal oxides by using atomic layer deposition.

variety of organic and inorganic moieties that can be used has prompted the use of MOFs in an almost limitless list of applications, among which catalysis and gas adsorption, separation, capture and storage are the most studied. More detailed accounts of MOF general properties can be found in the work of the founder of the field, Omar Yaghi[191, 192].

Considering the vast variety of MOFs, efforts to classify them are required. In this sense, the most common grouping method used is in form of families, MOF groups that share certain structural commonalities, be it a shared organic linker or that they were first synthesized in a certain group or university and that share a common structure. Among these families, one of the most studied in the field is the zeolitic imidazolate framework (ZIF) family[193]. ZIFs are a family of MOFs characterized by their zeolitic architecture that is particularly similar to aluminosilicate zeolites. In this type of zeolites, the traditional bonding structure is M-O-M, where M represents Si or Al; in comparison, the ZIF family bonding structure is typically M-Im-M, where M usually represents Zn or Co and Im is an imidazole organic linker. Based on this, ZIFs have properties that combine those of zeolites and MOFs, providing outstanding surface areas (few thousands of m^2/g), high crystallinity and tunability of their functionalities, and exceptional chemical, thermal and mechanical stability.

Within the ZIF family, there are two particularly important MOFs, namely ZIF-8 and ZIF-67, which are zinc and cobalt-based isostructural ZIFs[194]. This means that their crystalline structure is the same for both, except for the metallic nuclei, which is Zn for ZIF-8 and Co for ZIF-67. ZIF-8 is the most well-studied MOF of the ZIF family. It has a sodalite structure in which zinc is coordinated by 2-methyilimidazole linkers. One of its most important characteristics is the small pore aperture size, which is 0.34 Å, making it an ideal material for the separation of hydrogen from other larger gases such as nitrogen or CO_2[195]. Furthermore, ZIF-8 has shown impressive gas adsorption and storage capabilities, making it a target for diverse pollutant capture applications, such as in the capture of CO_2[196]. ZIF-67 is an isostructural MOF of ZIF-8, with cobalt as the metallic nuclei instead of zinc, that has been utilised in applications like capacitors[197]. The processing of these MOFs is always solution based, be it in a hydrothermal synthesis or a CBD basis.

Commonly, the growth of ZIF-8 is based on the use of organic solvents such as methanol, ethanol or dimethylformamide in which a zinc source and the organic linker (2-methylimidazole for these two MOFs) are dissolved. This opens up the possibility of integrating MOFs and ZnO NWs as no shadowing effect (as described in the previous section) can take place in a solution-based process. Furthermore, since ZIF-8 is based on zinc, the NWs can serve as a growth template, supplying the zinc required for the growth of the MOF to form a shell around them through surface conversion. This method can be achieved following different procedures as detailed in Chapter 7. ZIF-67 can also be integrated with the ZnO NWs, although the experimental requirements are different, due to the presence of Co instead of Zn. Integrating MOFs and NWs has a multitude of applications owing partly to the synergy between the surface to volume ratio of the NWs and the vast surface area of the MOFs. This means that the performance of this type of hybrid material in applications that require large surface areas, like gas sensing or catalysis, will be enhanced. Chapter 7 details the integration of ZIF-8 and Co-doped ZnO NWs, with a thorough description of the novelty of this integration, its processing and how the ZIF-8 shell greatly enhances the photoelectrochemical performance of the ZnO NWs towards water splitting, with Figure 3.16 showing an example of this integration

The integration of MOFs and NWs can be taken a step further, should the MOFs be converted into other functional materials. MOFs like ZIF-67 have been used as scaffolding for the direct thermal conversion of the MOF into another material of interest, Co_3O_4 in the particular case of ZIF-67[198]. Co_3O_4 has been widely used as a
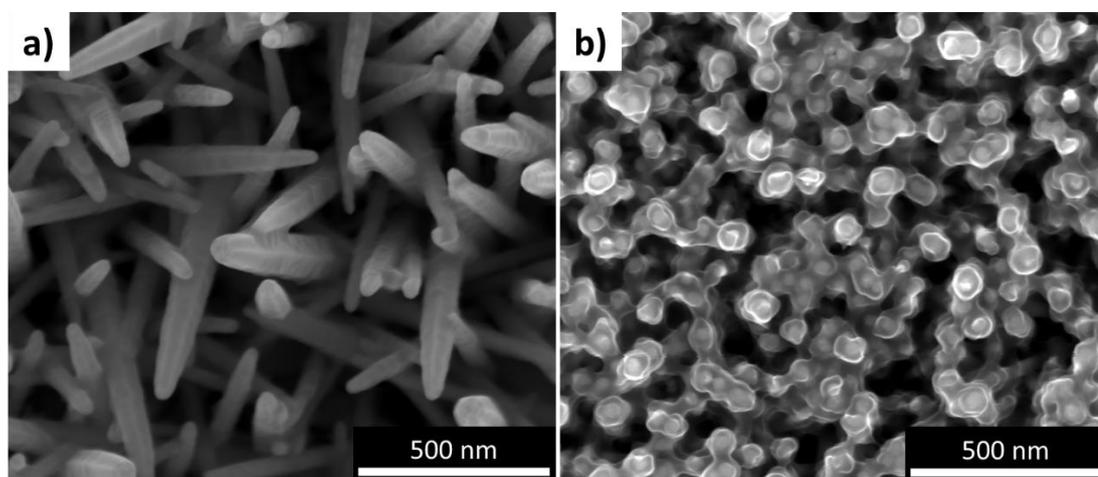
Figure 3.16. Scanning electron micrographs of ZnO core-ZIF-8 shell nanowires. The shells were deposited by **a)** spin coating and **b)** drop casting.

high activity, highly efficient photocatalyst for the production of hydrogen and water treatment. Direct carbonization of ZIF-67 at high temperatures will yield structured Co_3O_4 following the architecture of the MOF in an attempt to increase the available catalytic surface area of the cobalt oxide. This means that the integration of MOFs and NWs can provide a pathway for the controlled addition of co-catalysts to the ZnO NWs that can further improve their performance in photocatalytic applications. As such, this integration has been deemed an interesting approach for the implementation of ZnO NWs and co-catalysts for enhanced performance. An example of this is shown in Figure 3.17, in which ZIF-67 was utilised as scaffolding to convert it into a Co-nanocarbon composite by direct thermal carbonization. In this way, the cobalt-nanocarbon composite can be grown using the nanostructure of ZIF-67, which can be beneficial to applications such as catalysis or gas sensing/adsorption.

3.7.3 Surface decoration of ZnO nanowires

The sidewall of the NWs are an attractive foundation layer on which different nanomaterials can be deposited to enhance the properties of the NWs. This surface decoration should be done in a controlled manner to avoid the deposition of a continuous layer that would acts as a shell or barrier that could hinder the performance of a ZnO NW based device. Thus, the surface decoration of the ZnO NWs can be limited to the deposition of nanoparticles (NPs) of different sizes, from
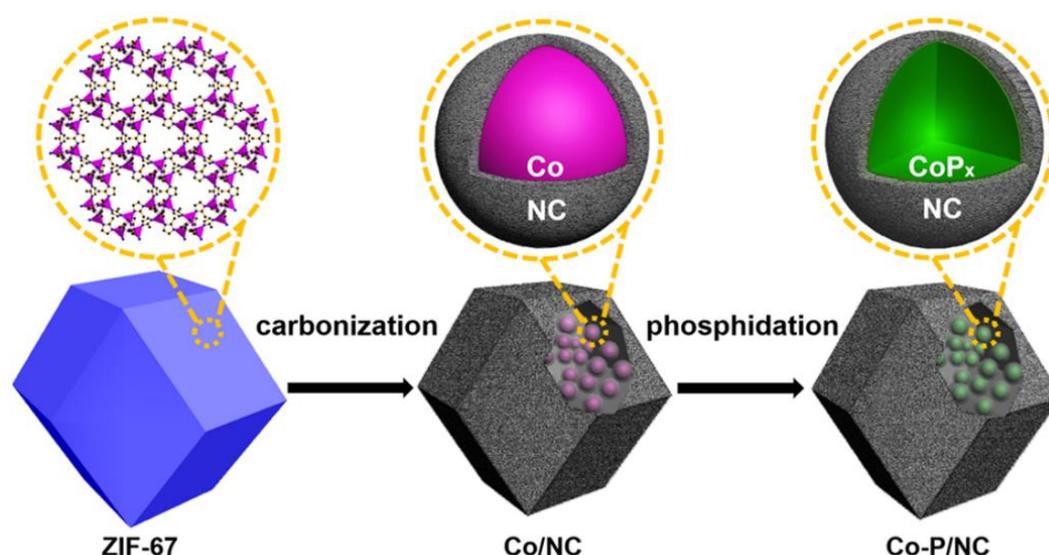
Figure 3.17. Schematic representation of the use of ZIF-67 as scaffolding for the direct transformation into a Co-P/nanocarbon composite[198].

few nanometre NPs to quantum dots[199] (QDs). The addition of the decorating NPs to the NWs can add new functionalities to the NWs, enhancing the electronic structure and improving the optoelectronic properties. In any case, the controlled deposition of these NPs is key to obtain reproducible and comparable results that can be contrasted with the as-grown NWs.

There are two main types of materials that have been utilised for this purpose: precious metals, such as gold, platinum or iridium and carbon-based NPs. Regarding the precious metals, these materials are well known for their outstanding adsorption of analytes to be sensed, making them remarkable sensors. However, making an entire sensor of a material like gold or platinum can be rather expensive, thus the need to find alternatives by which they can provide their catalytic attributes while being present in a much lower quantity in a device. Additionally, elements like gold are known to induce plasmonic effects on the surface of materials that they are deposited on. These surface plasmons will enhance the optoelectronic properties of the ZnO NWs, providing a more efficient photoresponse when used as photodetectors[200] of ultraviolet light. Platinum has traditionally been used as a very reliable and stable gas sensor with high sensitivity[201]. Thus, the coupling of Pt and ZnO NWs has been utilised to greatly enhance the gas sensing[202] response of ZnO NWs. These precious metal NPs are typically deposited either by chemical self-assembly or vapour-liquid-solid growth. In the case of iridium, its integration with ZnO NWs is almost non-existent in the literature, mainly due to the difficulty of accurately depositing controlled NPs. Nonetheless, iridium is widely regarded as one of the most successful photoelectrochemical water splitting catalysers, providing outstanding efficiencies and photogenerated current densities[203, 204]. As such, the integration of Ir and ZnO NWs is of increasing interest in the research on the improvement of the performance of ZnO NWs in photoelectrochemical applications. In this work, the integration of nanoscale Ir features was successfully achieved by making use of sputter deposition of iridium. One of the main problems for Ir deposition stems from the shadowing effects described in Figure 3.18. This issue was overcome by tuning the process parameters of the sputtering to specifically mitigate this shadowing effect, as described in detail in Chapter 4.6.2. The deposition strategy here developed lays the pathway for a new way of functionalizing the surface of NWs,
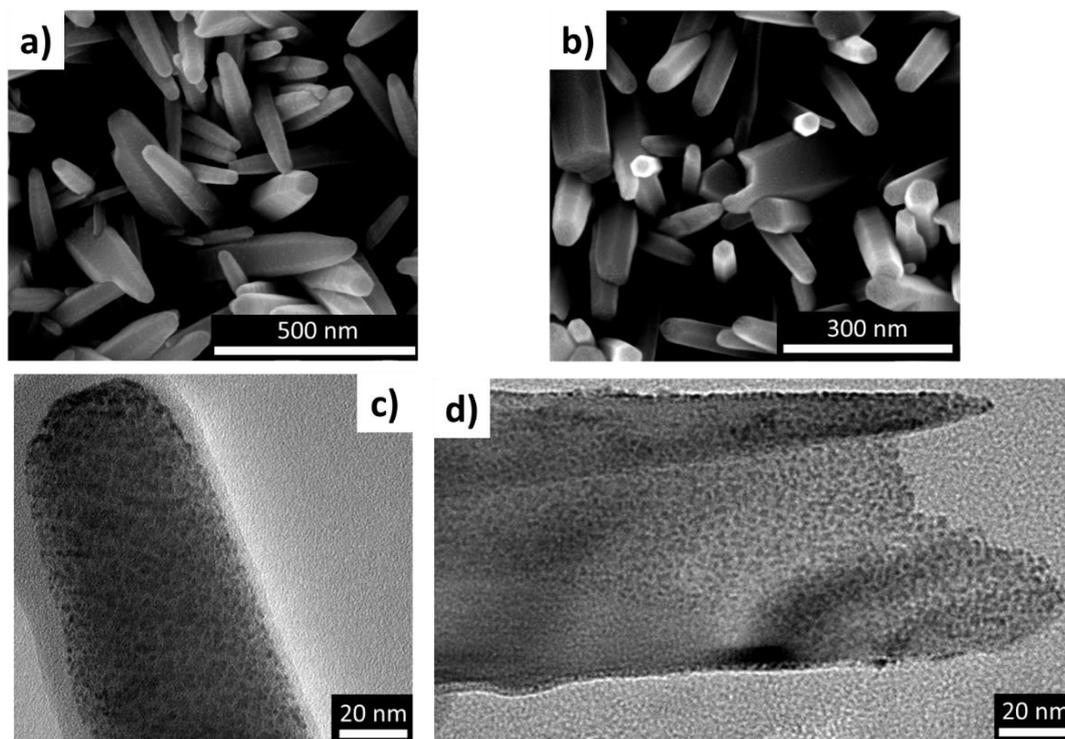
Figure 3.18. a), b) Scanning electron micrographs and **c), d)** transmission electron micrographs of ZnO nanowire samples decorated with iridium nanoparticles. The granulated lateral faces of the nanowires seen in the SEM images indicate the presence of iridium, which is corroborated by the TEM imaging.

avoiding shadowing effects, that can enhance their performance in gas sensing and optoelectronic applications.

Attending to the decoration using carbon-based materials, typically graphene QDs or some type of molecular anchor are used as decorating NPs. In both cases, the process to incorporate the decorating material is based on liquid phase deposition either by drop casting or submerging in a bath containing the NPs. In some cases, prior to the deposition of the carbon-based nanomaterial, the surface of the NWs has to be functionalized with another organic compound that can strongly bond the decorating material. Graphene QDs have been use as sensitizers for photoelectrochemical applications. Thus, similarly to how Ir can affect the performance of the NWs, graphene QD decoration has been explored as an easy alternative process that can provide outstanding results as a photoanode[205]. Another possibility of carbon-based decoration involves using specific molecules that will turn the ZnO NWs in biosensors able to detect a target molecule in air or solution. The selective detection of target biomolecules is an extensive research topics due to the incredible impact it can have in our everyday life. As such, the possibility of taking

advantage of the surface to volume ratio of the NWs to increase the selectivity and sensitivity of a biosensor[206] is a rather attractive alternative to other classical methods.

3.8 Summary

In this chapter, a topical review of ZnO as a material was provided. It began with a detailed description of the most relevant structural, mechanical and electrical properties of ZnO as a material, with an especial focus towards electronics. This was followed by a detailed account of the principal growth methodologies for ZnO and its different nanomorphologies, both in gas and liquid phase. Subsequently, a summary of the array of ZnO nanomorphologies was provided, where structuring is defined by the number of dimensions of the morphology. Here, it was also stated that NWs will be the focal point of this thesis and, as such, the rest of the chapter refers to NWs unless otherwise specified. The growth of NWs is achieved following a two-step process: first, a ZnO seed layer is deposited using either ALD or sol-gel processing; then, the NWs are grown by CBD. An in-depth discussion of these three techniques, their principles, shortcomings and how they were used in this work was given. Details on the doping of ZnO NWs and its importance due to the vast variety of dopants that can be used were provided, specifically its doping with cobalt and copper. Finally, the surface decoration of the ZnO NWs by core-shell structuring, MOFs or the decoration with precious metal or carbon-based NPs was explained.

Chapter 4

Sample preparation and analytical techniques

4.1 Introduction

This chapter describes in detail the growth methodologies used for the sample preparation along with all the morphological, chemical and spectroscopic characterisation of the samples in the thesis. To begin with, the preparation methodology for the different substrates used is described, followed by the details of the deposition of the ZnO seed layer through atomic layer deposition (ALD) or sol-gel processing. Following that, the growth of the ZnO NWs by chemical bath deposition and their functionalization by doping, core-shell structuring and *in-situ* grown nanoparticle decoration is described. The morphological characterization of the seed layers and the as-grown NWs was done using three different types of microscopy, namely atomic force microscopy (AFM), scanning electron microscopy (SEM) and transmission electron microscopy (TEM), and two x-ray-based techniques, x-ray diffraction (XRD) and x-ray reflectivity (XRR). The chemical environment of the as-grown materials was studied through x-ray photoelectron spectroscopy (XPS) and energy dispersive x-ray spectroscopy (EDX) mapping, while the optical properties were analysed by ultraviolet visible spectroscopy (UV-vis), fast transient absorption

spectroscopy (FTAS) photoluminescence (PL), and cathodoluminescence (CL). Different individual samples were used for each separate characterization technique. To ensure homogeneity in their properties, these samples were all prepared in the same batch. The samples were stored in simple plastic Petri dishes under air atmospheric conditions. Finally, descriptions of the photoelectrochemical characterization of the ZnO NWs used as photoanodes are discussed. Unless otherwise specified, all the experiments were carried out by the author. The methods here described serve as the basis for the understanding of the results shown in Chapters 5, 6, 7, 8 and 9.

The following list provides a summary of the materials that were utilised throughout this work. All of the chemicals used in these processes were utilised as received, with no further purification. As substrates, Si/SiO2 (1 0 0) from Testbourne (>10 Ω·cm) and in-house ITO (300 nm) on glass were utilised. The solvents and liquid phase chemicals utilised were sulphuric acid, 98% purity, hydrogen peroxide 30% volume in water, isopropanol alcohol, IPA, ≥99.8% purity, 2-methoxyethanol, $C_3H_8O_2$, anhydrous, 99.8% purity, and methanol, ≥99.9% purity, all from Merck. Regarding solid state chemicals, zinc chloride, pure, hexamethylenetetramine, HMTA, ≥99.5% purity, and 2-methylimidazole, HMIM, ≥99% purity, from Merck, zinc nitrate hexahydrate, 99% purity metals basis, from Alfa Aesar, and cobalt nitrate hexahydrate, 99% purity, and copper nitrate trihydrate, 99% purity, for analysis, from ACROS Organics, were used. In addition, N_2, 99.9% purity, from Air Liquide, and diethylzinc, DEZ, pure, from Merck, prepared for deposition systems, were the gas phase chemical used.

4.2 Preparation of the substrates

Two different types of substrates were utilised in this work, depending on the application and the analytical technique to use: thermally oxidized Si/SiO2 (1 0 0), with 50 nm of SiO2 from Testbourne (>10 Ω·cm), and 300 nm of indium tin oxide (ITO) on glass. The former was mainly used along with ALD for the growth of the seed layers, with the oxide layer acting as an insulator that prevents electrical conduction. The latter was the focus of the sol-gel deposition of seed layers and was also used for

all the photoelectrochemical experiments due to the high electrical conductivity provided by the ITO layer on glass.

Silicon substrates were cleaned in a piranha solution for 15 minutes to remove any dust, debris and inorganic contamination on the polished surface of the substrate. This piranha solution was prepared by mixing sulphuric acid (98% purity, from Merck) and hydrogen peroxide (30% volume in water, from Merck) in a 3:1 ratio. After cleaning with the piranha solution, the silicon substrates were dipped twice in deionized water (DI) and, afterwards, thoroughly washed with a DI water stream to ensure that all the possible residues from the piranha solution were removed. Finally, the substrates were blow dried with a nitrogen gas gun to remove any residual water that could influence the subsequent deposition of the seed layer. Cleaning with piranha solution also hydroxylates the surface of the substrate, which favours the ALD growth of ZnO films.

ITO/glass substrates were cleaned by rubbing the surface of the ITO film with a sterile napkin wet with isopropanol alcohol (IPA, ≥99.8% purity, from Merck) and subsequently blow drying the substrate with nitrogen to remove any fibres or particles from the cleaning process. Afterwards, the surface of the ITO was treated in an ozone cleaner for 15 minutes to enhance the addition of the sol-gel deposited ZnO seed layer to the substrate.

4.3 Atomic layer deposition of ZnO seed layers

Atomic layer deposition (ALD) is a thin film deposition technique based on the sequential use of precursors in gas phase to grow continuous films with atomic control of their thickness, roughness and structural properties. A more detailed description of the principles of the technique were provided in Chapter 3.4.1.

In this work, the system used was a Savannah S300 ALD system from Ultratech/Cambridge NanoTech. For ZnO, diethylzinc (DEZ, pure, from Merck, prepared for deposition systems) was used as the organometallic zinc precursor and water was used as the oxidant. The working temperatures for the deposition can range from 125°C up to 280°C, which is close to the thermal limit of the sealing rings in the system. In this thesis in particular, for ZnO seed layers, temperatures ranging from 200°C to 280°C were utilised as, within this range, the ZnO seed layer are

expected to have an (0 0 2) crystalline orientation with respect to the surface normal, which is desired for the growth of the ZnO NWs. A wide variety of pulse and purge times ranging from 0.01 s to 1 s were used for both water and DEZ, as detailed in Chapter 5.1. The carrier gas used was N_2 (99.9% purity, from Air Liquide) at a low vacuum of 0.3 Torr. The ALD process was controlled by the Ultratech in-built software, in which the deposition setup, system schematic, status and the pulse and purge train can be controlled. In addition, the temperature, base pressure, carrier gas flow and number of cycles were also controlled via this software.

Due to unforeseen practical health and safety issues, the ALD system could not be utilised for the later part of this work for the deposition of ZnO seed layers. Thus, the use of ALD was limited to the study of the controlled growth of ZnO NWs in Chapters 5 and 6, while the work described in Chapters 7 and 8 was based on the sol-gel deposition of seed layers on ITO/glass substrates.

4.4 Sol-gel deposition of ZnO seed layers

Sol-gel processing is a soft-chemistry solution-based process used to prepare thin films by direct deposition of a solution and subsequent heat treatment. The technique used to deposit the solution will determine the final outcome of the deposited thin film. Thus, in this work, spin coating was the sol-gel processing technique used for the deposition of the ZnO seed layer. The spin coating process is based on the application of centrifugal force by spinning at high speed in order to create a surface that is homogeneously coated with the target material. A detailed description of sol-gel deposition and spin coating is provided in Chapter 3.4.2.

To prepare the precursor solution for ZnO seed layers, zinc chloride (pure, from Merck) was chosen as the zinc source with 2-methoxyethanol ($C_3H_8O_2$, anhydrous, 99.8% purity, from Merck) as the solvent. In a typical seed layer deposition, 225 mg of $ZnCl_2$ were dissolved in 10 mL of $C_3H_8O_2$ and subsequently spin coated on to the substrate. The spin coating was carried out at 5000 rpm for one minute, with the acceleration set at 2500 rpm per second. Subsequently, the seed layers were thermally treated at 300°C for 1 hour to form the ZnO seed layer. The conditions described here were the only ones used for the sol-gel deposition of ZnO seed layer and no further investigations on different sol-gel conditions were studied.

4.5 Chemical bath deposition of ZnO nanowires

Chemical bath deposition (CBD) is a solution-based batch processing technique utilised to deposit thin films or nanomaterials on to a substrate. In the particular case of the CBD of oxides[126], the process is based on the hydrolysis of a metal salt precursor, which is described in more detail in Chapter 3.5.1.

For the CBD growth of ZnO NWs[158], a few metal salt precursors can be used[162], namely zinc chloride, zinc acetate dihydrate and zinc nitrate hexahydrate. The latter was chosen for this work. In a typical CBD growth of ZnO NWs[158], the desired concentrations of zinc nitrate hexahydrate (99% purity metals basis, from Alfa Aesar) and a hydroxide source, hexamethylenetetramine (HMTA, ≥99.5% purity, from Merck), were dissolved in 200 mL of DI water in a glass beaker. Subsequently, the solution was magnetically stirred until its colour became clear or grey, depending on the concentration of reagents used.

Next, the substrate with a previously deposited seed layer was submerged in the solution face down and the covered beaker was then introduced into an oven at 90°C. The following conditions were set as the benchmark for the ZnO NW growth: 25 mM equimolar concentration of zinc nitrate (1.487 g) and HMTA (0.701 g) dissolved in 200 mL of DI and placed in the oven at 90°C for 2 hours. Under these conditions, the pH of the solution was set at around 8 and it was not modified unless otherwise stated. Both the volume of the solution and the temperature were kept constant throughout this work, while the concentration and the synthesis time were used as growth control parameters, as described in detail in Chapter 5.3.

The sample holder, shown in Figure 4.1, is a custom-made in-house Teflon holder formed by a ring with three detachable legs and an outer ring; both rings have an internal diameter of 4.9 cm. Teflon was chosen as the ideal material due to being chemically inert and able to withstand the temperature and pH conditions of the NW growth. The samples were placed face down, i.e. with the ZnO seed layer facing downwards to avoid the settling out of any ZnO structures grown in solution on top of the as-grown NWs on the substrate. This is particularly important for the samples used in photoelectrochemical applications as these deposited ZnO structures could
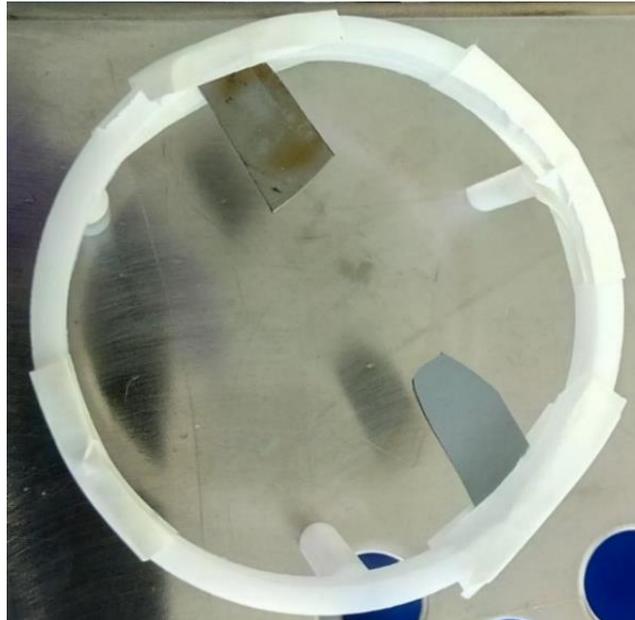
Figure 4.1. Top view photograph of the custom-made Teflon holder and two silicon samples placed face down in order to obtain an optimal growth of ZnO NWs. The inner diameter of the Teflon holder used is 4.9 cm.

hinder or interfere with the correct operation of the device. The importance of this positioning is demonstrated in Chapter 5.6.

After growing the NWs for the desired synthesis time, the glass beaker was taken out of the oven and naturally cooled to room temperature. Immediately after taking the beaker out of the oven, the sample holder was placed in a separate beaker filled with DI water. Then, the as-grown NW sample was thoroughly washed under a DI water stream and subsequently blow-dried with nitrogen to ensure that any possible growth residue was removed from the surface of the NWs.

4.5.1 Doping of ZnO

Doping of the ZnO NWs with cobalt or copper was carried out in-situ during the CBD growth[171], as detailed in Chapter 3.6. For this, cobalt nitrate hexahydrate (99% purity, ACROS Organics by Fisher) and copper nitrate trihydrate (99% purity, for analysis, ACROS Organics by Fisher) were used as the respective precursors. The appropriate concentration of the respective salts was dissolved in the same 200 mL DI water along with the other reagents and the growth procedure otherwise remained the same. The percentage values used to designate the different concentrations described in Chapter 6 refer to the atomic ratio between Co or Cu and Zn as in Eq. 4.1,

$$Doping \ \% = \frac{C_{dopant}}{C_{Zn}} \cdot 100 \qquad\qquad \text{[Eq. 4.1]}$$

where *Doping %* refers to the percentages described in Chapter 6, and *C_{dopant}* and *C_{Zn}* are the concentrations of the dopant (Co or Cu) and Zn precursors, respectively. However, these nominal values do not represent the real amount of dopant in the NWs[207], which is expected to be lower than the nominal value provided. The reason for this lies on the fact that part of the dopants will react in solution or will not react at all, which reduces the amount of dopant that will be integrated in the NWs. Depending on the dopant, the colour of the solution changed to red or blue as a function of cobalt or copper doping, respectively.

4.6 Functionalization of the ZnO nanowires

The ZnO NWs, both undoped and doped, were functionalized using different materials in order to enhance the intrinsic properties of ZnO and overcome some of the shortcomings mentioned in Chapter 3.2. Two different types of surface functionalization are discussed: iridium deposition and metal-organic framework (MOF) growth.

4.6.1 Iridium functionalization

ZnO NWs were also functionalized with iridium to investigate any enhancement in their photoelectrochemical performance as water splitting photoanodes due to the catalytic effect of Ir. The decoration of the NWs sidewalls with nanoscale iridium was achieved through radio frequency (RF) magnetron sputtering[208]. In a typical sputtering deposition process, a gas discharge plasma is generated inside the deposition chamber close to the target of the material to be deposited in such a way that the target is bombarded by high-energy ions from the plasma. This bombardment of ions onto the target causes the removal of atoms from the surface of the target, which then coalesce on the substrate to form a film of the target material. Typically, Ar gas is used as the working gas that is ionised to produce the plasma that bombards the target, which is chosen due to its large mass and being inert. The bombardment of the target causes the ejection of target atoms and secondary electrons, which help maintain the plasma. Once the target atoms reach the substrate, they can migrate to areas of the substrate where the surface energy is

more favourable to the adequate coalescing of the film. The distance between the target and the substrate must be short enough that the target atoms do not re-evaporate before coalescing on the substrate. For this, no impedance should be in the deposition chamber, thus the need for vacuum during deposition. To ensure a homogeneous deposition on the sample, the substrate is typically rotated.

In an ideal sputtering thin film deposition, the working gas pressure will be low enough (high vacuum, around 10^{-8} Torr) to ensure that the collisions between the target atoms and the working gas atoms will be minimal, ensuring almost unidirectional deposition vectors of the target material, which would be perpendicular to the substrate, creating a smooth, continuous thin film. Different parameters like target-substrate distance, interfacial properties of both substrate (cleanliness, surface energy) and target (possible contamination, irregular ejection of atoms), temperature of both target and substrate, deposition rate, working gas type and pressure as well as the power applied from the RF source play role on the final quality of the *in-situ* grown iridium decoration.

Typical conditions for producing high quality thin films are unlikely to create the nanoisland decoration that is targeted in this work. To achieve this, a low vacuum of 10^{-3} Torr was used. The reason behind this lies in the number of collisions between the target atoms and the working gas, as depicted in Figure 4.2. If a low vacuum is used, the pressure of the working gas is higher, which means that there will be more Ar atoms in the deposition chamber. Thus, when an atom is ejected from the target, it will collide with multiple Ar atoms, leading to multidirectional deposition vectors. Having these multidirectional deposition vectors ensures that the target atoms will deposit on the sidewalls of the ZnO NWs, yielding the targeted nanoisland decoration by self-assembly of the deposited Ir atoms on the sidewalls of the NWs. It is possible, to some extent, to control the size of the deposited nanoislands by controlling the deposition rate, deposition time and working gas pressure in the sputter system. Details of the different sputtering conditions used and their resulting morphological properties are provided in Chapter 7.2.1. This was carried out on a Mantis QPrep500 magnetron sputtering system at the Department of Physics of Durham University.
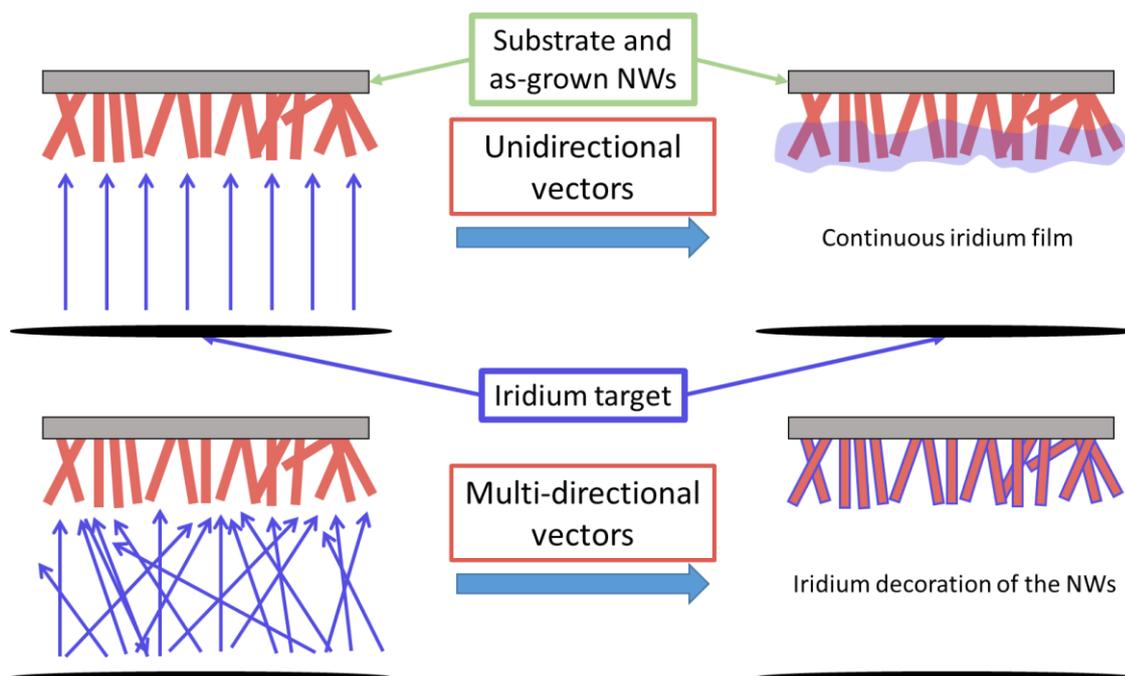
Figure 4.2. Schematic depicting the influence of the directional vectors during the sputtering of the iridium functionalization. The top frame shows that unidirectional deposition vectors lead to a continuous iridium film, while in the bottom frame, multi-directional vectors provide a homogeneous decoration of the NWs.

4.6.2 Metal-organic framework functionalization

Metal-organic frameworks[209] (MOFs) are organometallic compounds formed by metallic nuclei coordinated with an organic linker, as described in Chapter 3.7.2. In this work in particular, a MOF from the zeolitic imidazolate framework[193] (ZIF) family was used, ZIF-8, which is a zinc based MOF.

The growth of ZIF-8 was carried out through two different methods: drop casting and spin coating. In both cases, the MOF growth principle is based on utilising the hydrophilicity of the ZnO NWs to wet their sidewalls with the solution containing the organic linker of ZIF-8 (2-methylimidazole, HMIM, ≥99% purity from Merck), followed by a thermal treatment such that the zinc from the NWs would react with the HMIM on the sidewalls to form the MOF. For both processes, a HMIM solution in methanol (≥99.9% purity, from Merck) was prepared by dissolving the desired amount of organic linker in 10 mL of methanol and stirring until a clear solution was obtained. The solution was either drop casted or spin coated on to the as-grown NWs. For the former, five 0.05 mL droplets were used, enough to form a thin liquid layer on top of the NWs. For the latter, the spin coating process was performed at 5000 rpm for 30 seconds at an acceleration of 2500 rpm per second. Higher rpm

ensured an adequate coverage of the sidewalls of the NWs and led to the best and most controlled growth of the ZIF-8 shell, which is discussed in Chapter 7.3.2. The conditions here described for spin-coating are based on a process that was developed internally, as this was a novel approach to the integration of ZIF-8 and ZnO. After the deposition with either technique, a two-step thermal treatment on hot plates was utilised for the growth of ZIF-8. First, a pre-growth evaporation step at 65°C for 5 minutes was performed to ensure that all the remaining solvent from the starting solution was eliminated. Then, the growth step was carried out at 160°C for different times. This temperature is above the melting point of HMIM and leads to a liquid-solid reaction on the lateral faces of the NWs by which the ZIF-8 shell grows using the ZnO NWs as growth templates. After growth, the samples were rinsed with methanol and blow-dried with a nitrogen gas gun to remove any unreacted reagent. The different conditions used for the growth of the shell and the results obtained are described in detail in Chapter 7.

4.7 Microscopies for structural and morphological analysis

Three different microscopy techniques were utilized to fully characterize the structure and morphology of the ZnO seed layers and NWs: atomic force microscopy (AFM) was used to analyse the surface properties of the seed layers, while scanning electron microscopy (SEM) and transmission electron microscopy (TEM) were used to study the structural and morphological properties of the undoped, doped and functionalized ZnO NWs.

4.7.1 Atomic force microscopy

Atomic force microscopy[210] is a high-resolution type of scanning probe microscopy (SPM). SPM techniques are based on using a physical probe that scans the surface of a specimen to form images. In the case of AFM, sub-nanometre resolution can be achieved. The main parts of any AFM system are a flexible cantilever, placed parallel to the specimen, the tip protruding from the cantilever, which is the probe of the system and determines the highest achievable resolution, the support of the cantilever, a piezoelectric element that controls the oscillations of the cantilever, a laser detector to accurately measure the deflection and motion of the cantilever and the stage. A schematic of a typical AFM system is given in Figure 4.3.
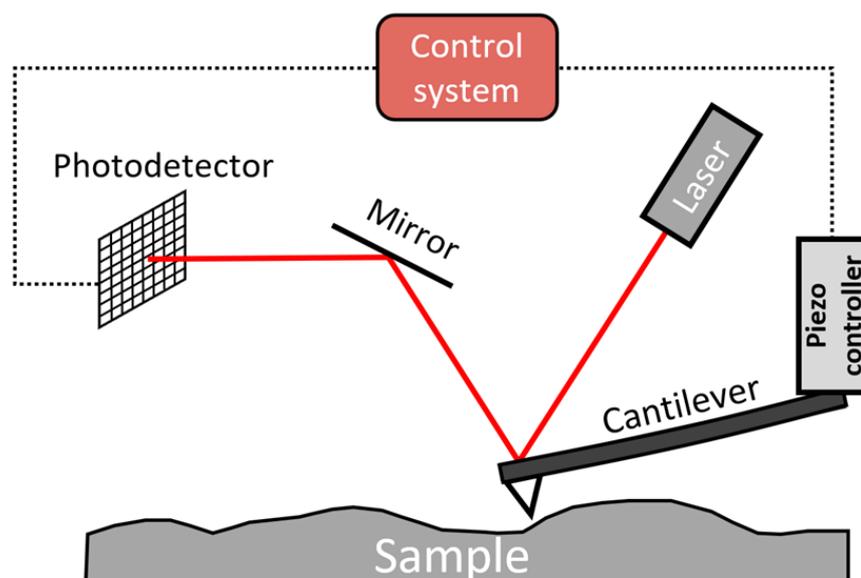
Figure 4.3. Schematic of the components of a typical atomic force microscopy system.

In an AFM scan, the tip of the cantilever is brought into close proximity of the specimen surface. When this distance is small enough, attractive forces between the tip and the specimen will lead to a deflection of the cantilever following Hooke's law that is generally represented by Eq. 4.2,

$$F_S = -k \cdot x$$ [Eq. 4.2]

where F_S is the force applied on the cantilever, k is a spring constant characteristic of the material of the cantilever and x is the total displacement from the relaxed or stable position. The force applied on the cantilever can have many sources such as direct mechanical force contact, van der Waals forces, chemical bonds, magnetic forces or electrostatic forces. Depending on these forces, an AFM can operate in different imaging modes and yield different information about the specimen, from its conductivity to chemical bond strength of the surface of the sample.

In this work, the first one was utilised, known as contact mode. The AFM operation under this mode consists of rastering the cantilever over the specimen. Tip interactions with features on the specimen surface will induce a force on the cantilever, deflecting it, which is registered by a laser-based detector and translated into a spatial map. More commonly though, the cantilever is locked in a specific position thanks to the piezoelectric controller in such a way that any deflection produced in the cantilever by the specimen during rastering is counteracted by a corresponding applied potential on the piezoelectric controller. Accordingly, the

potentials applied during the contact mode scanning are used to build the spatial map of the specimen. Other imaging modes such as tapping or non-contact mode exist and are discussed in more detail in the topical review of Jalili[211]. Schematics of the working principle of contact and tapping mode AFM are provided in Figure 4.4.

In tapping mode, the cantilever is forced to oscillate at its resonant frequency, which means that, in principle, the amplitude of the oscillations would be constant. However, when the tip of the cantilever is situated in proximity with the specimen analysed, it is likely that there will be an attraction force, be it Van der Waals or electrostatic forces, for example, that will induce a change in the amplitude of the oscillations of the cantilever. As this amplitude is to be kept constant, the piezoelectric components of the AMF will consequently react, varying the height of the cantilever to ensure a constant amplitude of the oscillation.

If the AFM scan is done in air, a liquid meniscus will form between the cantilever and the specimen as a result of the humidity of the air. It is because of this liquid meniscus that the tapping mode is necessary in air, as opposed to contact mode. The reason behind this is that, if the AFM is operated in contact mode in air, the liquid meniscus layer will considerably hinder the free movement of the cantilever and, thus, it will be remarkably more difficult to obtain a precise mapping
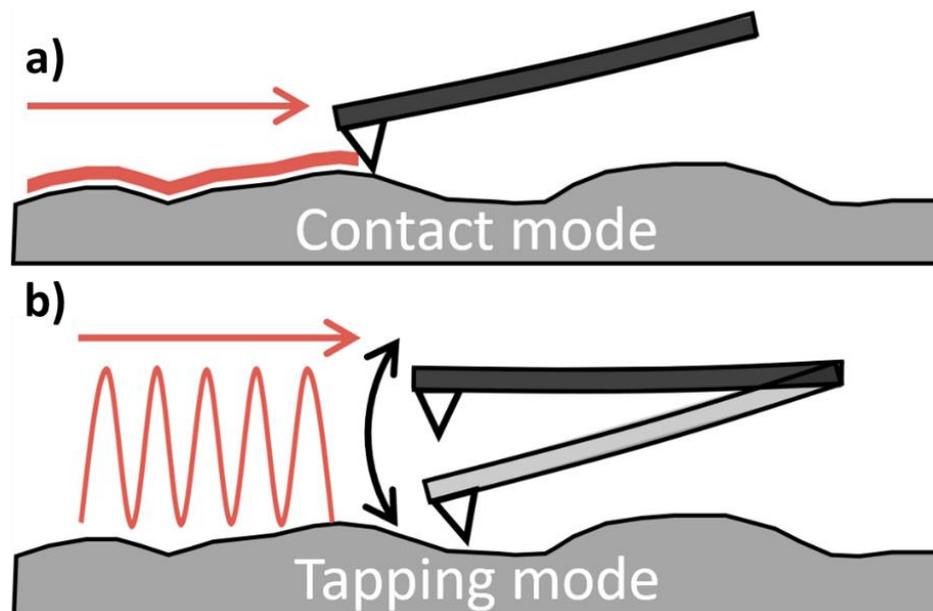
Figure 4.4. Schematic of the working principle of **a)** contact mode and **b)** tapping mode of an atomic force microscope.

of the surface. Under inert atmosphere however, the viability of this contact mode is feasible.

The most critical part of an AFM is the cantilever and its tip, which form the probe of the microscope. The tip of the cantilever is sharpened until it reaches almost atomic sharpness, meaning that the tip is formed by a single atom, as this sharpness will determine the resolution of the imaging. Tips may need to be re-sharpened or changed after several uses to ensure consistent high-quality imaging. The cantilever has to be properly maintained and calibrated to ensure that the spring constant does not drastically change, so consistent measurements can be achieved. Different tips and cantilevers are required for the different applications described before and more information on this topic can be found in the work of Haugstad[212].

The AFM system used in this work was a Veeco Nanoman II AFM system in tapping mode, in the Department of Engineering of Durham University. The microscope is placed on a platform to increase the signal-to-noise ratio by reducing external vibration. Moreover, the whole system can be fully covered to remove any external noise or vibration source. The stage is controlled by two sets of piezomotors that ensure precise movement and includes a vacuum chuck to lock the specimen in place. The microscope is placed on a z-axis stage used to approach the microscope to the specimen stage. The microscope itself contains the cantilever and tip at its bottom end, with motion controlled by a piezoelectric component. Inside the microscope, there is an optical camera to view the surface of the specimen that is being scanned and the laser detector. This laser can be repositioned using the two indicated knobs in Figure 4.5 so that it can be precisely placed on the cantilever to accurately determine the deflections to be matched by the piezoelectric controller during contact mode measurements. The microscope is then connected to an electronic control box and the computer and is controlled by dedicated software. Figure 4.5 shows a labelled photograph of the AFM system used in this work.

In a typical contact mode AFM experiment, the specimen is placed on top of the vacuum chuck of the stage to lock it in position. Then, the stage is moved in position, placing the cantilever and tip precisely on the region to be measured. To better determine the region to be measured, the optical camera on the microscope is used to observe any possible debris or dirt on the specimen that could yield an

107
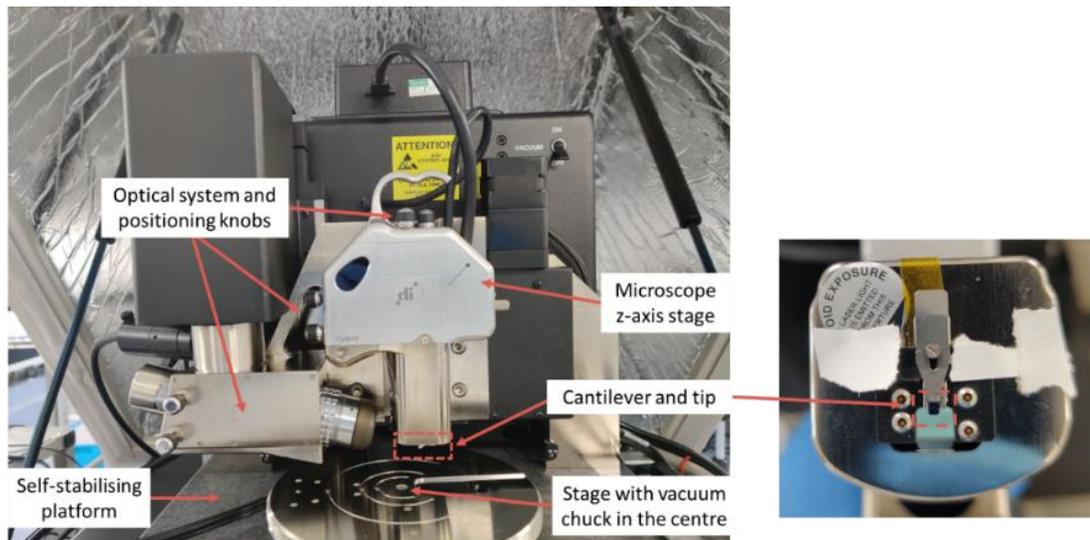
Figure 4.5. Labelled schematic of the Veeco atomic force microscopy system used in this work.

inaccurate signal during the rastering. After ensuring that the cantilever is properly calibrated, the microscope is moved through its z-axis stage close to the specimen. Then, the engage procedure is started in the software of the AFM. The engage procedure slowly approaches the tip and cantilever to the surface of the specimen until contact is achieved. This only works if the initial distance between tip and specimen is below 200 µm; otherwise, the process will stop after going down the 200 µm and the tip will have to be disengaged through the software. It is critical to follow the engage procedure safely or the tip and cantilever could be crashed against the specimen and irreparably broken. Once the engage process is successful, the experiment will start. Several process parameters can be tuned to achieve the desired spatial maps:

- The size of the region to be scanned. In this work, typical scan sizes ranged from 500x500 nm to 10x10 µm. Different scan sizes are used to resolve different properties of the specimens, with the smaller scans (500 nm x 500 nm) being used to determine the average size of the ZnO crystallites (few tens of nanometres) and the larger ones (10 µm x 10 µm) allowing the study of long-range homogeneity of the specimen texture and surface morphology.

- The proportional gain and integral part of the piezoelectric controller can be tuned to adjust the response of the cantilever to the surface features of the specimen. Depending on the values for these parameters, the resolution of

the image and the rastering speed will both change so they have to be finely tuned to ensure adequate imaging.

- The base bias applied to the cantilever (0.4 V in this work), which controls the scanning speed of the microscope. When a smaller bias is applied, scanning will be at a lower speed, providing higher resolution at the cost of an increased processing time.

4.7.2 Scanning electron microscopy

Scanning electron microscopy (SEM) is a type of electron microscopy based on scanning the surface of the specimen with a focused electron beam to generate images. The electron beam interacts with the atoms in the specimen in different ways, resulting in various types of signals such as secondary electrons (SE), used for imaging, back-scattered electrons (BSE), used for imaging with atomic number contrast, or the generation of characteristic x-rays, used for elemental identification and chemical mapping.

To generate the electron beam, an SEM can have different types of sources such as a tungsten filament, a thermionic LaB_6 emission gun or a field emission gun (FEG). These electron sources are characterized by a set of parameters that sets the resolution and quality of the imaging and analysis that can be done with the microscope[213], among which the source size and brightness are the most important:

- The source brightness is a measure of the beam current per unit area and solid angle. Thus, the higher the brightness is, the higher the electron count per unit area, which translates in a higher signal and, hence, better signal to noise, providing higher quality imaging.

- The source size represents the size of the electron beam as it leaves the source. As such, the smaller this size is, the better the resolution. If the probe is on the nanometre scale, then the imaging done will be on that scale, meaning that the source size is desired to be as small as possible to be able to resolve nanometric features on the specimen. In this regard and by the nature of the physics involved in the electron beam generation, FEG sources provide the smallest source size, along with the highest brightness, meaning that the achievable resolution with these types of sources is the best possible.

Once the beam is generated, it is attenuated and filtered to create a monochromatic beam which propagates through a set of magnetic condenser and objective lenses that will focus the beam to a spot of a specific size, mostly determined by the source, that acts as the probe of the microscope. As with any microscope, the specimen has to be adjusted to the adequate focal length and the lenses have to be calibrated and corrected to ensure minimum astigmatism effects and that the objects in the specimen plane are in the focal plane as well. Following these principles, an SEM image can be obtained. A schematic of a simple SEM is column is depicted in Figure 4.6.

SE are the main basis for any SEM and these are the ones utilised to generate the images. They are called secondary because they are generated from a material that is excited by the primary high energy source electrons. Due to their very low energies, typically below 50 eV, their mean free path in solid matter is limited, meaning than in an SEM, the SE will only be generated from the first few nanometres of the specimen. Nonetheless, the release of these SE is highly localized upon excitation, meaning that by precisely collecting the SE generated after excitation with the electron beam, a spatial map can be reconstructed with resolution up to 1 nm.
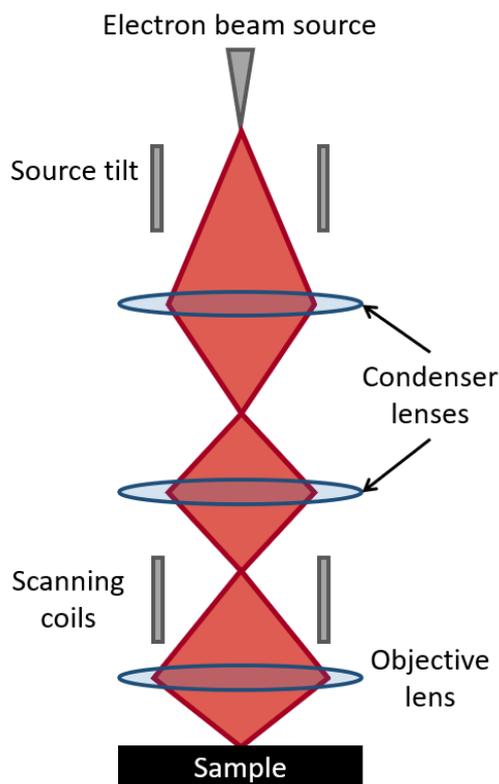
Figure 4.6. Schematic representation of a scanning electron microscope column, including the electron beam source and the different lenses.

Depending on the generated number of these SE in the specimen, a grey-scale mapping of the SE intensity is built, generating an image of the specimen surface. One crucial characteristic to consider is the electrical conductivity of the specimen. When the electron beam is scanning the specimen, primary electrons will be trapped in the specimen. Depending on its electrical conductivity, the specimen may become charged by the build-up of these electrons in the region that the beam is scanning. This charging effect can lead to permanent damage in the specimen and difficulty during imaging, impeding the formation of an adequately resolved image. In the case of ZnO NWs, the charge effect is mostly present for the smaller NWs (<200 nm in diameter and <25 nm in diameter) as their dimensions are not large enough to avoid electron build-up. To prevent this from happening, the specimens that required so were coated with carbon to provide a conductive layer that was transparent to the electron beam and would enable charge dissipation, allowing a better overall imaging.

The NW diameter and NW density, with the latter being understood as the number of NWs per unit area, were obtained from SEM imaging. For this, the free

software ImageJ was used for the required image processing. For each sample, 3-5 SEM images were taken at the same magnification. These images were then partitioned into sixteen equal sections and the diameter of the NWs in each section was measured. This diameter was measured as the distance between two opposite vertices on the hexagon on the tip of the NWs. The average diameter and size distribution of the NWs were thus obtained from these images, with at least 300 NWs measured per sample. To determine the NW density, the total number of NWs measured was divided by the size of the images and subsequently normalized to give the number of NWs per square micron ($\#/\mu^2$ or μ^{-2}). A conversion between pixels and nanometres was calculated to measure the size of the image. The SEM image scale was measured and the number of pixels obtained correlated to provide a pixel/nm relationship, subsequently exploited to calculate the size of the image in nm^2.

The SEM used in this work was a FEI Helios Nanolab 600 equipped with a FEG electron source, in the Department of Physics of Durham University. Typical operation for the specimens discussed in this work involve a working distance of 4 mm from the final lens aperture, with applied electron acceleration voltages ranging from 3 kV to 15 kV and electron beam currents between 21 pA to 0.34 nA, depending on the type of specimen and its substrate. The specimens were mounted on aluminium stubs using either conductive carbon adhesive disks or silver paint. The former is the simplest alternative, although the latter yields better results as it increases the stability of the specimen and the electron conduction from the sample, both critical when imaging at high magnification (>x150000). For routine and non-demanding imaging, carbon disks were used; otherwise, the specimens were mounted using silver paint. Figure 4.7 shows a photograph on four samples mounted on an SEM stub using silver paint.

4.7.3 Transmission electron microscopy

Transmission electron microscopy (TEM) is a type of electron microscopy in which an electron beam is transmitted through a specimen to form an image. As the imaging principle is based on the transmission of an electron beam, only thin specimens of up to 300 nm can be imaged. The electron source for a TEM is a FEG typically. The monochromatic electron beam is focused in a small, coherent beam by the
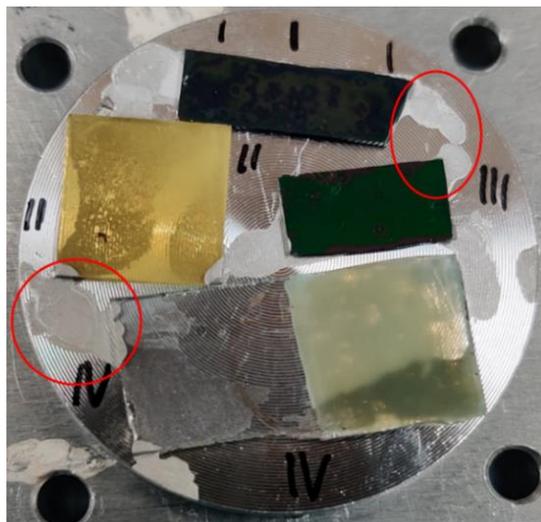
Figure 4.7. Photographs of different nanowire samples mounted on an SEM aluminium using silver paint, indicated by red lines.

condenser magnetic lenses before it probes the specimen. As the beam hits the specimen, parts of it will be transmitted depending on the thickness and electron transparency of the specimen, which are then focused by the objective lens onto either a phosphorus screen (used for standard operation) or an imaging system below, typically a charge-coupled device (CCD) camera, used to capture the images. In contrast to SEM, in TEM the whole specimen is imaged at the same time, instead of the different regions being scanned over time. The images generated are greyscale of intensities that depend upon the number of electrons transmitted through the specimen at each location. As such, darker regions have a lower electron transparency, which is correlated with higher density.

Thanks to the condenser lenses and other apertures that can be introduced in the column to block high-angle electrons, the electron beam probe is so small that the resolution achievable in a TEM is on the atomic scale. This enables the imaging of the atomic structure of nanomaterials by using high-resolution TEM (HRTEM). HRTEM uses both the transmitted and the scattered electrons to create an interference image which provides the phase contrast required to achieve atomic resolution. This technique is used throughout this work to understand the crystalline structure of the as-grown ZnO NWs and the different functionalizations used. A complementary technique to the structural characterization of HRTEM is selected-area electron diffraction (SAED). This is based on the diffraction of electrons from the electron beam incident upon the ordered atoms of the specimen. These atoms act

as a diffraction grating, meaning that each of the spots obtained from SAED forms a pattern that provides valuable insight on the crystalline structure of the specimen. One of the main applications of SAED is determining the space group of the crystalline specimen along with any possible defects. HRTEM and SAED are only possible when the specimen has been placed in a zone axis, which, in a crystalline material, is a high-symmetry orientation that typically refers to one of the directions of the crystalline lattice.

Another type of TEM analysis utilised in this work is based on scanning TEM (STEM). This TEM mode is based on focusing the beam to a fine spot below nanometric scale and then using a set of scanning coils to raster the beam across the specimen akin to the work principle of an SEM. The STEM images are formed by the electrons transmitted through the sample, but focused by the objective lens and recorded in the CCD camera. STEM is used as a simultaneous analytic and imaging tool thanks to the variety of detectors that are used during the scanning of the electron beam. Figure 4.8 includes an image for the different TEM imaging modes here described.

- A high-angle annular dark field detector is an annular detector placed outside of the path of the transmitted electron beam used for forward-scattered electrons. These scattered electrons contain information related to the
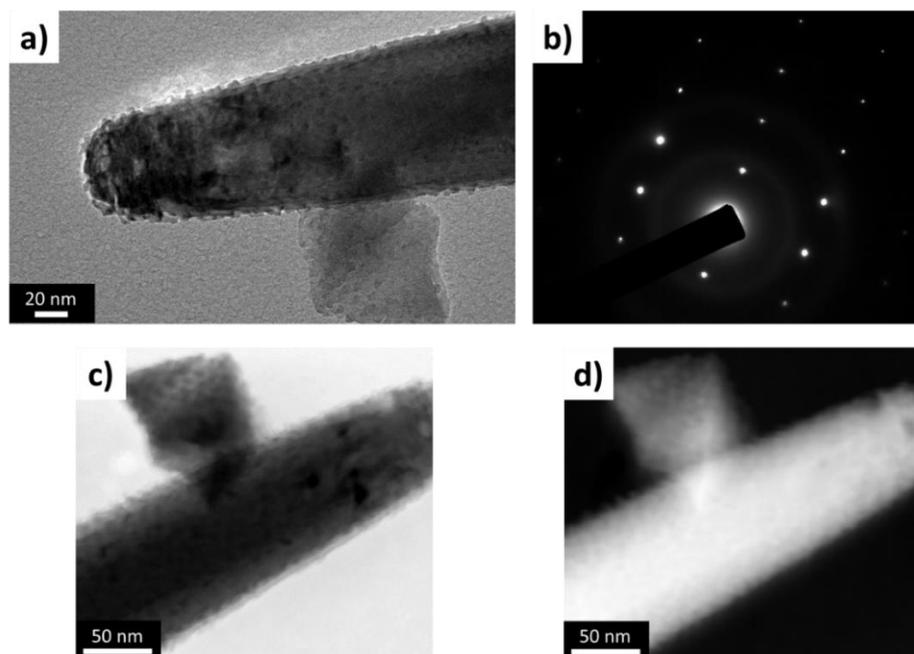
Figure 4.8. a) Typical TEM image of decorated ZnO NWs, **b)** selected area electron diffraction pattern from the same NWs, **c)** bright field and **d)** dark field image obtained for the same ZnO NW.

atomic number (Z) of the specimen as the energy related to the scattering process is different for each element, which means that dark field imaging in STEM mode provides Z-contrast images.

- A bright field detector situated directly in the path of the transmitted electron beam. Bright field imaging is complementary to dark field imaging and, typically, both images are produced at the same time.

- An electron or x-ray detector used for elemental chemical mapping. Depending on the signal used as probe (electrons or x-rays), two different elemental mapping techniques can be used (electron energy loss spectroscopy, EELS, or energy-dispersive x-ray spectroscopy, EDX). In this work, only EDX was used and details on this technique will be discussed later in this chapter. Both techniques provide elemental chemical mapping at high magnifications and resolution, which is particularly useful for core-shell and functionalized structures.

The TEM used in this work is a JEOL 2100 F FEG, with an electron acceleration voltage of 200 kV, in the Department of Physics of Durham University. This system includes a CCD camera as the imaging component and dark field, bright field, EDX and EELS detectors. The strict specimen size requirement imposed by TEM meant that the as-grown NWs could not be used directly. Instead, they were transferred to a 300 Mesh Cu holey carbon grid, from Agar Scientific. For this, a droplet of IPA was cast on the as-grown NWs, which were then carefully scraped off the substrate using a scalpel blade. Subsequently, the carbon grid was dipped in the IPA containing NWs to wet transfer them onto the grid. After drying in air conditions for 10 minutes, the sample was mounted on the TEM holder. For adequate imaging of the ZnO NWs, a double-tilt holder was utilised in order to position the NWs in such a way that their zone axis was parallel to the incoming electron beam. A zone axis is, in short, a set of lattice planes that are parallel to the same crystallographic direction. Tilting the stage is required to ensure that the NW being imaged is in the zone axis.

4.8 X-ray techniques

Two techniques based on x-rays were utilised to better understand the morphological properties of the seed layers and the NWs, complementing the studies carried out with the techniques described in the previous section. The two techniques are x-ray diffraction (XRD) and x-ray reflectivity (XRR). The former was used both on the seed layers and NWs to investigate the crystal structure of the material while the latter was only used on the seed layers to correlate their morphological and structural properties to those obtained by AFM.

4.8.1 X-ray diffraction

X-ray diffraction is based on an impinging x-ray radiation on a specimen[214]. The x-rays collide with the electrons in the specimen, causing constructive and destructive wave interference as a result of the atomic arrangement of the specimen. The emission of this scattered (or diffracted) waves is as x-ray diffraction[215]. The theoretical basis for XRD stems from Bragg's law of diffraction. Assuming that the incident X-ray radiation is a plane wave of wavelength λ, it will be scattered by the lattice planes of the specimen arranged at a set interplanar distance $d_{h,k,l}$. As explained before, this wave scattering can be destructive or constructive. The scattering will only be constructive if the scattered waves are in phase since the difference in their path lengths is proportional to a positive integer n. Under these conditions, the scattered radiation will undergo constructive interference at a Bragg angle ϑ. This interference effect is mathematically described by Bragg's law and represented in Figure 4.9,

$$2d_{h,k,l}sin\theta = n\lambda \qquad \text{[Eq. 4.3]}$$

where $d_{h,k,l}$ is the interplanar spacing of the lattice, expressed as,

$$d_{h,k,l} = \frac{a_0}{\sqrt{h^2 + k^2 + l^2}} \qquad \text{[Eq. 4.4]}$$

with a_0 being the lattice parameter for the crystalline direction *(h k l)*. An x-ray diffractometer measures the intensity of the constructive interferences of scattered waves described by Bragg's law as a function of the scattering angle. This way, strong intensities will generate Bragg peaks at the points where the scattering angle satisfies Bragg's conditions, which in crystalline materials corresponds to the diffractions peaks of the different crystal planes of the lattice. XRD thus offers the possibility of
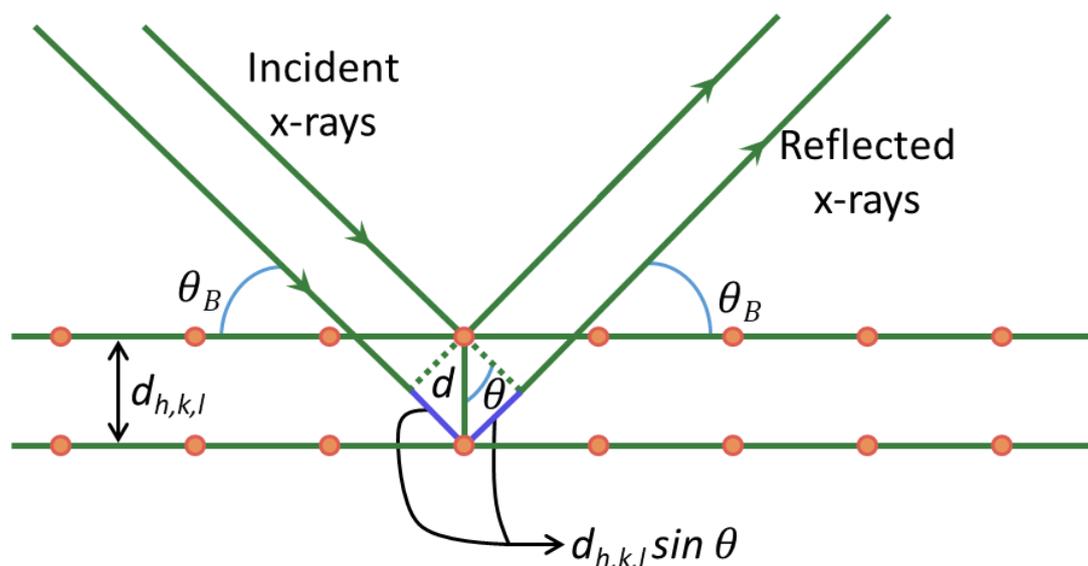
Figure 4.9. Schematic of Bragg's law represented accordingly with the mathematical representation of Equation 4.4.

obtaining the crystalline structure of a crystal and its lattice parameters by analysing the respective peaks in the XRD spectrum following Eq. 4.4.

XRD also allows the estimation of the nanometric crystallite size of any crystalline material by relating this size to the broadening of a peak in a diffraction pattern. This relation is established by Scherrer equation (Eq. 4.5),

$$\tau = \frac{K \cdot \lambda}{\beta \cdot \cos\theta} \qquad\qquad \text{[Eq. 4.5]}$$

where τ is the mean size of the crystallite (surface features of the seed layer in this work), K is a dimensionless shape factor, typically valued around 0.9, λ is the wavelength of the impinging x-ray radiation, β is the line broadening at half the maximum intensity (also known as the full width at half maximum) and ϑ is the Bragg angle. This relation is limited to nano-scale crystallites.

In this work, XRD was utilised on both the seed layers and the as-grown NWs. As detailed in Chapter 3, the ideal ZnO NW growth took place when the dominant crystalline orientation of the seed layer was (0 0 2). Thus, XRD was used to study the crystalline orientation of different seed layers and how that influenced the NWs growth, as detailed in Chapter 5.2 and 5.5. The crystalline orientation of the NWs was determined by XRD as well, in order to correlate these results with those obtained from SAED analyses. Crystallite sizes for ALD-deposited seed layers were estimated by Scherrer's equation (Eq. 4.5). However, the functionalization of the NWs with MOF

or Ir could not be studied with this technique as the size of the functionalizing nanomaterials was insufficient for a measurable signal to noise ratio within a reasonable experimental time.

The XRD experiments were carried out in a Bruker D8 Venture, equipped with High intensity Mo/Cu Dual IµS2 sources, in the Department of Chemistry of Durham University. To ensure the best sample alignment and signal acquisition, 2 cm x 2 cm samples were prepared for easier manipulation. The samples were laid flat on the x-ray sample holder and the automated measuring process was started. Since the significant peaks for ZnO are situated below 50° with Cu x-rays, a typical XRD analysis was carried out between 10° and 50° at a rate of 0.05° per second.

4.8.2 X-ray reflectivity

X-ray reflectivity (XRR) is a technique based on the reflection of an x-ray beam incident at grazing angle θ onto the specimen. Initially, the x-rays are incident on a flat specimen at an angle smaller than the critical angle θ_c such that the incident radiation undergoes total external reflection. For higher angles, part of the incident radiation will either propagate ($\theta = \theta_c$) or be refracted ($\theta > \theta_c$) inside the specimen. This critical angle depends on the electron density of the specimen. The reflected x-rays are collected by a detector in which information regarding their intensity and the incident angle is processed. In an ideal case of a perfectly smooth and flat surface, the reflected x-rays will be a specular image of the impinging x-rays (total reflection), meaning that both beams will have exactly the same incidence angle[216]. However, in reality, the surface of the specimen will not be smooth and flat and the reflected x-rays will have angles and intensity that deviates from the original impinging beam following Fresnel's law of reflectivity. For more information on the physical principles of reflectivity please refer to the detailed study of Mack[217]. A schematic of the working mechanism of XRR is presented in Figure 4.10. By studying the deviations in intensity of the reflected x-ray beam, XRR gives information about the surface and structural characteristics of the specimen, enabling the study of properties such as density, surface roughness and thickness. Moreover, if the specimen is formed of layers of different materials, XRR can provide valuable information on the thickness of the different layers, their interfaces, interface roughness and the density of the
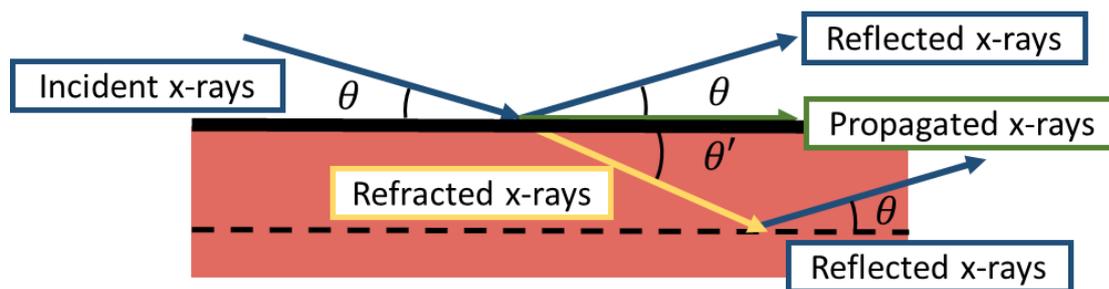
Figure 4.10. Schematic of the working mechanism of x-ray reflectivity, including the influence of the angle of the incident radiation in the outcome when compared with the critical angle.

different layers. This information is provided by the interference of the x-rays reflected from the top and lower interfaces, which are dependent on the angle. This interference gives rise to Kiessig fringes and it is the study of the spacing and periodicity of these fringes that provides the vital information about the different layers of a multi-layer system.

After XRR measurements, the data is fitted to a simulated model of the specimen's material. This is an iterative modelling process in which a set of control parameters (roughness, thickness, electron density, interfacial roughness) are implemented in order to obtain a converging model, within a constraining error. For single layer films, this modelling is typically straightforward as, at most, the specimen will contain the target material and its oxidized form. However, when it comes to multi-layered materials, the modelling becomes complicated due to the different possible interfaces that can form. To ease the iterative curve fitting, certain known values such as the layer thicknesses or their densities can be fixed to reduce the computational load. One of the most popular software packages used for the fitting of XRR measurements is an open-source program implemented in Python called GenX. This software was used here for the fitting of the XRR results obtained in this work.

In this work, XRR was utilised to analyse the structural properties of the ZnO seed layers deposited by ALD on silicon substrates. The system used was a Bede D1 high-resolution x-ray diffractometer using a monochromated Cu Kα1 radiation (1.5406 Å), in the Department of Physics of Durham University. Owing to the previously described high tunability degree of ALD, it is possible to control the density and roughness of the seed layers, which in turn can affect the NW growth, as further

detailed in Chapter 5. For this, 1 cm x 1 cm samples were placed on the disk-like stage of the XRR system using Kapton double-sided tape from RS Components. The samples were mounted completely flat to ensure a successful reflectivity measurement. After mounting the samples, an in-house script developed in Python was used to automate the alignment and measuring procedures of the XRR system. To fit the results, a single ZnO layer was considered, with its thickness, density and roughness being determined in the fitting process. The last two were the main target of the XRR studies as the influence of these parameters over the NW growth can be significant.

4.9 Spectroscopic chemical composition studies

The chemical composition of the NWs and functionalized materials was studied through two different spectroscopic techniques, namely x-ray photoelectron spectroscopy (XPS) and EDX. XPS was used on the seed layers and the NWs to understand their chemical composition and, in particular, the Zn:O ratio, which was of particular importance for the ALD deposited seed layers. EDX was mainly used for the functionalised ZnO NWs. In the TEM, EDX was used to map the ZIF-8 shell and the iridium content on both functionalized samples as well as the spatial distribution of the key elements of each of these functionalizations.

4.9.1 X-ray photoelectron spectroscopy

X-ray photoelectron spectroscopy is an analytic technique based on the photoelectric effect. In short, when a specimen is illuminated with electromagnetic radiation (x-rays in this case) it will absorb the energy from the excitation. If this energy is higher than that of the binding energy of an electron in the specimen atoms, then said electron will be ejected from the material[218]. The interaction between the x-rays and the electrons in the atoms is binary in the sense that either the energy of the incoming excitation is higher or lower than the binding energy of the electron. If it is higher, the electron will be emitted as a result; if it is lower, the energy will be re-emitted. For emitted photoelectrons, the remaining energy from the illumination will contribute to the kinetic energy of the electron. A more formal description of the photoelectric effect can be found in Einstein's work[219]. A schematic of a typical XPS experimental setup being depicted in Figure 4.11. XPS takes advantage of the photoelectric effect by using a monochromatic x-ray beam as illumination and
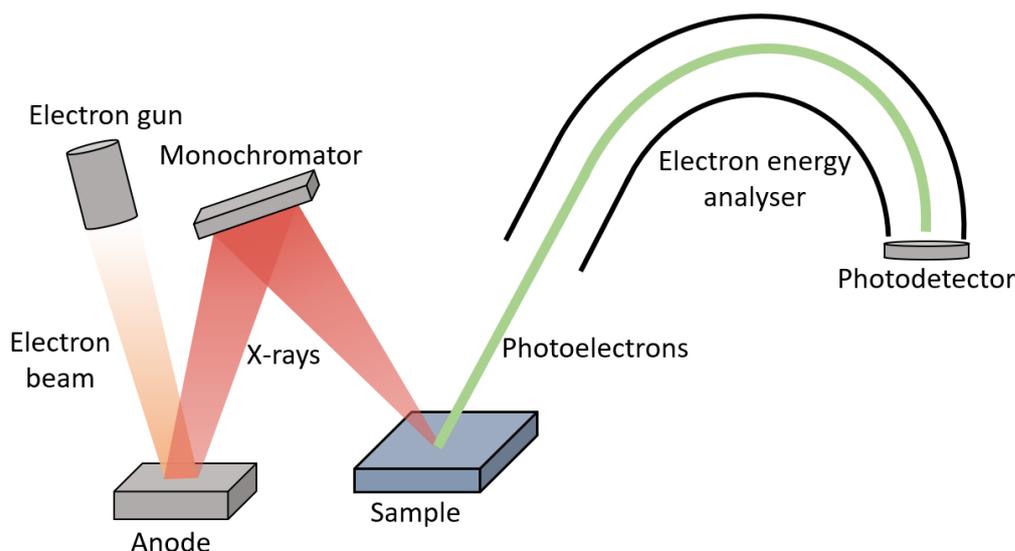
Figure 4.11. Schematic of an x-ray photoelectron spectrometer experiment in which an electron beam generates the x-rays that will probe the specimen, emitting the characteristic photoelectrons.

detectors for the kinetic energy of the electrons and for the total number of electrons per unit area[220]. As the binding energy of the electrons is characteristic of each element, the kinetic energy that is measured will correspond to specific elements. Thus, an XPS measurement consists in a correlation of the total number of electrons measured at an energy value. Moreover, the binding energies are characteristic of the different atomic orbitals, meaning that, in the analysed energy spectra, the contribution of different orbitals can be obtained. This means that XPS is a fingerprint technique that is utilised to accurately determine the chemical environment of a specimen. The main drawbacks of XPS are that the electrons are ejected by photoelectric effect only in the first 10 nm of the specimen.

In this work, XPS was used to study the chemical environment of ZIF-8 functionalized, Co-doped ZnO NWs (Chapter 7.3.3). For this, 1 cm x 1 cm samples were prepared and mounted on the sample holder. The XPS system used was an Omicron DAR 400 x-ray source using an Mg anode and an Omicron EA 125 hemispherical analyser, in the Université Clermont Auvergne, in France. For the NWs, the Zn 2p, O 1s, N 1s and Co 2p peaks were the focus of the analyses. A typical comparative spectrum is provided in Figure 4.12. Once the survey spectrum and the respective peak spectra were obtained, the curves were de-convoluted into their respective components using the CasaXPS software. More information on the
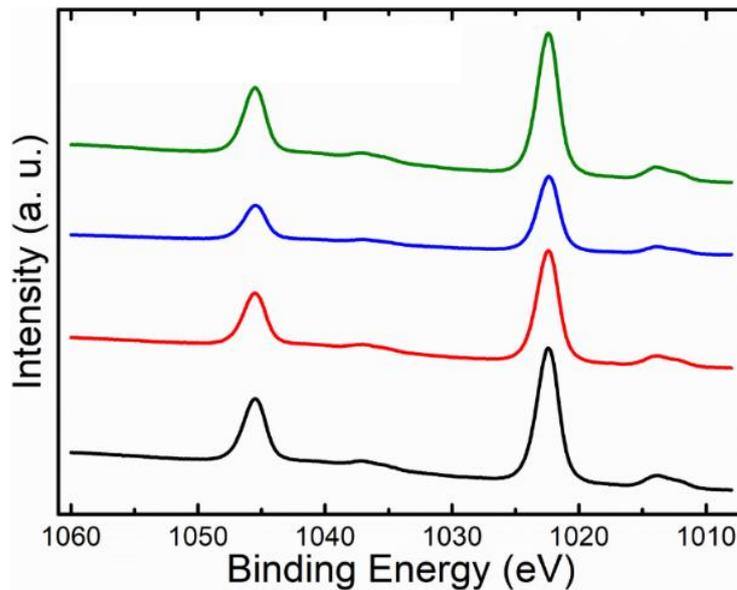
Figure 4.12. Example of comparative x-ray photoelectron spectrometer spectra of Zn 2p for different ZnO seed layers.

different deconvolutions and their contributions are provided in the corresponding chapters.

4.9.2 Energy-dispersive x-ray spectroscopy

Energy-dispersive x-ray spectroscopy (EDX) is an analytical technique used to determine the chemical composition and elemental characterization of a specimen. EDX is based on collecting the x-rays generated from the specimen after an electron beam strikes the surface[221]. The physical principle of this x-ray generation is based on the interaction between electrons from the beam and those in the specimen. In short, SE generated by the primary electron beam will create holes as they are ejected from the electron shell of the atoms. These holes can be subsequently filled by higher energy electrons from higher energy levels. In order to achieve energetical equilibrium, as these electrons occupy the vacant holes, the excess energy is released in the form of x-rays. The energy of these x-rays is characteristic of the orbital transitions and hence specific to every transition as it is based on a quantitative difference related to the atomic structure of the emitting element. As such, an EDX spectrum will consist of the number and energy of these x-rays that will yield a plot in which the total counts and the specific positions for each analysed element will be shown. Another possibility is obtaining a map of these intensities, overlapped with electron microscope image as shown in Figure 4.13. In this way, it is possible to obtain
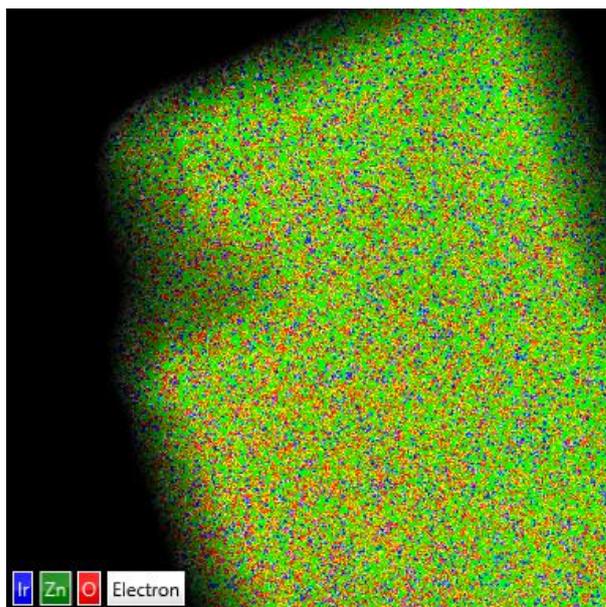
Figure 4.13. Energy-dispersive x-ray spectroscopy map of the tip of an iridium decorated ZnO NW, showing the distribution of the three elements analysed.

an approximation of the concentration of an element and its spatial distribution in the studied region.

EDX was used in this work for two main purposes, as detailed earlier: to study the ZIF-8 shells and to analyse the ZIF-8 and iridium surface functionalized ZnO NWs. These EDX analyses were carried out in the previously described TEM using an Oxford INCAx-sight Si (Li) detector with 50 mm^2 area detector at a 25° take off angle. To obtain the elemental mapping, it was necessary to operate the microscope in STEM mode as the EDX analysis is carried out by scanning the electron beam on the studied region of the sample and analysing the emitted x-rays as described previously. Hence, the EDX elemental map is typically superimposed on the electron image obtained from the bright field detector in STEM mode. Therefore, for these experiments, the samples were prepared as detailed previously. Taking advantage of the STEM/EDX coupling capabilities, chemical mapping of these samples was carried out to understand the elemental distribution of the functionalizing materials along and across the NWs.

4.10 Optical spectroscopic studies

The optical properties of undoped, doped and functionalized NWs were investigated using four different spectroscopic methods: UV-visible spectroscopy (UV-vis), fast-transient absorption spectroscopy (FTAS), photoluminescence spectroscopy (PL),

and cathodoluminescence spectroscopy. The focus of these analyses was to study the influence that cobalt and copper doping and the MOF functionalization have on the overall light absorption, bandgap, electronic band structure and defect density of the NWs. These properties of the NWs are key to the functional behaviour, as will be discussed in Chapter 8, for light-based applications like photoelectrochemical water splitting. The range of wavelengths between the near ultraviolet (UV) and the visible region of the electromagnetic spectrum (from 300 nm to 750 nm) are considered significant in this work and, thus, any discussion about the working principle of any of these techniques is focused on that energy range.

4.10.1 Ultraviolet-visible spectroscopy

Ultraviolet-visible spectroscopy (UV-vis) is an analytic technique based on the capability of a material to absorb or transmit light. For a semiconductor material in its stable, non-excited, ideal state, the valence band will be full of carriers while the conduction band will be empty, as discussed in Chapter 2.2.5. However, different forms of excitation can promote electrons from the valence to the conduction band. In the case of UV-vis, a monochromated white light is used as the excitation source[222]. When light is radiated on a semiconducting specimen, the incoming photons can either be absorbed or transmitted by the electrons of the specimen. If a photon is absorbed by an electron, it will be excited (in a process known as photoexcitation) from the valence to the conduction band thanks to the energy from the impinging photon; otherwise, the photon will be transmitted through the material. For this absorption to take place, as detailed in Chapter 2.2.5, the energy of the incoming photon has to be higher than that of the bandgap of the semiconductor, meaning that the energy of the photon has to be high enough to overcome the gap between valence and conduction band. The working principle of UV-vis consists of measuring the amount of photons transmitted or absorbed, depending on the operation mode, through the specimen compared to a blank substrate. For this, in a UV-vis experiment, white light is passed through a monochromator to obtain photons of single energy. Then, an energy sweep is performed from lower to higher values (in this work from 1.65 eV to 4.1 eV, which corresponds to the 750 nm to 300 nm range) and the amount of photons transmitted through the sample to a

photodetector is measured. The intensity of photons measured will correlate with the amount of absorbed photons in the specimen. This provides a spectrum correlating energy level with the amount of photons absorbed at each level, yielding valuable information on how much light can a material absorb and where in the visible and near-UV spectrum it is located. Additionally, UV-vis experiments allow the measurement of the bandgap of a material by analysing the band-edge absorption. For a more detailed and formal review on absorption of light in solids, please refer to the work of Fox[223]. An example of a comparative UV-vis spectrum obtained for different ZnO NWs is shown in Figure 4.14.

UV-vis was used in this work as a control and a qualitative analytical tool to assess the light absorption properties of the undoped, doped and functionalized NWs. Undoped ZnO NWs were taken as a benchmark, with their absorption spectrum serving as a reference point to compare the effect that different dopants and functionalizations have on the optical absorption and the bandgap of the NWs. The UV-vis experiments were carried out using a Shimadzu UV-1800 spectrophotometer in absorption mode, in the energy range between 300 nm and 750 nm, in the Department of Engineering of Durham University. All the samples were prepared on ITO/glass substrates as detailed earlier. Before the measurements were carried out, the baseline for the experiments was established using a blank ITO substrate.
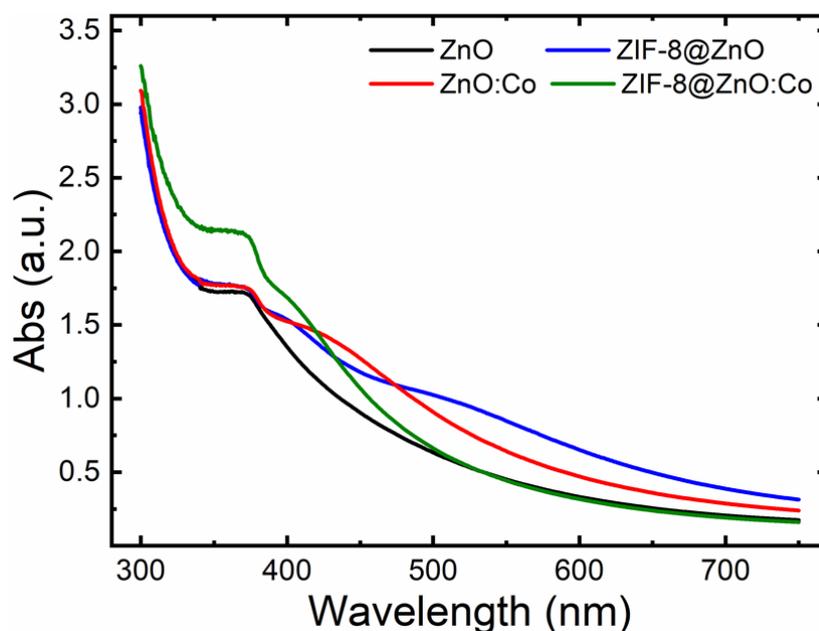
Figure 4.14. Examples of typical ultraviolet-visible spectrum obtained for different ZnO NW samples, showing the measurement range used for these experiments. As expected, the absorption of the ZnO is maximum in the ultraviolet region.

The UV-vis measurements were performed using a two-slit configuration in which a blank ITO substrate and the target sample were measured simultaneously, with the resulting absorption spectrum presented as the difference in absorbed photons between both slits.

4.10.2 Fast transient absorption spectroscopy

Fast transient absorption spectroscopy (FTAS) is an analytic optical spectroscopy used to probe the carrier dynamics of the NWs, based on the measurement of the change in the absorption/transmission of light on a sample. FTAS is based on a pump-probe mechanism to excite and analyse the electronic state of the charge carriers. In a typical FTAS experiment, a specimen in equilibrium is excited by a strong pump pulse, the energy of the pump is chosen according to the system under study. Upon pump excitation the carriers are excited from the valence band to the conduction band. This photoexcited sample is then probed by a weaker probe pulse at different time delays from the pump excitation. In this experiment we have used a white light supercontinuum generated in a CaF_2 crystal as the probe. This allows one to study the time evolution of the photoexcited carriers over a range of probe energy from UV-Vis to the near-infrared. Subsequently, a differential spectrum is calculated by comparing the results obtained in the pump-probe experiment with the ground state of the sample, i.e., the result obtained from probing the specimen while in equilibrium state, with no external excitation[224].

During the measurement, the pump and the probe are focused on the same spot on the sample. The pump is chopped off at a reference frequency with a controlled time delay after pump pulse. The pump and probe are focused on the same spot of the sample and the probe transmitted through the sample is detected by a CCD and analysed in a spectrometer. In fast transient absorption spectroscopy, the differential absorption (ΔA) of the sample is measured in transmission mode, i.e. by measuring the energy of the probe transmitted through the sample. The absorbance of the sample, A is defined in terms of its transmittance, T as

$$A = -\log(T) \qquad \text{[Eq. 4.6]}$$

Hence *ΔA* is defined as the difference in absorbance with and without the pump excitation.

$$\Delta A = A_P - A_0 \qquad \qquad \text{[Eq. 4.7]}$$

where, A_p is the absorption with pump and A_0 is absorption without pump excitation. Therefore,

$$\Delta A = \log\left(\frac{T_0}{T_P}\right) \qquad \qquad \text{[Eq. 4.8]}$$

where T_0 is the transmittance of probe pulse without pump excitation and T_P is the time-dependent transmittance with pump excitation. This *ΔA* is thus obtained as a function of the time delay between the pump and the probe as well as of probe energy. For ZnO, energy of the probe used is in the visible part of the spectral region. The *ΔA* signal corresponding to the bandgap is negative, referred to as ground state bleaching or absorption bleaching due to photoexcitation of the carriers from the valence band to the conduction band by the pump, leading to a depletion of carrier population in the valence band. Therefore, the absorption of the probe by the excited sample is less than the absorption of the probe by the non-excited sample.

It is thus possible to analyse the carrier dynamics of the specimen by measuring at different delay times between pump and probe. This provides information related to the bandgap, carrier lifetime or defect concentrations. The exhaustive works of Berera[224] and Prasankumar[225] provide a detailed overview of the technique physical basis, applications and shortcomings, which are not within the scope of this work. A typical false-colour map obtained from a FTAS measurement is provided in Figure 4.15 for ZnO, in which the signal corresponding to the bandgap can be observed, centred at around 3.3 eV. To build this false colour map, an energy sweep was carried out at different time delays. Thus, a single energy sweep corresponds to a single time delay and, the false colour map was built by plotting all the energy sweeps together at their respective time delay. The energy in the x-axis of this figure corresponds to the absorption signal obtained from the pump-probe measurements and represented the portion of the UV-visible spectrum in which the ZnO NWs absorb photons. In the measurement itself, the data collected comes from the energy of the photons transmitted through the sample. However, as detailed earlier, the information collected is presented as a differential absorption as per Eq. 4.8.

FTAS was used in this work to understand the charge dynamics of doped ZnO NWs and the ZIF-8 shells with the aim of providing a better understanding of the

processes taking place during light absorption and how these could affect the performance of NW-based optical devices. In addition, FTAS was used to correlate with the results obtained from UV-vis. As a pump for the FTAS experiments, the output of an Optical Parametric Amplifier was used; for the probe, the white light continuum generated in a femtosecond transient absorption spectrometer of IB Photonics (FemtoFrame II, IB Photonics) was used. The probe is generated by passing the small quantity of 800 nm into a rotating CaF_2 crystal which produces a supercontinuum in the spectral range of 350 - 800 nm. The pump-probe response was studied in the visible and near-UV region of the electromagnetic spectrum. The energy of the pump was 275 nm (4.5 eV) with an excitation intensity of 260 µJ cm^{-2}. The instrument response function was measured to be approximately 50 fs. The samples were prepared on ITO/glass substrates and used as-grown for the measurements. The FTAS experiments were carried out by Aswathi K. Sivan at the Istituto per la Microelettronica e i Microsistemi, Consiglio Nazionale delle Ricerche (CNR), in Rome, Italy.
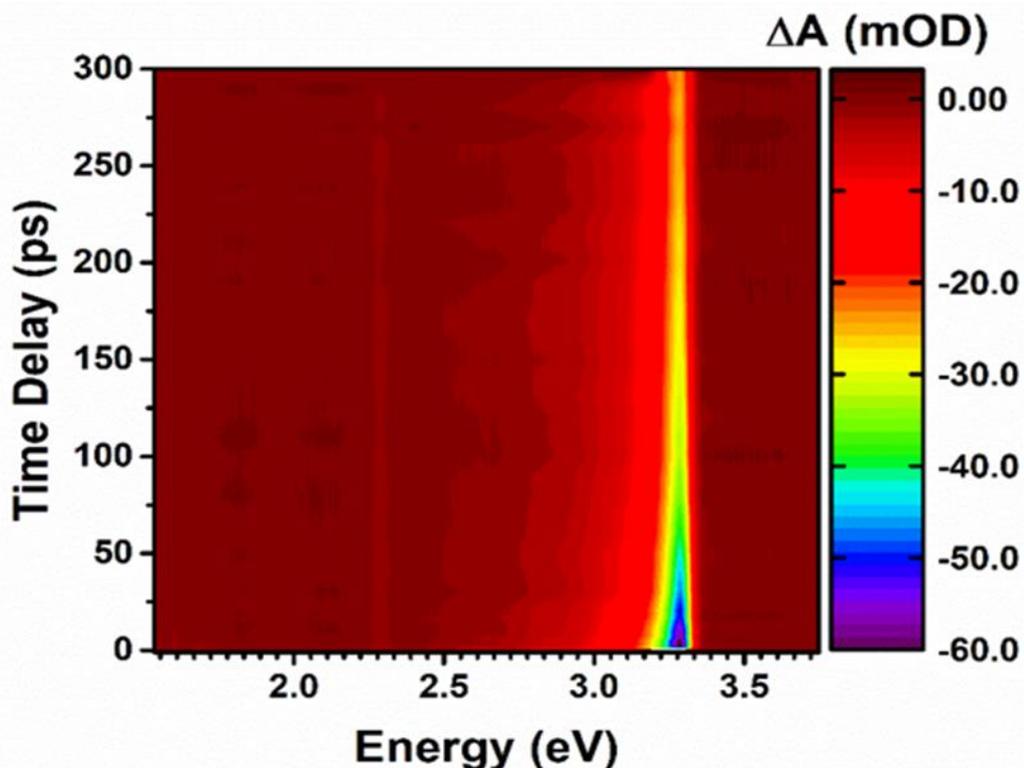
Figure 4.15. Two-dimensional colour map obtained in a fast-transient absorption spectroscopy measurement of ZnO NWs. The bandgap of ZnO is characterized with this technique, as seen in the absorption band at 3.3 eV.

4.10.3 Photoluminescence spectroscopy

Photoluminescence spectroscopy (PL) is an analytical optical characterization method used to investigate the electronic structure of materials. The working mechanism is based on a laser beam impinging on a specimen. The photons of the laser beam will excite electrons in the specimen (photoexcitation) to a higher energy level. After a certain period of time, the excited electrons will relax, returning to their equilibrium state. This relaxation will include an excess of energy, which will be released in a process known as emission. The emission may take different forms, divided into non-radiative and radiative emission, in which the latter is the emission of photons in a process known as photoluminescence. The energy of the light emitted in the PL process depends on the energy difference between the excited and equilibrium states of the electron, with the quantity of light being related to the contribution of the radiative emission to the total emission. More information on the photoluminescence of semiconductors can be found in the topical review of Gilliland[226]. Taking advantage of the radiative emission, PL is used to analyse the electronic structure by measuring the light emitted by a specimen after excitation with a laser. Similarly to UV-vis, a white light continuum coming from a laser is passed through a monochromator to obtain single energy photons. An energy sweep is thus performed and the light emitted by the specimen is collected with a photodetector, obtaining a spectrum correlating light intensity or quantity with the energy level at which it was recorded. An example of typical PL spectra is provided in Figure 4.16.

PL was used in this work to study the electronic structure of undoped and doped ZnO NWs as a correlation technique to obtain a complete picture of the overall optical characteristics of the NWs. The excitation source used was the same as the pump used for the FTAS, with an excitation energy of 4.5 eV. All the measured NW samples were prepared on glass/ITO substrates and analysed as-grown. The PL experiments were carried out in the same institution as the FTAS measurements.

4.10.4 Cathodoluminescence spectroscopy

Cathodoluminescence spectroscopy (CL) is an analytical technique utilised to measure the optoelectronic properties of materials. CL is a technique based on the excitation of electrons from the conduction to the valence band of a material and
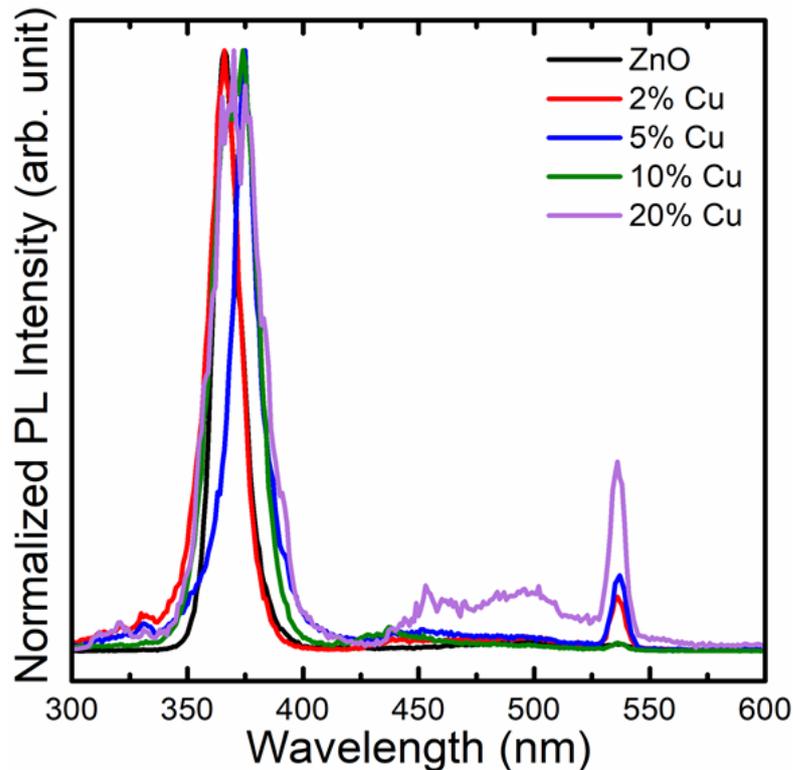
Figure 4.16. Examples of typical photoluminescence spectroscopy measurement, showing the characteristic peaks of ZnO and the changes due to copper doping.

their subsequent radiative recombination. However, the excitation source in CL is different from PL as it comes from an impinging electron beam. An electron beam interacting with a material produces the release of different signals (SE, BSE, x-rays), as described in Chapter 4.7.2. As such, a logical consequence of requiring an electron beam as the excitation source is the coupling of a CL system with an SEM. This provides a better analytical environment while, at the same time, allowing spatial resolution of the CL analysis. Due to this spatial resolution, CL can be utilised to analyse centres of illumination, study electronic properties and the electronic band structure of the material in question or study the concentration of defect-related emissions. It is also possible to obtain hyperspectral maps of the CL signal superimposed with an SEM image, which provides information on spatial and morphological distribution of electronic states. To extract the CL information, the CL-SEM system is equipped with an optical system (such as a mirror) that captures the emitted photons, which are subsequently sorted by a monochromator and analysed. Therefore, by scanning individual points with the electron beam and analysing the released photons, the CL-SEM system can produce hyperspectral maps and spatially

resolved CL. There are two key parameters that control the resolution of this technique and penetration depth of the electron beam, namely the acceleration voltage and the current of the electron beam. For more information on CL, please refer to the work of Yacobi[227]. In this work, this technique was used to prove the emission of cobalt-doped ZnO NWs and study the spatial distribution of the related defect-band (see Chapter 6). For this, an Attolight Allalin CL-SEM system was used, with the measurements carried out at 5 keV and two temperatures, room temperature and 10 K. The experiments were carried out with the help of a laser system consisting of Ti: Sapphire oscillator and a regenerative amplifier giving an output of 4 mJ, 35 fs wide laser pulses at 800 nm with a repetition rate of 1 kHz. The major portion of the 4 mJ, 800 nm output of the amplifier passes through an optical parametric amplifier (OPA) with a tuneable output. An example of a hyperspectral CL map obtained at 10 K with this technique for Co-doped ZnO NWs is shown in Figure 4.17. The CL measurements were carried out by Aswathi K. Sivan and Nicolas Tappy at the Interdisciplinary Centre for Electron Microscopy in the École Polytechnique Fédérale de Lausanne (EPFL), Switzerland.
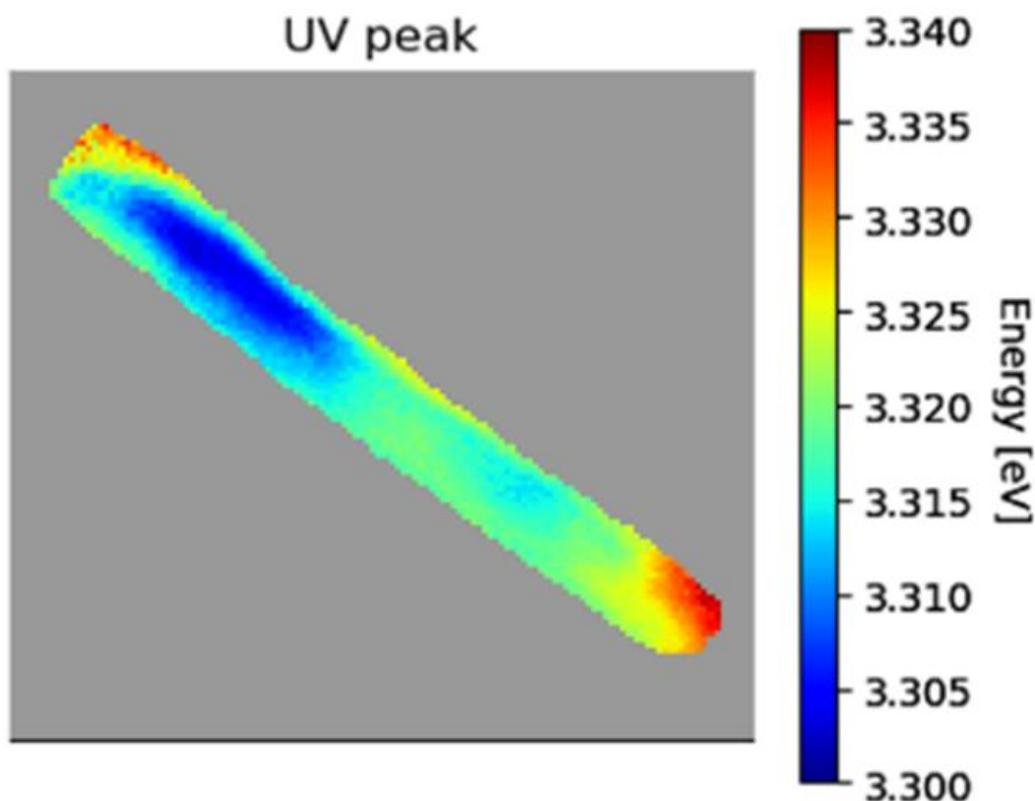
Figure 4.17. Example of a hyperspectral cathodoluminescence (CL) map obtained in a CL-scanning electron microscope coupled system, showing the spatial distribution of the emission of a cobalt-doped ZnO nanowire in the bandgap region of ZnO.

4.11 Photoelectrochemical characterization

Different doping and functionalization routes were studied in this work in an effort to obtain an enhanced optoelectronic functional performance of the ZnO NWs in photoelectrochemical (PEC) water splitting. The theoretical background for this application was provided in Chapter 2.4. Experimentally, the PEC characterization of the NW-based photoanodes is based on the use of a potentiostat, a three-electrode cell and an illumination source[22].

In this work, a three-electrode cell strategy[228] was implemented, in which a Pt electrode was used as the counter electrode (CE, photocathode), a Hg/HgO electrode was used as the reference electrode (RE) and the NW-based electrodes were used as the working electrode (WE, photoanode). These three electrodes are all submerged in the same electrolyte solution and all are connected to a potentiostat/galvanostat (PGSTAT), with the NW-based WE being directly illuminated by the light source. The light source used provided standard white light with an intensity of AM 1.5 G, as described in Chapter 2.4.2. Details on the working mechanism of the three-electrode setup were provided in Chapter 2.4, with a schematic of the PEC cell utilised in this work presented in Figure 4.18. It should be noted that the nitrogen gas flow shown in the schematic was only used in between experiments to ensure comparable experimental conditions.

All the measurements carried out in this work were referred to the reversible hydrogen electrode (RHE), as described in Chapter 2.4.3. For the cyclic voltammetry measurements, a potential sweep between -0.4 V to 1.4 V (vs the RHE) was used, with a voltage step of 10 mV per second measured over two consecutive cycles. The amperometric *I-t* curves were measured at an applied potential of 1.4 V (vs the RHE), for 300 seconds, switching between on/off states every 15 seconds. The light chopping in this analysis was done manually, which induced some shifts in the resulting curves, although these did not affect the accuracy or the reliability of the measurements. For the incident photon to current efficiency (IPCE) measurements, 1.4 V (vs the RHE) were applied and a wavelength sweep from 300 nm to 750 nm with a step of 5 nm every 10 seconds was used to study the efficiency at each wavelength. The 5 nm step was achieved by incorporating a monochromator at the
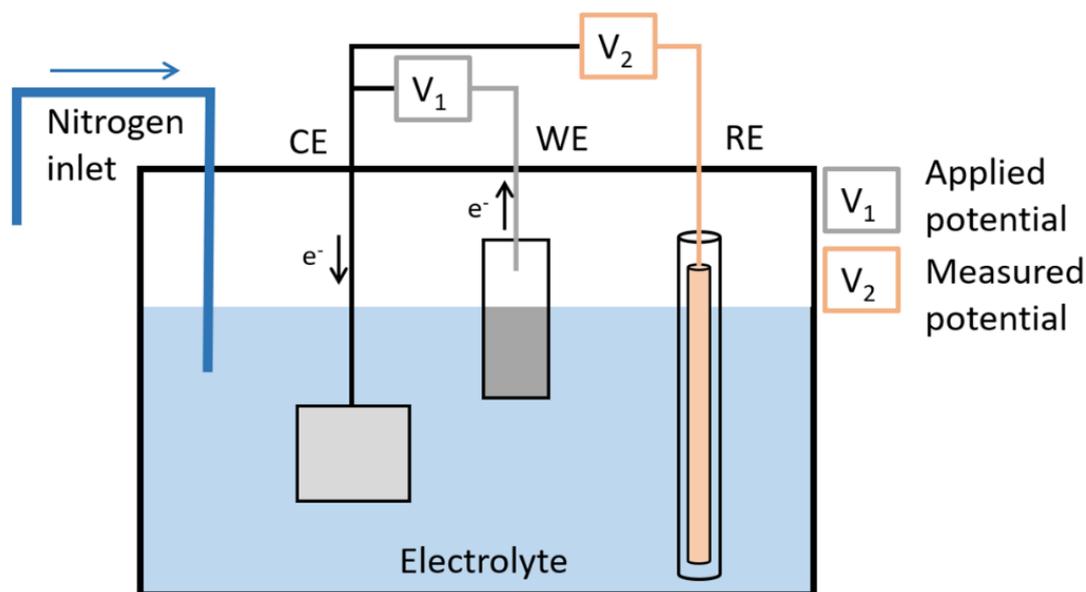
Figure 4.18. Schematic of the three-electrode cell used in this work, with the three electrodes, nitrogen inlet and the connections between the electrodes. Nitrogen was only bubbled in between experiments to ensure comparable experimental conditions.

output of the white light source. Electrochemical impedance spectroscopy (EIS) measurements were carried out at frequencies from 105 Hz to 0.1 Hz using an applied potential difference sweep between -0.5 V and -1.3 V (vs the RE). For all the measurements, a pH 13 aqueous electrolyte (KOH in water) was used.

All the photoanodes were prepared on ITO/glass substrates. Before the NW growth, a 1 cm x 0.8 cm region of the substrate was covered in Kapton tape to prevent any NW growth on the ITO substrate, ensuring a good electric contact. After the NW growth, the Kapton tape was removed and the surface of the ITO was gently cleaned to remove any residual adhesive that could hinder the electric conduction of the ITO layer. This cleaning was done by rubbing the ITO with a cleanroom wipe and acetone (≥99.5% purity, from Merck) and subsequent blow drying under a nitrogen stream.

The potentiostat used in this work was an Autolab PGSTAT302N, with illumination for the WE coming from a LOT ORIEL solar simulator LS0106 equipped with a Xe arc lamp that generates an AM 1.5 G illumination using a power density of 300 mW cm^{-2}. For the IPCE measurements, a LOT Oriel MSH-300 monochromator was used. These measurements were carried out by Javier Hernández-Ferrer and the author at the Instituto de Carboquímica, Consejo Superior de Investigaciones Científicas (CSIC), in Zaragoza, Spain.

4.12 Summary

In this chapter, all the experimental and characterization techniques used in this thesis were thoroughly described. At the beginning, the preparation of the different substrates prior to the seed layer deposition was described, with two different seed layer deposition techniques being specified. It progressed into the growth of the ZnO NWs through CBD and the integration of the different dopants and functionalizing materials, followed by the different types of microscopies (AFM, SEM and TEM) and x-ray based techniques (XRD and XRR) used to completely characterize the morphological and structural properties of the seed layers and as-grown NWs. The chemical environment of the seed layers and the NWs was studied using XPS and EDX. The optical characterization using UV-vis, FTAS and PL was covered to fully understand the light absorption capabilities of the as-grown NWs as well as their electronic structure, towards their photoelectrochemical applications. Finally, a brief description of the photoelectrochemical experiments carried out was provided. For all the techniques shown here, details of the specific systems, setups and experimental conditions were provided to ensure a good understanding of the experimental methods and the approach to obtain the results shown in the following chapters.

Chapter 5

Controlled growth of ZnO nanowires

5.1 Introduction

This chapter describes the results obtained from a detailed study of the controlled deposition of ZnO seed layers by two different techniques, atomic layer deposition (ALD) and sol-gel, and their influence in the subsequent growth of ZnO nanowires (NWs) by chemical bath deposition (CBD). First, the details of the seed layer deposition by ALD are provided, with special emphasis on the underpinning of the critical ALD parameters and their influence on the morphological and structural properties of the seed layer. This is followed by a detailed account of how their specific ALD parameters influence the CBD growth of ZnO NWs under a fixed set of NW growth conditions and why these seed layers are necessary for the controlled growth of ZnO NWs. A similar account of the sol-gel deposition of seed layers and their influence on the NW growth is provided in a comparative study to understand the different control parameters and properties of the as-grown NWs that depend on the seed layer deposition technique. Finally, different CBD conditions are described to understand how the dimensions of the NWs can be controlled during chemical growth for fixed seed layer deposition conditions. Morphological and

structural analyses of the seed layers are provided to correlate the different deposition conditions with their respective structural properties. The discussion in this chapter is supported by microscopic and statistical studies to provide a full understanding of the influence of the control parameters over the dimensions and growth orientations of the NWs and how these can be modulated.

5.2 Influence of the controlled deposition of seed layers by ALD on the growth of ZnO nanowires

Atomic layer deposition (ALD) offers a high degree of tunability owing to the multitude of parameters that control the deposition of the resulting ZnO seed layers. In particular, the temperature, number of ALD growth cycles and the pulse and purge times form the space parameter that was explored in this work. To understand the influence of the parameters, the roughness, texture and crystallite size[229] of the seed layers were studied. These characteristics are then correlated with their influence on the chemical bath deposition (CBD) growth of ZnO nanowires (NWs) under a fixed set of conditions, which was 2 hours of growth time at 25 mM equimolar concentration of both reagents. The theoretical and experimental details of these two techniques were provided in Chapters 3 and 4, respectively.

5.2.1 Influence of the seed layer deposition temperature

Three different ALD temperatures, 200°C, 250°C and 280°C, were investigated to assess their influence on the NW growth. The samples studied under these conditions were named S1, S2 and S3, respectively. For comparison purposes, the number of ALD cycles was kept at 250 cycles and the pulse time for both precursors was maintained at 0.015 s. The purge times of both precursors were equal and were also reduced with increasing deposition temperatures to avoid excessive precursor desorption that would result in different seed layer deposition conditions. As such, these purge times were set at 20 s, 15 s and 5 s for 200°C, 250°C and 280°C, respectively.

As demonstrated by the work of Pung[230], temperatures above 200°C are expected to yield a predominant (0 0 2) orientation, which is the preferred crystallographic orientation for the growth of the ZnO NWs and, thus, the three temperatures were chosen following this idea, with 280°C being the maximum

allowed temperature in the ALD system used. X-ray diffraction (XRD) measurements were performed on the seed layers at three different temperatures to investigate their preferred crystalline orientation, with the results shown in Figure 5.1. The spectra shown in Figure 5.1 clearly demonstrates that the preferred crystalline orientation for these three seed layers was the (0 0 2), which is indicated by the characteristic peak of the wurtzite crystalline structure at around 34.5°. The seed layer deposited at 200°C also shows a small (1 0 1) contribution, centered around 36.5°. As the temperature was increased to 250°C, this contribution was reduced and it was no longer present at 280°C. This confirms that the seed layers deposited at temperatures of or above 200°C have the required crystalline orientation that is beneficial for the CBD growth of NWs. The sample at 250°C also showed a slight deviation of the position of the (0 0 2) peak compared to the other two. The origin of this deviation is not yet known.

After confirming the crystalline structure, the microstructure and topography of the seed layers was investigated by atomic force microscopy (AFM). The AFM scans were performed in 1 µm x 1 µm regions so that the grain size of the crystallites (the surface features of the seed layers) could be resolved. To analyse the topography of the seed layers, line profile analyses were carried out on the AFM micrographs.
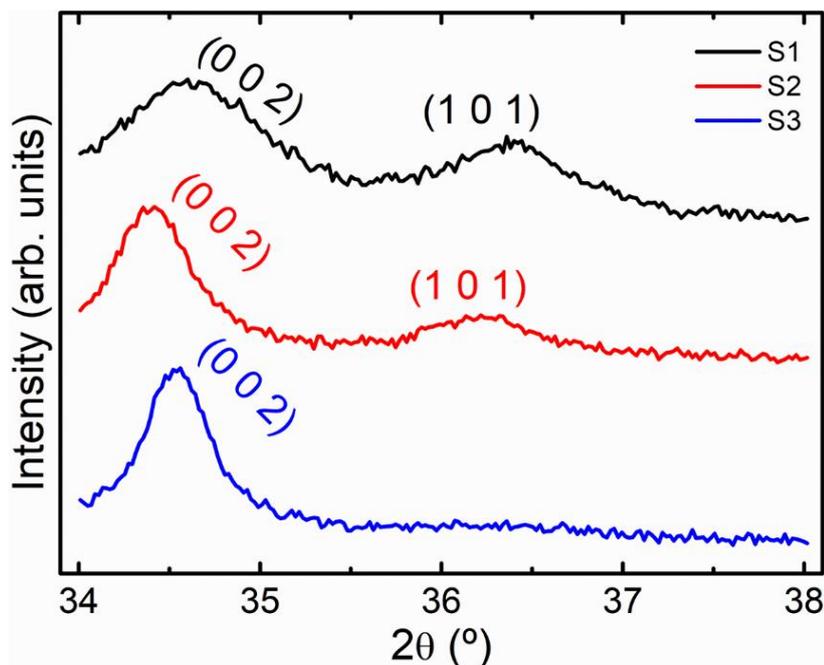
Figure 5.1. X-ray diffraction spectra of the seed layers deposited at 200°C (S1), 250°C (S2) and 280°C (S3), showing the preferential (0 0 2) growth orientation characteristic of the wurtzite phase of ZnO.

These structural analyses are presented in Figure 5.2. It is observed that, as the temperature increases from 200°C (Figure 5.2a) to 250°C (Figure 5.2b), the seed layer roughness (Rq) increases. Raising the temperature further to 280°C (Figure 5.2c) resulted in a seed layer formed by ZnO nanoislands along with randomly distributed ZnO grains, as opposed to S1 and S2 samples, which showed a typical ALD deposited textured seed layer microstructure. The reason for this non-ideal seed layer deposition stems from the low pulse time used at a high temperature. Higher temperatures increase the kinetics of the adsorption processes and the chemical reactions described in Chapter 3.4.1. Thus, as the pulse time is relatively low, the high temperature can result in an uncontrolled desorption of the ZnO precursors during the ALD process, which prompts the non-ideal growth of the seed layer, observed for the seed layer deposited at 280°C, S3. Nonetheless, the roughness of this seed layer was the lowest of the three investigated.

The AFM line profiles show a clear difference in terms of grain size and topography. The grain size of S1 was larger than that of S2 and S3, as represented by the wider peaks obtained from the respective line profiles shown in Figure 5.2. The topography of the first two (S1 and S2) is similar in peak height and typical of an ALD
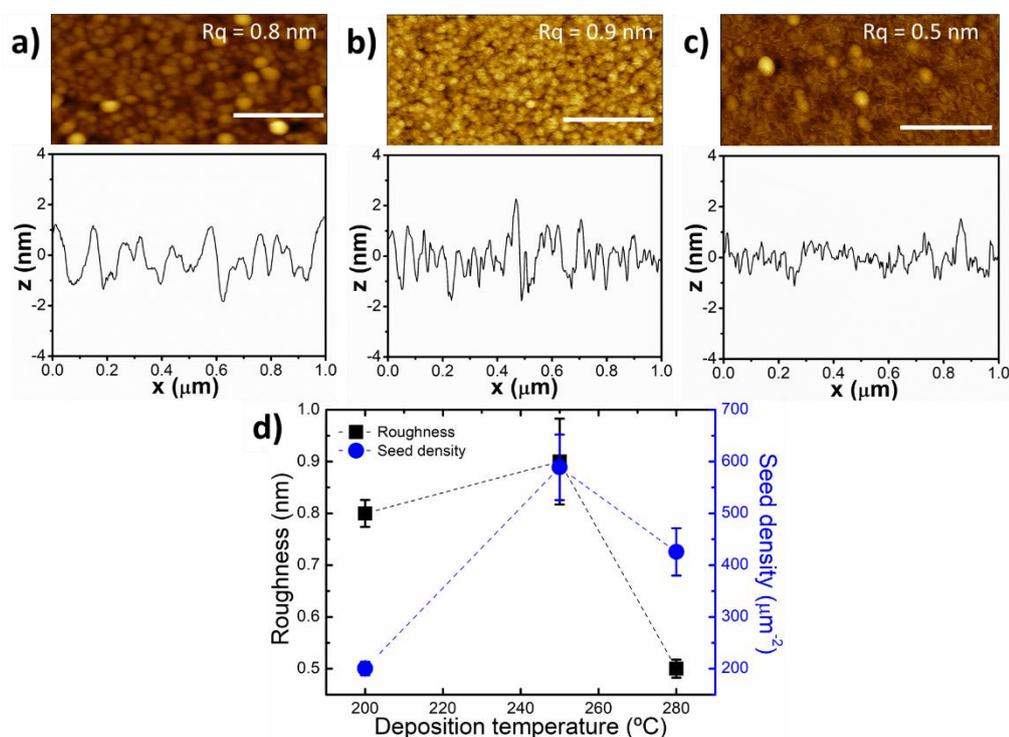
Figure 5.2. AFM micrographs and line profile analyses of seed layers deposited at **a)** 200°C, S1, **b)** 250°C, S2 and **c)** 280°C, S3. The scale bars indicates 400 nm. **d)** Comparative plot of the roughness and seed density at the three deposition temperatures studied.

textured seed layer, as reported in the works of Guillemin and Kim[231, 232], although the number of peaks is larger for S2. This indicates that the roughness of both seed layers is similar (0.8 nm and 0.9 nm for S1 and S2 respectively), while the seed density is much higher for S2 ($\sim$589 μm^{-2}) than that of S1 ($\sim$201 μm^{-2}), as shown in Figure 5.2d. Seed density here is defined as the number of surface features per unit area. Regarding the seed layer at 280°C, its topography is atypical for an ALD seed layer, which led to a lower roughness of 0.5 nm and a line profile showing a rather irregular surface microstructure. This irregular microstructure was interpreted as a decreased seed density ($\sim$426 μm^{-2}) compared to S2, although the surface features of this sample were not as easily distinguishable as for the other two. Moreover, the size of the crystallites was more heterogeneous, which is expected to lead to a wider size distribution of the as-grown NWs.

The growth of NWs on different deposition temperature seed layers was assessed using high-resolution field emission scanning electron microscopy (FESEM) Three main parameters of the as-grown NWs were analysed in the comparative investigation for these conditions and the other conditions discussed in this chapter:

- Their growth orientation, i.e., how orthogonal with respect to the substrate did the NWs grow. This is a qualitative analysis based on studying the ratio between NW tips and their sidewalls in such a way that the more NW sidewalls that are visible, the less orthogonal the NWs grew as a result of the initial growth orientations. These growth orientations stem from the surface microstructure and topography of the seed layer, as described in Figure 3.12 in Chapter 3.5.3.

- The NW diameter was measured as the distance between two opposite faces of a NW tip. Assessment of this dimension is critical to obtain a correlation with the crystallite size of the seed layer. Furthermore, analysing the size distribution of the NWs is key for certain applications that require a constrained NW size and size distribution.

- The NW density provides valuable information on the overall number of NWs per unit area, which can be crucial for certain applications[233, 234]. Moreover,

this can be correlated with the seed density of the seed layers to attain further knowledge on the nucleation of the NW growth.

Comparing the NWs grown on seed layers deposited at 200°C and 250°C, S1 and S2, (Figure 5.3a,b), it was shown previously that increasing the deposition temperature from 200 to 250°C resulted in a higher seed layer roughness with similar topography. After NW growth, this is translated to a more disoriented arrangement of the NWs grown on the seed layer at higher temperature (S2) compared to those grown on the seed layer deposited at 200°C (S1). At the same time, the diameter of the NWs grown on S2 (23 nm) was less than half that of the NWs grown on S1 (56 nm) while the distribution of the NWs diameter grown on S1 (±10 nm) was notably larger than for those grown on S2 (±4 nm). This was correlated with the higher seed density for the higher temperature, S2, compared to S1 (Figure 5.2d). It is suggested that for higher seed densities there will be a larger number of nucleation centres for NWs to grow, resulting in a higher NW density. Additionally, a higher seed density should result in a smaller crystallite size. This can be seen in the clear difference in NW diameter between S1 and S2, where the seed layer with lower seed density, and thus larger crystallites, S1, yields larger NWs than its counterpart S2. The NWs grown on S3 had a similar diameter (24 nm) to those in sample S2. However, as the topography of S3 was not typical for an ALD deposited ZnO seed layer, the resultant
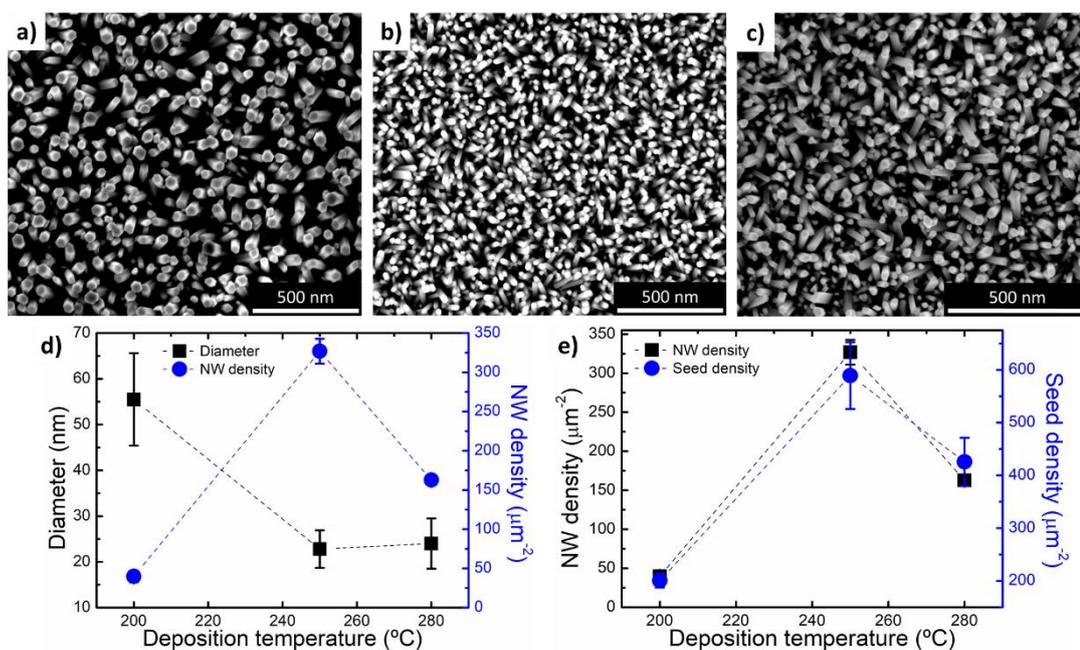
Figure 5.3. Scanning electron microscope images of ZnO nanowires grown on ALD deposited seed layers at **a)** 200°C, S1, **b)** 250°C, S2, and **c)** 280°C, S3. **d)** Comparative plot of the NW diameter, size

distribution and density at different temperatures. **e)** Comparison between the seed density and NW density, showing a clear correlation between both. The error bars on the NW diameter plot represent their size distribution.

orientation of the NWs grown had a more random alignment than for S2 (Figure 5.3c). As a result, there was a two-fold decrease in the NW density from S2 (~327 μm^{-2}) to S3 (~163 μm^{-2}), as shown in Figure 5.3d. Meanwhile, due to the diameter of the NWs of S1 being more than double that of S2, the NW density was eight times smaller for S1 (~40 μm^{-2}) than for S2. The seed layer surface features (Figure 5.2d) and nanowire (Figure 5.3d) density followed a similar trend, indicating that NW nucleation is dependent on the seed density (Figure 5.3e).

5.2.2 Influence of the precursor pulse time

The precursor pulse time is the deposition parameter that controls the dosage of precursors in the reaction chamber. This precursor dosing is critical to control the saturation of precursors and by-products on the surface of the substrate[235]. If the pulse time is too low, a non-ideal deposition will take place, as for S3. However, if the pulse time is too high, the surface will be saturated and more than a monolayer may be deposited, hindering the control over the deposition of atomic layers. Besides, excessive dosage of precursors can result in gas phase reactions and the excessive formation of by-products that could coalesce on the surface of the deposited film, yielding an undesired growth of the seed layer. Overall, the pulse time has a direct influence on the deposition regime, resulting in incomplete growth for a low dosage or a shift in the deposition regime from ALD to CVD regime for a large dosage of precursors. To assess the influence of pulse time on the seed layer deposition, two different seed layers were prepared, S4 and S5, with the deposition conditions indicated in Table 5.1 in comparison with those of S3.

The influence of the pulse time on the ALD seed layer deposition and NW growth was studied by comparing the results from samples S4 and S5 with those from S3. From now on, when referring to the pulse times, the first number indicates that of diethylzinc (DEZ), while the second one is for water. For S4, both pulse times were increased to 0.1 s to overcome the previously mentioned problems of the lower pulse times at high temperatures. Finally, for S5, the objective was to understand the limits of ALD as a technique for the deposition of ZnO seed layers. As such, the influence

Table 5.1. Atomic layer deposition conditions for seed layers S3, S4 and S5, in which the influence of precursor pulse times on the seed layer deposition is investigated.

Sample	Temperature (°C)	Nº cycles	Zn pulse time (s)	H_2O pulse time (s)	Purge time (s)
S3	280	250	0.015	0.015	5
S4	280	250	0.1	0.1	5
S5	280	250	1	0.1	5

of a significant excess of one of the precursors during the seed layer deposition and on the subsequent NW growth was studied to discern whether this large excess would result in an impediment of the NW growth. In addition, the chemistry of the seed layers deposited this way was probed. Figure 5.4a shows the AFM micrograph and corresponding line profile of S4. The ZnO crystallites of S4 are larger than for any of the other samples while showing a heterogeneous surface with a roughness of 1.4 nm. The AFM micrograph of S5 and its line profile are shown in Figure 5.4b. The surface roughness is 0.4 nm, similar to that of the underlying silicon substrate, with
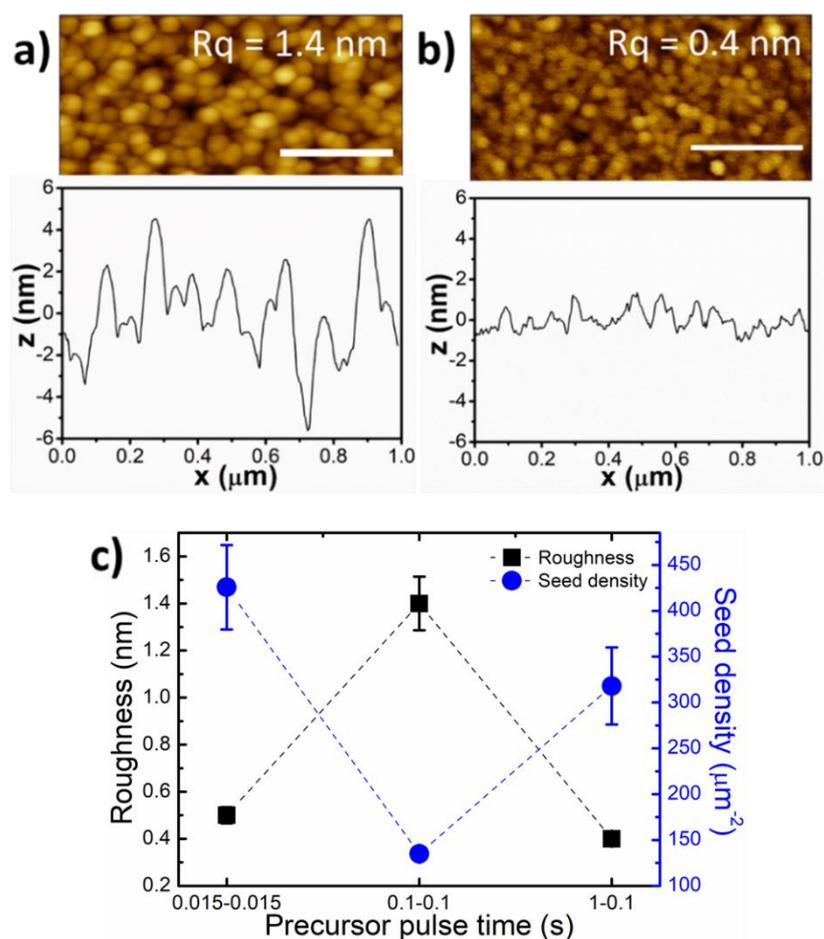
Figure 5.4. Atomic force microscopy micrographs and line profiles of samples grown with pulse times of **a)** 0.1 s – 0.1 s, S4, and **b)** 1-0.1 s, S5. The scale bars indicates 400 nm. **c)** Comparative graph of the surface roughness and seed density of these two samples with S3.

a homogeneous surface texture and crystallite size. As such, it can be seen that the increase in pulse time from 0.015 s (S3) to 0.1 s (S4) resulted in a large increase of the surface roughness, coupled with a considerable reduction in the seed density (from ~426 μm^{-2} to ~135 μm^{-2}) owing to the larger crystallite size (Figure 5.4c). Regarding S5, the reduced crystallite size and larger homogeneity compared to S4 resulted in a reduction of the surface roughness and a larger seed density of ~318 μm^{-2}.

To further understand the influence of the increased DEZ pulse time on the physicochemical properties of the ZnO seed layers, x-ray reflectivity measurements were carried out on S4 and S5, with the results shown in Figure 5.5a,b, respectively.
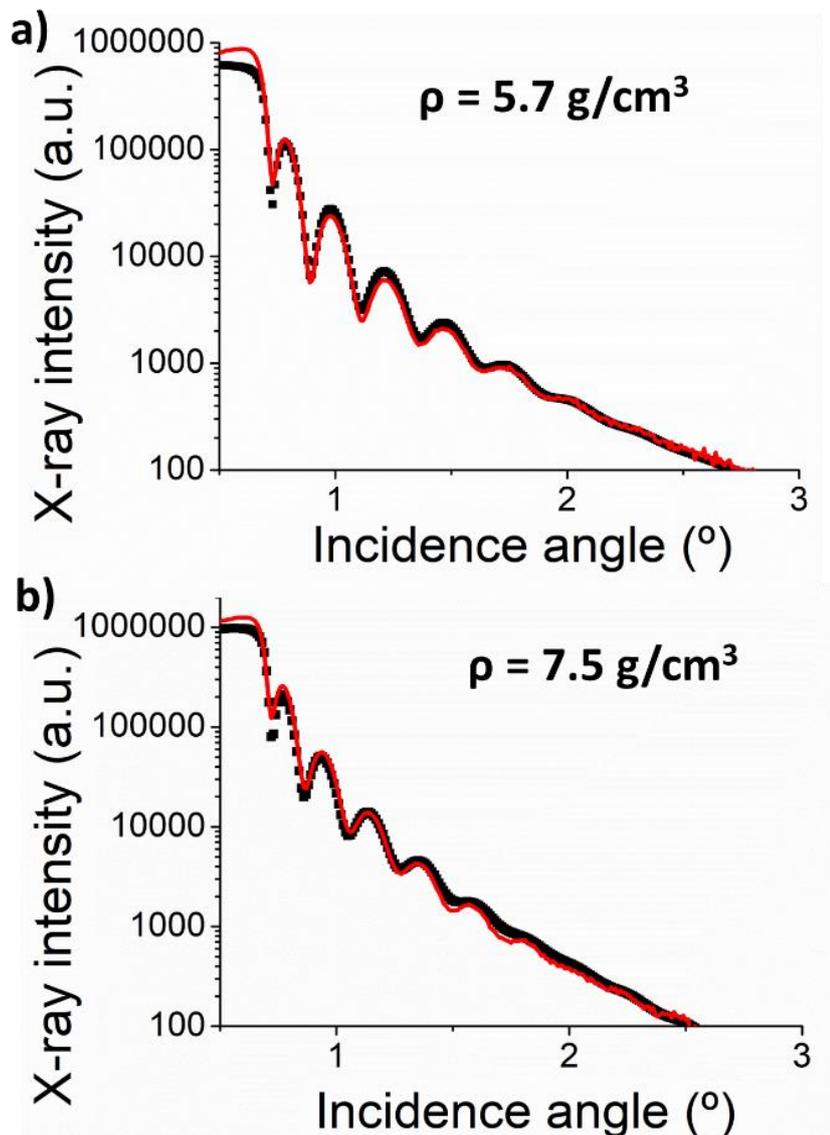
Figure 5.5. X-ray reflectivity measurements of samples **a)** S4 and **b)** S5, showing the distinct density values obtained for both samples. The black symbols represent the experimental data and the red lines are the best fitting simulations.

The basics of XRR were detailed in Chapter 4.8.2. The plots shown in Figure 5.5 represent the best fitting simulations (red lines) to the experimental data obtained (black symbols). Barring an initial dissonance for both samples, the fitting of the simulations correlates satisfactorily with the experimental data. The large excess of Zn precursor of S5 resulted in a large increase of the density of the ZnO seed layer, from 5.7 g cm^{-3} for S4 to 7.5 g cm^{-3}. Comparing these two values with the ideal density of ZnO[236] (5.6 g cm^{-3}), it is clear that the excess of DEZ led to a Zn-enriched seed layer, distant from the ideal stoichiometry of ZnO.

FESEM micrographs of as-grown ZNO NWs on S4 and S5 are provided in Figure 5.6a,b, respectively. In both cases, the growth orientation is widely distributed, more so for S4 than S5, as a result of the larger surface roughness. Nonetheless, a roughness as low as that of S5 should, in principle, provide a much better vertical alignment, but this discrepancy may be attributed to the Zn-rich seed layer that provides a different growth platform upon which the NWs growth is initiated. Regarding the size distribution and density of these NWs (Figure 5.6c), S4 shows a larger diameter (49 nm) and size distribution (±12 nm) with a smaller NW density (~66 μm^{-2}) than S3, which is attributed to the larger size of the seed layer crystallites and its surface texture. S5 shows, in comparison, a drastic reduction of the NW diameter and the size distribution (32±9 nm) compared to S4, which is coupled with an increase of the NW density (~106 μm^{-2}), although this increase in the NW density is not as significant as expected owing to the more random growth orientation. Figure 5.6d demonstrates that there is a direct correlation between the seed and NW density by which these two parameters have similar trends for these three samples. Only S5 shows a small deviation in which the NW density does not follow the upwards trend of the seed density due to the aforementioned characteristics of the seed layer.

5.2.3 Influence of the number of cycles

The number of cycles is the process parameter that controls the number of ALD cycles in a deposition. A cycle is defined as the sequential pulse and purge of both precursors. In a basic sense, the number of cycles is indicative of the overall thickness of the seed layer, with a larger number of cycles providing a larger thickness. However, there are additional side effects to the increase in the number of cycles,
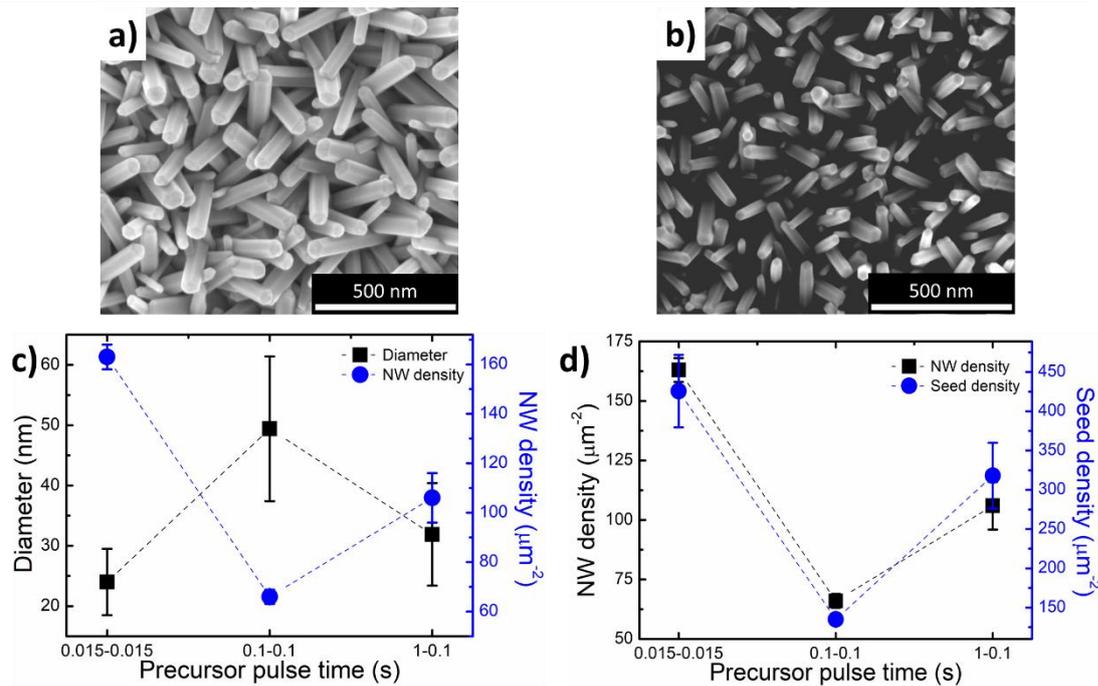
Figure 5.6. Scanning electron micrographs of as-grown NWs on seed layers **a)** S4 and **b)** S5. **c)** Comparative plot of the NW diameter, size distribution and density for different seed layer pulse times. **d)** Comparison between the seed density and NW density of S3, S4 and S5. The error bars on the NW diameter plot represent their size distribution.

particularly for samples deposited outside of the ideal ALD regime, as for the samples shown here. In particular, increasing the number of cycles can lead to a considerably increased surface roughness that will have direct influence on the orientation of the as-grown NWs[237, 238].

Figure 5.7a,b show the AFM micrographs of samples deposited at 150 (S6) and 500 (S7) cycles respectively; these two seed layers are compared with S4 and, hence, the other deposition parameters (temperature and pulse and purge times) were kept unchanged. For the lower number of cycles (150, S6), the seed layer texture is rather homogeneous, with surface features similar to those shown for S1 and S4 in terms of size and distribution, based on the characteristics of the line profile. The roughness of this seed layer was low, having a value of 0.6 nm. In comparison, when the number of cycles was increased to 500, the texture of the seed layer became considerably heterogeneous, as clearly shown in the line profiles of this sample; this, in turn, resulted in a two-fold increase of the surface roughness, rising to 1.3 nm. Two clear effects of the increased number of cycles can be extracted when comparing the results of these two samples with those of S4 (Figure 5.7c): first, the seed density decreased almost linearly with increasing number of cycles, from ~173 μm^{-2} to ~78
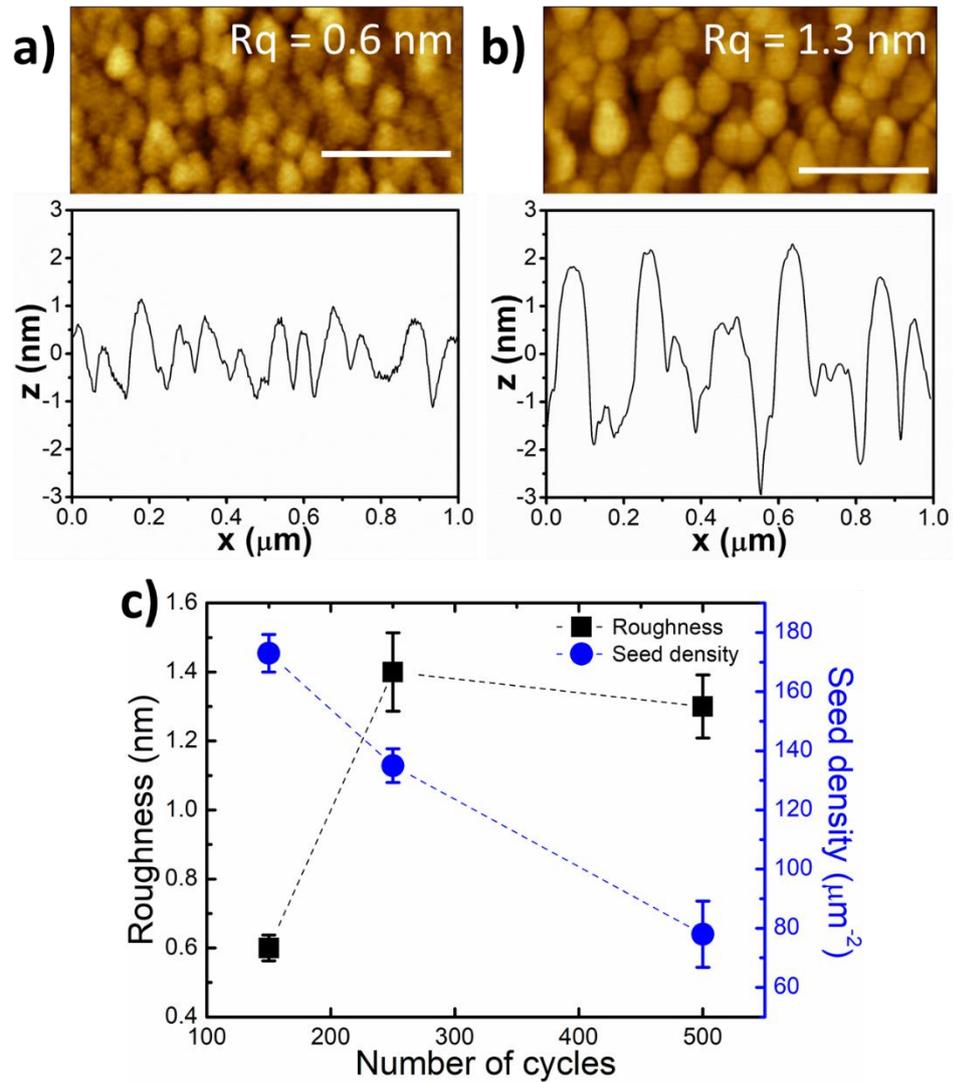
Figure 5.7. Atomic force micrograph of ZnO seed layers deposited with **a)** 150 and **b)** 500 ALD cycles. The scale bars indicates 400 nm. **c)** Comparative plot of the surface roughness and seed density for seed layers deposited with different number of cycles.

μm^{-2} for 150 and 500 cycles respectively; second, the seed layer roughness shows a sharp increase from 150 to 250 cycles, to values more than double that of S6 for S4, which then slightly decreases for S7 (from 0.6 nm to 1.4 nm and, finally, 1.3 nm). This seems to indicate that the roughness may linearly increase with the number of cycles until it reaches the plateau value shown here at around 1.3 nm. These two considerable effects induced by the changing number of ALD cycles will clearly affect the NW growth and can serve as the key control parameter to tune the orientation of the as-grown NWs due to the large variance in surface roughness and texture.

The corresponding FESEM micrographs of samples S6 and S7 are provided in Figure 5.8a,b, respectively. Owing to the homogeneous surface texture and low
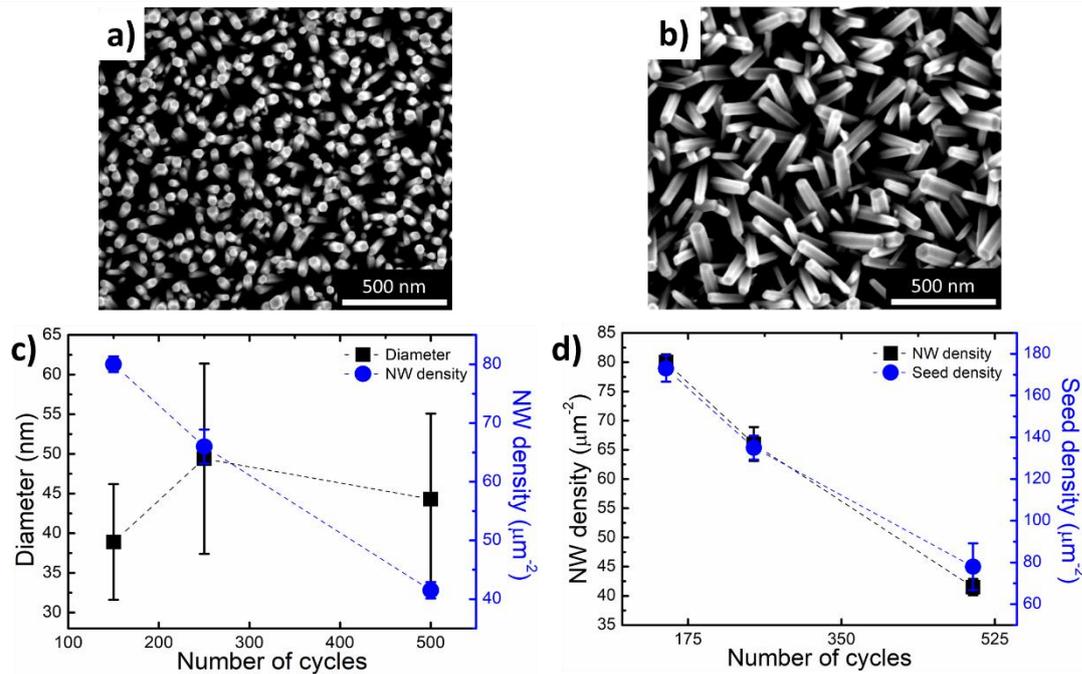
Figure 5.8. Scanning electron micrographs of as-grown NWs on seed layers deposited with **a)** 150 cycles, S6, and **b)** 500 cycles, S7. **c)** Comparative plot of the NW diameter and density and **d)** comparison of NW and seed density for as-grown NWs on seed layers with varying number of cycles. The error bars on the NW diameter plot represent their size distribution.

roughness, S6 shows vertically aligned NWs of a smaller diameter and reduced size distribution than S4 (39±7 nm compared with 49±12 nm). The opposite was observed for the as-grown NWs on S7, with a more random growth orientations and larger diameters and size distribution than S6 (44±11 nm) resulting from the previously described characteristics of the seed layer. Attending to the NW density, it follows a similar trend to the seed density (Figure 5.8d) by which its value was reduced with increasing number of cycles. As such, the NW density of S6 ($\sim$80 μm^{-2}) was considerably larger than that of S7 ($\sim$42 μm^{-2}), as shown in Figure 5.8c.

5.2.4 Influence of the purge time

The purge time between the precursor pulses is a key deposition parameter as it helps controlling the saturation of the substrate surface while regulating the presence of by-products and excess reagents[239]. As such, it is paramount to carefully tune the purge times of both precursors to ensure that any excess precursors and by-products are removed while preventing the desorption of the previously pulsed material. All the samples discussed up to now had both pulse and purge times equal; this, however, is not sufficient to exploit the tunability possibilities offered by ALD as

a deposition technique, as shown by the work of Park et al.[239] As such, one example of separately tuning the purge times is provided here to study their influence. This seed layer was deposited at 280°C for 250 cycles with a pulse and purge train of 0.1 s - 7 s - 0.1 s - 20 s, with the first two values being the pulse and purge times for DEZ and the last two being those of H_2O. This sample was labelled as S8. AFM and FESEM micrographs of this sample are provided in Figure 5.9. Regarding the seed layer characterization, it had a surface roughness of 1.1 nm with a seed density of ~138 μm^{-2}, very similar to that of S4; its texture was comparable to that of S7. Regarding the as-grown NWs, they showed an almost vertical growth orientation, a diameter of 46 nm with a size distribution of ±10 nm and a NW density of ~98 μm^{-2}, comparable only with the samples grown on seed layers deposited with 0.015 s pulse and purge times. These results show that carefully tuning the purge times of the seed layers can yield high density of average sized, vertically aligned NWs, enforcing the need to carefully address the pulse and purge times.
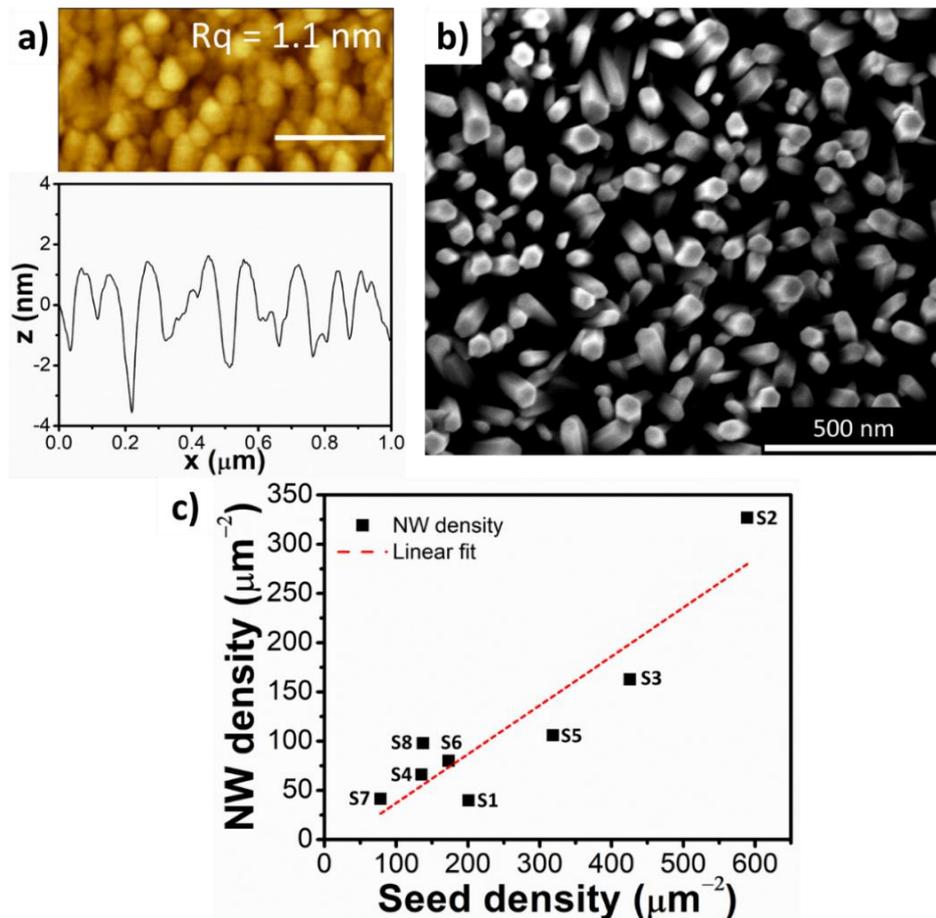
Figure 5.9. a) Atomic force and **b)** scanning electron micrographs of the sample with adjusted purge times, S8. Scale bar of atomic force micrograph indicates 400 nm. **c)** Correlation between seed density

and nanowire density, showing a linear relationship between characteristics for the conditions used here.

Figure 5.9c shows the correlation between seed density and NW density that has been discussed individually for each ALD parameter. This plot shows a direct, linear correlation with a slope of ~0.5, indicating that, on average, around half of the surface features of the seed layers become NWs. This relationship was stablished without considering the seed layer roughness, NW diameter or the orientation of the NWs, thus providing some valuable insight on the growth of ZnO NWs from textured seed layers.

Attending to the individual values, it can be seen that S2 is a clear outlier that shows the largest seed density and NW density, which was accompanied also by the smallest NW diameter. This is an indication that an optimal configuration was achieved for S2 that results in densities much larger than for the other studied seed layers, although this would require further studies to prove.

For clarity purposes and to provide a better platform to compare all the values for the different seed layer and NW parameters discussed here, Table 5.2 records the roughness, seed density, the NW diameter, size distribution and density for the eight samples discussed here. It can be seen that S8 had the highest ratio of NW density/seed density. Both S2 and S5 have comparable diameters and narrow size distributions for the smallest NW size recorded here. This collection of samples clearly showcases the high degree of tunability provided by ALD with which, by modifying only the seed layer deposition parameters, it is possible to control the dimensions, orientation and density of as-grown ZnO NWs.

Table 5.2. Summary of the main parameters of the seed layers and as-grown nanowires discussed for the study of the parametric influence of the atomic layer deposition of ZnO seed layers on nanowire growth.

Sample	Surface roughness (nm)	Seed density (μm^{-2})	NW diameter (nm)	NW density (μm^{-2})
S1	0.8	201	56±10	40
S2	0.9	589	23±4	327
S3	0.5	426	24±6	163
S4	1.4	135	49±12	66
S5	0.4	318	27±6	106
S6	0.6	173	39±7	80

| S7 | 1.3 | 135 | 44±11 | 42 |
| S8 | 1.1 | 138 | 46±10 | 98 |

5.2.5 Importance of the ZnO seed layer for the growth of nanowires

In order to better understand and verify the key role of the seed layer on the ZnO NW growth, a set of experiments was carried out in which it was attempted to grow ZnO NWs on a bare silicon substrate, with no seed layer. The growth conditions were 2 hours and 50 mM concentration to ensure that some material would grow on the silicon substrate. The results from these experiments are shown in Figure 5.10. It can be seen that the growth resulted in a heterogeneous distribution of NWs (Figure 5.10a), reflecting the critical role of the seed layer in the controlled growth of dimensionally tailored ZnO NWs. Nonetheless, interesting insights on the growth mechanism of the NWs can be extracted from these results.

Considering Figure 5.10b, the two vertical NWs grown show that, at their bottom end, there is a resemblance to a hexagonal seed layer upon which the NWs have grown. This can be seen clearly in the higher magnification micrograph of Figure 5.10c, where said base is shown along with the hexagonal prism shape characteristic of wurtzite phase ZnO NWs.

Figure 5.10. Scanning electron micrographs showing ZnO nanowires grown on a bare silicon/silicon dioxide substrate without the presence of a seed layer.

Figure 5.10d depicts one of these bases prior to the growth of a NW on top. However, there are other NWs that seem to grow without the presence of this hexagonal base, as seen in Figure 5.10 b. This indicates that further research would be necessary to fully understand the seedless growth of ZnO NWs. One distinguishing feature of this seedless growth is that, while the lateral faces of the NWs are smooth, the Zn bases are fairly rough and grainy, with a possible resemblance to a seed layer similarly to those previously shown. Nonetheless, these results clearly demonstrate the need of a seed layer for the controlled growth of tailored arrays of ZnO nanowires[240].

5.3 Parametric influence of the chemical bath deposition conditions on the growth of ZnO nanowires

The influence of the chemical bath deposition conditions on the nanowire growth was studied as a second route to tailor the dimensions of the nanowires to a desired application. For these, a new set of ALD conditions were used to form the seed layer,

in which the pulse and purge times were further tuned to obtain a high density of NWs. The pulse train used was 0.05-7-0.2-20, with the first two times referring to the pulse and purge times of DEZ and the last two referring to those of water. The number of cycles was kept at 250 and the temperature was set at 250°C, equivalent to S2, following the results obtained in the previous sections. To study the CBD influence on the NW growth, the synthesis time and the concentration of the precursors was changed; the temperature was kept constant at 90°C and the concentrations used were always equimolar for the Zn and OH$^-$ sources. In short, the conditions used were 2 h – 25 mM, 2 h – 50 mM, 6 h – 50 mM and 24 h – 50 mM. Figure 5.11 i shows a comparison of the NW diameter, density and length for the four samples here discussed.

First, the influence of the concentration was studied with the change from 25 mM (Figure 5.11a,e) to 50 mM (Figure 5.11b,f). It can be seen that this increase directly yields a larger diameter, length and corresponding size distributions going from 32±7 nm in diameter and 336±34 nm in length for 25 mM to 79±22 nm in diameter and 492±13 nm in length for 50 mM. It can be observed that the changes in the concentration drastically affect the NW diameter more than the NW length, as the former increased more than 200%, while the latter increased around 45%. In addition, the large increase in diameter resulted in a considerable increase in the size distribution, along with a reduction of the NW density (from ~208 μm^{-2} to ~78 μm^{-2} for 25 mM and 50 mM respectively). In summary, increasing the reagent concentration is a clear route to further control the dimensions of the as-grown NWs, especially the diameter.

The influence of the synthesis time was studied by studying three different growth times: 2 hours, 6 hours and 24 hours. For all three, the reagent concentration was kept constant at 50 mM for both reagents. Increasing the synthesis time from 2
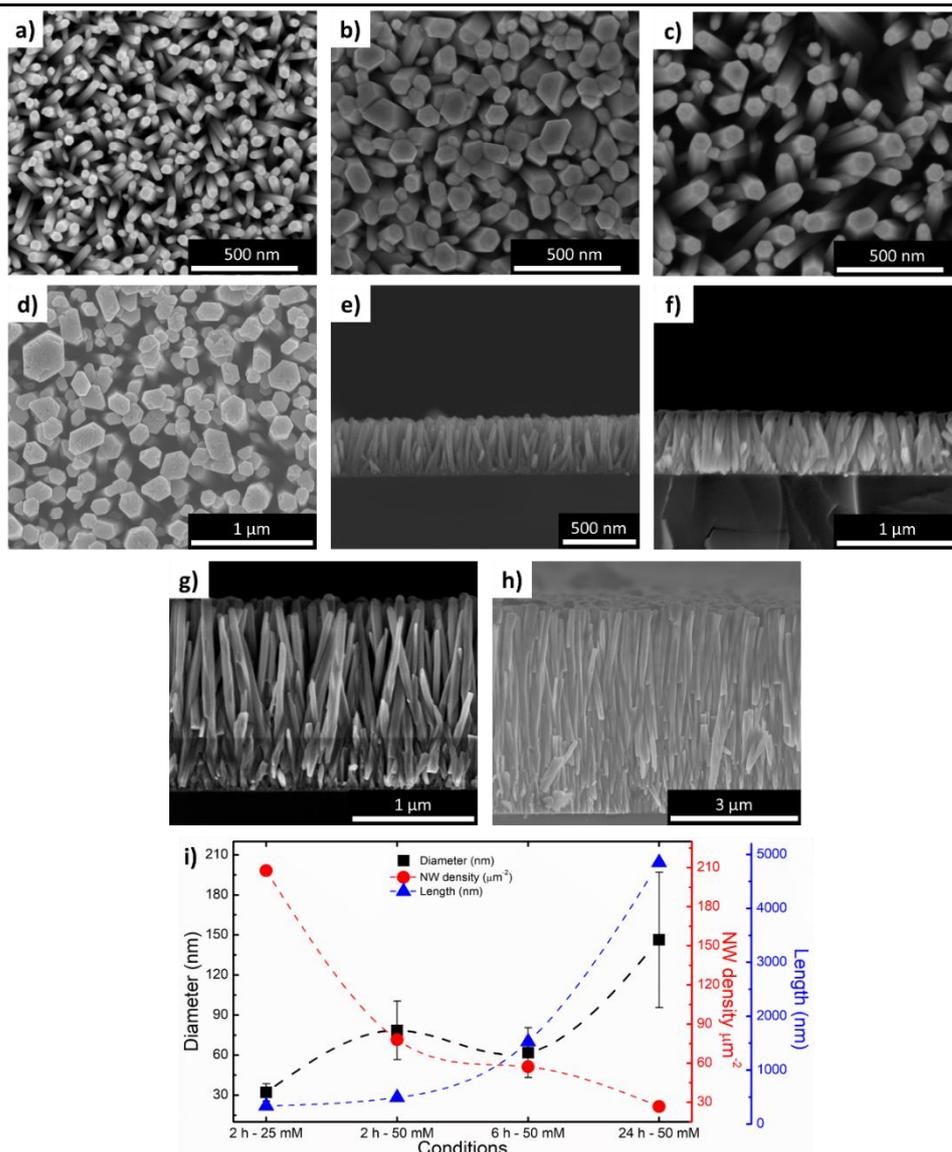
Figure 5.11. Top-view and cross-section scanning electron micrographs of ZnO nanowires grown with different chemical bath deposition conditions: **a), e)** 2 hours – 25 mM. **b), f)** 2 hours – 50 mM. **c), g)** 6 hours – 50 mM. **d), h)** 24 hours – 50 mM. **i)** Comparative plot of the diameter, length and nanowire density of the four different nanowire samples. The error bars on the NW diameter and length plots represent their size distribution. The error bars for the length are within the respective symbols in the plot. The dashed lines are included for clarity purposes.

hours to 6 hours (Figure 5.11c,g), led to two separate changes. On one hand, the NW diameter and NW density were reduced from 79±22 nm and ~78 μm^{-2} for the 2 hours growth to 62±19 and ~57 μm^{-2} for the 6 hours growth. On the other hand, the length of the NWs proportionally increased with growth time, going from 492±13 nm to 1527±42 nm. The reduction in NW diameter and density at the same time may seem counterintuitive considering the results described previously in this chapter. However, the orientation of the as-grown NWs plays a key role in the overall NW

density; in fact, the wider the orientation distribution is, the lower the NW density will be, which is the effect causing the reduction of the NW density for the 6 h – 50 mM compared to the 2 h – 50 mM samples. Further increasing the synthesis time from 6 hours to 24 hours (Figure 5.11d,h), while keeping the concentration at 50 mM resulted in a large increase of the dimensions and size distribution of the NWs. In particular, the diameter and length rose from 62±19 nm and 1527±42 nm for 6 h – 50 mM to 146±51 nm and 4849±90 nm for 24 h – 50 mM. Additionally, the NW density was further reduced from ~57 μm^{-2} to ~27 μm^{-2} as a result of the larger diameter of the NW grown for 24 hours. A comparison of all the dimensions and NW density obtained for the four samples here discussed in presented in Figure 5.11i. An important feature of the 24 hours growth is the loss of the typical hexagonal shape of the ZnO NWs. This is due the large diameter of these NWs, which forces the NWs to accommodate their shape to the available space. This means that, during growth, the NWs will be forced to grow in shapes akin to the typical hexagonal, although distorted, in order to fit with the neighbouring NWs. A similar effect is seen for the 2 hours – 50 mM growth (Figure 5.11b).

In summary, modifying the synthesis time and precursor concentration provides an additional degree of control over the dimensions of the ZnO NWs. A summary of the results obtained is given in Table 5.3 for easier comparisons. The reagent concentration mainly influences the NW diameter[163], with higher concentrations providing larger diameters. The synthesis time provides more control over the length of the NWs[241], with increasing synthesis times yielding longer NWs. Therefore, carefully tuning the ALD seed layer deposition and the CBD conditions allows a high degree of control over the dimensions and orientation of the ZnO NWs.

Table 5.3. Summary of the nanowire diameter, length and density for nanowires grown under different chemical bath deposition conditions.

Reagent concentration (mM)	Synthesis time (hours)	NW diameter (nm)	NW length (nm)	NW density (μm^{-2})
25	2	32±7	336±34	208
50	2	79±22	492±13	78
50	6	62±19	1527±42	57
50	24	146±51	4849±90	27

5.4 Growth of ZnO nanowires on sol-gel deposited seed layers

Following the issues discussed in Chapter 4.3, an alternative route to the deposition of ZnO seed layers had to be explored, with sol-gel processing being the chosen avenue. The experimental details of this process were provided in Chapter 4.4 and only those were used in this project. As the goal of the sol-gel seed layers was to serve as an underlayer for the growth of ZnO NWs for photoelectrochemical applications, no parametric study of the sol-gel deposition of ZnO seed layers was carried out. It was considered that a study of this type was not appropriate timewise, nor it would have given critical input on the subsequent functional performance of the NW-based devices. As such, the sol-gel deposition parameters of the seed layer were kept constant and changes only to the CBD conditions were studied. A detailed study of the sol-gel deposition of ZnO thin films by sol-gel processing can be found in the work of Znaidi[154].

A growth study was carried out to better understand the growth of NWs on sol-gel seed layers. For this, time-dependent growths were carried out, while keeping the reagent concentration and temperature fixed at 25 mM and 90°C. Four different growth times were used in this study, namely 60', 90', 2 hours and 6 hours. The aim of this study was to understand the minimum growth time to obtain NWs and to investigate the desired growth conditions for the envisioned application.

The 60 minutes synthesis is shown in Figure 5.12a, which illustrates the initial growth of ZnO nanomaterial. No recognizable NWs were grown; instead, preliminary seed-like nanostructures similar to those shown in Figure 5.10 d are formed. These nanostructure do not completely cover the underlying seed layer, possibly indicating that longer growth times would result in a complete coverage of the substrate. As the growth time was increased to 90 minutes (Figure 5.12b), ZnO nanorods (NRs)
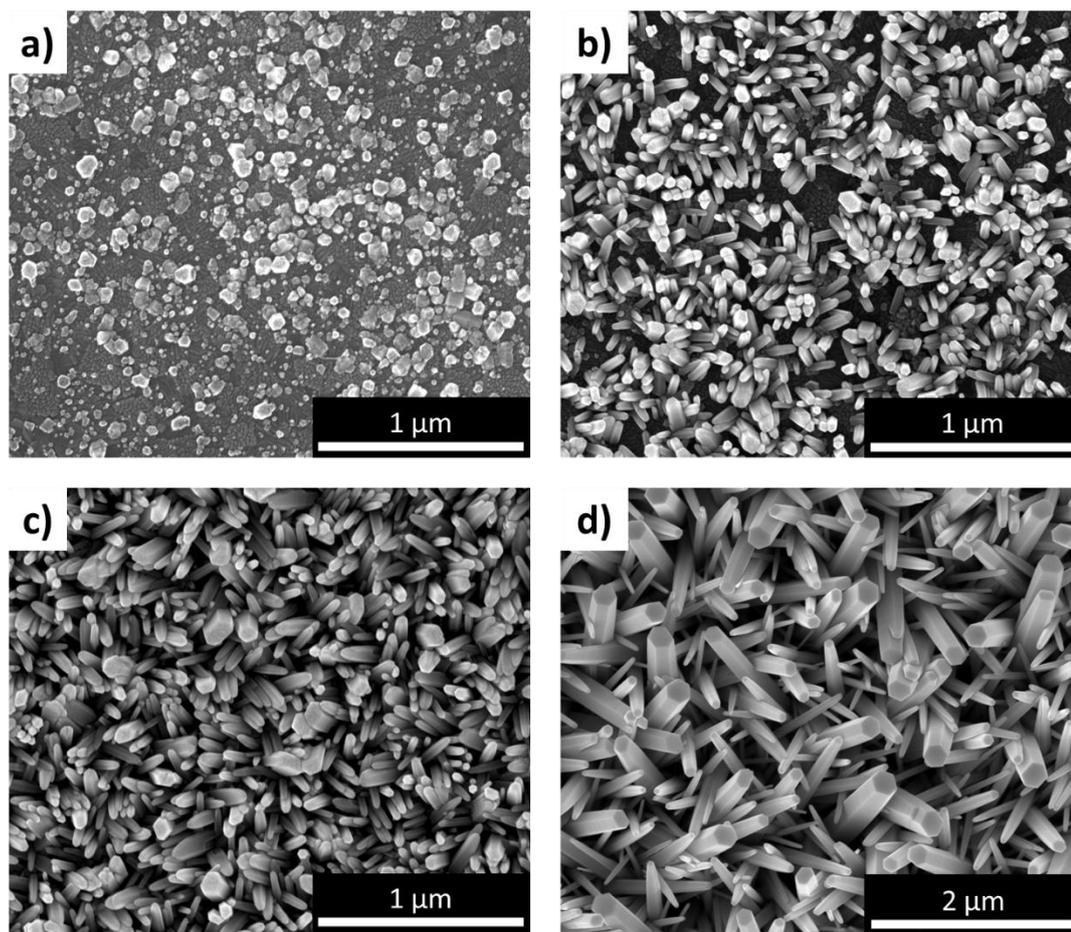
Figure 5.12. Scanning electron microscopy images of ZnO nanowires grown on sol-gel deposited ZnO seed layers at an equimolar reagent concentration of 25 mM for **a)** 60 minutes, **b)** 90 minutes, **c)** 2 hours and **d)** 6 hours.

were grown (see Chapter 2.3 for the difference between NWs and NRs). These NRs grew at various random orientations with a wide size distribution; the NR array was discontinuous, as there were regions of the substrate that were exposed still, not covered with the as-grown ZnO nanomaterial observed in Figure 5.12a. For the 2 h – 25 mM CBD conditions (Figure 5.12c), a continuous array of ZnO NWs was achieved, meaning that the substrate was completely covered by the ZnO NWs, similar to the results previously shown throughout this chapter.

One distinguishable characteristic of these NWs grown on sol-gel deposited seed layers is the tapered tips that a large number of the as-grown NWs display, a feature that was not observed for any of the ALD seed layer-based samples. This effect was more obvious for the NWs grown for 6 h – 25 mM (Figure 5.12d). For these, two different types of ZnO NWs can be identified: thinner ones, with tapered tips, and larger ones resembling the ones previously reported. Nonetheless, both types

have the typical hexagonal shape characteristic of the wurtzite crystalline structure. These tapered NWs have also been seen in ALD-based seed layers[242], though not in this work. More examples of ZnO NWs with tapered tips are provided in Chapters 6 and 7 as this was a common feature of the NWs grown on sol-gel deposited seed layers. Regarding the NW size and density, the values for the 2 hours growth were 38 ± 14 nm in diameter and ~27 μm^{-2} while those of the 6 hours growth were 75 ± 52 nm in diameter and ~11 μm^{-2}. A large increase in the diameter and the size distribution can be seen for the 6 hours growth, which led to a considerable decrease on the NW density. As will be discussed in Chapter 7, the latter growth conditions, 6 hours and 25 mM, were chosen as the base NW growth for the development of the ZnO NW-based photoelectrochemical functional structures.

5.5 Crystallography of the ZnO nanowires and seed layers

One key feature of any nanomaterial is its crystalline structure, in particular whether it is single crystal, or has defects or is polycrystalline or amorphous in structure. This can be vital for their functional performance once integrated as electronic devices, as the crystal structure and crystalline defects can be the cause of reduced charge mobility or may hinder the optical and mechanical properties[243, 244]. Therefore, understanding the crystalline structure of the NWs is key to obtain a suitable device performance. X-ray diffraction (XRD), high-resolution transmission electron microscopy (HRTEM) and selected area electron diffraction (SAED) were used to study the crystalline characteristics of the ZnO seed layers and NWs. The crystallinity of the seed layer is also important to obtain the best possible growth of the ZnO NWs, meaning that it will enable the growth of high-quality, single crystal wurtzite ZnO NWs, as was detailed in Chapter 3.5.3.

Figure 5.13a shows the XRD analyses of five ALD deposited seed layers, namely S1, S2, S3, S7 and S8. It is clear that, for all five, the (0 0 2) is the dominant orientation as part of the (0 0 0 1) plane following the [0 0 1] direction, with the presence of the (1 0 1) component in three of them (S1, S2 and S7). This (0 0 2) orientation corresponds with the wurtzite crystalline phase of ZnO, demonstrating that the seed layers deposited with ALD have a wurtzite crystalline phase, which is ideal for the growth of single crystal NWs. To ensure that the NWs were also wurtzite phase, XRD
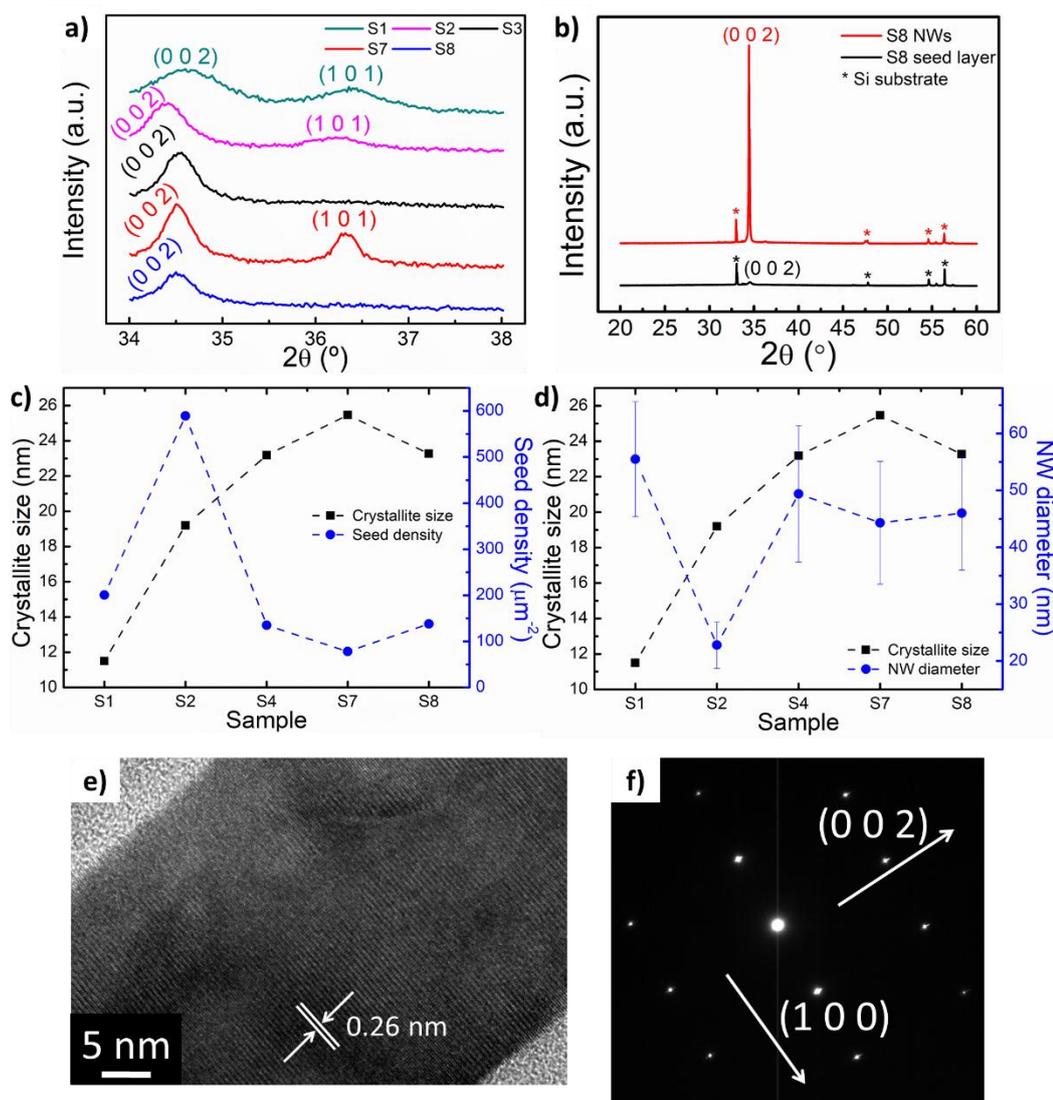
Figure 5.13. X-ray diffraction spectra of **a)** different seed layers deposited with ALD and **b)** comparison between the seed layer S8 and the as-grown NWs on that substrate. **c), d)** Plots comparing the crystallite size with the seed density and NW diameter, respectively, for the seed layers S1, S2, S3, S7 and S8. **e)** High-resolution transmission electron microscopy micrograph and **f)** selected area electron diffraction patter of as-grown ZnO nanowires on S8, showing the single crystal wurtzite phase properties of these NWs.

analyses were also performed, see Figure 5.13b. The NWs here studied were grown on S8 for 6 hours and a concentration of 25 mM equimolar. It can be seen that only the (0 0 2) orientation is present in the ZnO NWs, indicative of single-phase wurtzite NWs.

Further information was extracted from the XRD spectra of the seed layers by using Scherrer's equation (defined in Chapter 4.8.1), which was utilised to estimate the size of the crystallites (surface features) of these seed layers. This crystallite size is the out-of-plane size. The relation between crystallite size and seed density was provided in Figure 5.13c, which demonstrates a correlation between the size of the

surface features and their density by which larger crystallite sizes result in lower densities. Nonetheless, the previously mentioned relation is not clearly seen for S1 or S2. In the case of S1, this can be attributed to the wide (0 0 2) peak obtained in the XRD analyses, wider than any other, that induces a smaller crystallite size in the Scherrer's equation estimation. The AFM micrograph of S1, as previously discussed, also shows a broad size distribution that could help explain the discordance in the expected relation between the crystallite size and seed density. These two features in conjunction (a wide XRD peak and a broad distribution from AFM) can be the explanation of this irregular behaviour, as both indicate that, in principle, the crystallite size for S1 should be larger than what is estimated by Scherrer's equation. In the case of S2, a larger crystallite size than for S1 is accompanied by a larger seed density, which may seem counterintuitive. No immediate explanation can be provided for this difference other than the fact that the AFM micrograph for S2 (Figure 5.2b) was not perfectly resolved, which may pose an analytic problem for this comparison.

Concerning the relation between the crystallite size and NW diameter (Figure 5.13d), it can be seen that the NW size, including the size distribution, barely changes with varying crystallite size. S2 is an outlier in this trend, as previously stated, in which the NW diameter and NW and seed densities were remarkably different than for the other studied seed layers. The slight deviation for S7 can be attributed to the large roughness of this seed layer. From this comparative plot (Figure 5.13d), it can be inferred that a single ZnO NW typically requires more than a single crystallite to grow from, attending to the values of both sizes. This matches with what was previously seen in Figure 5.9c, where these two magnitudes followed a linear relationship by which the ration of NW density over seed density was ~0.5.

After investigating the crystal structure of the ZnO NWs by XRD, further analyses were carried out by TEM. The high-resolution TEM of Figure 5.13e shows the characteristic planar stacking of the wurtzite crystalline phase. No lattice defects such as twins or dislocations were observed during the TEM imaging, a sign of a single crystal nanostructure. This was further confirmed by the SAED pattern shown in Figure 5.13f, in which the two characteristics planar orientations, (0 0 2) and (1 0 0), of wurtzite ZnO NWs in TEM were obtained. In addition, the SAED pattern shows only

the spots characteristic of these two orientations, indicating no other growth orientations or crystalline phases. As a result of these analyses, it is possible to determine that the ZnO NWs grown in this work were single crystal wurtzite phase ZnO NWs. Their single crystal character is of special interest owing to the improved performance they enable in the functional measurements discussed in Chapter 8.

5.6 Importance of substrate positioning during nanowire growth

The positioning of the seeded substrates during the CBD growth of ZnO NWs is crucial to obtain a clean and homogeneous surface. In Chapter 4.5, it was detailed how, in this work, the seeded substrates were placed face down, supported by a custom-made holder, in order to avoid the settling out of the material grown in the growth solution. Face down means, in this case, that the seed layer is pointing downwards, towards the bottom of the reaction beaker, in such a way that the material grown in solution does not deposit due to gravity. There are works in the literature[245] that highlight how the positioning of the seeded substrate influences the NW growth. However, these works do not show what happens if the seed layer is placed facing upwards. If the seeded substrates are placed face up, settling out of material grown in solution will occur as shown in Figure 5.14 is presented.

Figure 5.14 shows an experiment on the settling out of materials grown in solution for NWs grown on the seed layer S2 with CBD conditions of 2 h – 25 mM. It is observed that the NW array is mostly covered by a heterogeneous film of ZnO nano and microstructures (Figure 5.14a,b), some of which are wires or flower-like structures (Figure 5.14c). The presence of these structures on top of the as-grown NWs will lead to irregular device performance. Moreover, the settling out of these ZnO microstructures can damage the as-grown ZnO NWs (Figure 5.14d), further hindering the characteristics of the NW film. As such, the critical influence of the positioning of the NWs during the CBD process is demonstrated to ensure a homogeneous and controlled film of as-grown NWs that will have the desired dimensions and orientation following the details previously provided in this chapter.
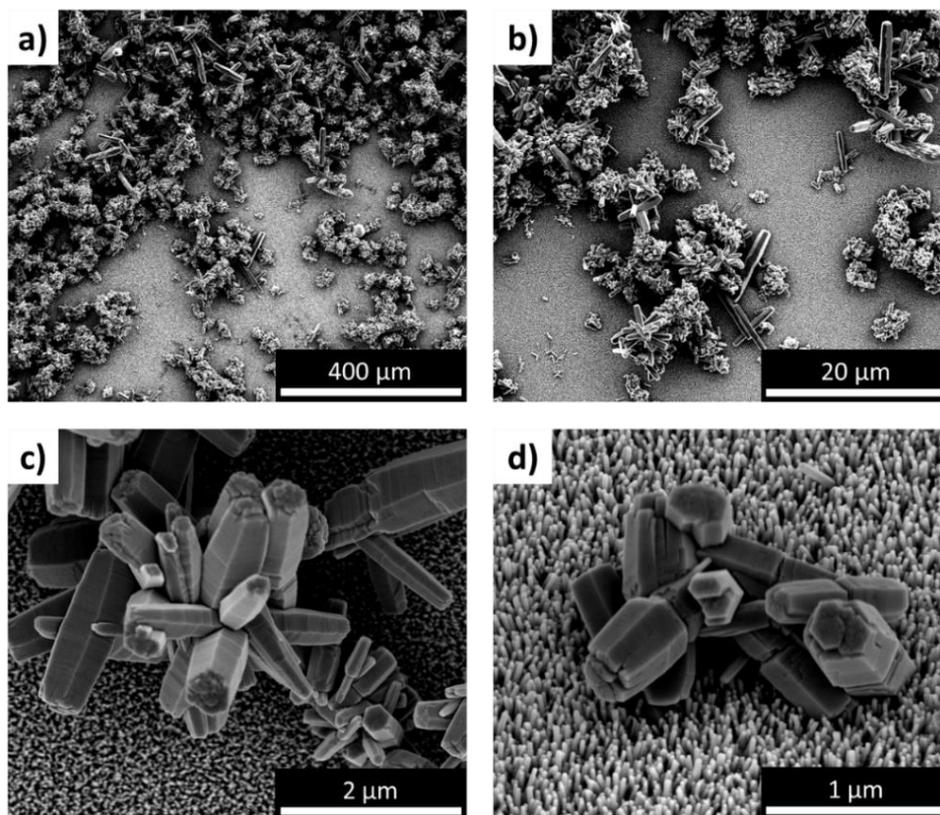
Figure 5.14. Scanning electron micrographs showing the results of a nanowire growth by chemical bath deposition with the substrate placed face up, clearly showcasing the detrimental effects of the settling out of ZnO nano and micromaterials grown in solution.

5.7 Conclusions

In this chapter, the results from a detailed study of the controlled growth of ZnO nanowires were presented and discussed, with a special focus on structural analyses carried out by scanning electron microscopy. First, a sequential and thorough description of the different atomic layer deposition parameters and their influences on the seed layer properties and how these affect the chemical bath deposition of ZnO nanowires was provided. In particular, the ALD parameters discussed were the temperature, pulse time, number of cycles and purge time. It was shown that seed layer characteristics such as the surface roughness, texture and seed density play a key role in controlling the diameter, density and orientation of the as-grown NWs. This was followed by a study of the influence of the chemical bath deposition conditions on the dimensions, size distribution and density of the ZnO NWs. The reagent concentration and synthesis time were the focal points of this study as those two were deemed the most influential on the dimensional tailoring of the as-grown ZnO NWs. It was proven how the reagent concentration predominantly influences

the NW diameter, while the synthesis time has a major influence on the NW length. The combination of these two studies serves as proof of how this ZnO NW growth process offers wide ranging control over the as-grown NWs dimensions and orientation, showcasing the usefulness for the application of these nanowires in working devices. Specifically, NWs with diameters ranging from 23 nm to 146 nm and size distributions between ±4 nm to ± 51 nm, lengths from 336±34 nm to 4849±90 nm and NW densities ranging from 27 μm^{-2} to 327 μm^{-2} were obtained with this process, showcasing the vast range of possibilities that the controlled deposition of ALD seed layer and NW growth offer.

Subsequently, a brief description of the nanowire growth on sol-gel deposited seed layers was provided, with an emphasis on the minimum growth time required to obtain an array of ZnO NWs. Only one set of conditions was used for this purpose and it was shown that, for this sol-gel process, the as-grown NWs had two different types of NWs (tapered and not tapered tips), with a broad size distribution and random growth alignment. After these NW growth studies, a review of the crystallography of the ALD seed layers and as-grown NWs was provided by means of XRD and TEM, which demonstrated that the ZnO NWs are single crystal wurtzite phase NWs. Finally, a small note on the positioning of the substrates during the CBD process was gives, emphasizing on the importance of placing the substrates face down to avoid the settling out of the ZnO micro and nanostructures grown in solution to ensure a clean and homogeneous surface and NW array.

Chapter 6

Doping of ZnO nanowires

6.1 Introduction

This chapter describes the results obtained from a thorough study on the doping of ZnO nanowires (NWs) with cobalt and copper. Doping of ZnO was described previously in Chapter 3.6 as one of the most prominent routes to enhance and tune the optoelectronic properties of ZnO. This is enabled by the ease with which dopant agents can be integrated into the wurtzite lattice of ZnO, either by direct substitution of Zn or O or as a defect in the structure. In this work, cobalt and copper were chosen as dopants in an effort to tune the bandgap of ZnO towards lower energy values, reducing it from its typical 3.3 eV, to provide enhanced functionality to ZnO in photoelectrochemical water splitting. The introduction of these dopants may also offer enhanced charge transport pathways that are beneficial for improved charge transfer within the NWs. The Co and Cu doping of the NWs was successfully achieved during chemical bath deposition (CBD) growth of the ZnO NWs, as it was described in Chapters 3.6 and 4.5. Cobalt and copper enter the wurtzite ZnO lattice by substituting for Zn atoms, which improves the optoelectronic properties while maintaining the high crystal quality discussed in Chapter 5.5. This chapter is divided in two main sections. First, the doping of ZnO NWs using copper is discussed, based

on a study of their morphology and optical properties. This is followed by a thorough account of the morphological properties of Co-doped ZnO NWs grown on textured ZnO seed layers deposited by atomic layer deposition (ALD) and sol-gel processing. Cobalt was the main focus of the doping study discussed in this chapter and, thus, this section details the influence that Co-doping has on the optoelectronic properties of ZnO NWs, with a special emphasis on the carrier dynamics and electronic band structure of these nanomaterials. An adequate understanding of these properties is crucial to comprehend the performance of functionalities based Co-doped ZnO NWs. Throughout the chapter, the cobalt and copper doping levels will be referred to in form of percentages following Eq. 6.1,

$$\%_i = \frac{n_i}{n_{Zn}} \qquad \text{[Eq. 6.1]}$$

where *%$_i$* refers to the nominal percentage doping of the *i* element (Co or Cu) and *n$_i$* and *n$_{Zn}$* refer to the number of moles of the dopant source and zinc source introduced in the CBD growth solution, respectively. As such, any doping percentage given represents the ratio between the dopant and zinc precursors in the NW growth solution. The actual values of the doping are expected to be lower the nominal values[207, 246, 247]. The discussion in this chapter will be provided on a comparative basis and, therefore, no accurate quantification of the exact doping values is provided. This quantification is challenging to assess and it was not deemed essential for the purpose of the discussion.

6.2 Copper-doped ZnO nanowires

Doping ZnO NWs with copper has two main influences, particularly in the growth kinetics of the NWs and in their optoelectronic properties. As such, the morphological properties of Cu-doped ZnO NWs were studied using scanning electron microscopy (SEM) to understand the influence that different copper doping levels have on the dimensions of the as-grown NWs. Cu-doped ZnO NWs were grown on seed layers deposited with ALD following the deposition conditions of sample S2 in Chapter 5.2. The NWs were grown using a 50 mM equimolar concentration for both reagents, with a growth time of 24 hours. The copper doping was integrated during growth as detailed in Chapter 4.5.1. The nominal doping levels studied were 2%, 5%, 10% and 20%, with the aim of understanding the influence that these

different levels have on the optoelectronic properties of the ZnO NWs towards improving their functional performance in photoelectrochemical water splitting. Figure 6.1 shows the top-view (Figure 6.1a) and cross-section (Figure 6.1b) SEM of the 10% Cu-doped ZnO NWs. It can be observed that the NWs maintain the characteristic hexagonal shape of ZnO NWs for the most part, with a diameter of 503±180 nm and a NW density of ~2.2 μm^{-2}. The length of these NWs, extracted from the cross-section image in Figure 6.1 b, was 4.4±0.3 μm. The diameter of these NWs is the largest obtained so far, even for a long growth time of 24 hours. This indicated that the presence of copper in the growth has a direct influence in the morphology of the as-grown NWs by which it increases the size of the ZnO nanomaterial. Considering the large size of the NWs here obtained, a term more correct to refer to them would be microwires, although the term nanowires will still be used for simplicity.

To assess the optoelectronic properties of the Cu-doped NWs, ultraviolet-visible spectroscopy (UV-vis) and photoluminescence (PL) were utilised. The UV-vis study is shown in Figure 6.2a and it shows how there is a large difference in the light absorption as the Cu-doping increases. The 2% Cu-doped NWs show a very sharp absorption feature starting at 450 nm that reaches its peak at 375 nm. Overall, the absorption shown by this sample in the UV-near blue region is larger than that of undoped ZnO. Attending to the 5% Cu-doped ZnO NWs, their absorption is larger than that of the ZnO NWs for the whole visible range and in the UV region down to 340 nm. From 340 nm to 300 nm, the undoped ZnO NWs show a larger absorption.
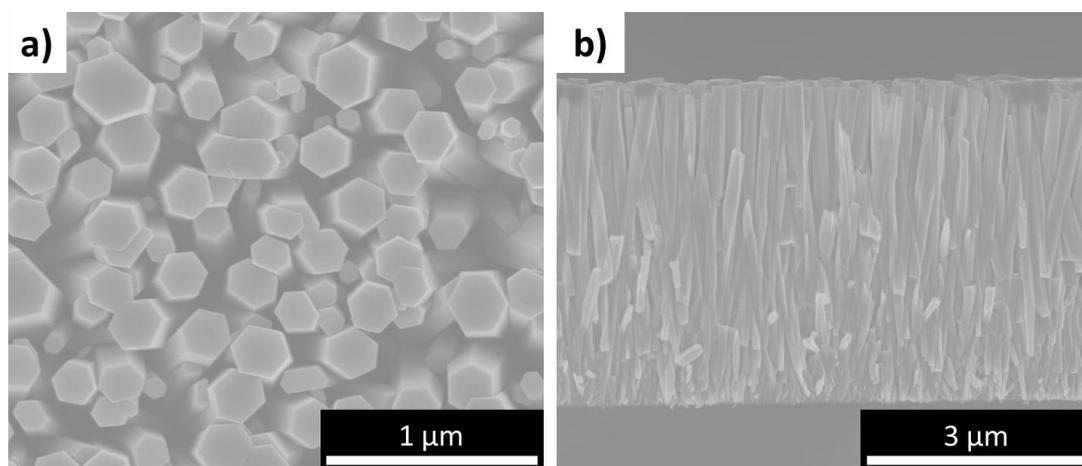
Figure 6.1. a) Top-view and **b)** cross-section scanning electron micrograph of 10% copper-doped ZnO nanowires, showing the typical hexagonal shape characteristic of ZnO nanowires.

Considering the 10% and 20% Cu-doped ZnO NWs, their light absorption properties are much lower in absolute value for almost the whole range of the experiment compared to the undoped NWs or those with a lower copper concentration, indicating that there is a maximum in the copper doping level at which the light absorption properties of the NWs are as good as possible. Nonetheless, no significant shift or considerable increase in the light absorption was observed for these samples, hinting at the possibility that this approach may not yield the best possible results with regards to the doped ZnO NWs.

Photoluminescence spectroscopy analysis (Figure 6.2b) was carried out to obtain a better understanding of the optoelectronic properties of the Cu-doped ZnO NWs. For the undoped NWs, the PL shows a narrow peak centered at around 370 nm attributed to the near bandgap emission of ZnO. This wavelength corresponds to 3.35 eV, which is in good agreement with the theoretical values of the ZnO bandgap provided in the literature review of Chapter 3. As the Cu doping level is increased, there is a slight shift of the bandgap signal towards higher wavelengths, i.e., lower energies, indicating that increasing concentrations of Cu doping lead to a red-shift of the bandgap. This is evidenced by the tail of the bandgap peak in the low energy region. Here, it can be observed that adding 2% Cu doping does not induce any meaningful change in the bandgap. However, for 5% and 20% there is an evident red-shift of around 15 nm, with the 10% Cu-doped NWs yielding a red-shift of 8 nm. In addition, the 10% and 20% samples show a clear broadening of the bandgap peak compared to the other studied samples.
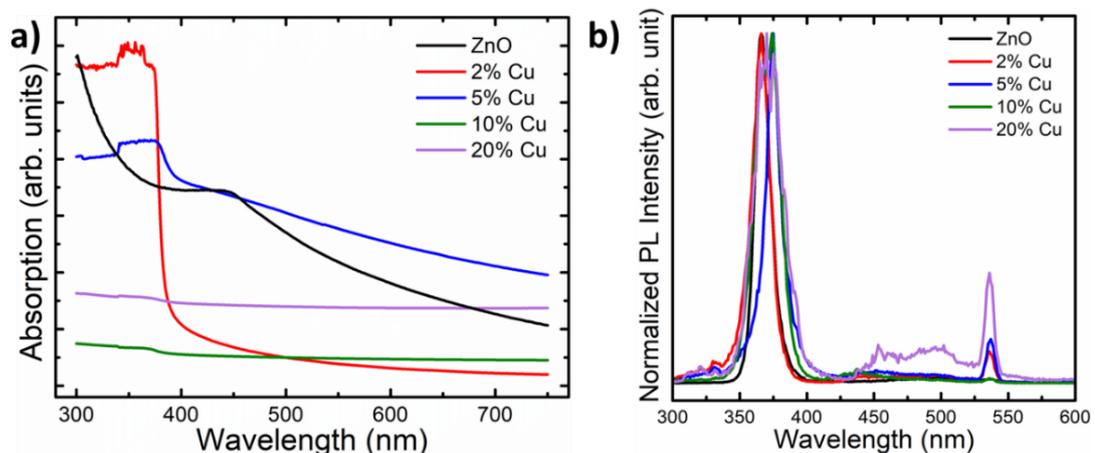
Figure 6.2. a) Ultraviolet-visible and **b)** photoluminescence spectroscopic analysis of undoped and copper-doped ZnO nanowires.

Finally, there is another peak centered at around 540 nm that can be attributed to the characteristic defects of ZnO, also discussed in Chapter 3. The importance of this defect peak increases with increasing doping level, achieving its maximum at 20% Cu-doping level. The 10% Cu-doped NWs do not follow this trend. All in all, while copper doping induced a clear red-shift in the bandgap signal for doping level above 5%, it also showed a very poor optical absorption in the UV-vis spectroscopy analysis at those doping levels[170, 171]. This indicates the possibility that, while the energy barrier of the bandgap can be reduced, the optoelectronic properties of the NWs may not be greatly enhanced and, therefore, no further analysis on using copper as a ZnO dopant were carried out. Instead, the focus was shifted towards cobalt.

6.3 Morphological study of cobalt-doped ZnO nanowires

Cobalt doping was integrated in the ZnO NWs during the CBD process using textures seed layers deposited with both ALD and sol-gel processing. A detailed morphological study of the growth of Co-doped ZnO NWs with different cobalt levels is provided to discuss the influence that the substitutional cobalt has on the growth kinetics. This is followed an extensive investigation of the optoelectronic properties of the Co-doped ZnO nanowires in which ultraviolet-visible spectroscopy (UV-vis), photoluminescence (PL), cathodoluminescence (CL) and fast-transient absorption spectroscopy (FTAS) were utilised to detail the electronic band structure, carrier dynamics and defect density that cobalt influences in the ZnO NWs.

Cobalt-doped ZnO NWs were grown on seed layers deposited with ALD and sol-gel processing to determine whether the seed layer deposition technique had any influence in the growth of the Co-doped NWs, akin to what was discussed in Chapters 5.2 and 5.4. For the ALD-based seed layer, the deposition conditions were 250°C, 250 cycles with a pulse train 0.05-7-0.2-10 seconds, with the first two being the pulse and purge times for diethylzinc and the last two being those of water. The CBD growth time was set at 24 hours and the concentration of the reagents at 50 mM for the Zn^{2+} and OH^- sources. Nominal doping levels of 1%, 10%, 20 % and 35% were used for the ALD seed layer based Co-doped ZnO NWs. Figure 6.3a shows vertically aligned 1% Co-doped NWs with a size similar to the one previously shown for a 24 hours growth in Chapter 5.3. This indicates that low amounts of cobalt doping do induce significant

Figure 6.3. Top-view scanning electron micrographs of ZnO nanowires grown on seed layers deposited with atomic layer deposition and doped with different levels of cobalt. **a)** 1%, **b)** 10%, **c)** 20% and **d)** 35%. **e)** Cross section image of the 10% Co-doped ZnO nanowires. **f)** Comparative plot of the nanowire diameter and density for different levels of cobalt doping. The dashed lines are included for clarity purposes.

changes in the dimensions of the NWs. The average diameter of these NWs was 109 nm with a size distribution of ±26 nm and a NW density of ∼22 μm^{-2}. Their shape is also akin to the aforementioned NWs, with the presence of different shapes other than the characteristic hexagonal prism shape of wurtzite phase ZnO NWs being

168

attributed to the large diameter of these NWs. As the cobalt doping was increased to 10% (Figure 6.3b) and 20% (Figure 6.3c), the diameter of the NWs was reduced to 101±38 nm and 91±36 nm, respectively. This is in accordance with the results presented by Godavarti et al.[248] A possible explanation for this reduction in the diameter is related to the smaller atomic radius of Co compared to Zn, although this hypothesis was not explored, as it was not considered within the scope of this work. The NW density for these two samples rose from ~22 μm^{-2} for 1% Co to ~47 μm^{-2} and ~58 μm^{-2} for 10% Co and 20% Co, respectively, following the expected trend. Once the doping was increased to 35% (Figure 6.3d), a drastic change in the morphology of the NW film was observed. The diameter increased considerably, going from 91±36 nm for 20% Co to 145±54 nm for 35%, more than a 50% increase, that resulted in an almost continuous thick film, instead of the typical array of clearly distinguishable ZnO NWs. As a result of the enlargement of the NW diameter when the doping was increased from 20% to 35%, the NW density was reduced in half, from ~58 μm^{-2} to ~29 μm^{-2}, respectively. A typical cross-section SEM of these Co-doped ZnO NWs (for 10% Co in this case) is provided in Figure 6.3e. These NWs show an average length of 4.5 μm, attributed to the long growth time used for this sample. No comparative study of the lengths of these NWs was made, as it was assumed that their lengths would be comparable based on the equal CBD conditions. The NW diameter and density trends here described are clearly displayed in Figure 6.3f.

Cobalt-doped ZnO NWs with doping levels of 1%, 5%, 10% and 20% were grown on sol-gel deposited seed layers on indium tin oxide (ITO) substrates. These NWs were grown for 6 hours with an equimolar reagent concentration of 25 mM. The 1% Co-doped ZnO NWs (Figure 6.4a) show NW diameter and density of 45±23 nm and ~25 μm^{-2}, respectively, which are comparable to the results obtained for the NW growth shown in Chapter 5.4. The large size distribution is attributed to the presence of two distinct ZnO NWs types, thinner and tapered and larger and prismatic. The large variety of growth orientations of these samples is considered to be the source for the low NW density. These two characteristics of ZnO NWs grown on sol-gel deposited seed layers were also discussed in Chapter 5.4. As the cobalt doping was increased to 5% (Figure 6.4b), the size of the NWs increased from 45±23 nm for 1% to 54±22 nm for 5%, while maintaining the same ~25 μm^{-2} NW density. Further
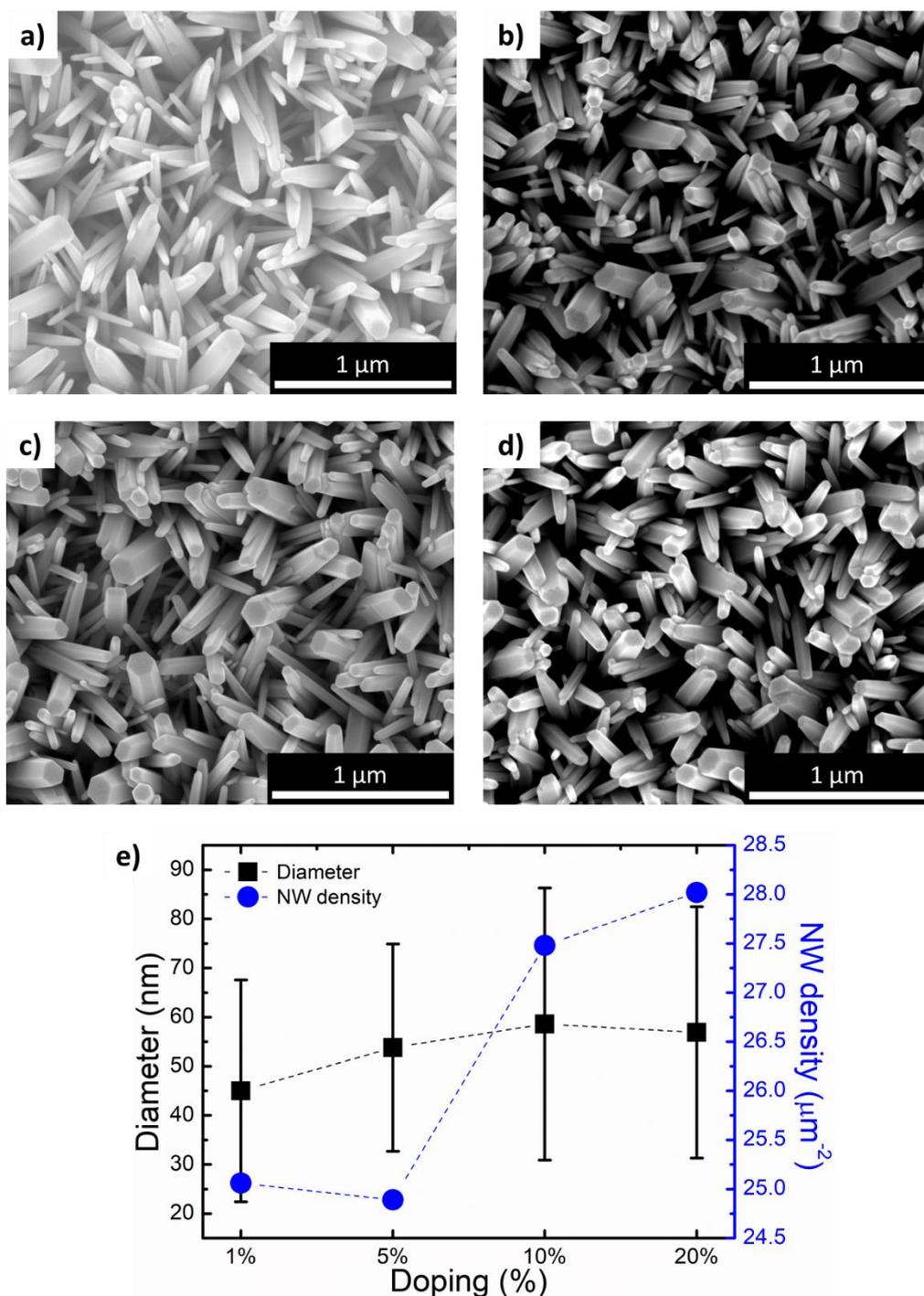
Figure 6.4. Top-view scanning electron micrographs of ZnO nanowires grown on seed layers deposited by a sol-gel process and doped with different levels of cobalt. **a)** 1%, **b)** 5%, **c)** 10% and **d)** 20%. **e)** Comparative plot of the nanowire diameter and density for different levels of cobalt doping. The dashed lines are included for clarity purposes.

increasing the cobalt doping to 10% (Figure 6.4c) resulted in NWs with a diameter of 57±28 nm and an increased NW density of $\sim$27 μm^{-2}. Finally, the 20% Co-doped ZnO NWs (Figure 6.4d) have a diameter of 57±26 nm and a density of $\sim$28 μm^{-2}.

For all doping levels, the two different types of NWs (tapered and prismatic) are present. The NW diameter and density trends are shown in Figure 6.4e. These trends do not follow what was previously seen in Figure 6.3. The reason for this is attributed to the two distinct types of NWs that do not follow the expected trend. No comparison between the NWs grown on ALD and sol-gel seed layers is made as the CBD growth conditions were not comparable.

6.4 Optoelectronic analysis of cobalt-doped ZnO nanowires

A comprehensive and thorough study of the cobalt doping influence on the optoelectronic properties of the ZnO NWs was carried out so the possible functional applications of these doped-NWs could be developed. For this, a set of spectroscopic techniques, namely ultraviolet-visible spectroscopy (UV-vis), photoluminescence (PL), cathodoluminescence (CL) and fast-transient absorption spectroscopy (FTAS) were utilised. All optical analyses were performed on the samples grown on ITO substrates and sol-gel deposited textured seed layers. The theoretical basis for the spectroscopic analytical techniques was provided in Chapter 4.10.

6.4.1 Ultraviolet-visible spectroscopy analysis

UV-vis spectroscopy analysis was carried out on Co-doped ZnO NWs with doping levels of 1%, 5%, 10% and 20% and the results compared with pristine ZnO (Figure 6.5a). The displayed absorption is in absolute values. It can be seen that only the 1% Co-doping increased the absorption over the pristine ZnO NWs. As expected for ZnO, the main absorption of the NWs is in the blue-near UV region, between 300 nm and 400 nm. The 1% Co also shows a shoulder in the absorption at 400 nm (marked by the red arrow), indicating a red-shift or enhancement of the light absorption at longer wavelengths. A red-shift is a shift of the bandgap energy level towards lower energy regions. The red-shift for the 1% Co-doping sample was confirmed by means of photoluminescence spectroscopy. Regarding the part of the spectra corresponding to the higher wavelength region (500 nm to 750 nm), it is proposed that the signal that is observed does not directly correspond with light absorption and, instead, it was attributed to the scattering of the visible light caused by the randomly aligned network of ZnO NWs[249]. Therefore, it is not expected that the Co-doped ZnO NWs will be photoactive in this higher wavelength region.
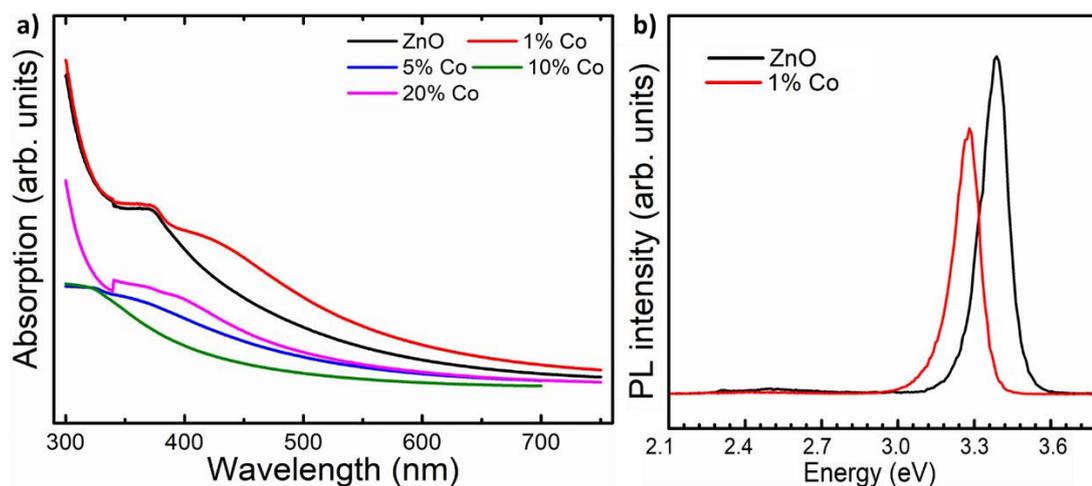
Figure 6.5. a) Ultraviolet-visible spectroscopy of undoped and Co-doped ZnO nanowires with doping levels from 1% to 20%. **b)** Photoluminescence spectroscopy of undoped and 1% Co-doped ZnO nanowires, showing a clear red-shift in the bandgap emission.

The PL spectra of Figure 6.5b shows the emission of undoped and 1% Co-doped ZnO NWs. The peaks presented correspond to the bandgap of the two samples, with that of the undoped ZnO centered around 3.4 eV and that of the 1% Co-doped centered at 3.25 eV. Comparing the positions of these two peaks, the position of the bandgap peak for 1% Co is shifted towards lower energies, compared to that of the undoped NWs, confirming the red-shift in the bandgap energy. UV-vis and PL spectroscopy provided useful information for the analysis of the optoelectronic properties of the Co-doped ZnO NWs. Nonetheless, additional characterization was required to fully understand the effects that Co-doping has on the properties of ZnO.

6.4.2 Fast-transient absorption spectroscopy study

As no red-shift was observed for Co doping levels other than 1%, FTAS was utilised to assess the possible red-shift for higher doping levels, as well as to understand the carrier dynamics of the Co-doped ZnO NWs. The FTAS measurements were carried out in a pump-probe setup, as described in Chapter 4.10.2. This spectroscopic technique was used for samples with 1%, 5% and 20% Co-doping, as well as undoped ZnO NWs; 1% Co was chosen as the benchmark value, while 5% and 20% doping levels were used to understand the influence of higher-level cobalt doping. The results from these experiments are provided in Figure 6.6. The false colour maps of the undoped, 1%, 5% and 20% Co-doped ZnO NWs, shown in Figure 6.6a,b,e,f, respectively, are a representation of the changes in the absorption of the material

(ΔA) as a function of the energy and time. Changes in ΔA can be registered as either ground state bleaching (for negative ΔA), which indicates the depletion of the ground state carriers to excited states, or as further excitation (for positive ΔA). Hence, changes in the ΔA false colour maps are interpreted in terms of carrier dynamics. The unit used to measure the change in the absorption are optical density (OD), which represents the optical attenuation of the material, i.e., the amount of light transmitted through the material.

For the undoped NWs, there is a negative ΔA signal centered at 3.3 eV in the false colour map, which is interpreted as an absorption bleaching peak that corresponds with the theoretical value of the bandgap of ZnO. Time dependent analysis of this absorption bleaching was carried out to understand the dynamics of the depletion of the ground state carriers. The time dependent bleaching signal study is shown in Figure 6.6c. Here, it is shown that the absorption bleaching signal reaches its maximum value at 5 ps, indicating a fast depletion of the valence band. The small narrow peak at ~2.25 eV is an experimental artefact due to the second order of the pump laser in the monochromator and is not a real signal; this signal is also observed for the other spectra in Figure 6.6. The absorption bleaching reaches zero at about 2.5 eV, indicating carrier activity for a region of almost 1 eV. Figure 6.6 b shows the false colormap of ΔA for the 1 % Co-doped ZnO NWs. There is a negative ΔA signal centered at 3.18 eV that is identified as an absorption bleaching peak. Comparing this bleaching peak with the one obtained for the undoped ZnO NWs, it can be seen that the signal has shifted to a lower energy region (from 3.3 eV to 3.18 eV), corresponding with the previously discussed red-shift induced by the cobalt doping. The time dependent analysis of this bandgap bleaching presented in Figure 6.6 d shows that the negative absorption bleaching tail extends over the entire probe range, while achieving the maximum at the 1 ps time, faster than for the undoped ZnO. In addition, the bleaching signal is observed in the whole spectral range.

The FTAS false colour map of the 5% Co-doped ZnO NW sample is shown in Figure 6.6 e. No clearly defined bandgap bleaching signal for the whole time scale is observed for this sample, in contrast with what was observed previously. Nonetheless, there were three small traces centered at 3.25 eV, 3.05 eV and 2.97 eV
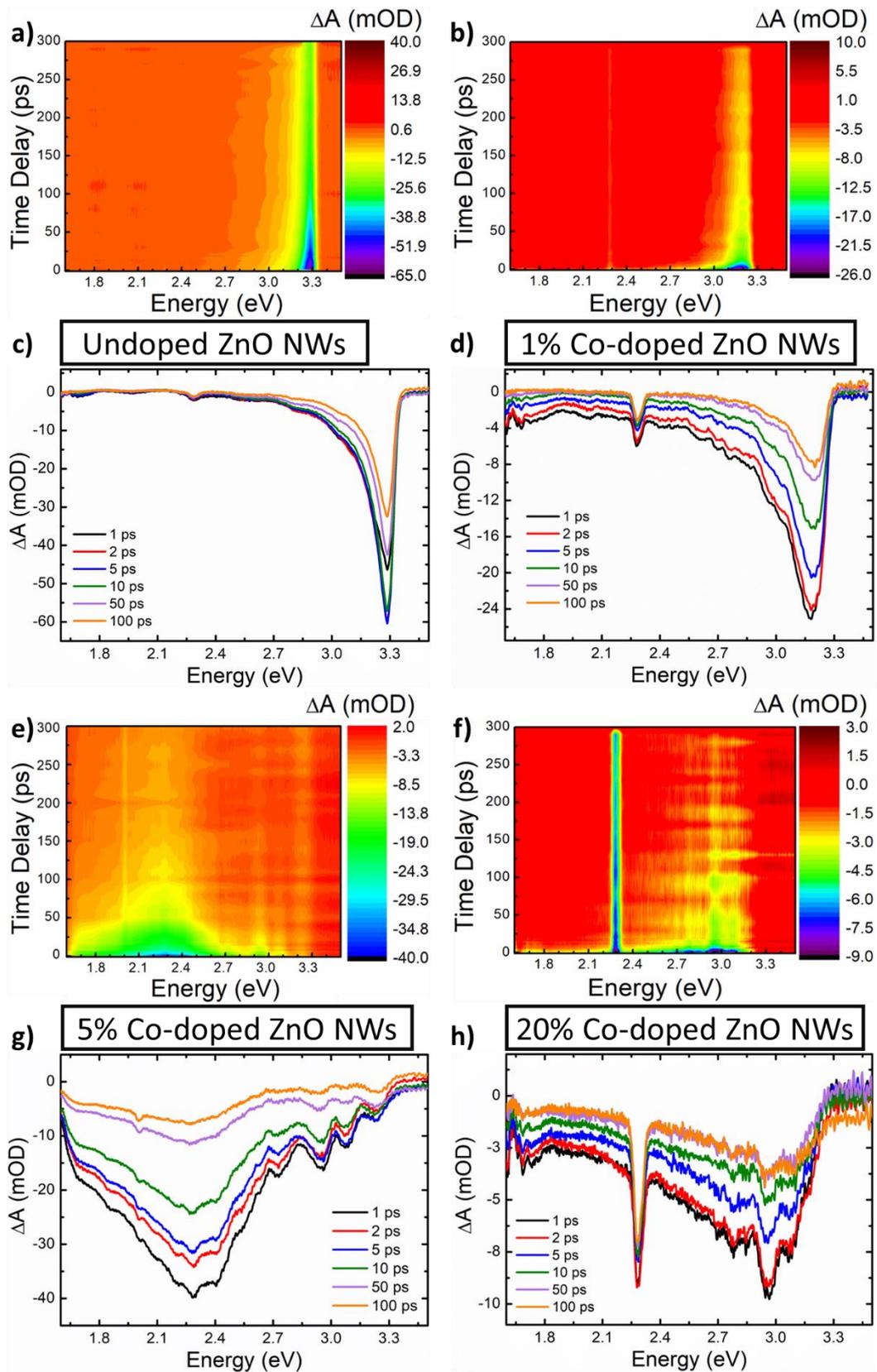
Figure 6.6. Fast transient absorption spectroscopy measurements of undoped, 1%, 5% and 20% Co-doped ZnO nanowires. For each samples, the 2D false colour map of ΔA and the time dependent absorption bleaching are provided for **a), c)** undoped, **b), d)** 1% Co-doped, **e), g)** 5% Co-doped and **f), h)** 20% Co-doped ZnO nanowire samples.

that were attributed to the ZnO and the effect of the Co-doping. In addition, a wide absorption bleaching signal centered at around 2.3 eV was observed. This signal was attributed to the presence of surface defects typical of ZnO[250]. Accordingly, the time dependent analysis of the bandgap bleaching shown in Figure 6.6g showed that the maximum of the large defect-related signal was reached at 1 ps, similarly to the 1% sample. More work was required to better understand this signal centered at around 2.3 eV, as it is shown in a later section of this chapter. Moreover, further work would be required to understand the origin the behaviour here observed for the 5% Co-doped sample to ascertain the origin of this behaviour and whether it was due to an experimental error or not.

The false colour map for the 20% Co-doped ZnO NWs is shown in Figure 6.6f. Here, a ΔA negative signal, interpreted as an absorption bleaching peak, is centered around 2.9 eV. This is proof that increasing levels of cobalt doping lead to further a red-shift in the bandgap bleaching signal. However, at 20 % doping, the absolute value of the ΔA is an order of magnitude smaller. Considering the time dependent absorption bleaching (Figure 6.6h), it can be seen that the maximum is achieved at a 1 ps delay time, the same as the other doped samples. Due to the low intensity of the bleaching signal, the one derived from the second order of the pump can also be clearly seen. Finally, the absorption bleaching is extended to the entire probe region, an effect previously attributed to the cobalt doping of the ZNO NWs. These results show that the introduction of Co-doping in the ZnO lattice induces a red-shift of the near bandgap edge (NBE) emission, red-shifting the bandgap towards lower energies. In addition, the cobalt doping seems to hasten the carrier dynamics of the NWs as observed in the time dependent analysis of the undoped and Co-doped NWs, in which it was observed that the doped NWs achieved maximum bleaching faster than the undoped NWs.

In order to obtain a better understanding of the carrier dynamics of the undoped and Co-doped NWs, Figure 6.7 shows the temporal dependence of the absorption bleaching signal at different probe energies, along with an estimation of the time constants that govern the decay of the carriers after being excited with the pump. This further analysis of the FTAS measurements was carried out for the undoped, 1% and 20% Co-doped NWs. The 5% sample was excluded from this

additional analysis as it was believed that the estimations provided may not accurately represent the reality due to the abnormally low signal observed in the FTAS false colour map of Figure 6.6e. The time dependence of all three samples studied (Figure 6.7a,c,e) for different probe energies followed the same expected trend by which the lower the probe energy, the larger the recovery of the ΔA signal was. These changes in ΔA are directly correlated with the decay of the absorption bleaching signal, which gives information regarding the carrier dynamics and their evolution over time.

The decay of the absorption bleaching was fitted with a multiexponential curve model with three different decay constants, τ_1, τ_2, and τ_3, to provide a quantitative idea of the improvement of the carrier dynamics after cobalt doping. These fits were carried out at probe energies around the value of the bandgap observed in the FTAS
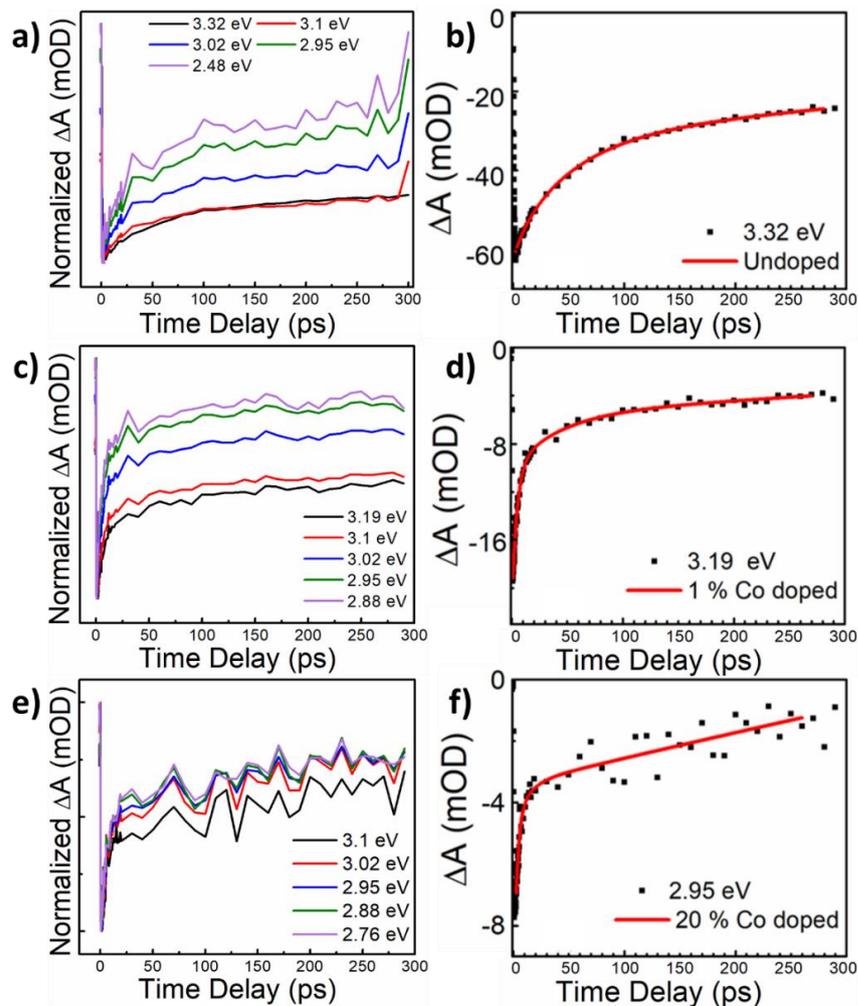
Figure 6.7. Time dependence of the absorption bleaching signal at different probe energies for **a)** undoped, **c)** 1% and **e)** 20% Co-doped ZnO nanowires. Experimental data (black dots) and best fitting model (red lines) for the decay of the absorption bleaching signal for **b)** undoped, **d)** 1% and **f)** 20% Co-doped ZnO nanowires.

false colour maps (indicated in the respective plots), hence the 5% Co-doped sample was not included. It was observed that the shortest decay time (τ_1), which corresponds to the initial rise of the fitting curves, depended on the probe energy, as evidenced by the change between undoped and 1% Co-doped NWs (Figure 6.7b,d, respectively). A similar observation was made in ZnO thin films by Bauer et al.[251] The fit of ΔA for the undoped ZnO NWs (Figure 6.7b), at 3.3 eV, indicates multiple decay paths with τ_1 = 20 ± 6 ps and τ_2 = 99 ± 18 ps. These two decay times relate to non-radiative recombination of charge carriers. The longest time constant, τ_3, although included in the fitting was not determined within the precision of the 300 ps wide temporal window, and has been assigned to the radiative recombination time. The analysis of this τ_3 decay constant is discussed later in this chapter. In the nominally 1% Co-doped sample (Figure 6.7d) a decrease of both τ_1 and τ_2, being τ_1 = 5.4±0.5 ps and τ_2 = 82±14 ps was observed, indicating faster carrier dynamics. For 20% Co-doped ZnO NWs (Figure 6.7f), the decay constants obtained from the fitting were further reduced to τ_1 = 4.7±0.7 ps and τ_2 = 32±14 ps.

The reduction of the τ_1 and τ_2 decay time constants, along with the red shift of the bandgap related absorption bleaching signal, were attributed to an increased sp-d exchange interaction in the presence of Co^{2+}, leading to positive and negative corrections to the energy of the valence and conduction band edges, respectively[252, 253]. These positive and negative modifications are the direct cause for the red-shift of the bandgap of the Co-doped ZnO NWs with respect to the undoped ZnO by narrowing the energy gap between the valence and conduction band. Furthermore, the faster decay times also indicate faster carrier dynamics that correlate with the previous observations of Figure 6.6. The faster carrier dynamics could be beneficial for optoelectronic applications in which the fast transmission of carriers can enhance the functional performance of a device.

Figure 6.8 shows a summary of the results of the carrier dynamics study carried out for the undoped, 1% and 20% Co-doped ZnO NWs. Figure 6.8a shows the evolution of the decay time of the absorption bleaching signal with time for the three samples. It is shown how increasing the cobalt doping resulted in faster carrier dynamics, as previously discussed. To further this analysis, the energy-dependence of the faster component of the decay time, τ_1, is shown in Figure 6.8b for the three

177
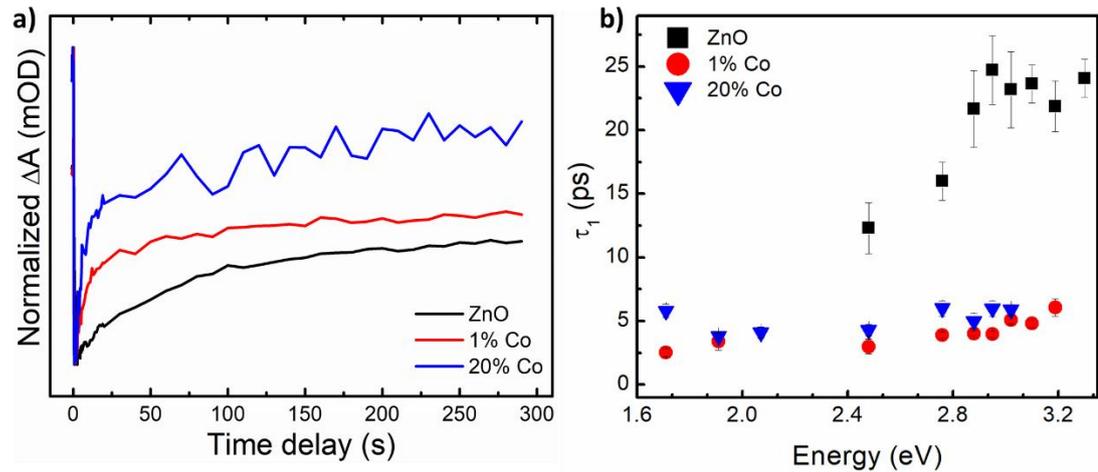
Figure 6.8. Summary of the fast transient absorption spectroscopy results for undoped, 1% and 20% Co-doped ZnO nanowires, showing the **a)** time dependent normalized ΔA and **b)** energy dependence of the fast component of the decay time, τ_1.

studied samples. There is a clear difference between undoped and Co-doped ZnO NWs by which τ_1 is remarkably lower for the doped samples than for the undoped ZnO NWs. This difference is an indication of increased carrier trapping in the doped samples that hastens the carrier dynamics. Johnson et al.[254] observed, for high excitation intensities, a sub-picosecond decay component and a slow decay component between of about 30-70 ps. This fast-sub-picosecond decay component was also observed by Sun et al.[255] for high excitations. In contrast, this sub-picosecond decay component was not present in our experiments. The lack of this component in this work was thus attributed to the formation of stable excitons, in line with the large exciton binding energy of ZnO. The trapping of carriers resulting from the fast τ_1 component for doped samples was attributed to an increased density of oxygen vacancies in the NWs as a result of the Co-doping.

It was previously discussed in Chapter 3.2 that ZnO has native defects, with oxygen vacancies being the most common. Oxygen vacancies in particular exist in three different states, namely neutral (V^0_O), singly charged (V^+_O) and doubly charged (V^{++}_O)[250] and their number density can be further increased by the addition of cobalt as dopant agent, as reported by Sett et al[256]. Therefore, the increasing amounts of cobalt doping will generate a higher concentration of oxygen vacancies that, in turn, will hasten the fast τ_1 component of the decay time, as shown in the results of Figure 6.8.

6.4.3 Spatial cathodoluminescence analysis

To further the investigation on the optoelectronic properties of Co-doped ZnO NWs, spatial CL was used as an analytical tool to study whether there was any spatial dependence of these properties for the doped NWs. For this, CL experiments were carried out in a CL system coupled with an SEM, as described in Chapter 4.10.4. This CL analysis was carried out for undoped, 1%, 5% and 20% Co-doped NWs. Before going into the detailed spatial CL mapping, the normalized CL spectra of the four samples over a whole NW are shown in Figure 6.9g. For the undoped NWs, this CL spectrum consists of a narrow UV peak centered at 3.28 eV and a broader peak in the green-orange region, centered around 1.9 eV. Considering the previous analyses shown in this chapter, the narrow UV peak was attributed to the excitonic, near bandgap emission (NBE), while the broadband peak spanning from 2.7 eV to 1.5 eV was considered to be linked to emissions related to different defects[257, 258]. This was correlated with other reports in the literature[207]. The CL spectra of all the Co-doped NWs are similar to those of the undoped NWs, albeit they differ in the relative intensity between the excitonic and the defect-related emission. Based on the literature, the defect-related emission, as discussed previously, was attributed to the oxygen related defects, particularly oxygen vacancies[250, 259]. In ZnO films, previous reports have shown that increasing levels of Co-doping result in a higher contribution of the defect-related band and a reduction of the luminescence from the excitonic recombination[260]. In these samples, only the higher contribution to the defect-related band was observed.

After determining the CL response of the undoped and Co-doped NWs, the CL spatial maps were obtained for 1% and 5% Co-doped NWs. The SEM micrographs of the analysed NWs are shown in Figure 6.7a,d, with the respective panchromatic CL maps presented in Figure 6.9b,e, obtained under identical excitation conditions. To obtain these panchromatic CL maps, the luminescence from each pixel was measured and subsequently integrated with the SEM image. For both panchromatic maps it can be seen that the CL intensity is stronger at the centre of the NW and diminishes towards the edges. In addition, a decrease in the relative intensity of the CL signal obtained from the 1% and 5% Co-doped NWs can be observed, which corresponds
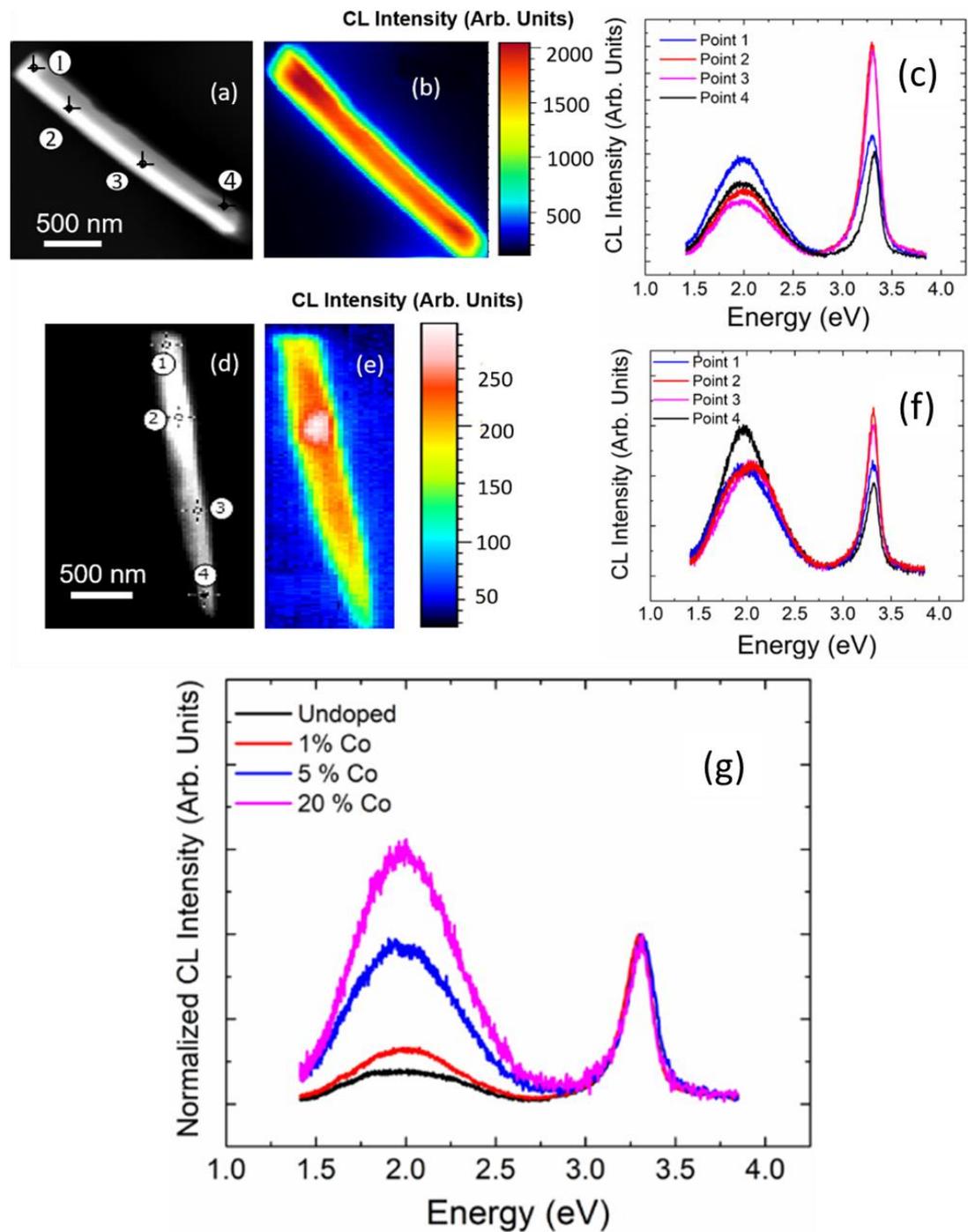
Figure 6.9. a), d) Scanning electron micrograph, **b), e)** panchromatic cathodoluminescence image and **c), f)** localized cathodoluminescence spectra of 1% and 5% Co-doped ZnO nanowires, respectively. The numbers in **a)** and **d)** indicate the points in which the cathodoluminescence spectra in **c)** and **f)** were taken. **g)** Normalized cathodoluminescence spectra, averaged over an entire nanowire, for undoped and 1%, 5% and 20% Co-doped ZnO nanowires.

with what was previously observed in the FTAS analysis. Nonetheless, it can be seen that the CL intensity is homogeneous along the whole length of the NW for both samples, indicating that the Co-doping should be homogeneously distributed in the doped NWs. There is an exception to this, which is the bright spot observed in the

central region of the 5% Co-doped NW. This spot was attributed to a possible local accumulation of electrons from the electron beam, indicating a possible heterogeneous section within the 5% Co-doped sample that would require further analysis in future work.

To accurately assess the real spatial distribution of the CL across and along the NWs, four points were selected on each SEM image (points 1-4 in Figure 6.9a,d) and the corresponding CL spectrum was extracted for each point. The results are shown in Figure 6.9c,f for the 1% and 5% Co-doped ZnO NWs, respectively, with the intensity values being as extracted from the system, without any normalization. The 1% sample shows a clear difference between points 1 and 4 and points 2 and 3 in the near bandgap edge emission peak by which the latter set shows a higher intensity in this region compared to the former set. This can be attributed to the placement of point 2 and 3 with regards to the panchromatic map, as these two seem to be in a more central region than the other two. This central region is where the highest CL intensity was achieved. Regarding the defect-related band, all points have a similar intensity with the exception of point 1, which showed a slightly higher intensity than the rest. However, this was considered within the admissible experimental error. Considering the 5% Co-doped ZnO NW (Figure 6.9f), a similar situation to that described for the 1% occurs. Points 2 and 3 are within the central red region of the panchromatic map and, hence, the intensity of their near bandgap edge peak is larger than for the other two. The defect-related band shows a similar intensity for points 1, 2 and 3. However, point 4 is a clear outlier in which this defect band has a larger intensity than the NBE peak. This is the only instance that this behaviour is observed and it may be attributed to the fact that point 4 was taken close to the bottom edge of the NW, which could possibly present a higher concentration of defects.

In order to further the insight on the distribution of the NBE and defect-related peaks on a single NW, the hyperspectral CL maps of a 1% Co-doped ZnO NW are shown in Figure 6.10. These two maps depict the energy level of the NBE (Figure 6.10a) and the defect-related broad band (Figure 6.10b). The UV peak is present mostly in the region between 3.31 eV and 3.325 eV, in good agreement with the CL presented earlier, while the defect-related one is mostly localized between 1.91 eV and 1.89 eV. The energy range for both peaks is very low, spanning 40 meV for the
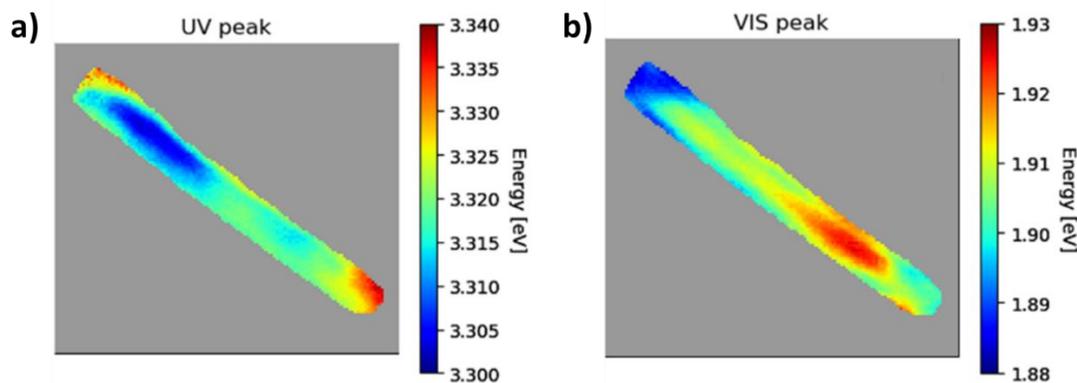
Figure 6.10. Hyperspectral cathodoluminescence map of a 1% Co-doped ZnO nanowire, showing the **a)** near bandgap edge emission peak and **b)** defect-related broad band peak.

UV peak and 45 meV for the defect-related one, indicating good homogeneity across and along the NW. Significantly, it can be observed that the regions where the energy of the UV peak is lowest correspond to the regions in which the defect-related one has its highest energy. This may be an indication of a larger density of surface defects in these regions, which might be directly related to a higher concentration of Co^{2+} ions substituting Zn^{2+} in the ZnO lattice. Nonetheless, further analysis would be required to prove this theory.

The results shown here demonstrate that ZnO has two main excitonic peaks, one related to the near bandgap edge emission, centered around 3.3 eV, and a second, broader peak related to surface defects. The CL analysis demonstrates that the increase of the surface defects density with increasing doping is reflected in the larger intensity of the defect-related CL peak centered at around 1.9 eV. This correlates with the FTAS results obtained in which it was observed that the doping induced a broadening of the absorption bleaching signal, with a long tail that was prolonged down to 1.65 eV. To understand this influence in terms of the defects of ZnO, it is necessary to remark that the typical defects present in ZnO are vacancies, interstitials and antisites of both zinc and oxygen[261]. The broad emission centered around 1.9 eV observed in the CL analysis is usually assigned to the transitions related to oxygen vacancies and Zn interstitials[262, 263]. In this work, the relative increase of the broad band and, hence, of the density of oxygen vacancies and Zn interstitials is attributed to the substitution of Zn^{2+} by Co^{2+} in the ZnO lattice, which has a smaller ionic radii[184]. In addition, similar CL emissions to those described in this work,

attributed to oxygen vacancies, were also shown for ZnO that was co-doped with IIIa elements as donors or Li as an acceptor by N. Ohashi et al[264].

These results show how the optoelectronic properties of the ZnO NWs can be controllably tuned with the addition of cobalt doping, making this a promising approach to improve the functional performance of NW-based devices. As stated previously, this thesis aims at the development of photoanodes based on ZnO NWs for photoelectrochemical applications. Reports in the literature have shown that surface defects in ZnO and, particularly oxygen vacancies, play a very important role in the photocatalytic activity of ZnO, especially related with its efficiency in photoelectrochemical applications[265, 266]. In this chapter it has been demonstrated that adding cobalt as a dopant to ZnO enhances the absorption of visible light and increases the density of oxygen vacancies that can act as carrier trapping sites. In the CL maps shown earlier in this chapter it was observed that the lowest energy emission occurs at the surface of the NWs, suggesting that the Co-doped ZnO NWs have a higher number of surface defects and, therefore, it is expected that the Co-doping will lead to an improvement in the photoelectrochemical performance of the ZnO NWs. These results are discussed in Chapter 8.4.

A theoretical band diagram of the Co-doped ZnO NWs is proposed in Figure 6.11. From the FTAS measurements it was observed that the bandgap of ZnO (3.3 eV) was shifted to lower energies (3.19 eV) by the introduction of a nominal 1% Co-doping. This was a result of the introduction, by Co-doping, of localized sp-d states in the bandgap of ZnO that are directly related with the surface defects introduced by the substitution of Zn^{2+} with Co^{2+} and the sp-d exchange interactions between the electrons in the d orbital of cobalt and the sp energy level of ZnO[267]. These states are situated below the energy level of the conduction band and act a charge carrier trapping sites. In short, after the NWs are photonically excited, the photogenerated electrons will have two available excitation pathways, namely the conduction band of the Co-doped ZnO and the available sp-d states coming from the exchange interaction from the orbitals. This means that electrons of energies below that of the conduction band can also be excited and take part in a process other than the recombination with available holes, reducing the effective bandgap of the Co-doped ZnO NWs. In addition, as the sp-d states act as trapping sites for the photogenerated

183
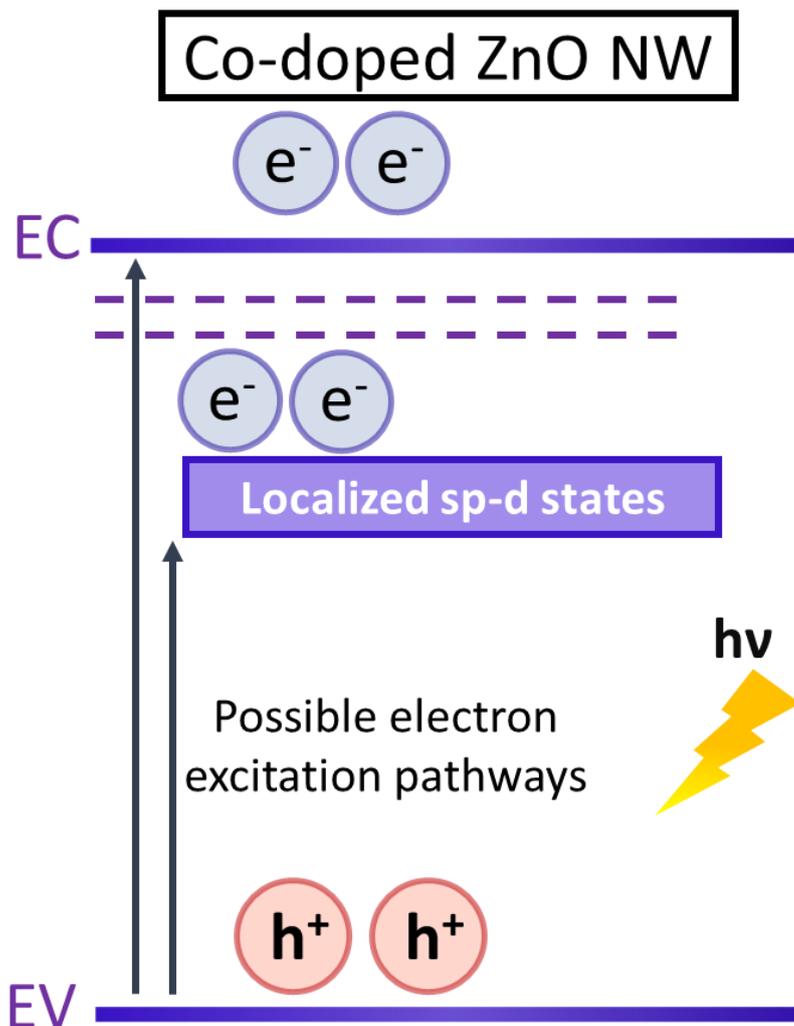
Figure 6.11. Theoretical schematic of the band structure of cobalt-doped ZnO nanowires, showing the presence of the localized sp-d states introduced in the bandgap of ZnO by cobalt doping and the valence and conduction band (EV and CV, respectively).

electrons, the charge separation of the Co-doped ZnO NWs is considerably improved, which is a critical effect on the photoelectrochemical performance of this material.

6.5 Conclusions

In this chapter, the results from a detailed study of doped ZnO NWs were presented and discussed. In particular, copper and cobalt were selected as the two dopant agents to be studied. The aim of this investigation was to determine whether the introduction of any of the two transition metals in the ZnO lattice would improve the optoelectronic properties of ZnO NWs and, if they do, what doping level was required for it. These analyses, which were based on optoelectronic spectroscopic techniques such as UV-vis, FTAS, PL or spatial CL, were carried out in a comparative basis

between the different levels of nominal doping and, therefore, no accurate quantification of the specific level of doping was determined for either of the dopants.

Copper-doped NWs were grown on seed layers deposited on ALD with doping levels from 2% to 20%. Morphological analyses using SEM showed that the introduction of copper resulted in a large increase in the diameter of the as-grown NWs, indicating a clear influence on the morphology during growth. With regards to their optoelectronic properties, the UV-vis analysis showed that 2% and 5% Cu-doped NWs had a comparable or better light absorption that the undoped ZnO NWs. Higher doping levels resulted in a considerable reduction of the light absorption and this result is detrimental for the functional performance of the NWs. The PL study showed two clear peaks, one centered at around 370 nm and related with the bandgap emission of ZnO and another, smaller, attributed to the defect band of ZnO. The intensity of the bandgap peak remained constant for increasing levels of doping, while that of the defect-related peak increased with higher doping level. This increase in the intensity of the defect band was an indication of an increasing concentration in the number of surface defects present in the ZnO NWs. In addition, it was observed that for doping levels higher than a nominal 2%, a clear red-shift between 8 nm and 15 nm was observed for the bandgap peak in the Cu-doped ZnO NWs. Even though some of the results obtained from this analysis showed promise, especially the red-shift observed in the PL analysis, the larger size of these NWs, along with the lack of any considerable improvement of the optoelectronic properties of the undoped ZnO NWs shifted the focus over the doping from copper to cobalt.

Cobalt-doped ZnO NWs were grown on seed layers deposited by both ALD and sol-gel processing. The doping levels used in this case ranged from 1% to 35%. There was a significant difference between the two seed layers on which the NWs grown. The sol-gel deposited seed layer yielded two different NW morphologies: one that followed the characteristic hexagonal shape of ZnO NWs and another that had tapered tips and a reduced diameter compared to the hexagonal ones. Other than that, no major disruptions in the morphology of the NWs were observed after integrating the Co-doping, as opposed to what was seen with Cu-doping.

UV-vis analysis of the Co-doped samples showed that a 1% Co-doping resulted in an improvement of the absorption of the light absorption in the visible region, starting from the 380 nm region with respect to undoped ZnO NWs. For the other doping levels studied (5%, 10% and 20%), the overall light absorption was remarkably worsened when the Co-doping was integrated. In order to understand whether there was any shift in the bandgap when the Co-doping was integrated, a PL spectroscopy study was carried out on undoped and 1% Co-doped NWs, which showed a red-shift of the bandgap, reducing it from 3.4 eV to 3.2 eV. Further optoelectronic investigations of the Co-doped NWs were carried in the form of FTAS analysis. This was carried out for undoped, 1%, 5% and 20% Co-doped NWs. these results showed how increasing the Co-doping level resulted in a further red-shift of the bandgap, being reduced down to 2.95 eV for the 20% Co-doped sample. Furthermore, it was demonstrated in time dependent analysis that the cobalt-doping hastened the carrier dynamics, achieving the maximum of the absorption bleaching signal at 1 ps mark, faster than what was observed for the undoped ZnO NWs. The faster carrier dynamics were further demonstrated by energy dependent analysis, in which the transient response at the energy of the bandgap for the respective samples was fitted to a multi-exponential model that contained three different decay times. The second component of the multi-exponential curve, which governs the carrier dynamics, showed a decrease in its value for the doped samples compared to the undoped NWs, further proving the faster carrier dynamics when the Co-doping was integrated. Regarding the first of the aforementioned components, it was shown that this time constant was also faster for the doped samples, which was attributed to increasing charge carrier trapping in the doped samples, indicative of a higher density of surface defects and, particularly, oxygen vacancies. The results obtained from the analysis here discussed were ascribed to a strong exchange interaction between the sp orbitals of ZnO and the d orbitals of cobalt that induced the presence of a set of localized states in the bandgap of ZnO, below the conduction band, that acts a carrier traps, while reducing the effective bandgap of the Co-doped ZnO NWs.

Spatial cathodoluminescence analyses were carried out to investigate in more detail the spatial distribution of the bandgap and defect-related peaks as well as to better understand the defects in the doped NWs. From the general CL analysis it was

observed that increasing the Co-doping level resulted in an increase of the intensity coming from the broad defect-related band, while that of the near bandgap edge emission remained the same. Spatial CL mapping was used to assess whether the NWs were homogeneous in their emission or the contrary. It was determined that the central region of the single NWs analysed had a higher CL intensity while the outer regions close to the edge showed a lower intensity. It was also observed that the NBE and defect-related peaks had a rather homogenous distribution along and across a single 1% Co-doped NW. Interestingly, it was observed that the regions where the intensity of the NBE peak was lowest, the defect-related peak had its highest intensity. The same occurred the other way around.

Given the high surface-to-volume ratio of NRs, their surface plays a more important role than in thin films or bulk. This is reflected in the photoresponse of the Co-doped ZNO NWs as the two excess electrons associated with an oxygen vacancy can also help improve the photoelectrochemical activity and, thus, the functional performance of doped NW-based devices. Therefore, this effect, along with the rest of the optoelectronic characterization, served as base to confidently state the Co-doping will be beneficial for the photocatalytic activity of ZnO NWs. To summarize the benefits obtained from this doping, a theoretical band structure model was also included, where all these benefits are highlighted.

Chapter 7

Surface functionalization of ZnO nanowires

7.1 Introduction

This chapter describes the results obtained from a study of the growth and characterization of two different methods to functionalize the surface of ZnO nanowires (NWs). The two methods refer to two different materials used as the functionalizing materials, namely iridium and a metal-organic framework (MOF). The theoretical basis for functionalization with these two types of materials was provided in Chapter 3.7. The first part of the chapter deals with the integration of iridium with ZnO NWs. This integration was envisioned as a way to enhance the functional performance in photoelectrochemical water splitting. For this, the lateral faces of the ZnO NWs were decorated with Ir self-assembled nanoparticles (NPs) using sputtering as the deposition technique. An in-depth morphological study using scanning electron microscopy (SEM) and high-resolution transmission electron microscopy (HRTEM) is presented for different Ir deposition conditions. This is followed by a brief description of the optical properties of these functionalized NWs, investigated by ultraviolet-visible (UV-vis) spectroscopy. The second part of the chapter discusses the functionalization of ZnO NWs with a MOF, in particular the zeolitic imidazolate

framework 8 (ZIF-8). As ZIF-8 is a Zn-based MOF, as per the description in Chapter 3.7.2, the integration of ZIF-8 and ZnO was achieved by successfully using the ZnO NWs as growth templates via a liquid phase processing and subsequent thermal treatment, resulting in the surface conversion of ZnO to form a core-shell structure in which the ZnO NWs are the core and the ZIF-8 forms the outer shell. The aim of the ZIF-8 functionalization of ZnO NWs was to improve the optoelectronic properties of the ZnO NWs to enhance the functional performance. The morphology of the ZIF-8 functionalization was analysed by SEM and HRTEM, while the optical properties were studied with UV-vis, fast transient absorption and photoluminescence spectroscopy. The details regarding the functionalization process for iridium and ZIF-8 are presented in Chapters 4.6.1 and 4.6.2, respectively. The MOF functionalization discussed in this chapter was integrated with undoped and doped ZnO NWs and, thus, the discussion of the results will be provided on this basis. The goal of both functionalizations discussed here was to enhance the performance of the ZnO NWs as photoanodes for photoelectrochemical (PEC) water splitting. Only the PEC performance of the ZIF-8 functionalization was studied as a result of the global circumstances, with the corresponding results shown in Chapter 8.

7.2 Surface functionalization with iridium nanoparticles

Iridium has been identified as one of the ideal catalysts for the photoelectrochemical water splitting process, and more particularly for the oxygen evolution reaction[268, 269], since the 70's[270]. The theoretical basis for this application was provided in Chapter 2.4. However, the availability of iridium has been an issue, as it is a rare and expensive transition metal, which makes its use in industrial level applications challenging. Thus, alternative routes like the one presented here, based on the functionalization of ZnO NWs, have to be explored. Here, sputtering was used to deposit iridium in the form of self-assembled nanoparticles (NPs) on the sidewalls of ZnO NWs. These NPs are in reality discontinuous nanoscale surface features that grow by self-assembly during the sputter process but, for convenience, are referred to as NPs. Control over the size and distribution of these NPs was achieved by tuning the deposition rate and growth pressure of the inert gas (Ar) inside the sputtering chamber. In order to assess this approach for the integration of these self-assembled iridium nanoparticles, a

thorough morphological analysis based on SEM and HRTEM was undertaken, in which the successful integration of the self-assembled Ir NPs and the ZnO NWs is demonstrated. The optical properties of these Ir-functionalized ZnO NWs were investigated by UV-vis spectroscopy to determine whether the presence of the self-assembled NPs yielded any improvement or reduction on the optoelectronic properties of the ZnO NWs. Unfortunately, due to the unforeseen current global circumstances related to COVID-19, it was not possible to carry out additional characterization of the properties of these functionalized NWs.

7.2.1 Morphological analyses of iridium functionalized ZnO nanowires

Two different sets of sputter deposition conditions were utilised to investigate the development of the self-assembled Ir NPs on the sidewalls of the ZnO NWs. Both were carried out at a relatively high base pressure of $2x10^{-4}$ Torr (flow rate of 40 sccm), with a nominal deposition rate of 0.25 Å s^{-1} and a power of 34 W. The difference between both samples was the deposition times, which were established at 40 s and 60 s for each sample. These deposition times were established as the corresponding times to nominally deposit a 1 nm and 1.5 nm thin film of iridium, respectively. This relation was established following the calibrated deposition of iridium thin films based on a recipe developed within the research group of Del Atkinson in the Department of Physics of Durham University. Hence, the two samples will be referred as 1 nm and 1.5 nm throughout the discussion. For the 1 nm sample, the NWs were grown on ALD-deposited seed layers. The seed layer deposition conditions were 250°C, 250 cycles with a pulse train 0.05-7-0.2-20 seconds, with the first two times being the pulse and purge for diethylzinc and the last two being those of water. For the 1.5 nm, the seed layer was deposited by sol-gel processing following the conditions previously described in Chapter 5. For both samples, the CBD growth time was 6 hours and the concentration of the reagents at 25 mM equimolar for the Zn^{2+} and OH^- sources.

Figure 7.1 shows scanning electron micrographs of the Ir-functionalized ZnO NWs. SEM was utilised as a survey tool to assess the presence and distribution of the Ir NPs on the sidewalls of the NWs. Figure 7.1a,b,c show the results of the 1 nm Ir deposition. In Figure 7.1, a standard ZnO NW growth akin to those shown in Chapters

5 and 6 is shown; nonetheless, the surface of the lateral faces of the NWs appears to have a granular texture, see particularly Figure 7.1c. The high magnification image shown in Figure 7.1b confirms that the lateral faces of the ZnO NWs have a textured surface, which contrasts with the otherwise smooth surface shown for the NWs grown in previous chapters (see Figure 5.11). Figure 7.1c provides a higher resolution
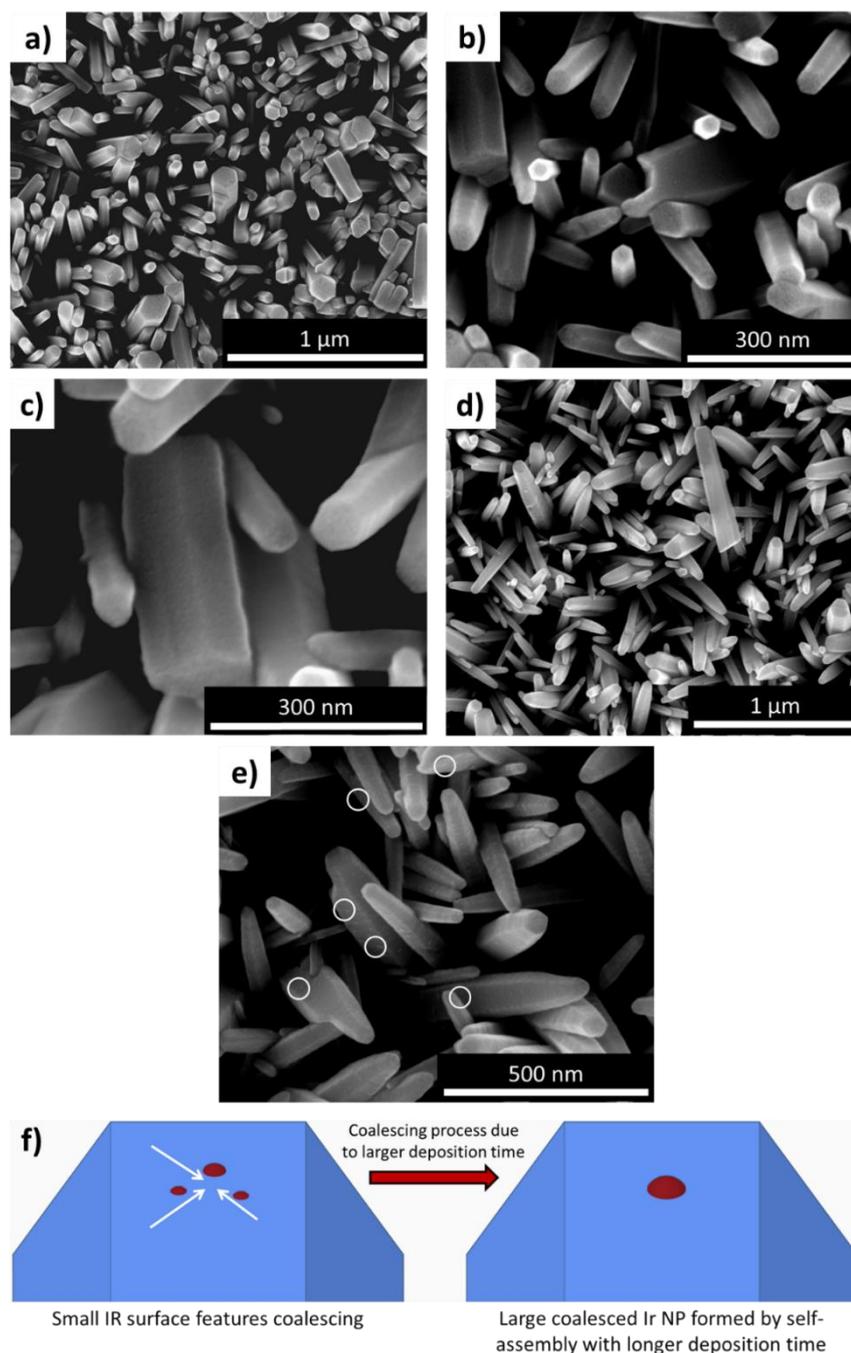
Figure 7.1. Scanning electron micrographs of **a), b), c)** 1 nm and **d), e)** 1.5 nm Ir-functionalized ZnO nanowires, showing the characteristic textured surface of the lateral faces of the nanowires as a result of the iridium functionalization. Some of the larger NPs of the 1.5 nm sample are marked by the white circles in **e)**. **f)** Schematic representation of the formation of the large Ir NPs by coalescence of the smaller surface features (red hemispheres) as a result of the longer deposition time on the lateral faces of the NWs (blue).

micrograph of this textured lateral surface, in which a distribution of grain-like features interpreted as self-assembled Ir NPs on the lateral surfaces of the ZnO NWs can be observed. Considering the nominal 1.5 nm Ir samples, Figure 7.1d shows a low magnification image, in which some large features considered to be Ir NPs are visible; no other iridium related features are observed in this micrograph. The large Ir NPs are shown in the high magnification image in Figure 7.1e on the lateral faces of the as-grown ZnO NWs. In contrast to the 1 nm sample, no granular texturing of the surface on the NWs is observed for the 1.5 nm in this micrograph, indicating a different morphology of the iridium functionalization. It is proposed that increasing the deposition time from nominal 1 nm to 1.5 nm resulted in the growth of a quasi-continuous layer of iridium on the lateral surface of the ZnO NWs instead of a surface feature decoration. In addition, the presence of the larger NPs on the lateral surface of the NWs (circled features of Figure 7.1e) suggests that some of the surface features coalesced, forming these larger NPs. A schematic of the growth of these large NPs by coalescence due to increasing deposition time is shown in Figure 7.1f.

From the SEM analyses it was clear that, in order to obtain a better understanding of the iridium functionalization of the ZnO NWs, high-resolution transmission electron microscopy was required. Figure 7.2 shows the TEM analyses carried out for the 1 nm Ir samples. Figure 7.2a,b show low magnification images of two separate Ir-functionalized ZnO NWs in which it is apparent that the formation of iridium nanoparticle functionalization of the NWs was successful, as indicated by the darker contrast island-like regions appearing in the outer part of the NWs. These surface features had not been previously seen and were attributed to the self-assembled Ir NPs. The distribution of these NPs on the lateral faces of the NWs is fairly homogeneous, indicative of an adequate coating, which supports the higher magnification images from the SEM micrographs of Figure 7.1c. The shape of these Ir NPs is irregular, with an average size of ~2 nm (see the Gaussian distribution of the NP size presented in Figure 7.2c). The higher magnification image in Figure 7.2d shows regions with different contrast that are attributed to the presence of the functionalizing Ir NPs. Nonetheless, no significant disruption of the typical lateral shape of the ZnO NWs can be seen. Selected area electron diffraction (SAED) was used to check the crystalline phase of the functionalized NWs (Figure 7.2e). It showed
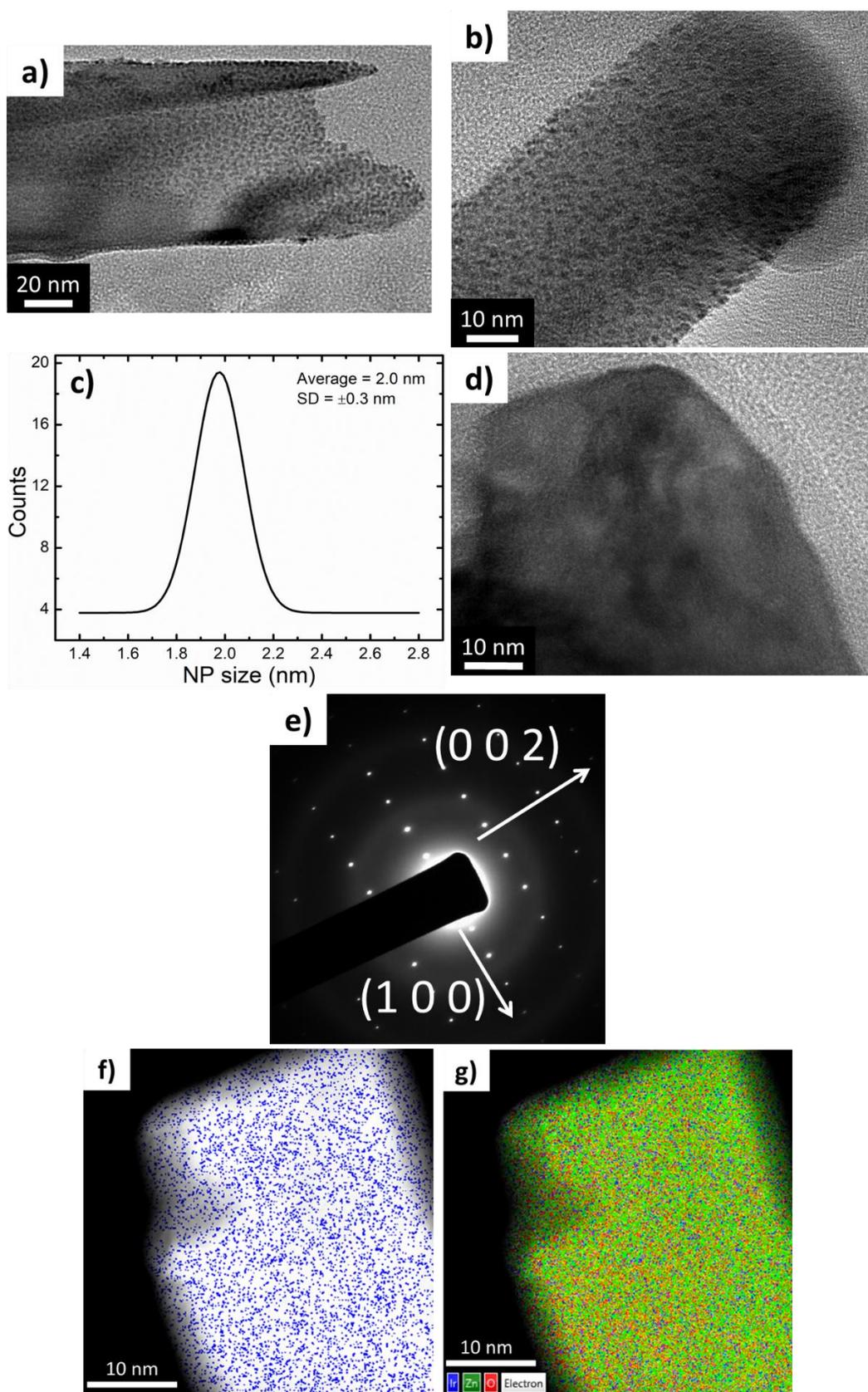
Figure 7.2. a), b) Low and **d)** high resolution transmission electron micrographs, depicting the lateral faces of the 1 nm Ir-functionalized ZnO NWs. **c)** Gaussian size distribution of the 1 nm Ir NPs, including the average size and standard deviation. **e)** Selected area electron diffraction pattern of the NWs, showing their typical single crystal wurtzite phase. Elemental maps of **f)** iridium (blue dots) and **g)** Ir (blue), O (red) and Zn (green).

that the NWs are single crystal wurtzite phase ZnO NWs, corresponding to the expected crystalline phase of ZnO NWs as discussed in previous chapters. Elemental mapping of the iridium functionalization was carried out to determine the distribution of iridium across and along the NWs.

Elemental maps of the elements forming the NWs were obtained by means of energy-dispersive x-ray spectroscopy (EDX), carried out in scanning transmission electron microscopy (STEM) mode. Details on this technique were provided in Chapter 4.9.2. The elemental map of iridium shown in Figure 7.2f demonstrates a homogeneous distribution of iridium, which corresponds with the homogeneous distribution of NPs shown in Figure 7.2a,b. To put this elemental distribution in contrast, Figure 7.2g shows the elemental map of Ir along with those of Zn and O. It can be seen that the distribution of the three elements is homogeneous and their mixing is good, with no clustering being present for any of them.

The TEM analyses of the 1.5 nm Ir sample are shown in Figure 7.3. A set of five Ir-functionalized ZnO NWs can be seen in Figure 7.3a. Here, the presence of a textured surface of the lateral faces of the functionalized ZnO NWs can be seen. This textured surface seems to homogeneously coat the lateral surface of the NWs, similarly to what was observed for the SEM analysis of the same sample in Figure 7.1e. This is in correlation with the discussion of the SEM micrographs of Figure 7.1d,e, in which it was suggested that a quasi-continuous Ir layer was grown around the ZnO NWs, along with the large iridium NPs formed by coalescence of the self-assembled surface features. Figure 7.3b shows a higher resolution TEM image for the 1.5 nm iridium sample in which the presence of the Ir NPs is evidenced. The size of these self-assembled NPs is ~3.3 nm (see the Gaussian distribution of the NP size presented in Figure 7.3c, that includes average size and standard distribution) with a homogeneous spatial distribution on the side walls of the NWs. These nanoparticles on the lateral faces of the NWs can be seen protruding at both sides of the NWs in Figure 7.3d, circled in white. The number density of particles for this sample is visibly larger than for 1 nm Ir, correlating with what has previously been discussed. Thus, it is apparent that increasing the deposition time from 40 s to 60 s led to a considerable increase in the density of the Ir surface features on the lateral faces of the ZnO NWs as well as to the coalescence of some of these to form larger NPs.
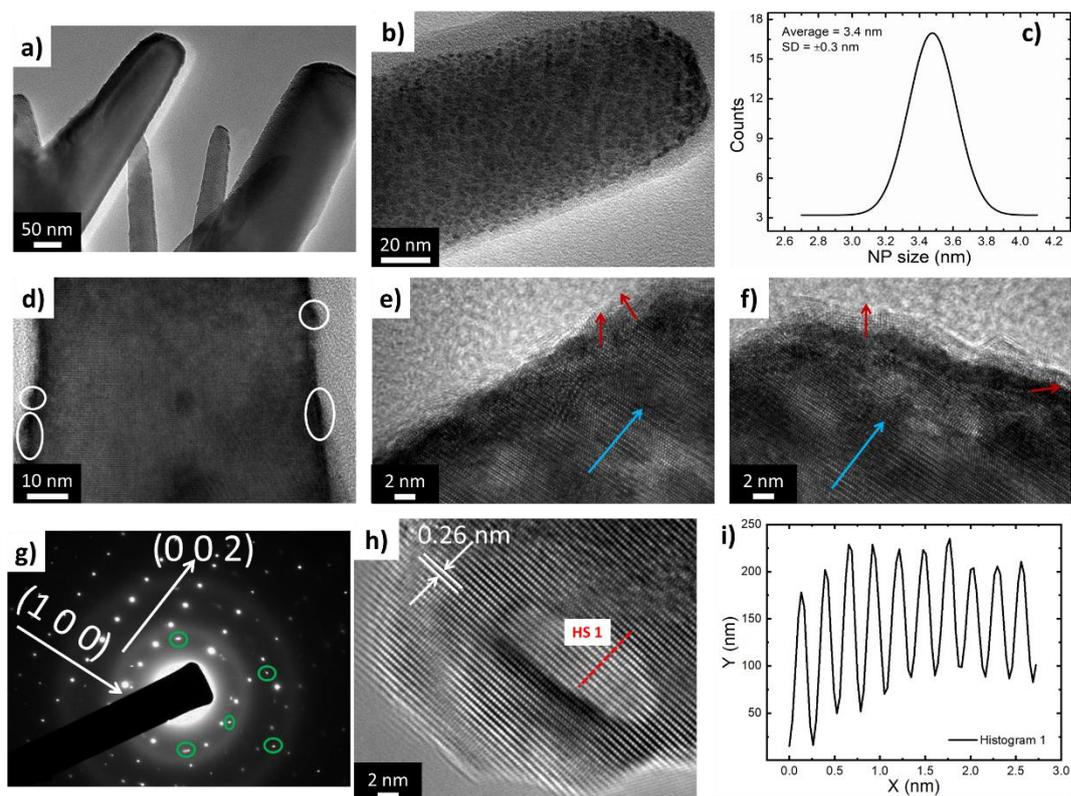
Figure 7.3. Microscopy analyses of the 1.5 nm Ir samples. **a), b), d)** Low magnification transmission electron micrographs. The white marks in **d)** indicate the presence of the protruding Ir NPs on the sidewalls of the ZnO NW. **c)** Gaussian size distribution of the 1.5 nm Ir NPs, including the average size and standard deviation. **e), f)** High resolution transmission electron micrographs. **g)** Selected area electron diffraction pattern of the NWs, showing their typical single crystal wurtzite phase along with other diffraction spots attributed to the presence of iridium. **h), i)** High resolution transmission electron micrograph and corresponding histogram used to confirm the wurtzite crystalline phase of the functionalized ZnO NWs.

The HRTEM analyses on this sample allowed the imaging of the Ir NPs, as evidenced by the presence of regions with different planar orientations other than that of the wurtzite ZnO NWs, marked in Figure 7.3e,f by the blue and red lines, respectively. This is indicative that a material other than ZnO has grown on the lateral faces of the NWs, which is attributed to iridium, and that seems to form an almost continuous shell around the ZnO core. Further proof of this is provided in the SAED pattern shown in Figure 7.3g, corresponding to the HRTEM micrograph of Figure 7.3e. It shows the typical spot pattern of single crystal wurtzite phase ZnO NWs. However, there are other sets of diffraction spots (circled in green) that indicate the presence of a different crystalline material, which is attributed to the self-assembled Ir NPs. Nonetheless, the analysis of this secondary crystalline phase was not conclusive, partially due to the small size of the NPs, and it would require further work. To ensure the crystalline phase of the ZnO NWs, an analysis on the planar

interspacing of the ZnO planes was carried out, based on the HRTEM micrograph of Figure 7.3h, with its corresponding histogram shown in Figure 7.3i. The peaks of this histogram have an average width of ~0.27 nm, in good agreement with the theoretical value of 0.26 nm.

7.2.2 Optical properties of the iridium functionalized ZnO nanowires

The optical properties of the two iridium-functionalized ZnO NWs were studied by UV-vis spectroscopy and compared with the spectrum of the undoped ZnO NWs (Figure 7.4). The spectrum of the 1 nm Ir sample follows that of the undoped ZnO in the UV and blue region, up to around 390 nm. The shoulder at around 370 nm (marked by the blue arrow) is characteristic of ZnO and was also observed for doped samples in Chapter 6. For wavelengths above 390 nm, the 1 nm Ir sample has a larger absorption than the undoped NWs. For this sample, there are two small shoulders in the absorption signal centered at approximately 420 and 540 nm (marked by red arrows), with their origin being unknown. Unfortunately, only an individual sample was analysed before the lockdown caused by the COVID-19 pandemic and, therefore, further work such as additional optoelectronic studies would be required to adequately analyse these shoulders. Nonetheless, the absorption of the 1 nm Ir sample in the visible region from 400 nm to 700 nm is larger than that of the base ZnO NWs, which is promising for the application of the Ir surface functionalization.

For the 1.5 nm Ir sample, the absorption spectrum is comparable to that of undoped ZnO, albeit with a slightly lower absorption. In particular, the absorption in the region between 350 nm and 400 nm is considerably lower, which is the main region of important for photonic-based applications of ZnO. For the visible region between 400 nm and 700 nm, the absorption of Ir 1.5 nm is slightly lower than that of the ZnO NWs. In addition, no shoulder in the spectrum is observed at 420 nm or 540 nm, contrasting with the spectrum for the 1 nm Ir sample. The difference in the absorption between the two iridium functionalized NW samples is attributed to the difference in size of the iridium surface functionalization. It was seen in the morphological analysis that the 1 nm deposition resulted in the lateral surface of the ZnO NWs being covered by individual surface features that were considered NPs. In contrast, the 1.5 nm deposition was proposed to yield a quasi-continuous coating of
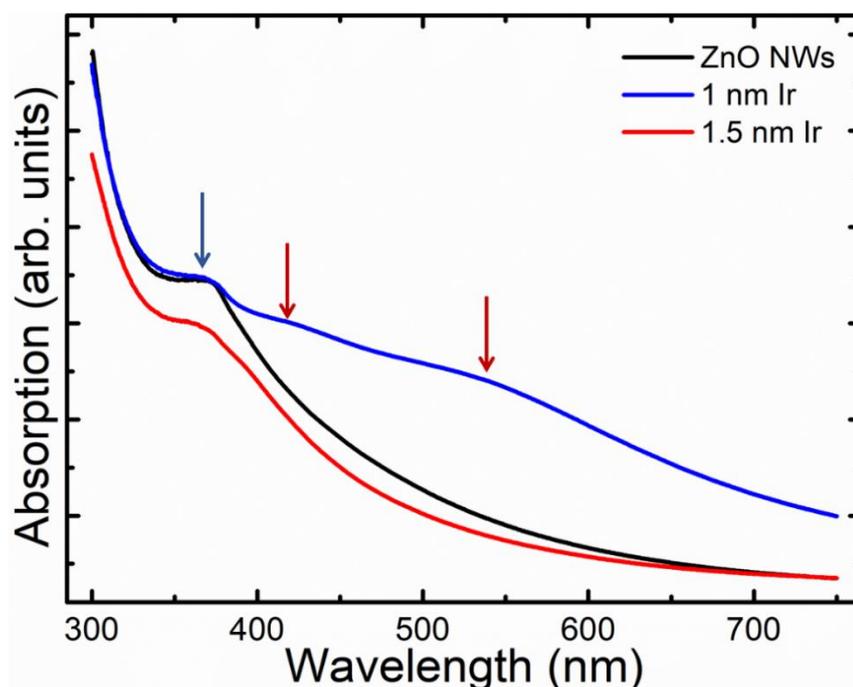
Figure 7.4. Ultraviolet-visible spectra of undoped NWs and iridium functionalized ZnO NWs with 1 nm and 1.5 nm of iridium, showing that the 1 nm Ir sample provides the best absorption of the studied samples. The blue and red arrows indicate the shoulders discussed in the main text.

the lateral faces of the ZnO NWs along with larger NPs formed by the coalescence of the self-assembled surface features. This iridium layer is considered the reason why the 1.5 nm Ir shows a poorer absorption than the 1 nm Ir and ZnO NWs. It is proposed that the quasi-continuous iridium layer acts as a reflecting coating, quenching the light absorption of the base ZnO NWs.

All in all, it was proven that the integration of ZnO NWs and iridium surface functionalization by means of self-assembled NPs can be successfully achieved by sputter deposition. For this, it was necessary to use a relatively high base pressure of 2×10^{-4} Torr during the deposition. Two different samples were grown using the same conditions while only varying the total deposition time to 40 s and 60 s, corresponding to a nominal thin film thickness of 1 nm and 1.5 nm. The microscopy studies carried to understand the morphology of these two samples showed that the 1 nm Ir sample yielded a surface functionalization formed by individual Ir NPs with an average size of ~2 nm, while the 1.5 nm Ir sample provided a quasi-continuous Ir coating around the ZnO NWs along with larger NPs as a result of the coalescence of individual surface features. The larger amount of iridium deposited on the ZnO NWs with the increasing deposition time resulted in a quenched UV-vis absorption compared to the pure ZnO NWs and 1 nm Ir samples. Further work on this research

197

strand is required to obtain a better understanding of the surface functionalization with iridium NPs. However, and due to the pandemic and lockdown situation, it was not possible to further this research.

7.3 Surface functionalization with a metal-organic framework

Metal-organic frameworks (MOFs) are an attractive class of nanomaterials with a vast variety of uses and applications. In this work, the MOF that was implemented with the ZnO NWs was the zeolitic imidazolate framework 8, ZIF-8, which is a zinc-based MOF. The background and theoretical basis of MOFs and ZIF-8 was provided in Chapter 3.7.2. ZIF-8 was selected as the ideal MOF for this integration due to it being a photoactive Zn-based MOF that could act as a passivation layer, protecting ZnO during the water splitting process[271, 272].

The integration of ZIF-8 and ZnO NWs was achieved using ZnO as a growth template in which the Zn required for the ZIF-8 growth is extracted directly from the ZnO NW lattice, yielding a core-shell structure in which ZIF-8 is the shell and ZnO is the core, labelled as ZnO@ZIF-8. To achieve this integration via a liquid phase process, the growth solution needs only to contain the organic linker that coordinates the ZIF-8 structure (2-methylimidazol, HMIM). The growth mechanism is defined as per the schematic in Figure 7.5.

Two different approaches to adding the HMIM solution for the ZIF-8 growth were explored in this work, namely drop casting and spin coating. These techniques were chosen as viable alternatives to the commonly used hydrothermal growth[195], which has two major drawbacks in the large reaction volumes required and the
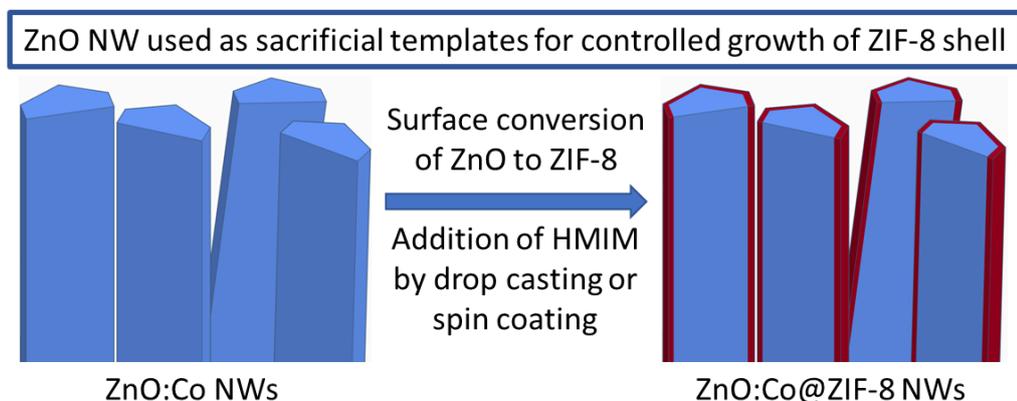
Figure 7.5. Schematic of the integration of the zeolitic imidazolate framework-8 shell and ZnO nanowires core by using the latter as growth template during growth. 2-methylimidazole, the organic linker used for the growth was deposited on the as-grown nanowires by either drop casting or spin coating.

longer growth times. In contrast, drop casting and spin coating are much faster techniques that require small reaction volumes (a few droplets of the organic linker solution) to controllably grow the ZIF-8 shell. The basis of these two approaches lies in the preparation of a methanol solution containing the desired concentration of HMIM, which is deposited onto the as-grown ZnO NWs in one of the two ways. The MOF integration by drop casting has been previously reported by Ki et al.[273], while the use of spin coating has only been reported in our recent work[90],showing the novelty in this specific application of spin coating. The experimental details of these two techniques are provided in Chapter 4.6.2. Morphological studies of the ZnO@ZIF-8 integration using these two techniques with SEM and HRTEM are provided. Finally, the optical properties of the core-shell NWs were investigated by UV-vis, fast-transient and photoluminescence spectroscopy.

7.3.1 Integration of ZIF-8 and ZnO by drop casting

Three key parameters control the growth of ZIF-8 using ZnO as a growth template: the growth temperature, the organic linker concentration in the methanol solution, and the growth time. The goal of this integration was to obtain a thin ZIF-8 shell that would enhance the PEC performance of the ZnO NWs. For this, the shell has to conformally coat individual NWs without bridging them, while also being thin. Should it be too thick, the NWs would not be accessible for the water splitting process, possibly hindering the performance. The growth temperature has to be such that the HMIM melts, which occurs at temperatures above 145°C; thus, the growth temperature was fixed at 160°C for all of the samples discussed in this work. Therefore, only the growth time and HMIM concentration were studied as growth control parameters. The results of the drop casting integration are shown in Figure 7.6. The growth times were varied from 10 minutes to 20 minutes to assess its influence on the morphology of the core-shell structure. The HMIM concentration was set at 0.25 M. For 10 minutes growth time (Figure 7.6a) the as-grown ZnO NWs are completely covered by a ZIF-8 shell; this shell is large enough to bridge the gaps between NWs in some regions. When the growth time was increased to 20 minute (Figure 7.6b), this overgrowth was more noticeable, to the point that a quasi-continuous ZIF-8 film was formed on top of the ZnO NWs. Thus, it was demonstrated

that careful control of the ZIF-8 growth time is paramount to obtain the targeted ZIF-8 shell coating instead of a continuous film of the MOF.

To study the influence of the concentration on the growth of the ZIF-8 shell, HMIM concentrations ranging from 0.15 M to 1 M were studied. The growth times
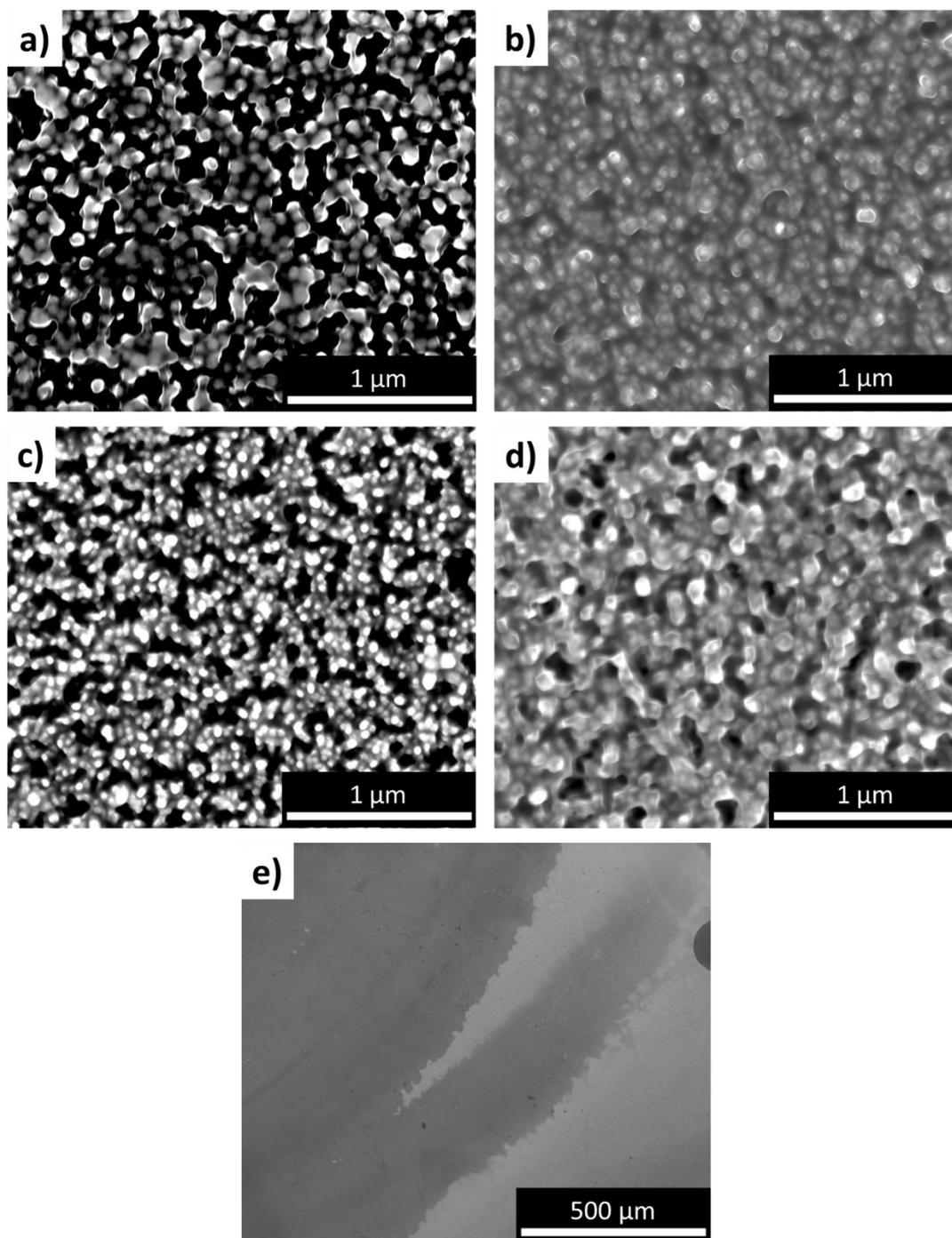
Figure 7.6. Scanning electron micrographs of ZIF-8 shells grown on ZnO nanowires by drop casting with different growth conditions. Different growth times, **a)** 10 minutes, **b)** 20 minutes, and different organic linker concentrations, **c)** 0.15 M, **d)** 1 M. **e)** Low magnification micrograph showing that irregular distribution of the growth of the ZIF-8 shell, representing areas in which the ZIF-8 shell was grown on the nanowires (dark region) and those in which it did not grow (bright region).

were kept constant at 15 minutes. Figure 7.6c shows the ZIF-8 shell growth using a 0.15 M concentration of HMIM. The results are similar to those shown in Figure 7.6a. However, the ZIF-8 shells in this sample are thinner, as evidence by the clearly defined tips of the NWs, which were not visible for the sample in Figure 7.6a. Nonetheless, the ZIF-8 shell still was large enough to bridge between many neighbouring NWs. When the HMIM concentration was increased to 1 M (Figure 8.6d), a quasi-continuous ZIF-8 film that covered the ZnO NWs was obtained. The long-range order of the core-shell structuring by drop casting was studied, with the result shown in Figure 7.6e, which corresponds to the growth conditions of the samples in Figure 7.6c. The dark region indicates the area in which the ZnO NWs have been covered with a ZIF-8 shell, while the lighter region represents a region of undoped ZnO NWs where no trace of ZIF-8 could be identified. This irregular long-range distribution makes this ZIF-8 growth technique unappealing, as homogeneity is key in obtaining a uniform functional performance. As such, drop casting was not deemed a suitable growth technique to control the integration of ZIF-8 and ZnO NWs.

7.3.2 Integration of ZIF-8 and ZnO by spin coating

Based on the results obtained from the drop casting growth of the ZIF-8 shell, spin coating was studied as an alternative processing technique that could provide a more uniform and controlled ZIF-8 shell coating. Critically, although spin coating is a widely used technique, its application to the growth of MOFs remains unexplored. The ZnO NWs used in this study were grown on sol-gel deposited seed layers on indium-tin oxide (ITO) substrates, with NW growth conditions of 6 hours, a 25 mM equimolar concentration and with a 1% Co concentration for doping.

The growth conditions of the ZIF-8 shell were set at 160°C, 15 minutes growth time and 1 M HMIM concentration. The control parameter studied to understand the growth of the ZIF-8 shell was the spin coating speed, which was varied from 500 rpm to 5000 rpm. The spin time was set at 30 seconds for all the samples. The main objective of this study was to assess whether the spin speed would provide sufficient control of the ZIF-8 shell thickness and provide a good long-range homogeneity. Figure 7.7a shows the shell growth for a spin speed of 500 rpm. The individual ZnO NWs can be identified as the brighter spots in the micrograph. The slow spin speed

used here resulted in the NWs being completely covered by a ZIF-8 layer that bridged individual NWs to form a quasi-continuous ZIF-8 layer that resembles the results obtained for the drop casting growth. Increasing the spin speed to 1000 rpm (Figure 7.7b) resulted in an external ZIF-8 coating of the ZnO NWs. However, this coating was
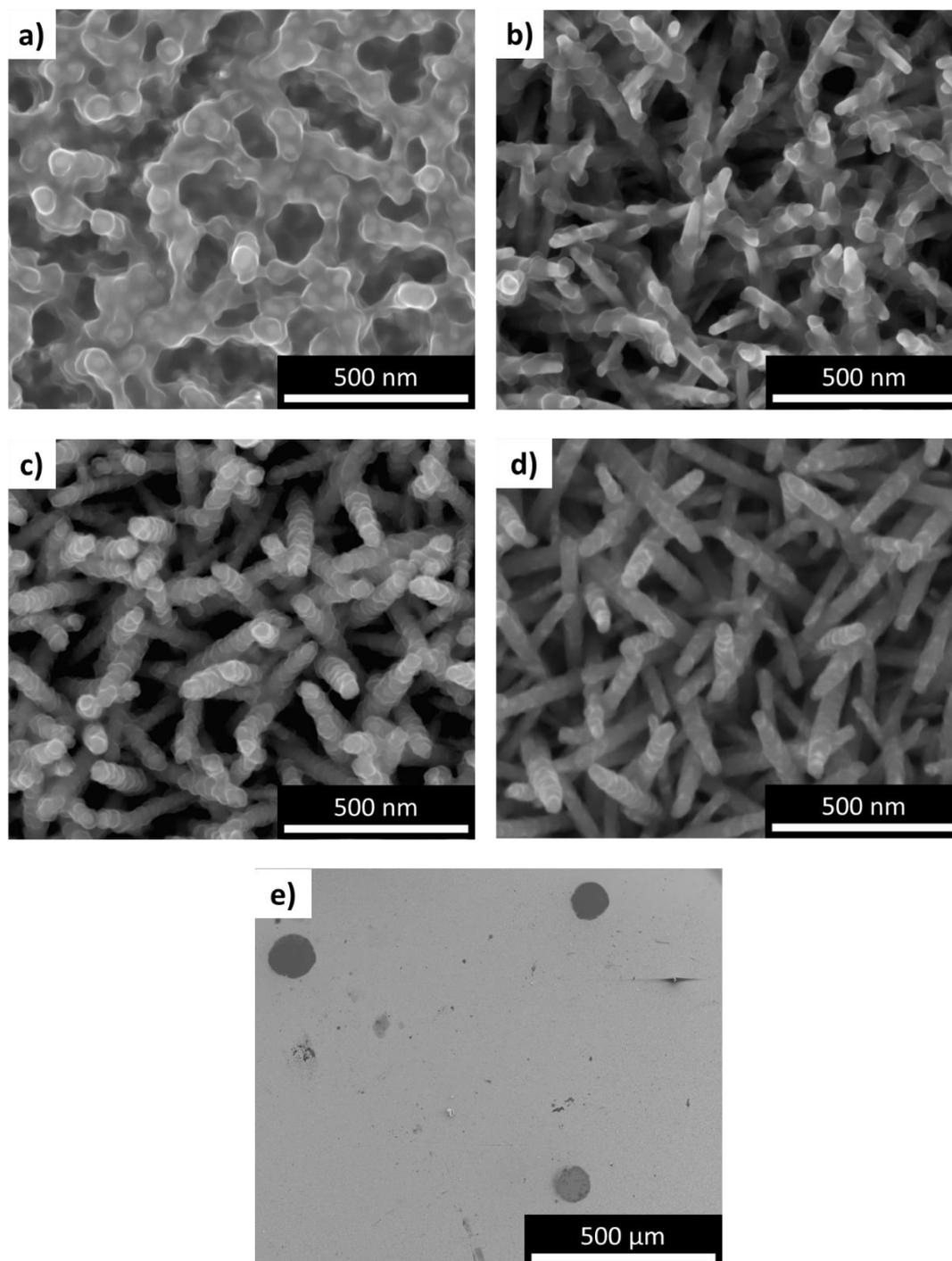
Figure 7.7. Scanning electron micrographs of ZIF-8 shells grown on ZnO nanowires by spin coating under different spin speeds, **a)** 500 rpm, **b)** 1000 rpm, **c)** 2000 rpm, **d)** 5000 rpm. **e)** Low magnification micrograph showing that regular distribution of the growth of the ZIF-8 shell. The darker regions in this case represent growth defective areas in which the NW growth was not successful, while the brighter regions indicate the growth of the ZnO@ZIF-8 core-shell nanowires.

rather irregular, with a heterogeneous thickness that resulted in regions of the NWs being exposed, almost the opposite result compared to the 500 rpm sample. Further increasing the spin speed to 2000 rpm (Figure 7.7c) yielded a conformal coating of the ZnO NWs in the form of a ZIF-8 shell. The shell obtained for this sample was the first one that provided a complete coating of the ZnO NWs without bridging the individual NWs, albeit the thickness of the ZIF-8 shell was larger than what was originally envisioned. In an attempt to achieve a thinner shell, the spin speed was increased to 5000 rpm (Figure 7.7d). This resulted in a conformal shell that completely coated the ZnO NWs with the desired thickness and morphology. In addition, this sample yielded a homogeneous growth of the ZIF-8 shell over large areas, as evidenced in Figure 7.7e, in which it can be seen that, with the exception of the three circle-like regions, the rest of the sample showed a bright tone that corresponds to the ZnO@ZIF-8 core-shell NWs.

The results shown in Figure 7.7 demonstrate that the spin speed is a very effective parameter to accurately control the growth of a ZIF-8 shell around ZnO NW cores. The reason why increasing spin speeds provide a more controlled and thinner ZIF-8 shell is based on the liquid layer formed during spin coating. ZnO NWs are known to be a hydrophilic nanomaterial that have an increasing hydrophilicity with larger densities of surface defects[274]. In Chapter 6 it was demonstrated the ZnO and ZnO:Co NWs had a large density of surface defects which, in turn, translates into the NWs being hydrophilic or super-hydrophilic. In addition to this, the solvent used for the spin-coating growth is methanol, which has a viscosity of 0.5 mPa·s, i.e. the same order of magnitude as water. Therefore, the wettability of the ZnO NWs towards methanol will be similar to that towards water. Thus, it is proposed that the HMIM methanol solution will completely wet the ZnO NWs, forming a liquid layer. The thickness of this liquid layer will be dependent on the spin speed of the spin coating process. As such, and based on the SEM analyses of Figure 7.7, higher spin speeds will thin the liquid layer on the ZnO NWs, resulting in a controlled thickness shell. In this way, the lower spin speed of 500 rpm was related with a greater volume of liquid, yielding the ZIF-8 coating that bridged adjacent NWs. In contrast, using the faster spin speed of 5000 rpm resulted a thin, conformal ZIF-8 shell on every individual NW.

Based on these results, spin coating was deemed a suitable technique for the growth of ZIF-8 shells on ZnO NW cores providing ease of production, low operative costs and control over the morphology of the shell. In order to further understand the growth, the influence of the growth time and HMIM concentration were studied. This study was conducted on the same NWs as those used in Figure 7.7 and these investigations were all carried out with a spin speed of 5000 rpm. Figure 7.8a is a high magnification image of the NWs shown in Figure 7.7d. Reducing the HMIM concentration from 1 M to 0.25 M while maintaining the growth temperature at 160°C and the growth time at 15 minutes resulted in an incomplete ZIF-8 coverage (Figure 7.8b) that decorated only the lateral faces of the NWs instead of providing a complete shell coating. As such, low HMIM concentrations were not sufficient to provide a continuous and homogeneous ZIF-8 shell around the ZnO NWs core. Increasing the HMIM concentration from 1 M to 2 M, while keeping the other growth conditions constant, resulted in a significantly thicker shell (Figure 7.8c), similar to the growth with a spin speed of 2000 rpm (Figure 7.7c). Thus, increasing or decreasing the HMIM concentration resulted in the corresponding effect on the shell thickness and its overall coverage of the ZnO NW core. To understand the influence of the growth time on the spin coating process, this was increased from 15 minutes to 30 minutes, while maintaining the growth temperature at 160°C and the growth concentration at 2 M. The results obtained are rather similar to increases in the growth time, with the ZIF-8 shell completely and conformally coating the ZnO NW cores. This indicates that all the organic linker that was deposited on the lateral faces of the NWs requires less than 30 minutes to fully react with the Zn atoms of the NWs to form the ZIF-8 shell. Therefore, 15 minutes was set as the base time for all further experiments discussed in this work.

The results shown here demonstrate that the novel use of spin coating has clear potential for the integration of ZIF-8 and ZnO as it allows the growth of a controllable ZIF-8 shell that conformally coats the ZnO cores. This control is obtained by carefully tuning the spin speed during the spin coating process, the growth time and the organic linker HMIM concentration. This approach controls the reagent volume through the NW array film, which is key to the formation of thin, uniformly
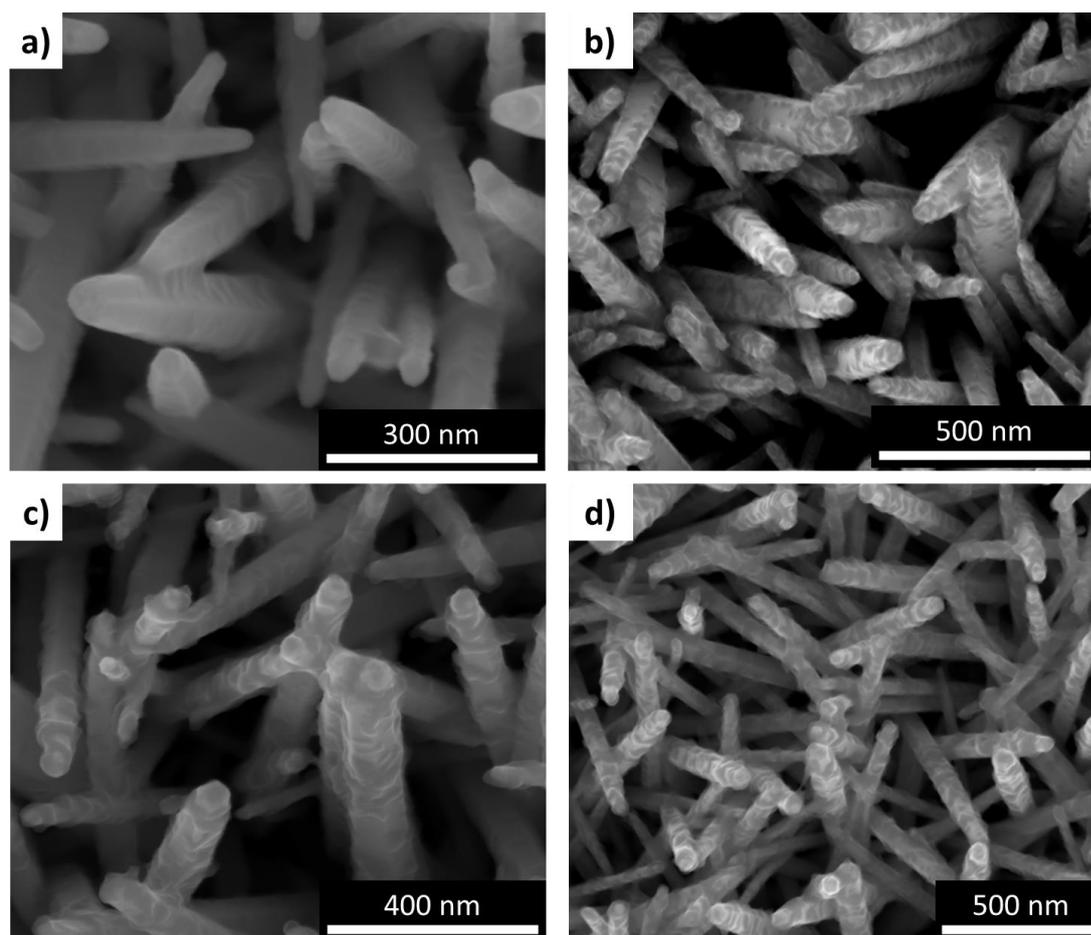
Figure 7.8. Scanning electron micrographs of ZIF-8 shells grown on ZnO nanowires by spin coating under different growth time and HMIM concentrations, with the growth temperature and spin speed constant at 160°C and 5000 rpm, respectively: **a)** 15 min, 1 M, **b)** 15 min, 0.25 M, **c)** 15 min, 2 M and **d)** 30 min, 2 M.

distributed MOF shells on ZnO NWs. Moreover, this approach can be generalised to the formation of other core-shell based reaction systems.

High-resolution transmission electron microscopy was used to obtain a better understanding of the interplay between the ZnO core and ZIF-8 shell. For this study, the ZIF-8 shell growth parameters were set at 5000 rpm, 160°C, 1 M and 15 min (Figure 7.8a), as these were identified as the optimum growth conditions. Figure 7.9a shows a low magnification TEM image of a core-shell ZnO@ZIF-8 NW. Comparing this to the TEM images previously shown of undoped ZnO NWs, it can be seen that the lateral faces of the core-shell NWs have surface features and texture (marked by the red and white lines) that are attributed to the ZIF-8 shell. The texture provided by the ZIF-8 shell can be seen in the higher magnification SEM micrographs previously shown. The HRTEM image of Figure 7.9b shows two crucial characteristics of these core-shell NWs: marked in white, the surface texture previously described and, in

205
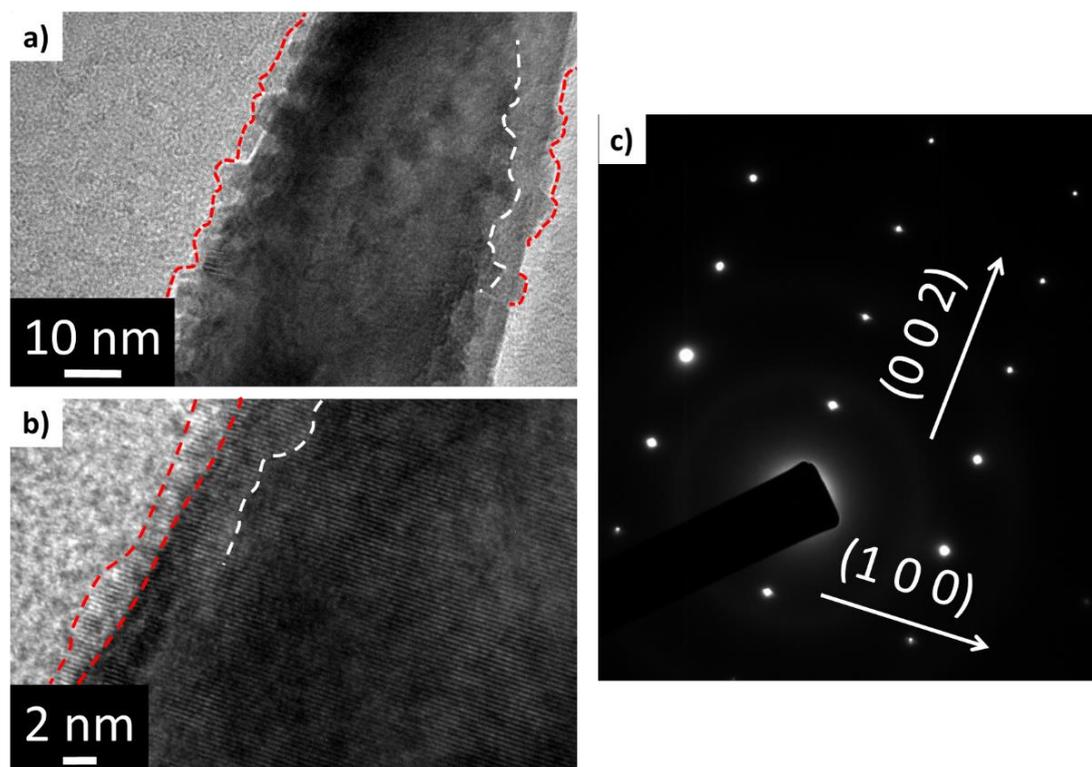
Figure 7.9. a), b) High-resolution transmission electron micrographs of ZnO@ZIF-8 core-shell nanowires, showing the characteristic surface texture and thickness of the ZIF-8 shell. The red and white lines serve as contour guidelines to outline the presence of the shell and of the surface features on the lateral face of the NW induced by the ZIF-8 shell. **c)** Selected area electron diffraction pattern of the ZnO@ZIF-8 core-shell nanowires, showing the typical pattern of the single crystal wurtzite phase ZnO nanowires and no signal corresponding to the ZIF-8 shell, deemed under the detection limit.

between two red lines, an outer signature of approximately 2 nm in thickness that outlines the ZIF-8 shell that coats the ZnO NW cores. ZIF-8 is known to be crystalline so SAED (Figure 7.9c) was used to determine whether the ZIF-8 shell grown on the ZnO NWs has any crystalline character. From the SAED shown in, it can be seen that only the diffraction pattern characteristic of the single crystal wurtzite ZnO NWs. No other ZIF-8 signal was observed, which is attributed to the ZIF-8 shell signal being under the detection limit.

In order to demonstrate the ZIF-8 growth, elemental mapping analyses were carried out using energy dispersive x-ray spectroscopy (EDX) in scanning TEM (STEM) to study the Zn, O, Co and N signals. These analyses had two main goals: first, to determine the distribution of the Co-doping across and along the NWs and second, to assess the presence of nitrogen on the NWs. Nitrogen was chosen as the element to identify the shell as it is the only element not present in the ZnO NWs; the chemical structure of ZIF-8 contains C, Zn, H and N, thus nitrogen was selected. The elemental

maps are shown as combinations of the four elements studied. Figure 7.10a shows the superimposed Co and Zn signals on a ZnO NW. Zn is expected to completely cover the NW, with the cobalt signal being scattered homogeneously along and across the NW, albeit the presence of Co around the edges of the NW was diminished. This indicates that the doping is adequately distributed in the NW. The nitrogen signal was studied in comparison with the Co signal in Figure 7.10b. The two signals are homogeneously distributed on the NW, with the nitrogen being more prominent on the bottom edge of the NW. The presence of a significant N signal is indicative of the satisfactory integration of ZIF-8 on the ZnO NWs. The oxygen and nitrogen signals are shown together in Figure 7.10c.

One key feature of the oxygen EDS data is that the signal does not completely cover the underlaying NW. This is attributed to the post-analysis signal processing
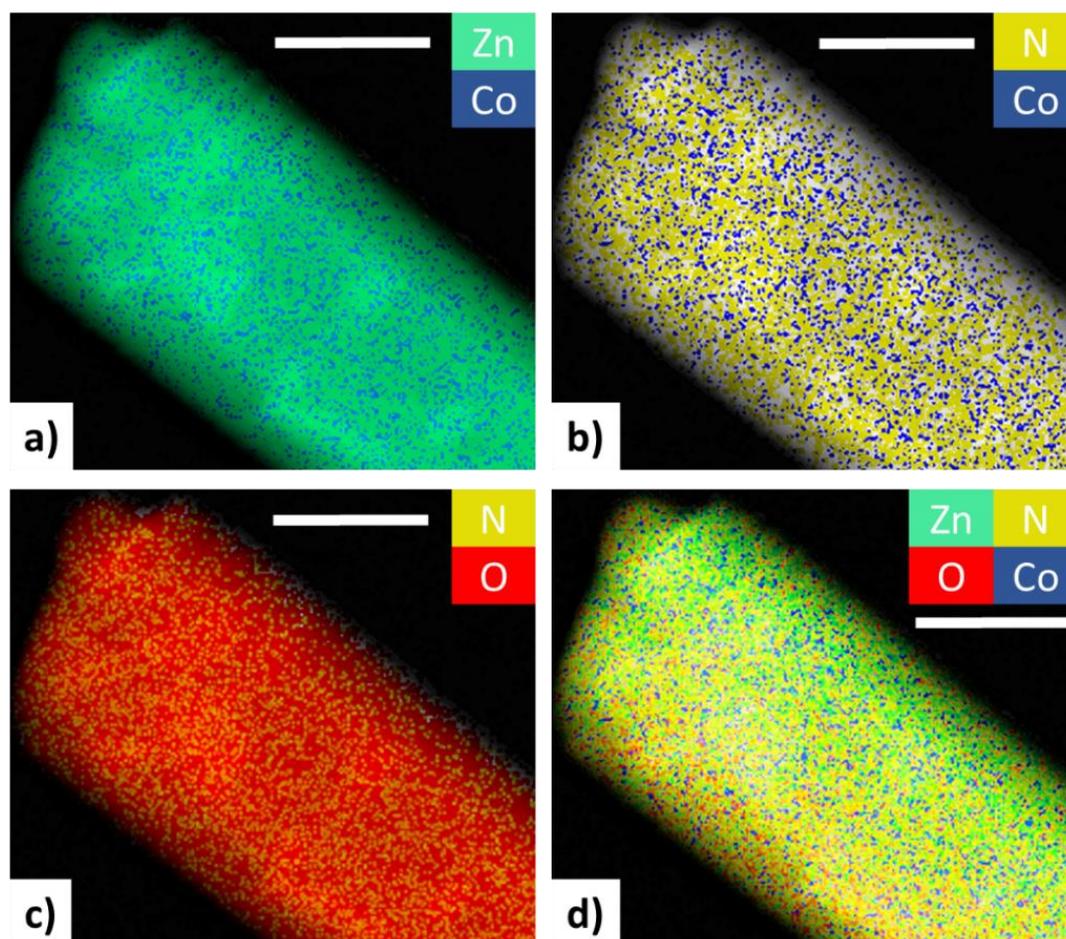
Figure 7.10. Energy dispersive x-ray spectroscopy elemental maps of **a)** Zn and Co, **b)** N and Co, **c)** N and O and **d)** Zn, N, O and Co obtained in scanning transmission electron microscopy, showing the homogeneous distribution of the four elements that compose the core-shell ZnO@ZIF-8 nanowires. The scale bar indicates 50 nm.

procedure used in which the noise from the signals was minimized, thus why this artefact is present. Apart from this, the oxygen signal is similar to that of Zn, being present in the whole NW. The four signals (Zn, O, Co and N) were overlapped together in Figure 7.10 d, showing the homogeneity with which they all intermix, indicating that the Co doping and the ZIF-8 integration were overall successful.

7.3.3 Structural spectroscopic studies of ZnO@ZIF-8 core-shell nanowires

Further characterization of the ZnO@ZIF-8 core-shell structure was required to confirm the presence of the ZIF-8 shell. For this, x-ray diffraction (XRD) and x-ray photoelectron spectroscopy (XPS) were used. The description of these two techniques was provided in Chapters 4.8.1 and 4.9.1, respectively. The samples are named based on them being undoped ZnO NWs (ZnO), Co-doped NWs (ZnO:Co), core-shell NWs (ZnO@ZIF-8) or doped core-shell NWs (ZnO:Co@ZIF-8). The Co-doping level of the NWs is a nominal 1% (see Chapter 4.5.1) unless specified otherwise; the shell growth conditions were 5000 rpm, 160°C, 1 M and 15 min unless stated to be different. ZIF-8 is a crystalline MOF with very clearly defined XRD peaks with Cu kα radiation, in the region between 5° and 30°[275]. The main ZnO peaks are located in the 35° region, as detailed previously in Chapter 5.2.1. Figure 7.11a shows the XRD spectra of ZnO@ZIF-8 and ZnO:Co@ZIF-8, two core-shell samples, in the 5° to 30° Bragg angle region. The signal seen at 12.5°for ZnO@ZIF-8 does not correlate with any ZIF-8 or ZnO peak and, therefore, additional work would be required to understand its origin. No significant signal related with the ZIF-8 phase was found for either of the two samples, which is attributed to the signal from the shell being below the detection limit of the instrument, as shown previously in the HRTEM experiments and in agreement with the literature[272]. To further support this claim, an estimation of the relative mass of the ZIF-8 shell was calculated. For this, a ZIF-8 shell of 2 nm was considered to conformally coat an ideal hexagonal prism (the ZnO core) with a diameter of 77 nm. Calculating these volumes and considering the densities of ZnO and ZIF-8, it was estimated that the ZIF-8 shell represented a 1% of the total mass of the core-shell NWs, thus proving the difficulty of obtaining a considerable signal from the spectroscopic techniques. Regarding the rise on the XRD signal peaking at 25°, this was attributed to be related with the amorphous ITO layer of the substrate[276].
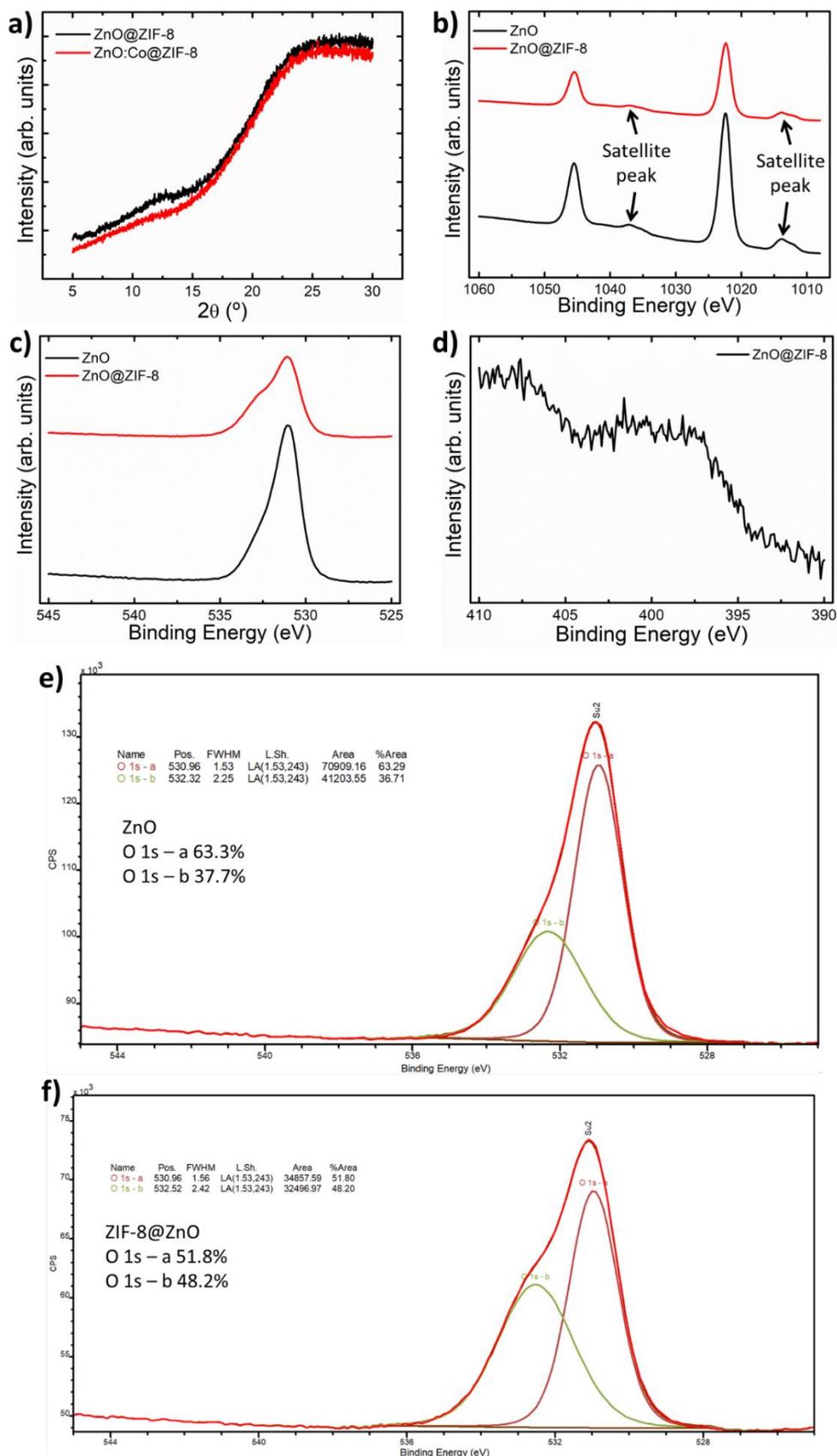
Figure 7.11. a) X-ray diffraction spectra with Cu kα radiation of ZnO and ZnO@ZIF-8 in the region of 5° to 30°. X-ray photoelectron spectroscopy of **b)** Zn 2p, **c)** N 1s and **d)** O 1s peaks for ZnO and ZnO@ZIF-8. **e), f)** Deconvolution of the O 1s peak for ZnO and ZnO@ZIF-8 showing the difference in the O 1s$_a$ and O 1s$_b$ components.

XPS was utilised to study the chemical environment of the core-shell NWs; for this, the Zn 2p, N 1s and O 1s peaks were studied as these were considered the most representative of the ZnO@ZIF-8 structure. Figure 7.11b shows the Zn 2p spectra for ZnO and ZnO@ZIF-8. The Zn 2p peak has two main peaks: the Zn 2p 1/2, centered at around 1045.5 eV, and the Zn 2p 3/2, centered around 1022.4 eV. These two peaks are present in both samples and are centered at the same positions in both cases. The intensity ratio between the Zn 2p 3/2 and Zn 2p 1/2 peaks for ZnO is ~2.2, while the same ratio for ZnO@ZIF-8 is ~2.3, values that are similar. Therefore, it is assumed that the introduction of the ZIF-8 shell does not induce any major change in the Zn 2p peak. Nonetheless, comparing the intensities of these two peaks between both samples, it is clear that the intensities for ZnO are considerably larger. By calculating the intensity ratio for Zn 2p 3/2 and Zn 2p 1/2 as the ratio of intensities between ZnO and ZnO@ZIF-8 it was observed that, for both peaks, the ZnO sample had an intensity around 2.3 times larger. This is attributed to a possible shielding effect caused by the ZIF-8 shell by which the intensity of the signal extracted during the experiment is reduced by the presence of the ZIF-8 shell. The two main peaks of Zn 2p are accompanied by two small satellite peaks, present for both samples. The origin of these two satellite peaks is unknown, although their presence does not seem to alter the chemical environment of the Zn in the NWs or core-shell NWs. To confirm the presence of the ZIF-8 shell, the N 1s peak was analysed, following a similar reasoning to the one detailed for the EDX studies. The spectra for the N 1s peak of ZnO@ZIF-8 is shown in Figure 7.11c. The region presented in this figure is that in which the N 1s peak typically is present, with the individual characteristic N 1s peak being typically centered at around 398 eV. However, no significant peak was identified in the spectrum, indicating that insufficient signal was obtained with the instrument. The two shoulder-like signals at 408 eV and 398 eV were recorded for all the analysed samples (with or without a ZIF-8 shell) and do not correlate with typical position of the N 1s peak[277]. Therefore, it was assumed that signals were part of the background the measurement itself and, hence, do not have any scientific value. As such, and as it occurred for the XRD analysis, the N 1s peak of the ZIF-8 was below the detection limit as the amount of nitrogen in the core-shell NWs was considerably low.

The O 1s peak was also investigated to assess any difference caused by the presence of the ZIF-8 shell. In principle, if the oxygen from ZnO reacts during the shell growth, forming water as a by-product, there should be a significant difference in the O 1s peak for the ZnO and the ZIF-8. This difference can be seen in the spectra provided in Figure 7.11d. Here, it is shown that the core-shell ZnO@ZIF-8 sample has a prominent shoulder centered at around 532 eV. To analyse this difference between both samples, the O 1s peak was deconvoluted for both samples. Typically, an O 1s peak for ZnO can be deconvoluted in to two contributions, named here O $1s_a$ and O $1s_b$. The former refers to the wurtzite lattice oxygens, while the latter indicates the presence of O^{2-} ions in oxygen deficient regions, related to the presence of oxygen vacancies. The compositional percentages for O $1s_a$ and O $1s_b$ are provided in the respective figures for ZnO (Figure 7.11e) and ZnO@ZIF-8 (Figure 7.11f). The increase in the O $1s_b$ component (and corresponding decrease of O $1s_a$) after the growth of the ZIF-8 shell indicates that the interfacial region of ZIF-8 and ZnO is oxygen deficient, which correlates with the theoretical explanation provided earlier. In addition, it was observed that $\sim$38% of the oxygen signal for ZnO was related to oxygen vacancies, in agreement with the results discussed in the optoelectronic study provided in Chapter 6 and with the literature[250]. As such, this analysis of the O 1s peak for ZnO and ZnO@ZIF-8 provides sufficient evidence, along with the previous characterization, to confirm the presence of the ZIF-8 shell on the ZnO NW cores.

7.3.4 Optoelectronic behaviour of ZIF-8 functionalized ZnO nanowires

UV-vis spectroscopy was used to study the optical properties of the ZnO@ZIF-8 core-shell ZnO NWs with different shells. Figure 7.12a shows a comparison of the UV-vis absorption of ZnO, ZnO:Co, ZnO@ZIF-8, and ZnO:Co@ZIF-8. For clarity, the legend in the figure refers only to the shell or doping integrated in the samples, using the HMIM concentration or the nominal percentual doping. A stacked representation of the UV-vis spectra here discussed has been included in Figure 7.12b for clarity purposes. The discussion of ZnO and ZnO:Co was provided in Chapter 6.3.2 and is included here for comparison. As a reminder, the red-shift observed for ZnO:Co is a result of the presence of a strong sp-d exchange interaction[278], with the shoulder at 380 nm being characteristic of ZnO (marked by black arrow) and the defect band
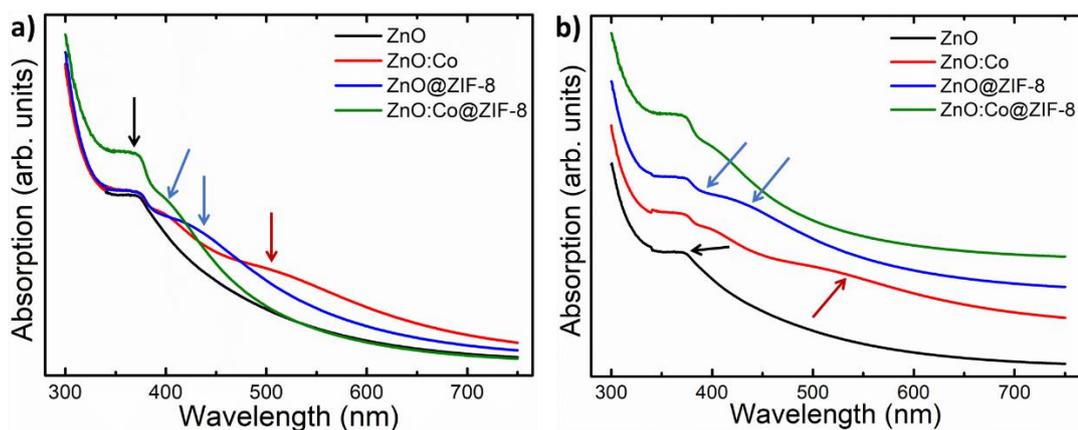
Figure 7.12. a) Ultraviolet-visible spectra of ZnO, ZnO:Co, ZnO@ZIF-8 and ZnO:Co@ZIF-8, showing the influence that the ZIF-8 shell has in the optical absorption properties of the ZnO NWs. The synergetic combination of Co-doping and ZIF-8 surface functionalization appears to be a promising approach for the enhancement of the functional performance of the ZnO NWs in photonic applications. The arrows indicate the shoulders discussed in the text: black for ZnO, red for Co-doping and blue for the ZIF-8 shell. **b)** Stacked representation of the UV-vis spectra shown in **a)**.

signal at 540 nm indicated by the red arrow. First, when the ZIF-8 shell is included, the absorption in the UV-blue range (300 nm to 375 nm) remains similar to that of ZnO and ZnO:Co. The absorption spectrum also shows two clear shoulders centered around 395 nm and 430 nm (marked by the blue arrows). The peak at 395 nm is characteristic of ZIF-8[279], while the one at 430 nm is still unidentified. The spectrum of ZnO:Co@ZIF-8 did not show this shoulder at 515 nm, suggesting that an in-depth analysis would be required to understand this shoulder. In addition, the shoulder at 395 nm characteristic of ZIF-8 was also seen for ZnO:Co@ZIF-8. This shoulder was combined with the one at 405 nm originated from the Co-doping of the NWs. The spectrum also showed a remarkably large UV-vis absorption in the 300 nm to 425 nm region, the largest of the four samples studied in this comparative analysis. In addition, there is a red-shift of the light absorption of about 15 nm as this sample achieves at 395 nm an absorption similar to what the other three samples provide at 380 nm. Therefore, the synergetic combination of Co-doping and ZIF-8 shell structuring shows promise in the enhancement of the optoelectronic properties for functional applications of the ZnO NWs.

The observation of the improvement of the light absorption properties of the functionalized ZnO NWs prompted further studies to unravel the influence of the ZIF-8 shell and its synergetic combination with Co-doping had on the optoelectronic properties of the ZnO NWs. The experimental details of the techniques used here are

described in Chapter 4.10. Fast-transient absorption spectroscopy (FTAS) analysis, measured by a pump-probe method, was carried out to determine the bandgap of the ZnO, ZnO:Co and ZnO:Co@ZIF-8 structures. The first two were discussed in detail in Chapter 6.4.2, while the last one is the focus of this discussion. Nonetheless, false colour maps for all three have been included here for comparison purposes. The pump energy was 4.5 eV (275 nm) and the broad probe was in the UV-vis region. As a reminder, the ZnO NWs showed a narrow, negative signal, indicative of an absorption bleaching centered at 3.3 eV, which corresponds to the bandgap of ZnO (Figure 7.13 a), while the cobalt doping of ZnO:Co (Figure 7.13 b) induced a redshift of the bandgap to lower energies, with the absorption bleaching signal centered at 3.18 eV, which equates to a wavelength shift of 15 nm. When the ZnO:Co NWs were functionalized with the ZIF-8 shell (Figure 7.13 c), the absorption bleaching signal is shifted further to 3.08 eV, with a less intense peak at the position of the bandgap of ZnO, which is attributed to the ZnO seed layer. The combined effect of this red-shift and the signal from the seed layer serve as an explanation for the large absorption observed in the UV-vis analysis shown in Figure 7.12. Nonetheless, the assumption that this signal is coming from the seed layer needs additional characterization to be confirmed. One significant feature of this FTAS analysis is how the bleaching signal of the ZnO:Co@ZIF-8 is much wider than for the other two samples studied, with a maximum of the bleaching signal going down to around 2.85 eV (435 nm). This can be correlated with the shift in the UV-vis absorption observed at around 405 nm in Figure 7.12. The FTAS signal observed at 2.25 eV for ZnO and ZnO:Co is an experimental artefact coming from the second order of the pump energy.

To better represent the red-shift of the bandgap after doping with cobalt and functionalizing with ZIF-8, the normalized difference in absorbance (ΔA) as a function of probe energy at a probe delay of 1 ps is shown in Figure 7.13 d. The red-shift in the absorption bleaching observed in the false colour maps is clearly shown here. In addition, the large width of the bleaching signal of ZnO:Co@ZIF-8 can be observed easily in this representation. Remarkably, the absorption signal of ZnO:Co@ZIF-8 extends over the entire probe range. The time dependence of the bandgap bleaching signal was studied for these three samples, as shown in Figure 7.13e. This analysis shows that a faster decay of the bandgap bleaching can be observed for ZnO:Co and

213
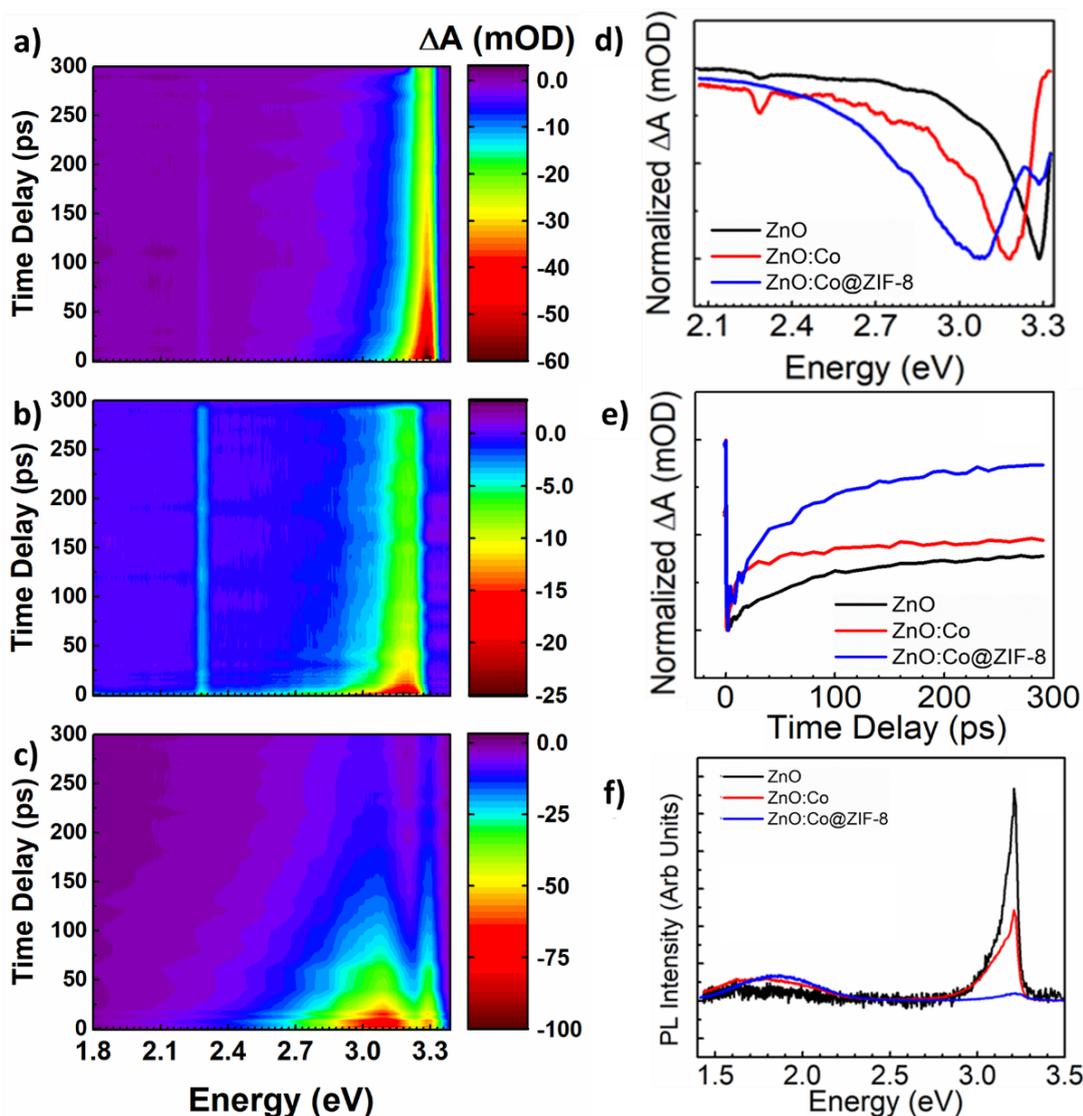
Figure 7.13. Fast transient absorption spectroscopy false colour maps of **a)** ZnO, **b)** ZnO:Co and **c)** ZnO:Co@ZIF-8. **d)** Energy and **e)** time dependent analysis of the absorption bleaching signal for the three studied samples. **f)** Photoluminescence spectroscopy of ZnO, ZnO:Co, and ZnO:Co@ZIF-8, showing a quenched signal around the bandgap of ZnO.

even faster for ZnO:Co@ZIF-8. This is attributed to alternative non-radiative decay pathways for the charge carriers, as a result of the introduction of a d-d transition in the bandgap by the effect of the Co-doping[280, 281] and due to the presence of the ZIF-8 shell.

Photoluminescence (PL) spectroscopy analysis was carried out on ZnO, ZnO:Co and ZnO:Co@ZIF-8 to provide a better understanding of the influence of the ZIF-8 shell on the optoelectronic properties of the ZnO NWs. The PL of ZnO shows a strong peak around 3.27 eV (Figure 7.13f), corresponding to the band edge (BE) recombination from the bandgap. For ZnO:Co, the intensity of the PL signal of the BE

recombination is significantly smaller, while a broader peak centered around 1.9 eV appears. This broad peak is attributed to the characteristic oxygen vacancies of ZnO.[250, 259] In the case of the ZnO:Co@ZIF-8 core shell NWs, the BE is highly quenched, while the defect band of the oxygen vacancies still shows luminescence. The decrease in the PL intensity of the BE combined with the decrease in the decay time for the absorption bleaching signal (Figure 7.13e) in the presence of the Co doping and the ZIF-8 suggests two distinct and simultaneous influences, namely, the availability of multiple non-radiative recombination pathways and increased carrier trapping from the increased surface defects density in the presence of both the doping and the ZIF-8. The availability of the non-radiative recombination pathways was observed in the time dependent FTAS analyses, while the higher concentration of oxygen vacancies was a result obtained from the XPS analyses in Figure 7.11. The confirmation of these two characteristics of the ZnO:Co@ZIF-8 core-shell NWs shows promise towards the enhancement of the PEC performance of water splitting photoanodes based on these nanowires.

7.4 Conclusions

In this chapter, the surface functionalization of ZnO NWs, either undoped or doped with cobalt, was presented and discussed. Two different materials and integration approaches were used separately as functionalizing agents, namely iridium self-assembled NPs and a MOF shell. The Ir self-assembled NPs were deposited by sputtering at relatively high base pressures, resulting in the development of Ir NPs on the lateral surface of ZnO NWs. The NWs were homogeneously decorated with these iridium NPs, which were observed in detailed morphological analyses by SEM and HRTEM that helped in demonstrating the integration of the Ir NPs on the ZnO NWs. It was shown that, by changing the deposition time in the sputter system, while maintaining other growth conditions constant, a direct increase of NP size from ~2 nm to ~3 nm was achieved. This change in NP size had a clear influence on the optical absorption properties of the Ir-functionalized ZnO NWs, with the samples with larger NP size yielding a poorer performance than those with smaller NPs. Significantly, the presence of the homogeneous decoration of Ir NPs on the surface of the ZnO NWs was demonstrated by means of EDX elemental mapping.

Regarding the MOF functionalization, ZIF-8, a Zn-based MOF, was chosen as the material to be used to form an outer shell that conformally coated the ZnO or ZnO:Co cores. Two different approaches, drop casting and spin coating, to integrate the MOF were investigated. Both were based on using the ZnO NWs as templates for the growth of the shell. Detailed SEM morphological analysis of both routes demonstrated that spin coating was the technique that was successful in terms of thickness control and long-range homogeneity. Drop casting yielded a ZIF-8 shell that bridged the gaps between individual NWs to the point of forming quasi-continuous ZIF-8 films, which was not the target outcome. In contrast, spin coating yielded shells with a controllable thickness that were constrained to their respective individual NWs. Changing the spin speed during the spin coating proved to be a successful strategy for controlling the thickness of these shells. HRTEM and EDX were used to study the morphological interplay between the ZnO:Co cores and ZIF-8 shells. This showed that the spin coated ZIF-8 shell conformally coated the ZnO:Co NW cores with a thickness of 2 nm. Moreover, the EDX elemental maps showed a homogeneous distribution of the Co-doping and nitrogen from the ZIF-8 shell, which served as further evidence of the successful integration of ZIF-8 and ZnO:Co NWs.

The chemical environment of these core-shell NWs was analysed using XPS. This analysis demonstrated that when comparing ZnO and ZnO@ZIF-8, an increase in the density of surface defects in the form of oxygen vacancies was observed, indicating the growth of the ZIF-8 shell. Finally, the optoelectronic properties of the ZnO:Co@ZIF-8 core-shell NWs were studied by means of UV-vis spectroscopy, FTAS and PL. The combined results of these three techniques demonstrated a synergetic integration of the ZnO:Co cores and ZIF-8 shells by which the optical absorption was largely improved in the UV and near blue region between 300 nm and 425 nm. In addition, this integration pointed towards the availability of non-radiative recombination pathways, which could have a beneficial use in functional photonic applications. Finally, the presence of an increasing density of oxygen vacancies was observed by these optical techniques, similarly to what was observed in Chapter 6, pointing towards a possible improvement of the functional application of these core-shell NWs. In summary, two different approaches for the surface functionalization of

ZnO NWs with enhanced optical properties were demonstrated, which show promise as enhancing functionalizations of the PEC performance of the ZnO NWs.

Chapter 8

ZnO nanowire based water splitting photoanodes

8.1 Introduction

This chapter describes the results obtained from a detailed study of the photoelectrochemical performance of the ZnO nanowire (NW) based photoanodes for water splitting. The nanomaterials used as photoanodes are those described in Chapters 5, 6 and 7, while the discussion of the theoretical principle of photoelectrochemistry is presented in Chapter 2.4. There are three main functional measurements used in this work to understand and quantify the performance of the NW-based photoanodes, namely cyclic sweeping voltammetry (CSV), both under illumination and in dark conditions, *I-t* amperometric measurements and the study of the incident photon-to-current efficiency (IPCE), which were described in Chapter 2.4.3. Regarding the CSV, prior to the measurement, the samples were stabilized by running a set of cyclic potential sweeps for 10 minutes to ensure that no transitionary effects were in place and that the measurement would accurately reflect the stable functional behaviour. These three techniques provide information regarding the maximum current density generated by the photoanodes, their on-off behaviour and the efficiency with which they convert the incoming photons into current. Different

types of ZnO NWs were studied in order to understand how the performance of base ZnO NWs could be enhanced by means of cobalt doping and through surface functionalization with a metal-organic framework (MOF). In this case, the zeolitic imidazolate framework 8 (ZIF-8) was selected. The overall goal was finding the optimal configuration that would maximise the photoelectrochemical (PEC) performance with the materials studied. The discussion presented in this chapter has this core concept as the focal point.

8.2 Key technical and experimental details

All of the nanowires discussed in this chapter were grown on indium-tin oxide (ITO) substrates, using a textured ZnO seed layer deposited by sol-gel processing. The NWs were grown by chemical bath deposition (CBD), with a growth time of 6 hours and equimolar reagent concentration of 25 mM. The specifics of the Co-doping and the ZIF-8 surface functionalization are discussed in this chapter in terms of the nominal percentage of cobalt doping and the concentration of the organic linker (2-methylimidazole, HMIM), respectively. The discussion of the morphology and the optical properties of the undoped, doped and surface functionalized NWs was provided in the earlier chapters.

All the photoelectrochemical measurements in this chapter were carried out under AM 1.5 G illumination (either continuous or time chopped, with the chopping done manually) and, unless stated otherwise, the applied potential was 1.33 V relative to the reversible hydrogen electrode (RHE), abbreviated here as 1.33 V_{RHE}. The definition of the illumination used was provided in Chapter 2.4.2. For the CSV measurements and unless otherwise specified, a single cycle is shown. More details on the experimental characteristics of the measurements were provided in Chapter 4.11.

8.3 Photoelectrochemical analysis of ZnO nanowires

The first step in the PEC analysis of the NW-based photoanodes was to assess the properties of undoped, non-functionalized ZnO NWs. Figure 8.1a shows the CSV in two different conditions, under illumination (labelled as light) and in dark conditions, with no illumination (labelled as dark). The CSV in dark conditions shows that the ZnO NWs do not generate any photocurrent within the studied potential region. There is
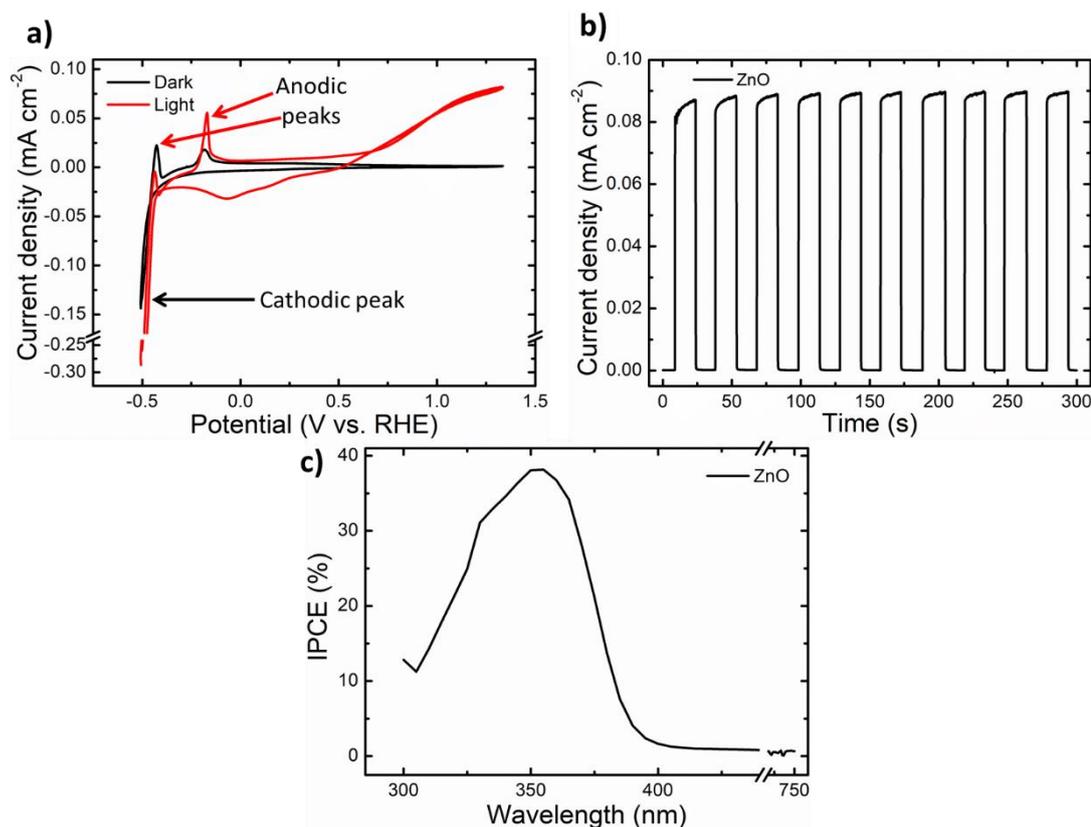
Figure 8.1. Photoelectrochemical characterization of ZnO nanowire-based photoanodes. **a)** Cyclic sweeping voltammetry (CSV) under illumination and in dark conditions. The red and black arrows indicate the anodic and cathodic peaks observed in the voltammetry as a result of the liquid junction potential. **b)** Transient amperometric analysis obtained at 1.33 V_{RHE} under time-chopped AM 1.5 G illumination. **c)** Incident photon-to-current efficiency, measured at 1.33 V_{RHE}.

a large cathodic peak at -0.51 V that was the result of a measurement artefact. The reference electrode used for this measurement was kept in deionized water (DI water) salt bridge (see Chapter 2.4.3), while the working electrolyte was an aqueous KOH solution of pH 13. Thus, a liquid junction potential was generated between the two different liquids, which resulted in the large cathodic peak observed, indicated by the red arrows. This experimental mistake was corrected for the other measured samples. The theory behind the liquid junction potential was provided in Chapter 2.4.3. There are two peaks corresponding to anodic currents at -0.43 V and -0.18 V (indicated by the red arrows) that are attributed to the stabilization of the electrode, due to the presence of the liquid junction potential between the DI water and the electrolyte. Therefore, the experimental error induced by the liquid junction potential resulted in the respective reduction and oxidation reactions for the cathodic and anodic peaks, thus the presence of these peaks. In summary, the CSV in dark conditions showed that, for the potential range studied, ZnO does not generate

any meaningful current density outside of those peaks coming from the formation of a liquid junction potential.

Under illumination, the CSV also shows the same cathodic and anodic peaks related to the formation of the liquid junction potential but the anodic peak is more prominent due to the additional photonic excitation induced by the light source. As the applied potential increases, the photogenerated current density increases, starting from around 0.05 V. This increased continuously until a maximum current density of 0.08 mA cm^{-2} was obtained at the maximum applied potential of 1.33 V$_{RHE}$. Regarding the cathodic part of the voltammogram, there is a broad negative peak in the current density in the potential region between -0.3 V and 0.3 V that was not observed in the dark voltammetry. This peak is related to the presence of stable oxygenated reaction intermediates (peroxides, superoxides) on the surface of the ZnO NWs[282]. These intermediates are stabilized by the abundant surface defects of ZnO, more specifically oxygen vacancies[283]. These oxygen vacancies were briefly mentioned in Chapter 3.2 and observed in the results shown in Chapter 6.4 and 7.3.

Considering now the time dependent response, the on-off response to illumination of the ZnO NW photoanode was studied by means of transient amperometric analysis (Figure 8.1b). This measurement was carried out under AM 1.5 G time-chopped illumination, with each on and off pulse corresponding to the illuminated and dark periods lasting 15 seconds, which was chosen to ensure enough time to obtain a stable signal. In the first three on-off illumination cycles, there is a steady increase in the maximum current density obtained. After the third cycle, the current density remains constant for all the subsequent switching cycles. The maximum value of the current density obtained was 0.9 mA cm^{-2}, almost 10% higher than what was seen in the CSV of Figure 8.1a. In addition, the initial illumination cycles show transitionary behaviour during the 15 second windows in which the current density slowly increases, which diminished in the later cycles. With regards to the off cycles, in dark conditions, it can be seen that the current density is at or close to 0 mA cm^{-2} for all the cycles, corresponding to what was observed in the dark CSV. All in all, the ZnO NW-based photoanode shows an adequate on-off behaviour in which the on and off switching of the illumination source is immediately followed

by the response of the photoanode, with very sharp edges that represent response times of around 200 ms.

The IPCE measurement of the ZnO NW-based photoanode is shown in Figure 8.1c. It was carried out as an energy sweep that ranged from 300 nm to 750 nm. For this, the light source was passed through a monochromator before impinging on the photoanode to select single wavelength photons. The IPCE is deeply bound to the optical properties of the ZnO NWs, which were detailed in Chapter 6. The active region of the as-grown ZnO NW-based photoanode is in the range from 300 nm to 400 nm. From 400 nm until 750 nm, the value of the IPCE remains close to 0%, hence the break in the x-axis in the plot. Significantly, the maximum IPCE is achieved at 350 nm, yielding a value of 38%. For shorter wavelengths down to 300 nm, the IPCE decreases steadily until it reaches a minimum of 11% at 305 nm. For longer wavelengths, the IPCE also decreases, reaching a value of 1.6% at 400 nm. Thus, the window in which the ZnO NWs are photoactive is constrained to the near ultraviolet (UV) and blue region. The UV-visible absorption spectra of Figure 6.2 showed that the ZnO NWs absorbed in the near UV and blue region, while the absorption signal in the rest of the visible region was attributed to the scattering of light caused by the NWs, hence why this signal does not necessarily translate into photocatalytic activity. Considering this light scattering and the characteristic overpotential[22, 284] of the water splitting process (see Chapter 2.4.1), which means that there is a minimum amount of energy that is required to initiate the water splitting process, it is safe to assume that the absorption signal at low energies was not a big enough contribution to overcome the oxidation of water overpotential OP_{OER}, which explains why the IPCE reaches almost zero at 400 nm, while the UV-visible absorption of the ZnO NWs spans almost the whole visible region.

8.4 Influence of cobalt doping on the photoelectrochemical performance of ZnO nanowires

The first enhancement of the photoelectrochemical (PEC) performance of the ZnO NWs that was studied was the use of cobalt doping. In this case, three different levels of nominal cobalt doping were studied, specifically 1%, 5% and 20%. Nominal doping refers to the ratio between cobalt nitrate and zinc nitrate introduced in the growth

solution, with the real value of cobalt integrated being difficult to accurately determine, but expected to be lower than the nominal percentage here provided, as described in Chapter 4.5.1. The results shown in Figure 8.1 for the undoped ZnO NWs were also included here on a comparative basis. The CSV in dark conditions for the undoped and Co-doped ZnO NWs are shown in Figure 8.2a. The main feature observed in this analysis is that the peaks related to the formation of a liquid junction potential for ZnO were not present for any of the doped samples. No current density was generated in the anodic sweep of the potential range, similarly to what was seen for ZnO. A small cathodic current was observed for 1% ZnO:Co and 20% ZnO:Co at around 0.12 V, which may be related to the presence of stable oxygenated reaction intermediates as previously explained. However, this was not seen for 5% or 10% doping so there is no certainty on whether this is a physical feature of the two systems or just an artefact during the measurement.

The CSV under illumination for the undoped and Co-doped ZnO NWs is presented in Figure 8.2b. Considering the 1% ZnO:Co, this doping level provides the highest current density out of the three levels studied, reaching a maximum current density of 0.12 mA cm^{-2} at 1.33 V$_{RHE}$, which is a 50% increase compared to ZnO. There is a very significant cathodic current in the 0.3 V to -0.3 V applied potential region, larger than that of ZnO, which is related to the increasing concentration of oxygen vacancies associated with the cobalt doping, as described in Chapter 6.4. The large amount of these surface states prompts the stabilization of a high number of oxygenated intermediate species that are the cause of the large cathodic current shown in this region[285]. In fact, this cathodic current increased with the number of CSV cycles studied. For this analysis, two consecutive cycles were analysed, with the results from the second cycle being used in the comparative figures. The second cycle was selected as the one to include in the comparative figures as it was deemed to be a more accurate representation of the real performance than the first one due to possible transitionary components that could be observed in the first cycle. Figure 8.2c shows the two cycles studied for 1% ZnO:Co. It can be seen that the cathodic current in the low applied potential regions increased from the first to the second cycle, a sign that the stabilization of the oxygenated intermediates was an ongoing
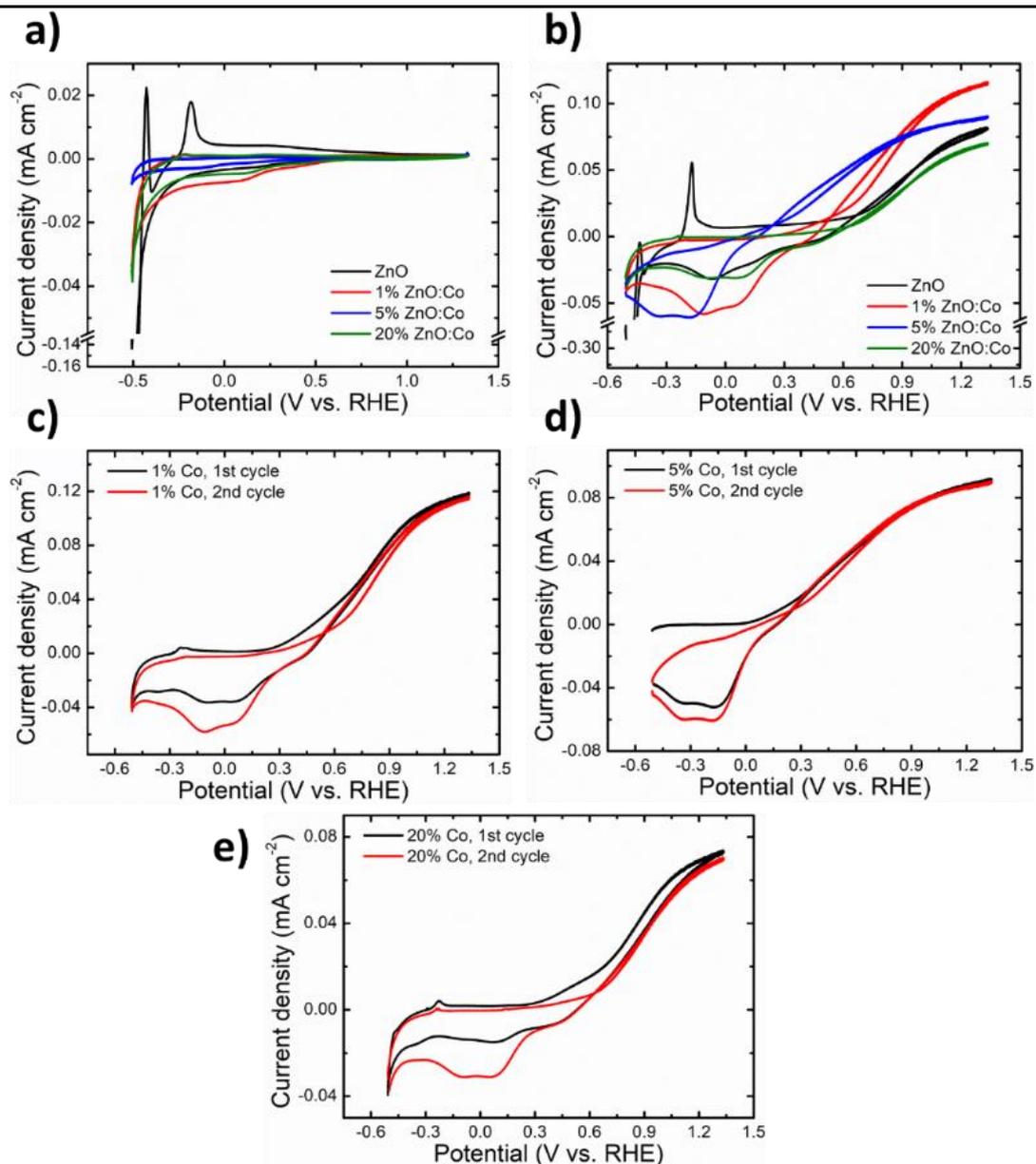
Figure 8.2. Cyclic sweeping voltammetry analysis of undoped and ZnO:Co samples in **a)** dark conditions and **b)** under illumination. Two consecutive cyclic sweeping voltammetry cycles of **c)** 1% ZnO:Co, **d)** 5% ZnO:Co and **e)** 20% ZnO:Co.

process. It is suspected that this cathodic current would reach a maximum once the surface states of 1% Co ZnO:Co are completely filled.

Once the doping level was increased to 5% ZnO:Co, the current density obtained at 1.33 V_{RHE} was reduced to 0.09 mA cm^{-2} compared to 1% ZnO:Co, a 25% reduction. The cathodic current in the low applied potential region is also present for this sample, although this current is shifted to the 0 V to -0.5 V potential region. The two CSV cycles shown in Figure 8.2d for 5% ZnO:Co show that the cathodic current is similar in both cycles, albeit slightly smaller for the second one, which contrasts with

what was observed for 1% ZnO:Co. Considering the 20% ZnO:Co sample, the current density obtained for this high doping level at 1.33 V_{RHE} was 0.07 mA cm^{-2}, which is smaller than that of undoped ZnO. The cathodic current observed for this sample was similar to the one of ZnO. In fact, this cathodic current was very small in the first cycle of the analysis (Figure 8.2e), but increased significantly in the second CSV cycle.

After analysing the influence of the Co-doping in the CSV analysis, the on-off illumination behaviour of these photoanodes was studied by transient amperometric measurements of the four samples (Figure 8.3a). The deviations observed in the on-off cycle times are due to the manual chopping of the illumination. The 1% ZnO:Co photoanode showed the largest current of the Co-doped photoanodes, yielding a maximum current density of 0.110 mA cm^{-2}, slightly lower than what was observed in the CSV. Significantly, there is a downwards trend of this current density for the last few cycles of the analysis, reaching 0.107 mA cm^{-2} for the last cycle. The on-off illumination behaviour of this sample is similar to that of undoped ZnO, while still showing the transitionary increase of the current density at each on cycle, similar to ZnO. Considering the 5% ZnO:Co photoanode, the current density obtained in the amperometric analysis was lower than that observed in the CSV, showing a value of 0.075 mA cm^{-2} compared to the 0.090 mA cm^{-2} of the CSV. This sets this current below that of ZnO while the opposite was observed in the CSV study. The reason for this may be attributed to the disappearance of the liquid junction potential, although more analysis would be required to prove this hypothesis. Nonetheless, the on-off behaviour of this photoanode is similar to that of the previously discussed samples. The transitionary increase of the current density in the on cycles is still present. The current density provided by the 20% ZnO:Co sample in the amperometric analysis is of 0.065 mA cm^{-2}, a value similar to the 0.070 mA cm^{-2} observed in the CSV. This photoanode shows a similar on-off behaviour to the other samples, with sharp transitions between the on and off states. The three doped samples show a similar transition response to the on-off illumination switching, with a response time between both states of 200 ms, same as that of ZnO.

The wavelength-dependent measurement of the IPCE of the undoped and Co-doped samples is shown in Figure 8.3b. The 1% ZnO:Co photoanode shows the largest
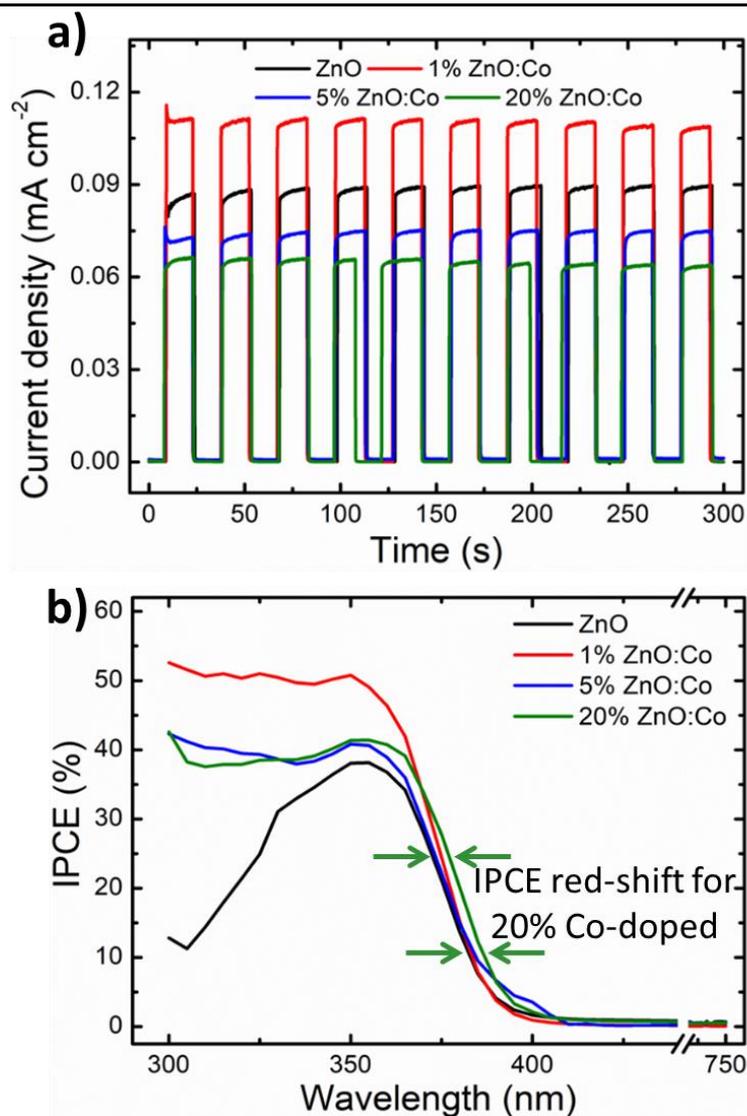
Figure 8.3. a) Transient amperometric analysis with chopped on-off illumination and **b)** incident photon-to-current efficiency measurement of undoped and cobalt-doped ZnO nanowire-based photoanodes. These were carried out at 1.33 V_{RHE} under AM 1.5 G illumination (chopped and continuous, respectively).

IPCE of the four samples studied, achieving 51% IPCE at 305 nm, which is almost a 40% increase with the respect to ZnO. Significantly, the cobalt doping boosts the IPCE in the UV region to values much larger than those observed for ZnO. The IPCE obtained in this region for ZnO was 11% at a wavelength of 305 nm. Considering the longer 350 nm wavelength, 1% ZnO:Co shows an IPCE of 52%, slightly larger than that of undoped ZnO. There is a small red-shift in the IPCE for 1% ZnO:Co compared to ZnO, observed at 370 nm, which correlates with the results obtained from the optoelectronic characterization discussed in Chapter 6.4. Considering the 5% ZnO:Co photoanode, the IPCE obtained at 350 nm is 41%, which is 10% lower than for the 1%

doped sample. The enhancement of the IPCE in the UV region is also present, albeit with a less impactful improvement than for the 1% Co-doped sample, achieving an IPCE of 41% at 305 nm. No significant red-shift was observed for this sample. Finally, the 20% ZnO:Co photoanode shows a very similar IPCE curve to 5% ZnO:Co, with almost no difference in the IPCE value obtained at 350 nm; considering the signal at 305 nm, the IPCE of 20% is reduced to 38%, a slight reduction compared to 5% doping. Nonetheless, the 20% samples showed a consistent 5 nm red-shift in the IPCE spectrum compared to ZnO. This red-shift does not directly match with what was observed in the optical characterization of the sample, which was attributed to the water splitting overpotentials mentioned earlier in Chapter 8.2.

The photoelectrochemical characterization provided here for the ZnO:Co photoanodes clearly showed that a 1% nominal doping yielded the best results in terms of current density photogenerated and IPCE. Remarkably, as the cobalt doping was increased, the PEC performance of the NWs diminished. The explanation for this effect can be directly related to the optoelectronic characterization shown in Chapter 6. Effectively, as the doping concentration was increased, the density of the surface defects on the NWs also increased. In principle, the surface defects act as non-radiative trap sites (mentioned in Chapter 6 as charge carrier trapping sites) that help the separation of the photogenerated electron-hole pairs, by trapping the electrons in these surface defects that are related to the sp-d localized states introduced by the cobalt doping[286, 287]. In this way, the photogenerated holes, which initiate the water splitting process (see Chapter 2.4.1), are separated from the electrons and can reach the water, initiating the water splitting process and contributing towards the photocurrent and, therefore, to the IPCE. This enables the high values obtained for both the photocurrent and IPCE for the cobalt-doped ZnO NW samples. However, this mechanism is true only for the 1% ZnO:Co sample, as evidenced by the trend shown in the PEC measurements. As the cobalt doping increases, it is proposed that the density of surface defects that produce trap states becomes so high that they form a continuous pathway through which the carriers can move. This correlates with the CL analysis provided in Chapter 6.4.3. Therefore, these trap states no longer act as non-radiative recombination sites that separate the photogenerated charges and, instead, act as a secondary pathway for these carriers. As a result, the rate at which

the photogenerated holes are separated from the electrons is greatly reduced, resulting in a lower current density, which is therefore less efficient, as shown in the CSV and IPCE measurements. Thus, 1% Co-doping was selected as the ideal nominal doping value owing to its superior photoelectrochemical performance due to its enhanced charge separation mechanism.

8.5 ZIF-8 shell influence on undoped ZnO nanowires

The second enhancement of the photoelectrochemical (PEC) performance of the ZnO NWs that was studied was the surface functionalization of the ZnO NWs with a ZIF-8 shell. For this, a study of the influence of the ZIF-8 on undoped ZnO NWs was carried out. The ZIF-8 shell was deposited accordingly to the conditions of the one that yielded the best morphological and optoelectronic properties, as per the results shown in Chapter 7.3. In short, this ZIF-8 shell was deposited by spin coating a methanol solution containing a 1 M concentration of the 2-methylimidazole organic linker, using a spin speed of 5000 rpm for 30 seconds. The subsequent step was the pre-growth evaporation of the solvent, carried out at 65°C for 5 minutes. Finally, the ZIF-8 shell was grown at 160°C for 15 minutes. Unless otherwise specified and from now, whenever the term ZIF-8 appears as part of the name of a sample, it will refer to this particular growth conditions. A detailed description of the growth of the ZIF-8 shell was provided in Chapter 4.6.2.

The CSV under dark conditions of ZnO and ZnO@ZIF-8 1 M is shown in Figure 8.4a. This voltammetry shows that the introduction of the ZIF-8 shell does not induce any dark current, replicating the results obtained for undoped and Co-doped ZnO NWs. There is a small cathodic current at around 0.15 V, although its magnitude was not significant. The CSV under illumination (Figure 8.4b) shows that the integration of the ZIF-8 shell as surface functionalization greatly enhances the PEC performance of the ZnO NW photoanodes. In particular, ZnO@ZIF-8 1 M shows a current of 0.120 mA cm^{-2} at 1.33 V$_{RHE}$, a 50% increase over ZnO. This increase was similar in value to the improvement seen for the 1% ZnO:Co, hinting at the possibility of integrating these enhancers together. More importantly, the presence of the ZIF-8 completely eliminates the cathodic current seen for the undoped and Co-doped NW-based photoanodes in the low applied potential region. This means that the stable
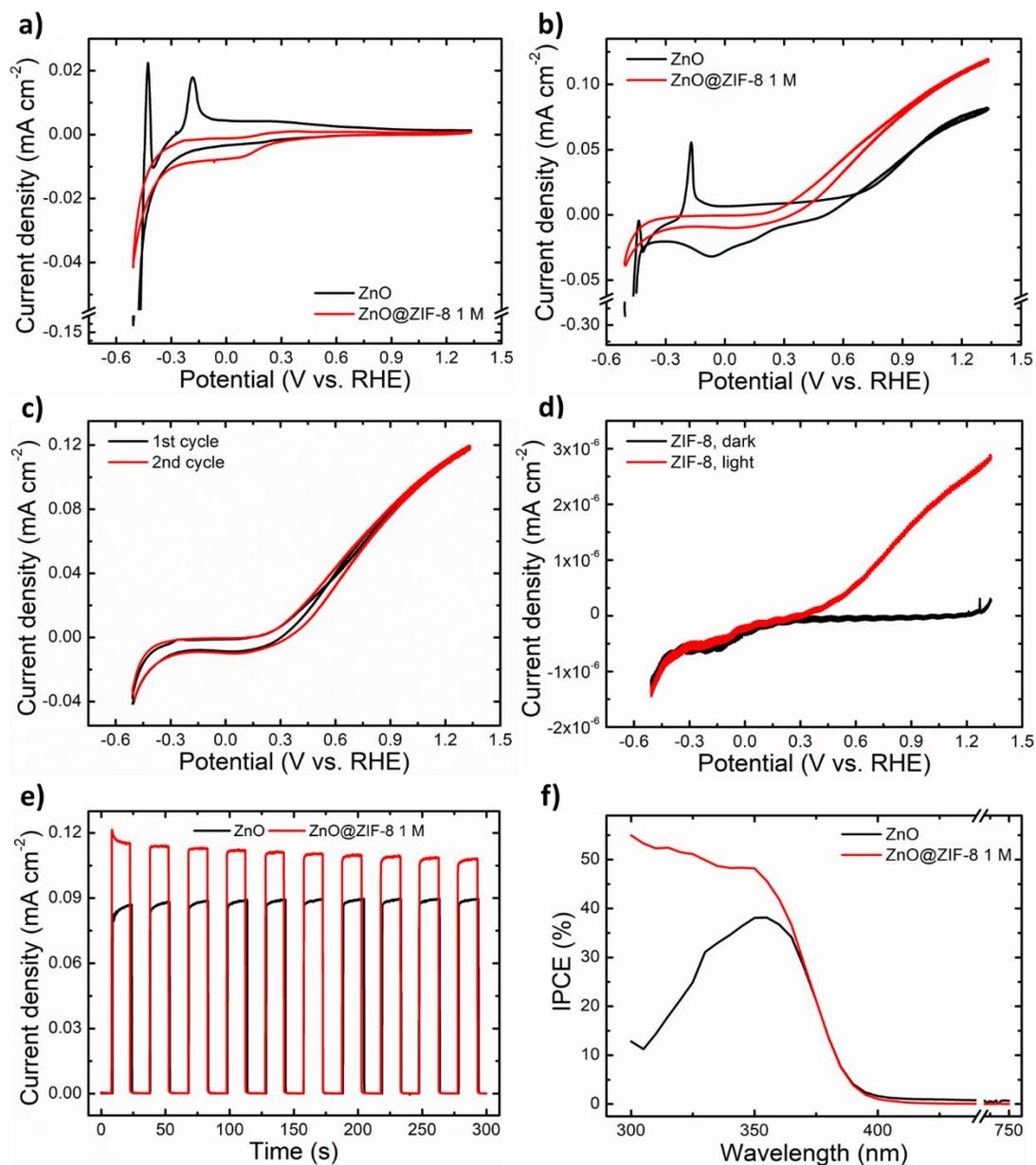
Figure 8.4. Cyclic sweeping voltammetry analysis of ZnO and ZnO@ZIF-8 **a)** in dark conditions and **b)** under illumination. **c)** Two consecutive voltammetry cycles under illumination. **d)** Linear sweeping voltammetry of a ZIF-8 thin film. **e)** Transient amperometric study and **f)** incident photon-to-current efficiency of ZnO and ZnO@ZIF-8. The amperometric study and incident photon-to-current efficiency were carried out at 1.33 V_{RHE} under AM 1.5 G illumination (chopped and continuous, respectively).

oxygenated intermediates that were the source of this cathodic current are no longer formed on the core-shell NWs. This is attributed to the fact that the ZIF-8 shell passivates the external surface of the NWs, quenching the formation of the stable intermediates as it supresses the surface defects of ZnO[273]. Considering the two subsequent CSV cycles under illumination shown in Figure 8.4c, it can be seen that the ZIF-8 shell stabilizes the performance of the photoanodes over the separate

cycles. In contrast, for both undoped and Co-doped NWs, it was shown that the cathodic current induced differences for the consecutive voltammetry cycles.

One additional topic to discuss with regards to the voltammetry of the core-shell NWs is where the photocurrent is being generated or, in other words, whether the ZIF-8 shell generates any meaningful current or not. In Chapter 7.3.4 it was demonstrated that the ZIF-8 shell enhances the optoelectronic properties of the ZnO NWs and, thus, it is possible that they have some photoactivity. To prove this, a ZIF-8 thin film was grown on an ITO substrate. For this, a ZnO seed layer was deposited and subsequently converted to ZIF-8 by the same process with which the ZIF-8 shell is grown. Then, a cyclic voltammetry study was carried out on this sample, both in dark conditions and under illumination, as shown in Figure 8.4d. While in dark conditions the ZIF-8 film generates no current density, it does generate a photocurrent when subjected to illumination. Nonetheless, this photogenerated current is rather low, being one order of magnitude smaller than any other reported current density so far. This correlates with the considerably smaller contribution of the ZIF-8 shell to the total mass of the core-shell NW structure discussed in Chapter 7. All in all, this demonstrates that ZIF-8 is photoactive, meaning that it generates electron-hole pairs that produce a current density when subjected to an illumination. This is in line with other works in the literature that use ZIF-8 for different photonics based applications[271, 288].

Attending to the transient amperometric studies of ZnO and ZnO@ZIF-8, Figure 8.4e shows on-off illumination behaviour equivalent to that previously discussed for undoped and doped samples, with sharp switching peaks between the two regimes. The core-shell sample shows two distinct components to this behaviour that contrast with the previously discussed photoanodes. First, the current density obtained in the initial amperometric cycle is similar to that observed in the CSV. However, this current steadily decreases with increasing cycles down to 0.108 mA cm^{-2} for the last cycle. This is attributed to a stabilization process of the shell that would take place in form of the removal of any residual molecules from the growth within the pores of ZIF-8, although there was no conclusive proof to demonstrate this hypothesis. Second, the current density obtained in this measurement is stable throughout the whole cycle (with the exception of the very first one), which is opposite to what was

previously observed for the NWs without a shell, in which the current density increased during each illumination cycle.

The IPCE of ZnO and ZnO@ZIF-8 is shown in Figure 8.4f. The integration of the ZIF-8 boosts the IPCE of the ZnO NWs similarly to 1% ZnO:Co, with the IPCE at 350 nm being 48% for the core-shell NWs. Furthermore, a greater enhancement from the shell occurs in the UV region, as demonstrated by the 53% IPCE obtained at 305 nm, which is larger than any of the previously discussed samples. The reason behind this improvement can be found in the optoelectronic properties of ZIF-8. ZIF-8 is a material known for its considerable light absorption in the UV region[289], as was shown in Figure 7.12 of Chapter 7.3.4. That large absorption in the UV region is translated into the enhancement of the IPCE in the 300 nm to 350 nm region. The fact that no spectral shift in the IPCE was observed is in good agreement with the aforementioned UV-vis results.

As a summary, the integration of the ZIF-8 shell with ZnO NWs resulted in a successful improvement of the PEC performance of the photoanodes. This is due mainly to the joint effects of the surface passivation provided by the ZIF-8 shell, which supresses the typical surface defects of ZnO, and the intrinsic photoactivity of ZIF-8. These results suggest that there is a synergetic interplay between the ZnO NW core and the ZIF-8 shell, which is explored and detailed in a later section of this chapter.

8.6 Influence of the ZIF-8 shell on the photoelectrochemical performance of cobalt doped ZnO nanowires

Based on the promising results that the Co-doping and ZIF-8 functionalization separately yielded on the PEC performance of the ZnO NW-based photoanodes, it was decided to bring these two strands of work together. For this, the ZnO NWs were doping with a nominal 1% Co-doping and subsequently functionalized with a ZIF-8 shell deposited with a 1 M concentration of the organic linker. The results of the detailed PEC study of this sample (1% ZnO:Co@ZIF-8 1 M, labelled as ZnO:Co@ZIF-8 for simplicity) are shown in Figure 8.5 and compared to those of ZnO, 1% ZnO:Co and ZnO@ZIF-8 1 M. The CSV in dark conditions (Figure 8.5a) shows that ZnO:Co@ZIF-8 has very similar behaviour to ZnO@ZIF-8, with no dark current generated at any applied potential and only a small cathodic current at 0.15 V. The CSV under

Figure 8.5. Comparative photoelectrochemical study of ZnO, ZnO:Co, ZnO@ZIF-8 and ZnO:Co@ZIF-8. Cyclic sweeping voltammetry **a)** in dark conditions and **b)** under illumination, **c)** transient amperometric study and **d)** incident photon-to-current efficiency measurement. The amperometric study and incident photon-to-current efficiency were carried out at 1.33 V_{RHE} under AM 1.5 G illumination (chopped and continuous, respectively).

illumination of ZnO:Co@ZIF-8 (Figure 8.5b) shows that the joint effects of Co-doping and ZIF-8 functionalization enhance the current density generated by this integrated photoanode, achieving a value of 0.150 mA cm^{-2} at 1.33 V_{RHE}, which is almost double the value of the base ZnO NWs. This demonstrates that there is a synergetic interaction between the ZnO:Co core and the ZIF-8 shell, by which the PEC performance is considerably boosted. Another interesting feature of this voltammetry is the presence of a small cathodic current around 0.15 V, which is attributed to the presence of the Co-doping in the ZnO NW core. The Co-doping in ZnO:Co induced a large cathodic current related to the introduction of surface defects on the ZnO NWs and, even if the ZIF-8 shell was proven to successfully supress these defects for ZnO, the presence of the Co-doping still induced the small cathodic current seen for ZnO:Co@ZIF-8 in this CSV.

The transient amperometric study of ZnO:Co@ZIF-8, shown in figure 8.5c, has two main crucial features compared to ZnO@ZIF-8. First, the transitionary state of

the initial illuminated cycles is much more significant, with the current density falling significantly for the first five cycles. Second, this decline is stabilized for the later cycles, a feature not present in ZnO@ZIF-8. This suggests that the photogenerated current density of ZnO:Co@ZIF-8 would, in principle, be more stable over a longer time for the doped-core-shell ZnO NWs. Once in a stable state, this current has a value of 0.14 mA cm^{-2}, which is comparable with the 0.15 mA cm^{-2} obtained from the CSV. The on-off illumination switching behaviour of ZnO:Co@ZIF-8 is comparable to the other samples studied, with very sharp switching edges. The IPCE analysis of the doped-core-shell NWs is shown in Figure 8.5d. The combined influence of the Co-doping and ZIF-8 surface functionalization boosts the IPCE of ZnO:Co@ZIF-8 to almost 78% in the UV region (at 305 nm), while the IPCE at 350 nm achieves a value of 75%, one and a half times higher than any other IPCE shown here. Furthermore, the IPCE of ZnO:Co@ZIF-8 shows a 15 nm red-shift compared to ZnO, which directly correlates with the optoelectronic characterization shown in Chapter 7.3.4. These results clearly demonstrate the potential improvement that the integration of cobalt doping and surface functionalization with ZIF-8 can have on the photoelectrochemical performance of ZnO NWs, especially in terms of the largely enhanced current generation efficiency in the near-ultraviolet and blue region of the electromagnetic spectrum.

8.7 Study of different ZIF-8 shells on the on the photoelectrochemical performance of cobalt doped ZnO nanowires

Overall, the integration of the 1 M ZIF-8 shell with the 1% ZnO:Co has been shown quantitatively to be the most effective photoanode studied so far. The synergetic combination of Co-doping and ZID-8 shell enhanced the photogenerated current density as well as the efficiency with which it is generated. Nonetheless, only one condition for the growth of the shell was investigated so far and there needs to be a clearer picture on whether using a 1 M concentration will yield the best performance. For this, a study of the PEC performance of doped-core-shell NWs with different shell growth concentrations was carried out. As the mechanistic benefits of the core-shell integration were discussed previously, only the CSV under illumination and the IPCE

are discussed for the different shells. Two organic linker concentrations (0.25 M and 0.5 M) were studied. As shown from the CSV under illumination in Figure 8.6a, the highest current density is still achieved by the 1 M shell. Both 0.25 M and 0.5 M provide similar current densities (0.130 mA cm^{-2} and 0.135 mA cm^{-2}, respectively), with values lower than the current density obtained for ZnO:Co@ZIF-8 1 M (0.150 mA cm^{-2}). Nonetheless, the influence of the shell on the cathodic current around 0.15 V is still visible, with this current being almost completely supressed.

With regards to the IPCE (Figure 8.6b), a similar result was obtained: ZnO:Co@ZIF-8 1 M provides a considerably larger efficiency than either ZnO:Co@ZIF-8 0.25 M or ZnO:Co@ZIF-8 0.5 M. These two samples provide IPCE values of 51% and 57% at 350 nm, far lower than the outstanding 75% of ZnO:Co@ZIF-8 1 M. Interestingly, there is also a shift in the IPCE trend in the UV region. From 370 nm to 320 nm, which is the region of highest IPCE, the ZnO:Co@ZIF-8 0.5 M samples shows higher efficiency than the 0.25 M sample. However, from 320 nm 300 nm, the ZnO:Co@ZIF-8 0.25 M sample shows more efficient performance, with the respective IPCE at 305 nm being 64% and 51% for ZnO:Co@ZIF-8 0.25 M and ZnO:Co@ZIF-8 0.5 M. From these results, it can be seen that the 1 M concentration of the organic linker provided the best PEC performance out of those studied. Using higher concentrations was deemed unnecessary as it was believed that the shell would be thicker than envisioned (based on the SEM study from Chapter 7.3.2), which means that the ZnO:Co core would not be as readily available for the photogeneration of carriers to start the water splitting process, ultimately rendering the ZIF-8 shell functionalization meaningless. Therefore, it has been proven that the synergetic combination of cobalt doped ZnO cores and ZIF-8 shell drastically enhances the PEC performance of the base ZnO NWs. Nonetheless, a deeper understanding of the mechanism behind this enhancement is required to fully develop this core-shell photoanodes as a competitive alternative to other materials.

Figure 8.6c shows a comparative plot of the IPCE values obtained at the discussed wavelengths (305 nm and 350 nm) for ZnO NWs without surface functionalization and those with the different studied shells, i.e. those with different organic linker concentration. At 305 nm, the trend observed resembles a multi-
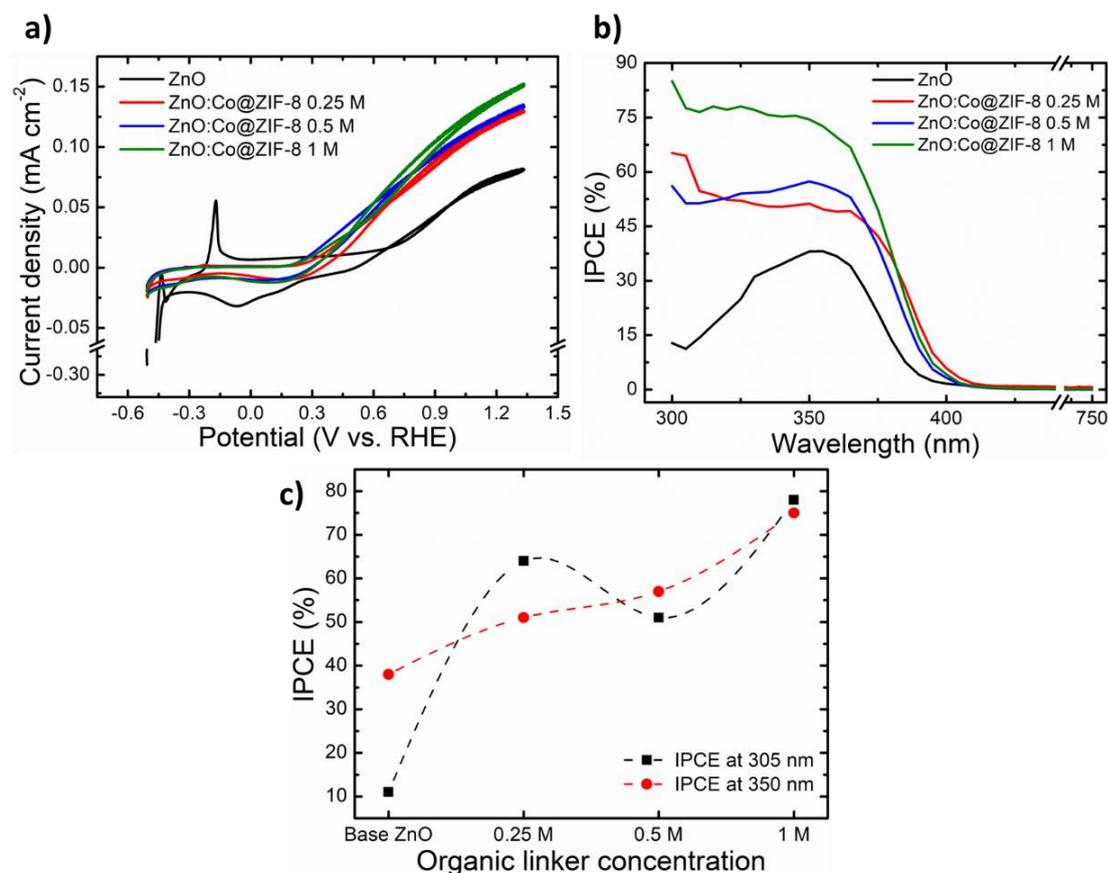
Figure 8.6. a) Cyclic sweeping voltammetry under AM 1.5 G illumination and **b)** incident photon-to-current efficiency study of doped-core-shell nanowire photoanodes. The shells were grown using different organic linker concentrations. **c)** Comparative plot of the incident photon-to-current efficiency values obtained at 305 nm and 350 nm for the different organic linker concentrations studied. The dashed lines are included for readability purposes.

exponential curve, with 0.25 M concentration providing a larger IPCE than 0.5 M. Considering the 350 nm wavelength, it can be observed that the IPCE increases with higher organic linker concentration following an almost linear trend. No numerical fitting of these two curves was carried out as it was deemed that more experimental values of the HMIM concentration should be explored before confidently establishing a trend that governs the relation between IPCE and HMIM concentration. The excellent results obtained in this thesis in terms of IPCE, in particular for the ZnO:Co@ZIF-8, as detailed in our recent publication[90], clearly demonstrate that the results obtained in this work are not only competitive, but they also outperform the data reported in the literature for similar material systems, such as that of Li et al.[89] and those discussed in Chapter 2.4.4. Furthermore, this work clearly demonstrates that a careful modulation of the properties of the ZnO NWs is crucial for device performance. For instance, this work shows how the performance

of the photoanodes can be tuned from subpar to an excellent performance by smartly addressing the main intrinsic shortcomings of ZnO as a material for water splitting photoanodes.

8.8 Working mechanism for functional performance of core-shell ZnO nanowires

In order to understand the functional mechanism that governs the carrier generation and transfer within the ZnO:Co@ZIF-8 NWs, additional photoelectrochemical analyses are required. For this, one key metric of the performance of the photoanodes is missing from the previous analysis: the stability. Stability here refers to the variation over time of the photogenerated current. Here, the current density was studied over a period of 5000 seconds under AM 1.5 G illumination and an applied potential of 1.33 V_{RHE}. The results of this stability analysis are shown in Figure 8.7a for ZnO, ZnO:Co, ZnO@ZIF-8 and ZnO:Co@ZIF-8. Before delving into the details of the analysis it is worth mentioning that the numbers shown at the end of each plot, and coloured accordingly, refer to the total current density lost during the experimental time measured from an initial stable point (1000 seconds) until the end point (5000 seconds). 1000 seconds was selected as a stable time due to the initial transitionary state that all the samples present, which would have made the comparisons inaccurate. As such, the percentage values shown in Figure 8.7 a were obtained accordingly to the following expression,

$$\%_{decay} = 100 - \frac{j_{t=5000\,s}}{j_{t=1000\,s}} * 100 \qquad \text{[Eq. 8.1]}$$

where $j_{t=1000\,s}$ and $j_{t=5000\,s}$ correspond to the current densities obtained at the respective times and $\%_{decay}$ represents the total current lost during the experiment. Considering first ZnO, it can be seen that 36.6% of the initial current is lost at the end of the experiment. By 2000 s, the current density was already decaying, indicating very poor stability under the working conditions described here. The stability of ZnO in photoelectrochemistry is known to be an issue[290] that is directly related to the surface defects of the material. This is especially true for the ZnO NWs due to the large surface to volume ratio. These surface defects stabilize the aforementioned intermediate oxygenated species (peroxides, superoxides), which are the principal

cause of the photocorrosion of ZnO[291, 292]. Photocorrosion is a light-induced process caused by photogenerated carriers that results in the degradation of the surface of the light absorbing material. As the external surface of the ZnO NWs is the location of the catalytic activity for the water splitting process, this region is the most affected by the photocorrosion. Therefore, the presence of these oxygenated species (evidenced by the cathodic current seen in the low applied potential region) is a direct indication of the photocorrosion processes that cause the large $\%_{decay}$ seen for ZnO.

Regarding ZnO:Co, the introduction of the doping reduces the current decay with respect to ZnO, resulting in a $\%_{decay}$ of 29.8%. It is suggested that this reduction is related to the sp-d states introduced in the bandgap by the Co-doping, which act as charge separation centres and, therefore, reduce the number of charge carriers available to take part in the photocorrosion process[247]. The introduction of the ZIF-8 shell in ZnO@ZIF-8 further reduced the $\%_{decay}$ to 21.9%, a 10% reduction compared to ZnO:Co. This reduction in the decay over time of the current density is attributed to the suppression of the surface defects by the ZIF-8 shell[272]. As seen in the CSV in Figure 8.4b, the shell eliminated the cathodic current resulting from the surface defects, thus increasing the average lifetime of the photoanode. Finally, ZnO:Co@ZIF-8 showed a further reduction of the $\%_{decay}$ down to 17.7% over the time of the analysis, as predicted from the transient amperometric analysis of Figure 8.5c. This improvement in the current decay can be attributed to the synergetic interplay between the Co-doping and the ZIF-8 shell. Thus, not only is ZnO:Co@ZIF-8 the highest performing photoanode, but it is also the one with the longest functional lifetime owing to its current decay.

Mott-Schottky measurements were carried out in an effort to better understand the relative position of the conduction band of the photoanodes that helped develop a theoretical mechanistic model of the water splitting. Details of the Mott-Schottky measurements and the theory behind them were provided in Chapter 2.4.3. The relative positions of the conduction bands with respect to the applied potential are indicated by the intercepts of the linear best fitting lines (flatband potential) shown in Figure 8.7b. As these positions are relative, the discussion will be made on a comparative basis.
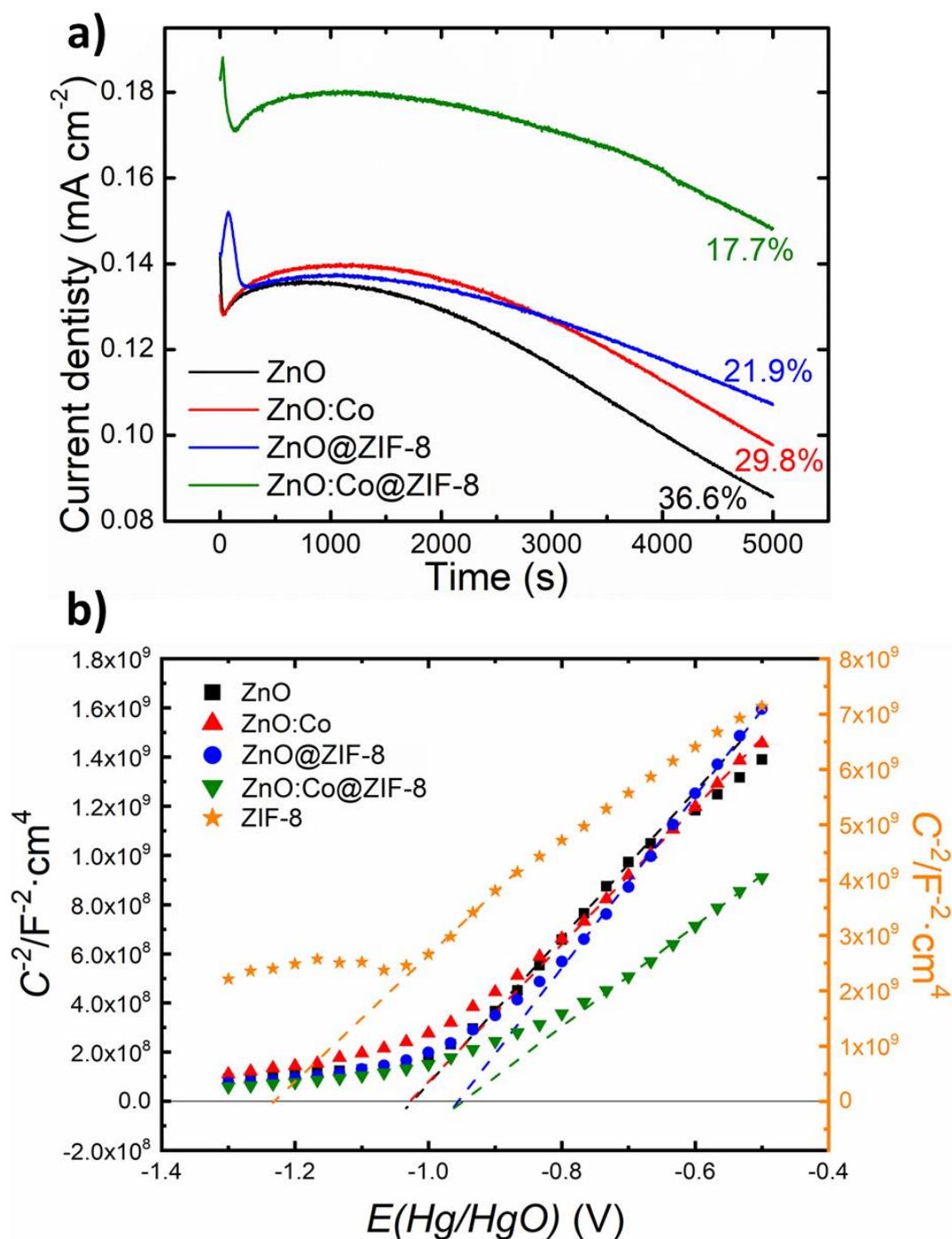
Figure 8.7. a) Stability over time of the photogenerated current and **b)** Mott-Schottky measurements of ZnO, ZnO:Co, ZnO@ZIF-8 and ZnO:Co@ZIF-8 showing the changes in the current density over time and the relative positions of the conduction band of the photoanodes. The numbers in the stability plot indicate the total current density lost at the end of the measurement (4000 seconds) with respect to the stable point at 1000 seconds for each photoanode. The Mott-Schottky measurements were taken at frequencies from 105 Hz to 0.1 Hz in the potential range of -0.5 V to -1.3 V vs Hg/HgO electrode. The dashed lines indicate the best linear fits, the intercepts of which indicate the relative positions of the conduction band. The orange coloured axis corresponds only to the ZIF-8 signal (orange coloured data).

Considering ZnO and ZnO:Co, it is shown that the introduction of the cobalt doping does not shift the position of the conduction band. This is in agreement with the optoelectronic analyses and band structure proposed in Chapter 6, where it was theorised that the reduction of the bandgap as a result of the introduction of the cobalt doping was induced by the presence of localized sp-d states[267]. Therefore, these states were the cause of the reduction in the bandgap, while the conduction band remained in the same relative position as for ZnO. This relative position was -1.03 V (vs Hg/HgO reference electrode). When the ZIF-8 shell is integrated for ZnO@ZIF-8, the relative position of the conduction band shifted to a lower potential of -0.95 V. A similar result was observed for ZnO:Co@ZIF-8, with its relative position of the conduction band being almost identical to ZnO@ZIF-8. The relative position of ZIF-8 alone was included here for reference, showing that it is at a higher potential of -1.2 V.

Apart from the relative position of the conduction band, the Mott-Schottky measurements provide information on the density of carriers of a photoanode. This information can be extracted from the slope of the best linear fit, with smaller slopes indicating a higher density of charge carriers. In this regard, it can be seen that the density of photogenerated charge carriers for ZnO:Co is slightly higher than for ZnO. Considering the integration of the ZIF-8 shell, the slope of ZnO@ZIF-8 is larger than that of ZnO and ZnO:Co, indicating a somewhat lower carrier density. This can be attributed to the fact that the Co-doping induced a shift of the bandgap towards lower energies, which can directly lead to a larger photogeneration of carriers. However, this was not true for the ZIF-8 shell and, thus, this can explain the difference in the carrier density for both samples. Considering ZnO:Co@ZIF-8, the slope obtained from the Mott-Schottky measurements is much smaller than any of the other three, indicating a considerable increase in the concentration of charge carriers. Such an increase can only be attributed to the synergetic combination of ZnO:Co and the ZIF-8 shell that results in an effective change transfer between core and shell, with electrons freely transferring to the ZnO:Co cores while the photogenerated holes are injected into the ZIF-8 shell and, from there, to the electrolyte, where they initiate the water splitting process. This is facilitated by the

presence of the additional energy levels in the bandgap introduced by the cobalt doping.

The analyses carried out in this chapter, along with the discussion and models proposed in Chapter 6, are sufficient to propose a mechanistic model that described the behaviour resulting from the synergetic integration of Co-doping and ZIF-8 surface functionalization and how this boosts the photoelectrochemical performance of the ZnO:Co@ZIF-8 core-shell NW-based photoanodes. This theoretical model is shown schematically in Figure 8.8. In Figure 6.11 of Chapter 6 it was proposed that cobalt doping of ZnO NWs introduces localized sp-d states in the bandgap of ZnO that are the source of the red-shift of the bandgap. This is shown in the left part of the band structure provided in Figure 8.8a. In this schematic band diagram, EV and EC refer to the energy of the valence and conduction band, respectively.

The integration of the ZIF-8 shell with the ZnO core is presented in the schematic of the molecular structure presented in Figure 8.8b. In short, ZIF-8 grows from the ZnO core using the Zn present in the ZnO lattice. During this growth, the oxygen atoms from the ZnO structure react with the solvent, forming water in the process. As such, up to two N atoms from the ZIF-8 shell will be bonded to a Zn from the surface of the ZnO NWs[293], as shows in the molecular schematic. In this way, the ZIF-8 shell grows to conformally coat the ZnO core. The energy levels of this ZIF-8 shell are different to those of the ZnO:Co core, as evidenced by the Mott-Schottky measurements in Figure 8.7 b, where it was shown that the relative position of the conduction band of ZIF-8 was located at a higher energy level. In addition, the bandgap of ZIF-8 has been reported to be at around 3.3 eV[271]. This means that the band structure of ZIF-8 is almost identical to that of ZnO, albeit shifted towards higher energies. Therefore, this was accordingly represented in the band diagram of Figure 8.8 a.

After defining the proposed electronic band structure of the ZnO:Co@ZIF-8 core-shell NW structure and their molecular schematic, it is necessary to discuss what happens to the photogenerated charge carriers once the NWs are subjected to illumination. Under illumination, electron-hole pairs are photogenerated at both the ZnO:Co core and the ZIF-8 shell, as demonstrated by the respective CSV under

illumination shown earlier in this chapter. The electrons generated in the ZnO:Co core have two available excitation pathways: the conduction band of ZnO:Co or the localized sp-d states in the bandgap introduced by the Co- doping[287, 294]. Otherwise, electrons with insufficient energy will simply recombine. Regarding the photogenerated holes, their only possibilities are transfer to the ZIF-8 shell or recombination. For the former to take place, the energy difference between the valence band of ZnO:Co and ZIF-8 has to be sufficiently small to allow the hole transfer to the shell. From the Mott-Schottky measurements it was observed that this difference is of 0.25 eV, which was deemed sufficiently small to allow band bending to take place, thus allowing the transfer of photogenerated holes to the ZIF-8 shell. Therefore, the shell can be considered as a hole transfer layer that

allows the injection of holes from the ZnO:Co core directly to the electrolyte through the ZIF-8 shell. This means that the ZIF-8 shell not only boosts the PEC performance of the core-shell photoanodes by suppressing the undesired cathodic current, but also by enhancing the charge separation properties of the NWs. This effect can be interpreted as an improvement of the $\eta_{interface}$ that was detailed in Chapter 2.3.1. Thus, the combined effect of electron trapping from the surface defects, introduced by the Co-doping, and the hole injection of the ZIF-8 shell are the sources that greatly enhanced the PEC performance of this photoanode.

This is particularly true for the IPCE: as it was seen, values above 75% efficiency were obtained for 360 nm to 300 nm region, indicating that the efficiency with which the incoming photons were converted to current was higher in that region owing to the higher charge separation efficiency and hole transfer of these core-shell NWs. Concerning the photogenerated carriers in the ZIF-8 shell, the holes are directly injected into the electrolyte to initiate the water splitting process. The electrons are transferred from the conduction band of the ZIF-8 shell to the conduction band of the ZnO:Co core. The charge carrier transfer processes described here for the electrons and holes in the ZIF-8 shell are made possible by the chemical structure of the imidazole linker that coordinates the ZIF-8 structure. It has been reported that the valence band of ZIF-8 is localized in the nitrogen atoms from the two amine groups of the imidazole, while the conduction band of ZIF-8 is formed by the empty orbitals of the Zn nuclei[295]. Based on this, any excited electrons will go from the amine
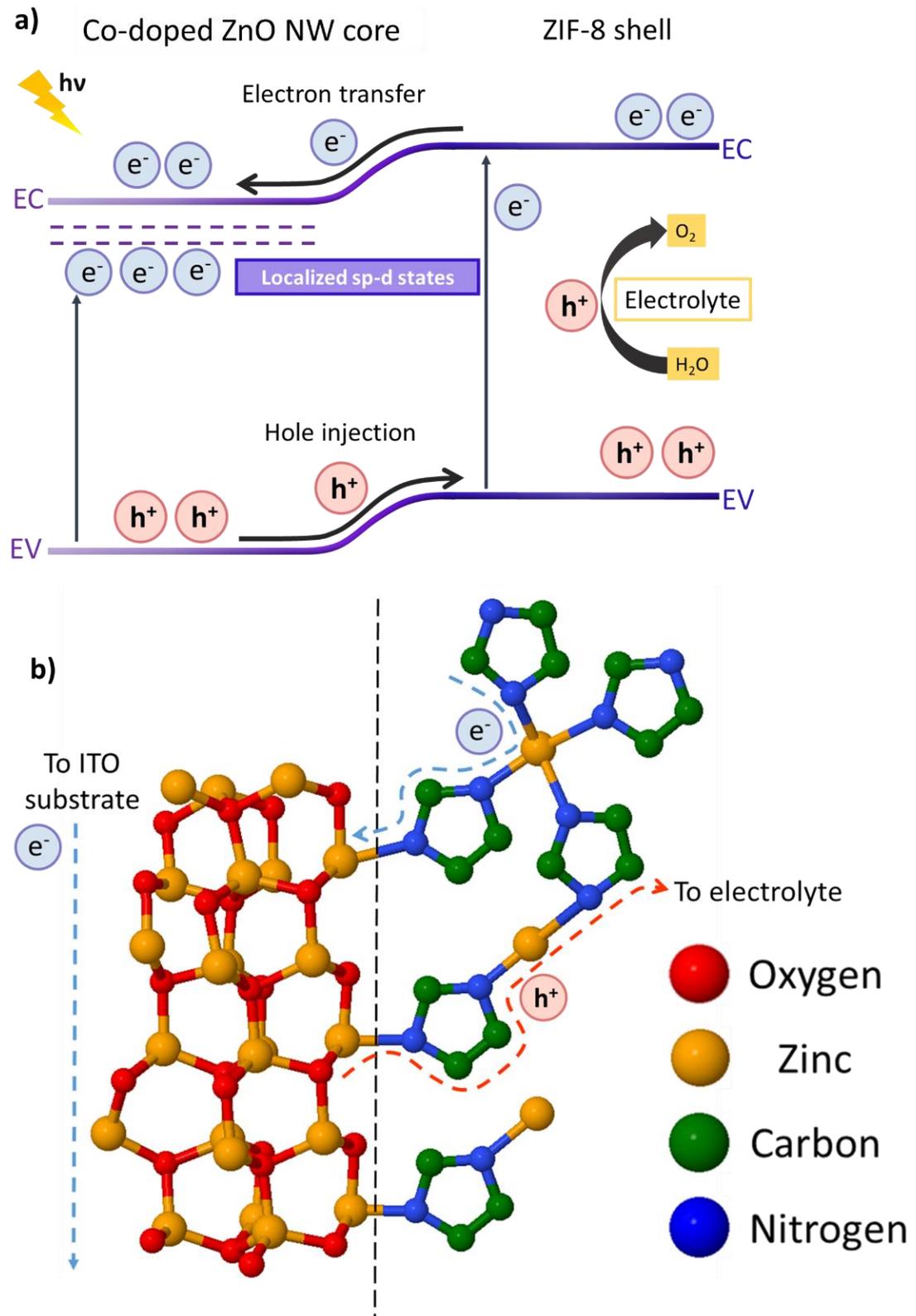
Figure 8.8. a) Schematic of the proposed electronic band diagram showing the interface between the ZnO:Co core and the ZIF-8 shell, as well as the charge transfer processes occurring between one another. **b)** Schematic of the molecular structure of the ZnO:Co@ZIF-8 core-shell structure, showing the hexagonal wurtzite structure of ZnO and the coordinated ZIF-8 shell. For clarity purposes, this schematic only represents a tetrahedral unit of ZIF-8 in two dimensions. The flow of charge carriers is presented here to support the proposed electronic band diagram.

groups of the imidazole to the Zn nuclei of the ZIF-8 structure due to the photoexcitation and, from there, to the ZnO:Co, via a process known as ligand-to-cluster charge transfer[296]. At the same time, the photogenerated holes (or those injected from the ZnO:Co) will be directly transferred to the electrolyte through the amine groups of the ZIF-8 structure and initiate the water splitting process. For this, water molecules will be adsorbed by the amine groups of ZIF-8 through their hydrogen atoms. The charge carrier transfer and injection processes here described are represented in the proposed electronic band diagram and molecular schematic by blue and red circular symbols with an e^- or h^+ that respectively represent the photogenerated electrons and holes.

8.9 Conclusions

In this chapter, the results forming a thorough study of the photoelectrochemical performance of different ZnO NW-based water splitting photoanodes are discussed. The focus of this study was to determine the influence that cobalt doping and surface functionalization with a MOF, ZIF-8 in particular, have on the performance of the photoanodes with the aim of designing the optimal functional performance. This discussion is supported by the optoelectronic analysis detailed in Chapters 6 and 7. For this discussion, first, the PEC properties of the ZnO NWs were described. It was shown that the ZnO NWs yielded a maximum current density of 0.08 mA cm^{-2} at 1.33 V$_{RHE}$, with an IPCE of 38% at 350 nm. These metrics were used as the basis for the subsequent comparative study. Cobalt doping was the first PEC performance enhancement investigated. For this, different nominal values of cobalt doping (1%, 5% and 20%) were proposed as candidates, based on the optoelectronic study of Chapter 6. It was demonstrated that the 1% nominal Co-doping provided the best performance out of the different values studied, yielding a maximum current density of 0.12 mA cm^{-2} at 1.33 V$_{RHE}$, with an IPCE of 51% at 350 nm. This proved to be a considerable improvement of the PEC performance for ZnO NW-based photoanodes. This was attributed to the enhanced charge separation properties of this photoanode compared to ZnO, owing to the localized sp-d states introduced in the bandgap by the cobalt doping, which act as electron traps that prevent the recombination of the photogenerated charge carriers. However, the presence of Co-doping also increased

243

the undesired cathodic current that is attributed to stable oxygenated reaction intermediates, which are the cause of the photocorrosion of the NWs. This was attributed to the increasing density of surface defects (the localized sp-d states) that acts as anchoring points that stabilize these oxygenated intermediates.

The surface functionalization of the ZnO NWs with a ZIF-8 shell was the next enhancement studied. For this, only a 1 M ZIF-8 shell was used, based on the morphological analyses shown in Chapter 7. The addition of the shell was proven to greatly boost the performance of the photoanodes, with the ZnO@ZIF-8 core-shell structure showing a maximum current density of 0.12 mA cm^{-2} at 1.33 V$_{RHE}$, with an IPCE of 48% at 350 nm. In addition, it was shown that the ZIF-8 shell suppresses the cathodic current observed for the undoped and Co-doped ZnO NWs, which was explained by the passivation of the characteristic surface defects of ZnO.

The performance values obtained for ZnO@ZIF-8 resemble those obtained for the ZnO:Co NWs, but the physical basis for the enhancement was different, suggesting that if both strands were brought together, the PEC performance of the NW-based photoanodes could be synergistically boosted by this combination. This was proven by integrating 1% ZnO:Co doped cores with a 1 M ZIF-8 shell in ZnO:Co@ZIF-8. The combined effect of both enhancements boosted the PEC performance of the photoanodes, resulting in a maximum current density of 0.15 mA cm^{-2} at 1.33 V$_{RHE}$, with an IPCE of 75% at 350 nm. These represent a current density almost double the value that is generated with a very large efficiency, demonstrating the synergetic contribution of Co-doping and ZIF-8 surface functionalization. In addition, the aforementioned cathodic current was suppressed by the ZIF-8 shell, which was translated into an improved stability over time that was twice as good as that of the ZnO NWs. Nonetheless, it was necessary to explore the possibility that a different ZIF-8 shell could provide a better performance. For this, shells deposited with an organic linker concentration of 0.25 M and 0.5 M were studied. The results showed that the 1 M sample was the best performing photoanode and, as such, it was the one studied in detail.

Finally, a theoretical functional model for the electronic band diagram and the molecular structure of the core-shell was proposed with the goal of summarizing the physical processes related to the photogeneration and transfer of carried in the

ZnO:Co@ZIF-8 NWs. The schematic band diagram, which was based on the optoelectronic and Mott-Schottky analyses and the literature, showed that the ZIF-8 shell acts as a hole injection layer, directly transferring the photogenerated holes from the ZnO:Co core to the electrolyte, where they initiate the water splitting process. At the same time, the electrons generated in both the core and the shell are transferred to the ZnO:Co core and, from there, to the conducting substrate. This model highlights the synergetic combination of cobalt doping and ZIF-8 surface functionalization that was observed in the photoelectrochemical characterization shown in this chapter.

Chapter 9

Conclusions and further work

9.1 Conclusions

In this thesis, the growth of ZnO nanowires (NWs), their doping and surface functionalization were studied with the aim of developing highly efficient photoelectrochemical (PEC) water splitting photoanodes. To understand the PEC performance of the ZnO NW-based photoanodes, first a growth study of ZnO NWs was carried to underpin how the different parameters that govern the growth affect the dimensions and orientation of the as-grown NWs. As the control over the growth of the ZnO NWs was demonstrated, the next step was to modulate their optoelectronic properties by separately introducing two different transition metals as dopants, copper and cobalt. Different quantities of the two dopants were studied and their influence on the ZnO NWs was analysed from a structural and optical point of view to assess whether there was any optimal value that showed promise towards enhancing the PEC performance of the ZnO NWs. The final step before analysing the water splitting capabilities of the ZnO NW-based photoanodes was a detailed study on the surface functionalization of the NWs using two different materials, iridium and the zeolitic imidazolate framework-8 (ZIF-8), a metal-organic framework (MOF). The

influence that these two different surface functionalizations have on the optoelectronic properties of the ZnO was studied to understand their viability as possible enhancements of the PEC performance of the ZnO NWs. Finally, the PEC water splitting performance of the different sets of ZnO NWs (undoped, doped, functionalised and doped and functionalised) was studied in order to find an optimal combination that would represent the best attainable performance possible with the materials used in this thesis.

The growth study of ZnO NWs was presented in Chapter 5. The ZnO NWs were grown in this by a seeded mediated chemical bath deposition (CBD). As such, the first influence that was studied was that of the seed layer on which the NWs grew. This textured ZnO seed layer was deposited using atomic layer deposition (ALD) and the parameter space enabled by this technique was studied in terms of the deposition temperature, number of ALD cycles and pulse and purge times of the precursors. While these parameters were varied, the CBD conditions were maintained constant at 2 h synthesis time and 25 mM equimolar concentration for both reagents. As a result of this study, it was observed that it was possible to control the dimensions and growth orientation of the ZnO NWs by changing the ALD seed layer deposition. As such, careful modulation of these parameters allowed the growth of ZnO NWs ranging from vertically oriented NWs with a diameter of 23±4 nm and a NW density of ~327 μm^{-2} to randomly aligned NWs of 44±11 nm in diameter and a ~42 μm^{-2} NW density. The size statistics of the as-grown ZnO NWs were correlated with the morphological properties of the ALD seed layers (roughness, seed density and texture), reaching a conclusion by which, under the CBD conditions utilised in this study, it was observed that the correlation between seed density in the seed layer and the NW density was approximately 0.5. This means that around half of the surface features identified as seeds on the seed layer were used to grow NWs.

To further understand the growth of the ZnO NWs, the CBD growth time and concentration of the precursors were varied from 2 h to 24 h and from 25 mM to 50 mM, respectively. These experiments were carried out on ALD seed layers deposited under the same parameters to ensure that only the CBD conditions affected the NW growth. It was thus observed that increases in the CBD growth time and the reagent concentration resulted in larger diameter and length of the as-grown NWs and, as a

result, a reduced NW density. Based on these two studies (ALD and CBD conditions), it was demonstrated that the dimensions and orientation of the ZnO NWs could be tailored to the desired application with this process, which can be significantly appealing for different applications[229]. However, and due to external circumstances, the ALD system could not be used and, hence, an alternative route to the deposition of the ALD seed layers was developed in the form of sol-gel processing. This technique is based on the spin coating and subsequent thermal treatment of a solution containing $ZnCl_2$. After the thermal treatment, a textured ZnO seed layer was obtained. A subsequent NW growth study was carried out to understand how the sol-gel processing influenced the NW growth. As a result, it was observed that two different types of ZnO NWs were obtained, hexagonal and tapered, with the first ones being those characteristic of the ZnO NW growth. As a final analysis, the crystallinity of the NWs was studied by means of transmission electron microscopy (TEM) and x-ray diffraction. This showed that the ZnO NWs are single crystal and have a wurtzite crystalline phase, which is the desirable crystal quality and phase for any ZnO NW-based application.

The ZnO NWs were doped with two transition metals, copper and cobalt, to modulate the electronic band structure and carrier dynamics of the NWs. Copper-doped ZnO NWs were first discussed and it was shown that, for the CBD conditions used (24 hours growth time and 50 mM concentration), these Cu-doped NWs have large diameters of the order of 500 nm, and very low NW densities of ~ 2 μm^{-2}. This, along with the SEM images provided, showed that instead of individual, separate NWs, an almost continuous film of Cu-doped ZnO NWs was formed. The introduction of copper did not lead to a significant and clear improvement of the optoelectronic properties of the ZnO NWs, as observed from the ultraviolet-visible (UV-vis) and photoluminescence (PL) spectroscopy. It was observed that only nominal 2% and 5% Cu-doping improved the light absorption as per the UV-vis. In addition, the PL analysis demonstrated that increasing amounts of copper doping induced a shift of the bandgap of the ZnO towards lower energies, meaning that the bandgap was red-shifted and, therefore, reduced. However, due to the poor light absorption properties and the comparatively large size of these NWs, these were not deemed ideal for their application in PEC water splitting.

In contrast, cobalt doping showed more potential. A growth study of Co-doped ZnO NWs (with both ALD and sol-gel seed layers) showed that the dimensions of these doped NWs were similar to those of the undoped ZnO NWs. Moreover, the UV-vis and PL analysis on these samples showed promise for the nominal 1% Co-doping as the introduction of this amount of cobalt doping resulted in a red-shift of the bandgap and light absorption that was larger than that of undoped ZnO across the whole visible spectrum. Fast-transient absorption spectroscopy (FTAS) and spatial cathodoluminescence (CL) spectroscopy were used to deepen the understanding of the effects that Co-doping had on the ZnO NWs. These analyses were carried out for nominal 1%, 5%, 10% and 20% Co-doped NWs and these showed that the bandgap of ZnO can be reduced from its original 3.3 eV to 3.15 eV for 1% Co-doping and further down to 2.95 eV for the 20% Co-doped sample. From this optical study it was concluded that the introduction of cobalt doping leads to a strong exchange interaction between the sp orbitals of ZnO and the d orbitals of cobalt. As a result, the electronic band structure of ZnO was modified by the addition of a set of localized states that act as carrier traps. These states are also the source for the red-shift in the bandgap and, help explain the increasing red-shift effect with increasing Co-doping, as the larger the amount of cobalt is, the higher the density of these trap states, as observed in the spatial CL measurements. These results demonstrate that the introduction of Co-doping can be a successful strategy for the improvement of the PEC performance of ZnO.

The surface functionalization of the ZnO NWs (undoped and doped) was studied with two different materials in an effort to devise an additional strategy that could be combined with doping to further boost the PEC performance of the NWs. The functionalizing material investigated was iridium, which was deposited in the form of self-assembled nanoparticles (NPs) on the lateral faces of the ZnO NWs. Iridium is a well-known PEC catalyst and, as such, this integration was thought of as a catalytic sensitization of the NWs. It was demonstrated by high-resolution TEM imaging that, by controlling the deposition parameters of the sputtering process, the Ir NPS conformally coated the lateral faces of the NWs with sizes varying from 2.0 nm to 3.4 nm. The smaller Ir NPs also show an interesting improvement in the light

absorption as seen in the UV-vis analysis. However, due to the global situation related to COVID-19, this research line could not be taken any further here.

The second functionalizing material that was studied was ZIF-8, which is a zinc-based MOF. The growth of this material was based on using the ZnO NWs as template material to obtain a complete, continuous and conformal coating of the MOF around the NWs by surface conversion, yielding a core-shell structure. To achieve this integration, two different solution-based techniques were used: drop casting and spin coating. It was observed that drop casting yielded quasi-continuous films of ZIF-8 that covered and bridged the individual ZnO NWs and, as such, it was not deemed a good approach for the integration of ZIF-8 and ZnO NWs. In contrast, spin coating yielded a conformal coating that only covered individual NWs, without forming any quasi-continuous layer. Moreover, it was demonstrated that spin coating also provided a much better long-range homogeneity across whole samples. Thus, this process was selected as the route to integrate ZIF-8 shells and ZnO NWs. Three growth parameters, spin speed, organic linker concentration and shell growth time, were used to tune the thickness of the ZIF-8 shell coating the ZNO core. Results showed that the best conditions were demonstrated to be 5000 rpm, 1 M and 15 minutes of growth time, which resulted in a ZIF-8 shell of approximately 2 nm in thickness.

It was then decided to combine doping and surface functionalization in an effort to obtain the best possible performing photoanode. The resulting ZnO:Co@ZIF-8 core-shell NWs showed a large improvement in the light absorption and, in addition, much faster carrier dynamics. This was attributed to the influence of the Co-doping previously described along with the availability of multiple non-radiative recombination pathways, meaning that the charge separation of the photogenerated electron-hole pairs was considerably better than for any other samples investigated.

Once the different sets of undoped, doped, surface functionalised and doped and surface functionalised ZnO NWs had been studied from a morphological and optoelectronic point of view, their PEC performance as water splitting photoanodes was analysed. For this analysis, metrics such as the photogenerated current density or the incident photon-to-current efficiency (IPCE) were studied. This analysis

showed that the separate integration of Co-doping and ZIF-8 surface functionalization considerably increased the photocurrent generated from 0.080 mA cm^{-2} for ZnO to 0.120 mA cm^{-2} for both 1% ZnO:Co and ZnO@ZIF-8 1 M. In addition, the values of the IPCE were drastically improved for both sets of integrations. IPCE values of 51% and 48% were obtained at 350 nm for 1% ZnO:Co and ZnO@ZIF-8 1 M, respectively, compared to the 38% observed for ZnO. Moreover, the IPCE in the near UV region was remarkably increased for these two enhancements, yielding values of 52% and 53% for 1% ZnO:Co and ZnO@ZIF-8 1 M, respectively, which dwarfs the 11% observed for the base ZnO NWs. When both enhancements were brought together in the form of the ZnO:Co@ZIF-8 core-shell NWs, the PEC performance of these photoanodes was boosted further, showing a current density double that of ZnO (0.150 mA cm^{-2}), with outstanding IPCE values of 75% at 350 nm and 78% at 305 nm. This demonstrated that the combined integration of Co-doping and ZIF-8 surface functionalization was a new valid strategy to develop enhanced ZnO NW-based PEC water splitting photoanodes that could be competitive with other more expensive materials, especially provided their large efficiency.

Further analyses were carried out to develop a theoretical electronic band structure model that explained the enhanced performance of these photoanodes. It was proposed that the ZIF-8 shell protected the photoanodes from photocorrosion, enhanced the charge separation and, thus, the efficiency with which holes were transmitted to the electrolyte. As such, the ZIF-8 shell acted as a hole injecting layer, while the cobalt doping contributes by introducing trap states into the bandgap that reduced the recombination rate of the charge carriers. In addition, it was also demonstrated that the ZIF-8 shell was photoactive and that it generated charge carriers when under illumination, which contributed to the increase in photogenerated current density. Therefore, the PEC results along with the proposed theoretical model are expected to serve as a steppingstone in the development of new and enhanced semiconductor water splitting photoanodes, whose properties can be directly modulated by the introduction of a dopant or a functionalising agent.

9.2. Further work

The thesis has demonstrated the growth and enhancement of ZnO NWs towards their application as PEC water splitting photoanodes. Nonetheless, there are many avenues stemming from this work that could be studied to further boost the performance of the ZnO NWs in an effort to make them competitive against other semiconductors of higher cost.

The PEC analysis were carried out on a single set of CBD growth conditions. In this thesis it was shown that the seed mediated CBD growth of the ZnO NWs allowed large control over the dimensions and orientations of the as-grown NWs. As such, it would be interesting in the future to study ZnO NWs grown under different CBD conditions than those presented in the PEC study as it is possible that the aspect ratio of these NWs can affect the water splitting performance. This could mean that thinner and longer NWs or shorter ones, for example, could yield a better performance that the ones that were utilised in this thesis. In addition, the orientation of the as-grown NWs could play a role on this performance and, as such, it would be an interesting topic to explore.

Cobalt and copper doping were selected as substitutional dopants in this study due to the ease with which these can be integrated in the ZnO wurtzite lattice. One missing feature from the analysis on doped-NWs is the accurate determination of the real percentage of doping integrated in the NWs. This would be necessary to further the understanding of the doping process as well as the decrease of the PEC performance with increasing nominal doping concentration. In addition, it has been demonstrated that there are a multitude of possible dopants that can also be integrated with ZnO and, hence, it would be remarkably interesting to study other dopant agents and compared their PEC performance with the Co-doped NWs here presented. Some of these dopants could be iron, nitrogen or lithium, to name a few.

Regarding the surface functionalization, the most obvious piece of further work would be to assess the PEC performance of the Ir-decorated ZnO NWs. Iridium is a well-known PEC catalyst and, as such, it is expected to enhance the performance of the ZnO NWs. However, there may be degradation or instability problems that could hinder this and, thus, a detailed study on these samples would be beneficial. To

further this, the integration of iridium and a MOF could also greatly boost the performance of the ZnO NWs. This could be achieved by joining both functionalization processes described in the thesis, resulting in an iridium decoration protected by a ZIF-8 layer, for example, that would ensure that any the iridium catalyst is protected from any electrochemical degradation or corrosive process.

On the note of surface functionalization, only a single MOF, ZIF-8 was studied. Further research is required to exactly determine the nature of the ZIF-8 shell as, in this work, this nature has only been suggested by the experimental techniques utilised. Moreover, the MOF field is vast and it would be quite interesting to explore other MOFs as possible surface functionalization. An example of this could be ZIF-67, a MOF from the same family as ZIF-8 that is based on cobalt. Its most interesting property is that its light absorption is centered around 550 nm, which could greatly enhance the light absorption and charge carrier photogeneration of the ZnO NWs. In addition, it could be interesting to explore MOFs from other families that could perhaps provide a different benefit to the PEC water splitting performance of the ZnO NWs.

References

[1] Faraday, M., Experimental researches in electricity. *Phil. Trans. R. Soc.* **1832,** *122*, 125-162.

[2] Bardeen, J., Semiconductor Research Leading to the Point Contact Transistor. *Nobel Lectures* **1956,** *Physics 1942-1962*.

[3] Moore, G. E., Cramming more components onto integrated circuits. *Electronics* **1965,** *38*, 1-4.

[4] Lewis, N. S., Toward Cost-Effective Solar Energy Use. *Science* **2007,** *315*, 798-801.

[5] Carlson, D. E.; Wronski, C. R., Amorphous silicon solar cell. *Appl. Phys. Lett.* **1976,** *28*, 671-673.

[6] Yoshikawa, K.; Kawasaki, H.; Yoshida, W.; Irie, T.; Konishi, K.; Nakano, K.; Uto, T.; Adachi, D.; Kanematsu, M.; Uzu, H.; Yamamoto, K., Silicon heterojunction solar cell with interdigitated back contacts for a photoconversion efficiency over 26%. *Nat. Energy* **2017,** *2*, 17032.

[7] Blakemore, J. S., Semiconducting and other major properties of gallium arsenide. *J. Appl. Phys.* **1982,** *53*, 123-181.

[8] Sivula, K.; Formal, F. L.; Grätzel, M., Solar Water Splitting Progress. Using Hematite (α-Fe2O3) Photoelectrodes. *Chem. Sus. Chem.* **2011,** *4*, 432-449.

[9] Daghrir, R.; Drogui, P.; Robert, D., Modified TiO2 For Environmental Photocatalytic Applications: A Review. *Ind. Eng. Chem. Res.* **2013,** *52*, 3581-3599.

[10] Özgür, Ü.; Alivov, Y. I.; Liu, C.; Teke, A.; Reshchikov, M. A.; Doğan, S.; Avrutin, V.; Cho, S. J.; Morkoç, H., A comprehensive review of ZnO materials and devices. *J. Appl. Phys.* **2005,** *98*.

[11] Djurisic, A. B.; A.M.C.Ng; X.Y.Chen, ZnO nanostructures for optoelectronics. Material properties and device applications. *Prog. Quantum. Electron.* **2010,** *34*, 191-259.

[12] Özgür, Ü.; Hofstetter, D.; Morkoç, H., ZnO Devices and Applications: A Review of Current Status and Future Prospects. *Proc. IEEE* **2010,** *98*, 1255-1268.

[13] Pagliaro, M.; Konstandopoulos, A. G.; Ciriminna, R.; Palmisano, G., Solar hydrogen. Fuel of the near future. *Energy Environ. Sci.* **2010,** *3*, 279-287.

[14] Hanley, E. S.; Deane, J.; Gallachóir, B. Ó., The role of hydrogen in low carbon energy futures–A review of existing perspectives. *Renew. Sustain. Energy Rev.* **2018,** *82*, 3027-3045.

[15] Bedding, T. R.; Mosser, B.; Huber, D.; Montalbán, J.; Beck, P.; Christensen-Dalsgaard, J.; Elsworth, Y. P.; García, R. A.; Miglio, A.; Stello, D.; White, T. R.; Ridder, J. D.; Hekker, S.; Aerts, C.; Barban, C.; Belkacem, K.; Broomhall, A.-M.; Brown, T. M.; Buzasi, D. L.; Carrier, F.; Chaplin, W. J.; Mauro, M. P. D.; Dupret, M.-A.; Frandsen, S.; Gilliland, R. L.; Goupil, M.-J.; Jenkins, J. M.; Kallinger, T.; Kawaler, S.; Kjeldsen, H.; Mathur, S.; Noels, A.; Aguirre, V. S.; Ventura, P., Gravity modes as a way to distinguish between hydrogen- and helium-burning red giant stars. *Nature* **2011,** *471*, 608-611.

[16] Staffell, I.; Scamman, D.; Abad, A. V.; Balcombe, P.; Dodds, P. E.; Ekins, P.; Shah, N.; Ward, K. R., The role of hydrogen and fuel cells in the global energy system. *Energy Environ. Sci.* **2019,** *12*, 463-491.

[17] Turner, J. A., Sustainable Hydrogen Production. *Science* **2004,** *305*, 972-974.

[18] Palo, D. R.; Dagle, R. A.; Holladay, J. D., Methanol Steam Reforming for Hydrogen Production. *Chem. Rev.* **2007,** *107*, 3992-4021.

[19] Holladay, J. D.; Hu, J.; King, D. L.; Wang, Y., An overview of hydrogen production technologies. *Catalysis Today* **2009,** *139*, 244-260.

[20] Fujishima, A.; Honda, K., Electrochemical Photolysis of Water at a Semiconductor Electrode. *Nature* **1972,** *238*, 37-38.

[21] Grätzel, M., Photoelectrochemical cells. *Nature* **2001,** *414*, 338-344.

[22] Walter, M. G.; Warren, E. L.; McKone, J. R.; Boettcher, S. W.; Mi, Q.; Santori, E. A.; Lewis, N. S., Solar water splitting cells. *Chem Rev* **2010,** *110*, 6446-73.

[23] Abeles, B.; Tiedje, T., Amorphous Semiconductor Superlattices. *Phys. Rev. Lett.* **1983,** *51*, 2003-2006.

[24] Park, J. S.; Maeng, W.-J.; Kim, H.-S.; Park, J.-S., Review of recent developments in amorphous oxide semiconductor thin-film transistor devices. *Thin Solid Films* **2012,** *520*, 1679-1693.

[25] Dimitrakopoulos, C. D.; Mascaro, D. J., Organic thin-film transistors: A review of recent advances. *IBM J. Res. Dev.* **2001,** *45*, 11-27.

[26] Samuel, I. D. W.; Turnbull, G. A., Organic Semiconductor Lasers. *Chem. Rev.* **2007,** *107*, 1272-1295.

[27] Facchetti, A., Semiconductors for organic transistors. *Mater. Today* **2007,** *10*, 28-37.

[28] Mishra, U. K.; Singh, J., *Semiconductor Device Physics and Design*. 1st ed.; Springer: 2008; p 559.

[29] Neamen, D. A., *Semiconductor Physics and Devices*. 3rd ed.; McGraw-Hill: 2003; p 566.

[30] Wells, A. F., The geometrical basis of crystal chemistry. XII. Review of structures on three-dimensional 3-connected nets. *Acta Cryst.* **1976,** *B32*, 2619-2626.

[31] Mighell, A. D., The reduced cell: its use in the identification of crystalline materials. *J. Appl. Cryst.* **1976,** *9*, 491-498.

[32] Dubrovskii, V. G.; Sibirev, N. V.; Harmand, J. C.; Glas, F., Growth kinetics and crystal structure of semiconductor nanowires. *Phys. Rev. B* **2008,** *78*, 235301.

[33] Yang, P.; Yan, R.; Fardy, M., Semiconductor Nanowire: What's Next. *Nano Letters* **2010,** *10*, 1529-1536.

[34] Lim, J.; Bae, W. K.; Kwak, J.; Lee, S.; Lee, C.; Char, K., Perspective on synthesis, device structures, and printing processes for quantum dot displays. *Optical Materials Express* **2012,** *2*, 594-628.

[35] Rössler, U., Energy Bands of Hexagonal II-VI Semiconductors. *Phys. Rev.* **1969,** *184*, 733-738.

[36] Levinshtein, M. E.; Rumyantsev, S. L.; Shur, M. S., *Properties of advanced semiconductor materials : GaN, AlN, InN, BN, SiC, SiGe.* Wiley: 2001.

[37] Wang, Z. L.; Song, J., Piezoelectric Nanogenerators Based on Zinc Oxide Nanowire Arrays. *Science* **2006,** *312*, 242-246.

[38] Yang, Y.; Guo, W.; Pradel, K. C.; Zhu, G.; Zhou, Y.; Zhang, Y.; Hu, Y.; Lin, L.; Wang, Z. L., Pyroelectric Nanogenerators for Harvesting Thermoelectric Energy. *Nano Letters* **2012,** *12*, 2833-2838.

[39] Sun, S.; Zhang, X.; Cui, J.; Liang, S., Identification of the Miller indices of a crystallographic plane: a tutorial and a comprehensive review on fundamental

theory, universal methods based on different case studies and matters needing attention. *Nanoscale* **2020**.

[40] Romano, L.; Privitera, V.; Jagadish, C., *Defects in Semiconductors*. 1st ed.; 2015; Vol. 91, p 458.

[41] Nowick, A. S.; Heller, W. R., Anelasticity and stress-induced ordering of point defects in crystals. *Adv. Phys.* **1963,** *12*, 251-298.

[42] Fahey, P. M.; Griffin, P. B.; Plummer, J. D., Point defects and dopant diffusion in silicon. *Reviews of Modern Physics* **1989,** *61*, 289-384.

[43] Rockett, A., *The Materials Science of Semiconductors*. Springer: Boston, MA, 2008.

[44] Estermann, L.; Stern, O., Beugung von Molekularstrahlen. *Zeitschrift für Physik* **1930,** *61*, 95-125.

[45] Memming, R., *Semiconductor Electrochemistry*. 2nd ed.; 2015.

[46] Kahn, A., Fermi level, work function and vacuum level. *Mater. Horiz.* **2016,** *3*, 7-10.

[47] Mead, C. A.; Spitzer, W. G., Fermi Level Position at Metal-Semiconductor Interfaces. *Phys. Rev.* **1964,** *134*, A713-A716.

[48] Erwin, S. C.; Zu, L.; Haftel, M. I.; Efros, A. L.; Kennedy, T. A.; Norris, D. J., Doping semiconductor nanocrystals. *Nature* **2005,** *436*, 91-94.

[49] Kenyon, A. J., Recent developments in rare-earth doped materials for optoelectronics. *Prog. Quantum. Electron.* **2002,** *26*, 225-284.

[50] Zhang, S. B.; Wei, S.-H.; Zunger, A., Intrinsic n-type versus p-type doping asymmetry and the defect physics of ZnO. *Phys. Rev. B* **2001,** *63*, 075205.

[51] Park, C. H.; Zhang, S. B.; Wei, S.-H., Origin of p-type doping difficulty in ZnO: The impurity perspective. *Phys. Rev. B* **2002,** *66*.

[52] Stranks, S. D.; Burlakov, V. M.; Leijtens, T.; Ball, J. M.; Goriely, A.; Snaith, H. J., Recombination Kinetics in Organic-Inorganic Perovskites: Excitons, Free Charge, and Subgap States. *Phys. Rev. Appl.* **2014,** *2*, 034007.

[53] Alkauskas, A.; Dreyer, C. E.; Lyons, J. L.; Walle, C. G. V. d., Role of excited states in Shockley-Read-Hall recombination in wide-band-gap semiconductors. *Phys. Rev. B* **2016,** *93*, 201304.

[54] Abakumov, V. N.; Perel, V. I.; Yassievich, I. N., *Nonradiative Recombination in Semiconductors*. 1st Edition ed.; Elsevier: 1991; Vol. 33, p 336.

[55] Jelle, B. P.; Breivik, C.; Røkenes, H. D., Building integrated photovoltaic products. A state-of-the-art review and future research opportunities. *Sol. Energy Mater. Sol. Cells* **2012,** *100*, 69-96.

[56] Street, R. A., *Technology and Applications of Amorphous Silicon*. 1 ed.; Springer-Verlag Berlin Heidelberg: 1999; p 417.

[57] Kamins, T., *Polycrystalline Silicon for Integrated Circuit Applications*. 1 ed.; Springer US: 1988; p 290.

[58] Braga, A. F. B.; Moreira, S. P.; Zampieri, P. R.; Bacchin, J. M. G.; Mei, P. R., New processes for the production of solar-grade polycrystalline silicon. A review. *Sol. Energy Mater. Sol. Cells* **2008,** *92*, 418-424.

[59] Park, J.-S.; Chae, H.; Chung, H. K.; Lee, S. I., Thin film encapsulation for flexible AM-OLED: a review. *Semicond. Sci. Technol.* **2011,** *26*, 034001.

[60] Thompson, D. A.; Romankiw, L. T.; Mayadas, A. F., Thin film magnetoresistors in memory, storage, and related applications. *IEEE Trans. Magn* **1975,** *11*, 1039-1050.

[61] Comstock, R. L., Review Modern magnetic materials in data storage. *J. Mater. Sci.: Mater. Electron.* **2002,** *13*, 509-523.

[62] Raut, H. K.; Ganesh, V. A.; Nair, A. S.; Ramakrishna, S., Anti-reflective coatings: A critical, in-depth review. *Energy Environ. Sci.* **2011,** *4*, 3779-3804.

[63] Frey, H.; Khan, H. R., *Handbook of Thin Film Technology*. 1 ed.; Springer, Berlin, Heidelberg: 2015; p 380.

[64] Casini, M., *Smart Buildings: Advanced Materials and Nanotechnology to Improve Energy-Efficiency and Environmental Performance*. 2016; Vol. 1, p 384.

[65] Prasad, R.; Bhattacharyya, A.; Nguyen, Q. D., Nanotechnology in Sustainable Agriculture. Recent Developments, Challenges, and Perspectives. *Front. Microbiol.* **2017,** *8*, 1-13.

[66] Ramasamy, M.; Lee, J., Recent Nanotechnology Approaches for Prevention and Treatment of Biofilm-Associated Infections on Medical Devices. *BioMed Res. Int.* **2016,** *2016*, 1-17.

[67] Delley, B.; Steigmeier, E. F., Quantum confinement in Si nanocrystals. *Phys. Rev. B* **1993,** *47*, 1397-1400.

[68] Park, N.-M.; Choi, C.-J.; Seong, T.-Y.; Park, S.-J., Quantum Confinement in Amorphous Silicon Quantum Dots Embedded in Silicon Nitride. *Phys. Rev. Lett.* **2001,** *86*, 1355-1357.

[69] Chatterjee, D. K.; Fong, L. S.; Zhang, Y., Nanoparticles in photodynamic therapy An emerging paradigm. *Adv. Drug Deliv. Rev.* **2008,** *60*, 1627-1637.

[70] Liqiang, J.; Yichun, Q.; Baiqi, W.; Shudan, L.; Baojiang, J.; Libin, Y.; Wei, F.; Honggng, F.; Jiazhong, S., Review of photoluminescence performance of nano-sized semiconductor materials and its relationships with photocatalytic activity. *Sol. Energy Mater. Sol. Cells* **2006,** *90*, 1773-1787.

[71] Wood, V.; Bulović, V., Colloidal quantum dot light-emitting devices. *Nano Rev.* **2010,** *1*, 5202.

[72] Xing, L.-L.; Ma, C.-H.; Chen, Z.-H.; Chen, Y.-J.; Xue, X.-Y., High gas sensing performance of one-step-synthesized Pd–ZnO nanoflowers due to surface reactions and modifications. *Nanotechnology* **2011,** *22*, 215501.

[73] Wu, X.; Hou, M.; Ge, J., Metal–organic frameworks and inorganic nanoflowers. a type of emerging inorganic crystal nanocarrier for enzyme immobilization. *Catal. Sci. Technol.* **2015,** *5*, 5077-5085.

[74] Chen, Z.; Dinh, H.; Miller, E., *Photoelectrochemical Water Splitting*. 1 ed.; Springer-Verlag New York: 2013; p 126.

[75] Tang, J.; Durrant, J. R.; Klug, D. R., Mechanism of Photocatalytic Water Splitting in TiO2. Reaction of Water with Photoholes, Importance of Charge Carrier Dynamics, and Evidence for Four-Hole Chemistry. *J. Am. Chem. Soc.* **2008,** *130*, 13885-13891.

[76] Jiang, C.; Moniz, S. J. A.; Wang, A.; Zhang, T.; Tang, J., Photoelectrochemical devices for solar water splitting – materials and challenges. *Chem. Soc. Rev.* **2017,** *46*, 4645-4660.

[77] Materials, A. S. f. T. a. Standard Tables for Reference Solar Spectral Irradiances: Direct Normal and Hemispherical on 37° Tilted Surface. https://www.astm.org/Standards/G173.htm (accessed 06/08/2020).

[78] Dotan, H.; Mathews, N.; Hisatomi, T.; Grätzel, M.; Rothschild, A., On the Solar to Hydrogen Conversion Efficiency of Photoelectrodes for Water Splitting. *J. Phys. Chem. Lett.* **2014,** *5*, 3330-3334.

[79] Dotan, H.; Sivula, K.; Grätzel, M.; Rothschild, A.; Warren, S. C., Probing the photoelectrochemical properties of hematite (α-Fe_2O_3) electrodes using hydrogen peroxide as a hole scavenger. *Energy Environ. Sci.* **2010,** *4*, 958-964.

[80] Shet, S.; Ahn, K.-S.; Deutsch, T.; Wang, H.; Nuggehalli, R.; Yan, Y.; Turner, J.; Al-Jassim, M., Influence of gas ambient on the synthesis of co-doped ZnO:(Al,N) films for photoelectrochemical water splitting. *Journal of Power Sources* **2010,** *195*, 5801-5805.

[81] Chen, H. M.; Chen, C. K.; Chang, Y.-C.; Tsai, C.-W.; Liu, R.-S.; Hu, S.-F.; Chang, W.-S.; Chen, K.-H., Quantum Dot Monolayer Sensitized ZnO Nanowire-Array Photoelectrodes. True Efficiency for Water Splitting. *Angew. Chem. Int. Ed. Engl.* **2010,** *122*, 6102-6105.

[82] Zhang, X.; Liu, Y.; Kang, Z., 3D Branched ZnO Nanowire Arrays Decorated with Plasmonic Au Nanoparticles for High-Performance Photoelectrochemical Water Splitting. *ACS Appl. Mater. Interfaces* **2014,** *6*, 4480-4489.

[83] Prasad, M.; Sharma, V.; Aher, R.; Rokade, A.; Ilaiyaraja, P.; Sudakar, C.; Jadkar, S., Synergistic effect of Ag plasmon- and reduced graphene oxide-embedded ZnO nanorod-based photoanodes for enhanced photoelectrochemical activity. *Journal of Material Science* **2017,** *52*, 13572-13585.

[84] Kang, Z.; Si, H.; Zhang, S.; Wu, J.; Sun, Y.; Liao, Q.; Zhang, Z.; Zhang, Y., Interface Engineering for Modulation of Charge Carrier Behavior in ZnO Photoelectrochemical Water Splitting. *Adv. Funct. Mater.* **2019,** *29*, 1808032.

[85] Yang, H.; Bright, J.; Kasani, S.; Zheng, P.; Musho, T.; Chen, B.; Huang, L.; Wu, N., Metal–organic framework coated titanium dioxide nanorod array p–n heterojunction photoanode for solar water-splitting. *Nano Res.* **2018,** *12*, 643-650.

[86] Tang, P.-Y.; Han, L.-J.; Hegner, F. S.; Paciok, P.; Martí Biset-Peiró; Du, H.-C.; Wei, X.-K.; Jin, L.; Xie, H.-B.; Shi, Q.; Andreu, T.; Lira-Cantú, M.; Heggen, M.; Dunin-Borkowski, R. E.; Núria López; Galán-Mascarós, J. R.; Morante, J. R.; Arbiol, J., Boosting Photoelectrochemical Water Oxidation of Hematite in Acidic Electrolytes by Surface State Modification. *Adv. Energy Mater.* **2019,** *9*, 1901836.

[87] Wolcott, A.; Smith, W. A.; Kuykendall, T. R.; Zhao, Y.; Zhang, J. Z., Photoelectrochemical Study of Nanostructured ZnO Thin Films for Hydrogen Generation from Water Splitting. *Adv. Funct. Mater.* **2009,** *19*, 1849-1856.

[88] Wang, M.; Ren, F.; Zhou, J.; Cai, G.; Cai, L.; Hu, Y.; Wang, D.; Liu, Y.; Guo, L.; Shen, S., N Doping to ZnO Nanorods for Photoelectrochemical Water Splitting under Visible Light: Engineered Impurity Distribution and Terraced Band Structure. *Sci Rep* **2015,** *5*, 12925.

[89] Li, X.; Liu, S.; Fan, K.; Liu, Z.; Song, B.; Yu, J., MOF-Based Transparent Passivation Layer Modified ZnO Nanorod Arrays for Enhanced Photo-Electrochemical Water Splitting. *Adv. Energy Mater.* **2018,** *8*, 1800101.

[90] Galán-González, A.; Sivan, A. K.; Hernández-Ferrer, J.; Bowen, L.; Mario, L. D.; Martelli, F.; Benito, A. M.; Maser, W. K.; Chaudhry, M. U.; Gallant, A.; Zeze, D. A.; Atkinson, D., Cobalt-Doped ZnO Nanorods Coated with Nanoscale Metal–Organic Framework Shells for Water-Splitting Photoanodes. *ACS Appl. Nano Mater.* **2020**.

[91] Markets, M. a. Zinc Oxide Market by Process, Grade, Application, Region - Global Forecast from 2018 to 2024. https://www.marketsandmarkets.com/Market-Reports/zinc-oxide-market-116672256.html (accessed 27/03/2020).

[92] Kolodziejczak-Radzimska, A.; Jesionowski, T., Zinc Oxide-From Synthesis to Application: A Review. *Materials (Basel)* **2014**, *7*, 2833-2881.

[93] Huang, J.; Yin, Z.; Zheng, Q., Applications of ZnO in organic and hybrid solar cells. *Energy Environ. Sci.* **2011**, *4*.

[94] Zhu, L.; Zeng, W., Room-temperature gas sensing of ZnO-based gas sensor: A review. *Sens. Actuator A Phys.* **2017**, *267*, 242-261.

[95] Shi, L. E.; Li, Z. H.; Zheng, W.; Zhao, Y. F.; Jin, Y. F.; Tang, Z. X., Synthesis, antibacterial activity, antibacterial mechanism and food applications of ZnO nanoparticles: a review. *Food Addit. Contam. Part A Chem. Anal. Control Expo. Risk Assess.* **2014**, *31*, 173-86.

[96] Kumar, B.; Kim, S.-W., Energy harvesting based on semiconducting piezoelectric ZnO nanostructures. *Nano Energy* **2012**, *1*, 342-355.

[97] Lee, K. M.; Lai, C. W.; Ngai, K. S.; Juan, J. C., Recent developments of zinc oxide based photocatalyst in water treatment technology: A review. *Water Res* **2016**, *88*, 428-448.

[98] Hamid, S. B. A.; Teh, S. J.; Lai, C. W., Photocatalytic Water Oxidation on ZnO: A Review. *Catalysts* **2017**, *7*.

[99] Coleman, V. A.; Bradby, J. E.; Jagadish, C.; Munroe, P.; Heo, Y. W.; Pearton, S. J.; Norton, D. P.; Inoue, M.; Yano, M., Mechanical properties of ZnO epitaxial layers grown on a- and c-axis sapphire. *Appl. Phys. Lett.* **2005**, *86*.

[100] Porter, F. C., *Zinc Handbook: Properties, Processing, and Use In Design*. 1st ed.; Taylor & Francis Group: CRC Press, 1991; p 648.

[101] Hofmann, D. M.; Pfisterer, D.; Sann, J.; Meyer, B. K.; Tena-Zaera, R.; Munoz-Sanjose, V.; Frank, T.; Pensl, G., Properties of the oxygen vacancy in ZnO. *Appl. Phys. A* **2007**, *88*, 147-151.

[102] Tsukazaki, A.; Ohtomo, A.; Onuma, T.; Ohtani, M.; Makino, T.; Sumiya, M.; Ohtani, K.; Chichibu, S. F.; Fuke, S.; Segawa, Y.; Ohno, H.; Koinuma, H.; Kawasaki, M., Repeated temperature modulation epitaxy for p-type doping and light-emitting diode based on ZnO. *Nat. Mater.* **2004**, *4*, 42-46.

[103] Janotti, A.; Van de Walle, C. G., Fundamentals of zinc oxide as a semiconductor. *Rep. Prog. Phys.* **2009**, *72*.

[104] Kaur, G.; Mitra, A.; Yadav, K. L., Pulsed laser deposited Al-doped ZnO thin films for optical applications. *Prog. Nat. Sci.* **2015**, *25*, 12-21.

[105] Solanki, R.; Collins, G. J., Laser induced deposition of zinc oxide. *Appl. Phys. Lett.* **1983**, *42*, 662-663.

[106] Ellmer, K., Magnetron sputtering of transparent conductive zinc oxide. Relation between the sputtering parameters and the electronic properties. *J. Phys. D: Appl. Phys* **2000**, *33*, 17-32.

[107] Konstantinidis, S.; Hemberg, A.; Dauchot, J. P.; Hecq, M., Deposition of zinc oxide layers by high-power impulse magnetron sputtering. *J. Vac. Sci. Technol. B* **2007,** *25*.

[108] Bagnall, D. M.; Chen, Y. F.; Shen, M. Y.; Zhu, Z.; Goto, T.; Yao, T., Room temperature excitonic stimulated emission from zinc oxide epilayers grown by plasma-assisted MBE. *J. Cryst. Growth* **1998,** *184/185*, 605-609.

[109] Suja, M.; Bashar, S. B.; Morshed, M. M.; Liu, J., Realization of Cu-Doped p-Type ZnO Thin Films by Molecular Beam Epitaxy. *ACS Appl Mater Interfaces* **2015,** *7*, 8894-9.

[110] Chen, X. L.; Xu, B. H.; Xue, J. M.; Zhao, Y.; Wei, C. C.; Sun, J.; Wang, Y.; Zhang, X. D.; Geng, X. H., Boron-doped zinc oxide thin films for large-area solar cells grown by metal organic chemical vapor deposition. *Thin Solid Films* **2007,** *515*, 3753-3759.

[111] Kim, J. S.; Marzouk, H. A.; Reucroft, P. J.; C. E. Hamrin, J., Characterization of high quality c axis oriented ZnO thin films grown by metal organic chemical vapor deposition using zinc acetate as source material. *Thin Solid Films* **1992,** *217*, 133-137.

[112] Bhachu, D. S.; Sankar, G.; Parkin, I. P., Aerosol Assisted Chemical Vapor Deposition of Transparent Conductive Zinc Oxide Films. *Chem. Mater.* **2012,** *24*, 4704-4710.

[113] Zhao, C.; Chen, A.; Ji, X.; Zhu, Y.; Gui, X.; Huang, F.; Tang, Z., Growth of vertically aligned ZnO nanowire arrays on ZnO single crystals. *Mater. Lett.* **2015,** *154*, 40-43.

[114] Tynell, T.; Karppinen, M., Atomic layer deposition of ZnO: a review. *Semicond. Sci. Technol.* **2014,** *29*.

[115] Lim, Y. T.; Son, J. Y.; Rhee, J. S., Vertical ZnO nanorod array as an effective hydrogen gas sensor. *Ceram. Int.* **2013,** *39*, 887-890.

[116] Pulidindi, K.; Rajpathak, T. Electronic Protection Device (EPD) Coatings Market Size, By Material, By Mode Of Application, By End-User, Industry Analysis Report, Regional Outlook, Application Growth Potential, Price Trends, Competitive Market Share & Forecast, 2018 – 2025. https://www.gminsights.com/industry-analysis/electronic-protection-device-coatings-market (accessed 22-05-2020).

[117] Izaki, M.; Omi, T., Transparent zinc oxide films prepared by electrochemical reaction. *Appl. Phys. Lett.* **1996,** *68*, 2439-2440.

[118] Illy, B.; Shollock, B. A.; Macmanus-Driscoll, J. L.; Ryan, M. P., Electrochemical growth of ZnO nanoplates. *Nanotechnology* **2005,** *16*, 320-4.

[119] Cao, B.; Li, Y.; Duan, G.; Cai, W., Growth of ZnO Nanoneedle Arrays with Strong Ultraviolet Emissions by an Electrochemical Deposition Method. *Cryst. Growth Des.* **2006,** *6*, 1091-1095.

[120] Xu, C.; Kim, B.-S.; Lee, J.-H.; Kim, M.; Hwang, S. W.; Choi, B. L.; Lee, E. K.; Kim, J. M.; Whang, D., Seed-free electrochemical growth of ZnO nanotube arrays on single-layer graphene. *Mater. Lett.* **2012,** *72*, 25-28.

[121] ToptionLab https://www.toptionlab.com/ (accessed 25-05-2020).

[122] Byrappa, K.; Yoshimura, M., *Handbook of Hydrothermal Technology*. William Andrew LLC: 2001; p 893.

References

[123] Liu, B.; Zeng, H. C., Hydrothermal Synthesis of ZnO Nanorods in the Diameter Regime of 50 nm. *J. Am. Chem. Soc.* **2003,** *125*, 4430-4431.

[124] Yu, J.; Yu, X., Hydrothermal Synthesis and Photocatalytic Activity of Zinc Oxide Hollow Spheres. *Environ. Sci. Technol.* **2008,** *42*, 4902-4907.

[125] Byrappa, K.; Subramani, A. K.; Ananda, S.; Rai, K. M. L.; Dinesh, R.; Yoshimura, M., Photocatalytic degradation of rhodamine B dye using hydrothermally synthesized ZnO. *Bull. Mater. Sci.* **2006,** *29*, 433-438.

[126] Hodes, G., Semiconductor and ceramic nanoparticle films deposited by chemical bath deposition. *Phys Chem Chem Phys* **2007,** *9*, 2181-96.

[127] Tiwari, J. N.; Tiwari, R. N.; Kim, K. S., Zero-dimensional, one-dimensional, two-dimensional and three-dimensional nanostructured materials for advanced electrochemical energy devices. *Prog. Mater. Sci.* **2012,** *57*, 724-803.

[128] Sirelkhatim, A.; Mahmud, S.; Seeni, A.; Kaus, N. H. M.; Ann, L. C.; Bakhori, S. K. M.; Hasan, H.; Mohamad, D., Review on Zinc Oxide Nanoparticles: Antibacterial Activity and Toxicity Mechanism. *Nanomicro Lett* **2015,** *7*, 219-242.

[129] Espitia, P. J. P.; Soares, N. d. F. F.; Coimbra, J. S. d. R.; de Andrade, N. J.; Cruz, R. S.; Medeiros, E. A. A., Zinc Oxide Nanoparticles: Synthesis, Antimicrobial Activity and Food Packaging Applications. *Food Bioproc. Tech.* **2012,** *5*, 1447-1464.

[130] Becheri, A.; Dürr, M.; Lo Nostro, P.; Baglioni, P., Synthesis and characterization of zinc oxide nanoparticles: application to textiles as UV-absorbers. *J. Nanopart. Res.* **2007,** *10*, 679-689.

[131] Beek, W. J. E.; Wienk, M. M.; Janssen, R. A. J., Efficient Hybrid Solar Cells from Zinc Oxide Nanoparticles and a Conjugated Polymer. *Adv. Mater.* **2004,** *16*, 1009-1013.

[132] Reddy, K. M.; Feris, K.; Bell, J.; Wingett, D. G.; Hanley, C.; Punnoose, A., Selective toxicity of zinc oxide nanoparticles to prokaryotic and eukaryotic systems. *Appl Phys Lett* **2007,** *90*, 2139021-2139023.

[133] Jiang, J.; Pi, J.; Cai, J., The Advancing of Zinc Oxide Nanoparticles for Biomedical Applications. *Bioinorg Chem Appl* **2018,** *2018*, 1062562.

[134] Lavand, A. B.; Malghe, Y. S., Synthesis, characterization and visible light photocatalytic activity of nitrogen-doped zinc oxide nanospheres. *J. Asian Ceram. Soc.* **2018,** *3*, 305-310.

[135] Tong, D. G.; Wu, P.; Su, P. K.; Wang, D. Q.; Tian, H. Y., Preparation of zinc oxide nanospheres by solution plasma process and their optical property, photocatalytic and antibacterial activities. *Mater. Lett.* **2012,** *70*, 94-97.

[136] Jin, T.; Sun, D.; Su, J. Y.; Zhang, H.; Sue, H. J., Antimicrobial efficacy of zinc oxide quantum dots against Listeria monocytogenes, Salmonella Enteritidis, and Escherichia coli O157:H7. *J Food Sci* **2009,** *74*, M46-52.

[137] Huang, Q.; Zeng, D.; Li, H.; Xie, C., Room temperature formaldehyde sensors with enhanced performance, fast response and recovery based on zinc oxide quantum dots/graphene nanocomposites. *Nanoscale* **2012,** *4*, 5651-8.

[138] Bhanjana, G.; Dilbaghi, N.; Kumar, R.; Kumar, S., Zinc Oxide Quantum Dots as Efficient Electron Mediator for Ultrasensitive and Selective Electrochemical Sensing of Mercury. *Electrochim. Acta* **2015,** *178*, 361-367.

[139] Liu, Y.; Ai, K.; Yuan, Q.; Lu, L., Fluorescence-enhanced gadolinium-doped zinc oxide quantum dots for magnetic resonance and fluorescence imaging. *Biomaterials* **2011**, *32*, 1185-92.

[140] Ramsperger, U.; Uchihashi, T.; Nejoh, H., Fabrication and lateral electronic transport measurements of gold nanowires. *Appl. Phys. Lett.* **2001**, *78*, 85-87.

[141] Greene, L. E.; Yuhas, B. D.; Law, M.; Zitoun, D.; Yang, P., Solution-Grown Zinc Oxide Nanowires. *Inorg. Chem.* **2009**, *45*, 7535-7543.

[142] Wang, R. M.; Xing, Y. J.; Xu, J.; Yu, D. P., Fabrication and microstructure analysis on zinc oxide nanotubes. *New J. Phys.* **2003**, *5*, 115.1-115.7.

[143] Jie, J.; Wang, G.; Han, X.; Yu, Q.; Liao, Y.; Li, G.; Hou, J. G., Indium-doped zinc oxide nanobelts. *Chem. Phys. Lett.* **2004**, *387*, 466-470.

[144] Fulati, A.; Ali, S. M.; Riaz, M.; Amin, G.; Nur, O.; Willander, M., Miniaturized pH Sensors Based on Zinc Oxide Nanotubes/Nanorods. *Sensors (Basel)* **2009**, *9*, 8911-23.

[145] Choopun, S.; Hongsith, N.; Mangkorntong, P.; Mangkorntong, N., Zinc oxide nanobelts by RF sputtering for ethanol sensor. *Physica E Low Dimens. Syst. Nanostruct.* **2007**, *39*, 53-56.

[146] Cui, J., Zinc oxide nanowires. *Mater. Charact.* **2012**, *64*, 43-52.

[147] Zhou, W.; Zhang, X.; Zhao, D.; Gao, M.; Xie, S., ZnO nanorods: morphology control, optical properties, and nanodevice applications. *Sci. China Phys. Mech.* **2013**, *56*, 2243-2265.

[148] Antoine, T. E.; Mishra, Y. K.; Trigilio, J.; Tiwari, V.; Adelung, R.; Shukla, D., Prophylactic, therapeutic and neutralizing effects of zinc oxide tetrapod structures against herpes simplex virus type-2 infection. *Antiviral Res* **2012**, *96*, 363-75.

[149] Zeng, J. H.; Jin, B. B.; Wang, Y. F., Facet enhanced photocatalytic effect with uniform single-crystalline zinc oxide nanodisks. *Chem. Phys. Lett.* **2009**, *472*, 90-95.

[150] Park, J. K.; Kim, Y. J.; Yeom, J.; Jeon, J. H.; Yi, G. C.; Je, J. H.; Hahn, S. K., The topographic effect of zinc oxide nanoflowers on osteoblast growth and osseointegration. *Adv Mater* **2010**, *22*, 4857-61.

[151] Weckman, T.; Laasonen, K., Atomic Layer Deposition of Zinc Oxide: Diethyl Zinc Reactions and Surface Saturation from First-Principles. *J. Phys. Chem. C* **2016**, *120*, 21460-21471.

[152] Guziewicz, E.; Godlewski, M.; Wachnicki, L.; Krajewski, T. A.; Luka, G.; Gieraltowska, S.; Jakiela, R.; Stonert, A.; Lisowski, W.; Krawczyk, M.; Sobczak, J. W.; Jablonski, A., ALD grown zinc oxide with controllable electrical properties. *Semicond. Sci. Technol.* **2012**, *27*.

[153] Hench, L. L.; West, J. K., The sol-gel process. *Chem. Rev.* **1990**, *90*, 33-72.

[154] Znaidi, L., Sol–gel-deposited ZnO thin films: A review. *Mater, Sci, Eng, B Solid State Mater, Adv, Technol,* **2010**, *174*, 18-30.

[155] Scherer, G. W.; Brinker, C. J.; Roth, E. P., Sol → gel → glass. III. Viscous sintering. *J. Non-Cryst. Solids* **1985**, *72*, 369-389.

[156] Demianets, L. N.; Kostomarov, D. V., Mechanism of zinc oxide single crystal growth under hydrothermal conditions. *Ann. Chim. Sci. Mat.* **2001**, *26*, 193-198.

[157] Demianets, L. N.; Kostomarov, D. V.; Kuzmina, I. P., Chemistry and Kinetics of ZnO Growth from Alkaline Hydrothermal Solutions. *Inorg. Mater.* **2002,** *38*, 124-131.

[158] Greene, L. E.; Law, M.; Tan, D. H.; Montano, M.; Goldberger, J.; Somorjai, G.; Yang, P., General Route to Vertical ZnO Nanowire Arrays Using Textured ZnO Seeds. *Nano Letters* **2005,** *5*, 1231-1236.

[159] Pradhan, B.; Batabyal, S. K.; Pal, A. J., Vertically aligned ZnO nanowire arrays in Rose Bengal-based dye-sensitized solar cells. *Sol. Energy Mater. Sol. Cells* **2007,** *91*, 769-773.

[160] Lin, Y.; Jiang, Q., Effect of substrates and anions of zinc salts on the morphology of ZnO nanostructures. *Appl. Surf. Sci.* **2011,** *257*, 8728-8731.

[161] Akgun, M. C.; Afal, A.; Unalan, H. E., Hydrothermal zinc oxide nanowire growth with different zinc salts. *J. Mater. Res.* **2012,** *27*, 2401-2407.

[162] Abbasi, M. A.; Khan, Y.; Hussain, S.; Nur, O.; Willander, M., Anions effect on the low temperature growth of ZnO nanostructures. *Vacuum* **2012,** *86*, 1998-2001.

[163] Jung, J.; Myoung, J.; Lim, S., Effects of ZnO nanowire synthesis parameters on the photovoltaic performance of dye-sensitized solar cells. *Thin Solid Films* **2012,** *520*, 5779-5789.

[164] Strano, V.; Urso, R. G.; Scuderi, M.; Iwu, K. O.; Simone, F.; Ciliberto, E.; Spinella, C.; Mirabella, S., Double Role of HMTA in ZnO Nanorods Grown by Chemical Bath Deposition. *J. Phys. Chem. C* **2014,** *118*, 28189-28195.

[165] Solís-Pomar, F.; Martínez, E.; Meléndrez, M. F.; Pérez-Tijerina, E., Growth of vertically aligned ZnO nanorods using textured ZnO films. *Nanoscale Res. Lett.* **2011,** *6*, 1-11.

[166] Parize, R.; Garnier, J.; Chaix-Pluchery, O.; Verrier, C.; Appert, E.; Consonni, V., Effects of Hexamethylenetetramine on the Nucleation and Radial Growth of ZnO Nanowires by Chemical Bath Deposition. *J. Phys. Chem. C* **2016,** *120*, 5242-5250.

[167] Baruah, S.; Dutta, J., pH-dependent growth of zinc oxide nanorods. *J. Cryst. Growth* **2009,** *311*, 2549-2554.

[168] Verrier, C.; Appert, E.; Chaix-Pluchery, O.; Rapenne, L.; Rafhay, Q.; Kaminski-Cachopo, A.; Consonni, V., Effects of the pH on the Formation and Doping Mechanisms of ZnO Nanowires Using Aluminum Nitrate and Ammonia. *Inorg Chem* **2017,** *56*, 13111-13122.

[169] Cheng, Q.; Ostrikov, K., Temperature-dependent growth mechanisms of low-dimensional ZnO nanostructures. *CrystEngComm* **2011,** *13*.

[170] Samadi, M.; Zirak, M.; Naseri, A.; Khorashadizade, E.; Moshfegh, A. Z., Recent progress on doped ZnO nanostructures for visible-light photocatalysis. *Thin Solid Films* **2016,** *605*, 2-19.

[171] Hassanpour, A.; Guo, P.; Shen, S.; Bianucci, P., The effect of cation doping on the morphology, optical and structural properties of highly oriented wurtzite ZnO-nanorod arrays grown by a hydrothermal method. *Nanotechnology* **2017,** *28*, 435707.

[172] Thomas, M. A.; Sun, W. W.; Cui, J. B., Mechanism of Ag Doping in ZnO Nanowires by Electrodeposition: Experimental and Theoretical Insights. *J. Phys. Chem. C* **2012,** *116*, 6383-6391.

[173] Sheini, F. J.; Joag, D. S.; More, M. A., Electrochemical synthesis of Sn doped ZnO nanowires on zinc foil and their field emission studies. *Thin Solid Films* **2010,** *519*, 184-189.

[174] Lee, W.; Jeong, M.-C.; Joo, S.-W.; Myoung, J.-M., Arsenic doping of ZnO nanowires by post-annealing treatment. *Nanotechnology* **2005,** *16*, 764-768.

[175] Wu, C.; Shen, L.; Zhang, Y.-C.; Huang, Q., Solvothermal synthesis of Cr-doped ZnO nanowires with visible light-driven photocatalytic activity. *Mater. Lett.* **2011,** *65*, 1794-1796.

[176] Jia, T.; Wang, W.; Long, F.; Fu, Z.; Wang, H.; Zhang, Q., Fabrication, characterization and photocatalytic activity of La-doped ZnO nanowires. *J. Alloys Compd.* **2009,** *484*, 410-415.

[177] Wan, Q.; Li, Q. H.; Chen, Y. J.; Wang, T. H.; He, X. L.; Gao, X. G.; Li, J. P., Positive temperature coefficient resistance and humidity sensing properties of Cd-doped ZnO nanowires. *Appl. Phys. Lett.* **2004,** *84*, 3085-3087.

[178] Hongsith, N.; Viriyaworasakul, C.; Mangkorntong, P.; Mangkorntong, N.; Choopun, S., Ethanol sensor based on ZnO and Au-doped ZnO nanowires. *Ceram. Int.* **2008,** *34*, 823-826.

[179] Kim, D.; Kim, W.; Jeon, S.; Yong, K., Highly efficient UV-sensing properties of Sb-doped ZnO nanorod arrays synthesized by a facile, single-step hydrothermal reaction. *RSC Adv.* **2017,** *7*, 40539-40548.

[180] Deka, S.; Joy, P. A., Synthesis and magnetic properties of Mn doped ZnO nanowires. *Solid State Commun.* **2007,** *142*, 190-194.

[181] Xing, G. Z.; Yi, J. B.; Tao, J. G.; Liu, T.; Wong, L. M.; Zhang, Z.; Li, G. P.; Wang, S. J.; Ding, J.; Sum, T. C.; Huan, C. H. A.; Wu, T., Comparative Study of Room-Temperature Ferromagnetism in Cu-Doped ZnO Nanowires Enhanced by Structural Inhomogeneity. *Adv. Mater.* **2008,** *20*, 3521-3527.

[182] Lee, J.; Cha, S.; Kim, J.; Nam, H.; Lee, S.; Ko, W.; Wang, K. L.; Park, J.; Hong, J., P-type conduction characteristics of lithium-doped ZnO nanowires. *Adv Mater* **2011,** *23*, 4183-7.

[183] Lu, M.-P.; Lu, M.-Y.; Chen, L.-J., p-Type ZnO nanowires: From synthesis to nanoenergy. *Nano Energy* **2012,** *1*, 247-258.

[184] Yuhas, B. D.; Zitoun, D. O.; Pauzauskie, P. J.; He, R.; Yang, P., Transition-metal doped zinc oxide nanowires. *Angew Chem Int Ed Engl* **2006,** *45*, 420-3.

[185] Zhang, Y.; Lu, H. L.; Wang, T.; Ren, Q. H.; Gu, Y. Z.; Li, D. H.; Zhang, D. W., Facile synthesis and enhanced luminescent properties of ZnO/HfO2 core-shell nanowires. *Nanoscale* **2015,** *7*, 15462-8.

[186] Zhang, Y.; Lu, H. L.; Wang, T.; Ren, Q. H.; Chen, H. Y.; Zhang, H.; Ji, X. M.; Liu, W. J.; Ding, S. J.; Zhang, D. W., Photoluminescence enhancement of ZnO nanowire arrays by atomic layer deposition of ZrO2 layers and thermal annealing. *Phys Chem Chem Phys* **2016,** *18*, 16377-85.

[187] Law, M.; Greene, L. E.; Radenovic, A.; Kuykendall, T.; Liphardt, J.; Yang, P., ZnO–Al2O3 and ZnO–TiO2 Core–Shell Nanowire Dye-Sensitized Solar Cells. *J. Phys. Chem. B* **2006,** *110*, 22652-22663.

[188] Wei, L.; Liu, Q. X.; Zhu, B.; Liu, W. J.; Ding, S. J.; Lu, H. L.; Jiang, A.; Zhang, D. W., Low-Cost and High-Productivity Three-Dimensional Nanocapacitors Based on Stand-Up ZnO Nanowires for Energy Storage. *Nanoscale Res Lett* **2016,** *11*, 213.

References

[189] Li, H.; Eddaoudi, M.; O'Keeffe, M.; Yaghi, O. M., Design and synthesis of an exceptionally stable and highly porous metal-organic framework. *Nature* **1999,** *402*, 276-279.

[190] Farha, O. K.; Eryazici, I.; Jeong, N. C.; Hauser, B. G.; Wilmer, C. E.; Sarjeant, A. A.; Snurr, R. Q.; Nguyen, S. T.; Yazaydın, A. O. z. r.; Hupp, J. T., Metal–Organic Framework Materials with Ultrahigh Surface Areas. Is the Sky the Limit. *J. Am. Chem. Soc.* **2012,** *134*, 15016-15021.

[191] Furukawa, H.; Cordova, K. E.; O'Keeffe, M.; Yaghi, O. M., The chemistry and applications of metal-organic frameworks. *Science* **2013,** *341*, 1230444.

[192] Yaghi, O. M.; O'Keeffe, M.; Ockwig, N. W.; Chae, H. K.; Eddaoudi, M.; Kim, J., Reticular synthesis and the design of new materials. *Nature* **2003,** *423*, 705-714.

[193] Chen, B.; Yang, Z.; Zhu, Y.; Xia, Y., Zeolitic imidazolate framework materials: recent progress in synthesis and applications. *J. Mater. Chem. A* **2014,** *2*, 16811-16831.

[194] Park, K. S.; Ni, Z.; Côté, A. P.; Choi, J. Y.; Huang, R.; Uribe-Romo, F. J.; Chae, H. K.; O'Keeffe, M.; Yaghi, O. M., Exceptional chemical and thermal stability of zeolitic imidazolate frameworks. *Proc. Natl. Acad. Sci. U.S.A.* **2006,** *103*, 10186-10191.

[195] Cacho-Bailo, F.; Seoane, B.; Téllez, C.; Coronas, J., ZIF-8 continuous membrane on porous polysulfone for hydrogen separation. *J. Membr. Sci.* **2014,** *464*, 119-126.

[196] Seoane, B.; Coronas, J.; Gascon, I.; Etxeberria Benavides, M.; Karvan, O.; Caro, J.; Kapteijn, F.; Gascon, J., Metal-organic framework based mixed matrix membranes: a solution for highly efficient CO2 capture? *Chem Soc Rev* **2015,** *44*, 2421-54.

[197] Torad, N. L.; Salunkhe, R. R.; Li, Y.; Hamoudi, H.; Imura, M.; Sakka, Y.; Hu, C. C.; Yamauchi, Y., Electric double-layer capacitors based on highly graphitized nanoporous carbons derived from ZIF-67. *Chemistry* **2014,** *20*, 7895-900.

[198] You, B.; Jiang, N.; Sheng, M.; Gul, S.; Yano, J.; Sun, Y., High-Performance Overall Water Splitting Electrocatalysts Derived from Cobalt-Based Metal–Organic Frameworks. *Chem. Mater.* **2015,** *27*, 7636-7642.

[199] Wang, G.; Yang, X.; Qian, F.; Zhang, J. Z.; Li, Y., Double-Sided CdS and CdSe Quantum Dot Co-Sensitized ZnO Nanowire Arrays for Photoelectrochemical Hydrogen Generation. *Nano Letters* **2010,** *10*, 1088-1092.

[200] Dhara, S.; Giri, P. K., On the origin of enhanced photoconduction and photoluminescence from Au and Ti nanoparticles decorated aligned ZnO nanowire heterostructures. *J. Appl. Phys.* **2011,** *110*.

[201] Matsumiya, M.; Shin, W.; Izu, N.; Murayama, N., Nano-structured thin-film Pt catalyst for thermoelectric hydrogen gas sensor. *Sens. Actuators B Chem.* **2003,** *93*, 309-315.

[202] Zhang, Y.; Xu, J.; Xu, P.; Zhu, Y.; Chen, X.; Yu, W., Decoration of ZnO nanowires with Pt nanoparticles and their improved gas sensing and photocatalytic performance. *Nanotechnology* **2010,** *21*, 285501.

[203] Velasco-Vélez, J. J.; Jones, T. E.; Streibel, V.; Hävecker, M.; Chuang, C. H.; Frevel, L.; Plodinec, M.; Centeno, A.; Zurutuza, A.; Wang, R.; Arrigo, R.; Mom, R.; Hofmann, S.; Schlögl, R.; Knop-Gericke, A., Electrochemically active Ir NPs on

graphene for OER in acidic aqueous electrolyte investigated by in situ and ex situ spectroscopies. *Surf. Sci.* **2019,** *681*, 1-8.

[204] Böhm, D.; Beetz, M.; Schuster, M.; Peters, K.; Hufnagel, A. G.; Döblinger, M.; Böller, B.; Bein, T.; Fattakhova-Rohlfing, D., Efficient OER Catalyst with Low Ir Volume Density Obtained by Homogeneous Deposition of Iridium Oxide Nanoparticles on Macroporous Antimony-Doped Tin Oxide Support. *Adv. Funct. Mater.* **2019,** *30*.

[205] Guo, C. X.; Dong, Y.; Yang, H. B.; Li, C. M., Graphene Quantum Dots as a Green Sensitizer to Functionalize ZnO Nanowire Arrays on F-Doped SnO2Glass for Enhanced Photoelectrochemical Water Splitting. *Adv. Energy Mater.* **2013,** *3*, 997-1003.

[206] Liu, J.; Guo, C.; Li, C. M.; Li, Y.; Chi, Q.; Huang, X.; Liao, L.; Yu, T., Carbon-decorated ZnO nanowire array: A novel platform for direct electrochemistry of enzymes and biosensing applications. *Electrochem. Commun.* **2009,** *11*, 202-205.

[207] Kaphle, A.; Hari, P., Variation of index of refraction in cobalt doped ZnO nanostructures. *J. Appl. Phys.* **2017,** *122*, 165304.

[208] Kelly, P. J.; Arnell, R. D., Magnetron sputtering. A review of recent developments and applications. *Vacuum* **2000,** *50*, 159-172.

[209] Seoane, B.; Castellanos, S.; Dikhtiarenko, A.; Kapteijn, F.; Gascon, J., Multi-scale crystal engineering of metal organic frameworks. *Coord. Chem. Rev.* **2016,** *307*, 147-187.

[210] Zhong, J.; Yan, J., Seeing is believing: atomic force microscopy imaging for nanomaterial research. *RSC Adv.* **2016,** *6*, 1103-1121.

[211] Jalili, N.; Laxminarayana, K., A review of atomic force microscopy imaging systems: application to molecular metrology and biological sciences. *Mechatronics* **2004,** *14*, 907-945.

[212] Haugstad, G., *Atomic Force Microscopy: Understanding Basic Modes and Advanced Applications*. Wiley: 2012; Vol. 1, p 528.

[213] Hafner, B. *Scanning Electron Microscopy Primer*; University of Minnesota - Twin Cities: Characterization facility, 2007; p 29.

[214] Giannini, C.; Ladisa, M.; Altamura, D.; Siliqi, D.; Sibillano, T.; De Caro, L., X-ray Diffraction: A Powerful Technique for the Multiple-Length-Scale Structural Analysis of Nanomaterials. *Crystals* **2016,** *6*.

[215] Ameh, E. S., A review of basic crystallography and x-ray diffraction applications. *Int. J. Adv. Manuf. Technol.* **2019,** *105*, 3289-3302.

[216] Stoev, K. N.; Sakurai, K., Review on grazing incidence X-ray spectrometry and reflectometry. *Spectrochim. Acta B* **1999,** *54*, 41-82.

[217] Mack, C. A., *Filed Guide to Optical Lithography*. 2006; Vol. FG06, p 136.

[218] Greczynski, G.; Hultman, L., X-ray photoelectron spectroscopy: Towards reliable binding energy referencing. *Prog. Mater. Sci.* **2020,** *107*.

[219] Einstein, A., On a Heuristic Point of View about the Creation and Conversion of Light. *Ann. Phys. (Berl.)* **1905**.

[220] Oswald, S., X-Ray Photoelectron Spectroscopy in Analysis of Surfaces. In *Encyclopedia of Analytical Chemistry*, 2013.

[221] Scimeca, M.; Bischetti, S.; Lamsira, H. K.; Bonfiglio, R.; Bonanno, E., Energy Dispersive X-ray (EDX) microanalysis: A powerful tool in biomedical research and diagnosis. *Eur J Histochem* **2018,** *62*, 2841.

[222] Tissue, B. M., Ultraviolet and visible absorption spectroscopy. In *Characterization of Materials*, 1st ed.; Kaufmann, E. N., Ed. John Wiley & Sons: Virginia Polytechnic Institute and State University,Blacksburg, Virginia, 2012; Vol. 2, pp 688-698.

[223] Fox, M., *Optical Properties of Solids*. Second ed.; Oxford University Press: 2010; Vol. 1, p 396.

[224] Berera, R.; van Grondelle, R.; Kennis, J. T., Ultrafast transient absorption spectroscopy: principles and application to photosynthetic systems. *Photosynth Res* **2009,** *101*, 105-18.

[225] Prasankumar, R. P.; Upadhya, P. C.; Taylor, A. J., Ultrafast carrier dynamics in semiconductor nanowires. *physica status solidi (b)* **2009,** *246*, 1973-1995.

[226] Gilliland, G. D., Photoluminescence spectroscopy of crystalline semiconductors. *Mater. Sci. Eng. R Rep.* **1997,** *18*, 99-440.

[227] Yacobi, B. G.; Holt, D. B., *Cathodoluminescence Microscopy of Inorganic Solids*. 1st ed.; Springer US: 1990; p 292.

[228] Autolab, M., Autolab Application Note EC08. 2011.

[229] Galan-Gonzalez, A.; Gallant, A.; Zeze, D. A.; Atkinson, D., Controlling the growth of single crystal ZnO nanowires by tuning the atomic layer deposition parameters of the ZnO seed layer. *Nanotechnology* **2019,** *30*, 305602.

[230] Pung, S.-Y.; Choy, K.-L.; Hou, X.; Shan, C., Preferential growth of ZnO thin films by the atomic layer deposition technique. *Nanotechnology* **2008,** *19*.

[231] Guillemin, S.; Consonni, V.; Appert, E.; Puyoo, E.; Rapenne, L.; Roussel, H., Critical Nucleation Effects on the Structural Relationship Between ZnO Seed Layer and Nanowires. *J. Phys. Chem. C* **2012,** *116*, 25106-25111.

[232] Kim, H.; Wang, Z.; Hedhili, M. N.; Wehbe, N.; Alshareef, H. N., Oxidant-Dependent Thermoelectric Properties of Undoped ZnO Films by Atomic Layer Deposition. *Chem. Mater.* **2017,** *29*, 2794-2802.

[233] Bonde, S.; Berthing, T.; Madsen, M. H.; Andersen, T. K.; Buch-Månson, N.; Guo, L.; Li, X.; Badique, F.; Anselme, K.; Nygård, J.; Martinez, K. L., Tuning InAs Nanowire Density for HEK293 Cell Viability, Adhesion, and Morphology. Perspectives for Nanowire-Based Biosensors. *ACS Appl. Mater. Interfaces* **2013,** *5*, 10510-10519.

[234] Deng, M. T.; Vaitiekėnas, S.; Hansen, E. B.; Danon, J.; Leijnse, M.; Flensberg, K.; Nygård, J.; Krogstrup, P.; Marcus, C. M., Majorana bound state in a coupled quantum-dot hybrid-nanowire system. *Science* **2016,** *354*, 1557-1562.

[235] Weckman, T.; Laasonen, K., Atomic Layer Deposition of Zinc Oxide: Diethyl Zinc Reactions and Surface Saturation from First-Principles. *J. Phys. Chem. C* **2016,** *120*, 21460-21471.

[236] Moezzi, A.; McDonagh, A. M.; Cortie, M. B., Zinc oxide particles Synthesis, properties and applications. *Chem. Eng. J.* **2012,** *185-186*, 1-22.

[237] Chaaya, A. A.; Viter, R.; Bechelany, M.; Alute, Z.; Erts, D.; Zalesskaya, A.; Kovalevskis, K.; Rouessac, V.; Smyntyna, V.; Miele, P., Evolution of microstructure and related optical properties of ZnO grown by atomic layer deposition. *Beilstein J. Nanotechnol.* **2013,** *4*, 690-698.

[238] Bielinski, A. R.; Kazyak, E.; Schlepütz, C. M.; Jung, H. J.; Wood, K. N.; Dasgupta, N. P., Hierarchical ZnO Nanowire Growth with Tunable Orientations on Versatile Substrates Using Atomic Layer Deposition Seeding. *Chem. Mater.* **2015,** *27*, 4799-4807.

[239] Park, H. K.; Yang, B. S.; Park, S.; Kim, M. S.; Shin, J. C.; Heo, J., Purge-time-dependent growth of ZnO thin films by atomic layer deposition. *J. Alloys Compd.* **2014,** *605*, 124-130.

[240] Jeong, J. S.; Lee, J. Y., Investigation of initial growth of ZnO nanowires and their growth mechanism. *Nanotechnology* **2010,** *21*, 475603.

[241] Chevalier-César, C.; Capochichi-Gnambodoe, M.; Leprince-Wang, Y., Growth mechanism studies of ZnO nanowire arrays via hydrothermal method. *Applied Physics A* **2013,** *115*, 953-960.

[242] Bielinski, A. R.; Kazyak, E.; Schlepütz, C. M.; Jung, H. J.; Wood, K. N.; Dasgupta, N. P., Hierarchical ZnO Nanowire Growth with Tunable Orientations on versatile substrates using atomic layer deposition seeding. *Chem. Mater.* **2015,** *27*, 4799-4807.

[243] Zhao, J.; Buia, C.; Han, J.; Lu, J. P., Quantum transport properties of ultrathin silver nanowires. *Nanotechnology* **2003,** *14*, 501-504.

[244] Han, N.; Hou, J. J.; Wang, F.; Yip, S.; Yen, Y.-T.; Yang, Z.-x.; Dong, G.; Hung, T.; Chueh, Y.-L.; Ho, J. C., GaAs Nanowires. From Manipulation of Defect Formation to Controllable Electronic Transport Properties. *ACS Nano* **2013,** *7*, 9138-9146.

[245] Syrrokostas, G.; Govatsi, K.; Yannopoulos, S. N., High-Quality, Reproducible ZnO Nanowire Arrays Obtained by a Multiparameter Optimization of Chemical Bath Deposition Growth. *Cryst. Growth Des.* **2016,** *16*, 2140-2150.

[246] Wang, T.; Liu, Y.; Xu, Y.; He, G.; Li, G.; Lv, J.; Wu, M.; Sun, Z.; Fang, Q.; Ma, Y.; Li, J., Synthesis of 1D and heavily doped Zn1–xCoxO six-prism nanorods, Improvement of blue–green emission and room temperature ferromagnetism. *J. Mater. Chem.* **2011,** *21*, 18810–18816.

[247] Sivan, A. K.; Galan-Gonzalez, A.; Mario, L. D.; Tappy, N.; Hernandez-Ferrer, J.; Catone, D.; Turchini, S.; Benito, A. M.; Maser, W. K.; Steinvall, S. E.; Morral, A. F. i.; Gallant, A.; Zeze, D. A.; Atkinson, D.; Martelli1, F., Optical properties and carrier dynamics in Co-doped ZnO nanorods. *arXiv* **2020**.

[248] Godavarti, U.; Mote, V. D.; Dasari, M., Role of cobalt doping on the electrical conductivity of ZnO nanoparticles. *J. Asian Ceram. Soc.* **2018,** *5*, 391-396.

[249] Tiginyanu, I.; Ghimpu, L.; Gröttrup, J.; Postolache, V.; Mecklenburg, M.; Stevens-Kalceff, M. A.; Ursaki, V.; Payami, N.; Feidenhansl, R.; Schulte, K.; Adelung, R.; Mishra, Y. K., Strong light scattering and broadband (UV to IR) photoabsorption in stretchable 3D hybrid architectures based on Aerographite decorated by ZnO nanocrystallites. *Sci. Rep.* **2016,** *6*, 32913.

[250] Janotti, A.; Van de Walle, C. G., Oxygen vacancies in ZnO. *Appl. Phys. Lett.* **2005,** *87*, 122102.

[251] Bauer, C.; Boschloo, G.; Mukhtar, E.; Hagfeldt, A., Ultrafast relaxation dynamics of charge carriers relaxation in ZnO nanocrystalline thin films. *Chem. Phys. Lett.* **2004,** *387*, 176-181.

[252] Lee, Y. R.; Ramdas, A. K.; Aggarwal, R. L., Energy gap, excitonic, and "internal" Mn2+ optical transition in Mn-based II-VI diluted magnetic semiconductors. *Phys. Rev. B* **1988,** *38*, 10600-10610.

[253] Kim, K. J.; Park, Y. R., Spectroscopic ellipsometry study of optical transitions in Zn1−xCoxO alloys. *Appl. Phys. Lett.* **2002,** *81*, 1420-1422.

[254] Johnson, J. C.; Knutsen, K. P.; Yan, H.; Law, M.; Zhang, Y.; Yang, P.; Saykally, R. J., Ultrafast Carrier Dynamics in Single ZnO Nanowire and Nanoribbon Lasers. *Nano Letters* **2004,** *4*, 197-204.

[255] Sun, C.-K.; Sun, S.-Z.; Lin, K.-H.; Zhang, K. Y.-J.; Liu, H.-L.; Liu, S.-C.; Wu, J.-J., Ultrafast carrier dynamics in ZnO nanorods. *Appl. Phys. Lett.* **2005,** *87*, 023106.

[256] Sett, D.; Basak, D., Highly enhanced H2 gas sensing characteristics of Co-ZnO nanorods and its mechanism. *Sens. Actuators B Chem.* **2017,** *243*, 475-483.

[257] Schneider, J. J.; Hoffmann, R. C.; Klyszcz, J. E.; Erdem, E.; Jakes, P.; Eichel, R.-A.; Pitta-Bauermann, L.; Bill, J., Synthesis, Characterization, Defect Chemistry, and FET Properties of Microwave-Derived Nanoscaled Zinc Oxide. *Chem. Mater.* **2010,** *22*, 2203-2212.

[258] Willander, M.; Nur, O.; Sadaf, J. R.; Qadir, M. I.; Zaman, S.; Zainelabdin, A.; Bano, N.; Hussain, I., Luminescence from Zinc Oxide Nanostructures and Polymers and their Hybrid Devices. *Materials* **2010,** *3*, 2643-2667.

[259] McCluskey, M. D.; Jokela, S. J., Defects in ZnO. *J. Appl. Phys.* **2009,** *106*, 071101.

[260] Baiqi, W.; Xudong, S.; Qiang, F.; Iqbal, J.; Yana, L.; Honggang, F.; Dapeng, Y., Photoluminescence properties of Co-doped ZnO nanorods array fabricated by the solution method. *Physica E Low Dimens. Syst. Nanostruct.* **2009,** *41*, 413-417.

[261] Janotti, A.; Van de Walle, C. G., Native point defects in ZnO. *Phys. Rev. B* **2007,** *76*, 165202.

[262] Vlasenko, L. S.; Watkins, G. D., Optical detection of electron paramagnetic resonance in room-temperature electron-irradiated ZnO. *Phys. Rev. B* **2005,** *71*, 125210.

[263] Pal, B.; Giri, P. K., High temperature ferromagnetism and optical properties of Co doped ZnO nanoparticles. *J. Appl. Phys.* **2010,** *108*, 084322.

[264] Ohashi, N.; Ebisawa, N.; Sekiguchi, T.; Sakaguchi, I.; Wada, Y.; Takenaka, T.; Haneda, H., Yellowish-white luminescence in codoped zinc oxide. *Appl. Phys. Lett.* **2005,** *86*, 091902.

[265] Zheng, Y.; Chen, C.; Zhan, Y.; Lin, X.; Zheng, Q.; Wei, K.; Zhu, J.; Zhu, Y., Luminescence and Photocatalytic Activity of ZnO Nanocrystals. Correlation between Structure and Property. *Inorg. Chem.* **2007,** *46*, 6675-6682.

[266] Zhang, X.; Qin, J.; Xue, Y.; Yu, P.; Zhang, B.; Wang, L.; Liu, R., Effect of aspect ratio and surface defects on the photocatalytic activity of ZnO nanorods. *Sci. Rep.* **2015,** *4*, 4596.

[267] Wang, B.; Xia, C.; Iqbal, J.; Tang, N.; Sun, Z.; Lv, Y.; Wu, L., Influences of Co doping on the structural, optical and magnetic properties of ZnO nanorods synthesized by hydrothermal route. *Solid State Sci.* **2009,** *11*, 1419-1422.

[268] Diaz-Morales, O.; Raaijman, S.; Kortlever, R.; Kooyman, P. J.; Wezendonk, T.; Gascon, J.; Fu, W. T.; Koper, M. T. M., Iridium-based double perovskites for efficient water oxidation in acid media. *Nat. Commun.* **2016,** *7*, 12363.

[269] Grimaud, A.; Demortiere, A.; Saubanere, M.; Dachraoui, W.; Duchamp, M.; Doublet, M.-L.; Tarascon, J.-M., Activation of surface oxygen sites on an iridium-based model catalyst for the oxygen evolution reaction. *Nat. Energy* **2016,** *2*, 16189.

[270] Gottesfeld, S.; Srinivasan, S., Electrochemical and optical studies of thick oxide layers on iridium and their electrocatalytic activities for the oxygen evolution reaction. *J. Electroanal. Chem. Interf. Electrochem.* **1978,** *86*, 89-104.

[271] Li, P.; Li, J.; Feng, X.; Li, J.; Hao, Y.; Zhang, J.; Wang, H.; Yin, A.; Zhou, J.; Ma, X.; Wang, B., Metal-organic frameworks with photocatalytic bactericidal activity for integrated air cleaning. *Nat. Commun.* **2019,** *10*, 2177.

[272] Li, X.; Liu, S.; Ke Fan, Z. L.; Song, B.; Yu, J., MOF-Based Transparent Passivation Layer Modified ZnO Nanorod Arrays for Enhanced Photo-Electrochemical Water Splitting. *Adv. Energy Mater.* **2018,** *8*, 1800101.

[273] Kim, H.; Kim, W.; Park, J.; Lim, N.; Lee, R.; Cho, S. J.; Kumaresan, Y.; Oh, M.-K.; Jung, G. Y., Surface conversion of ZnO nanorods to ZIF-8 to suppress surface defects for a visible-blind UV photodetector. *Nanoscale* **2018,** *10*, 21168-21177.

[274] Hu, H.; Ji, H.-F.; Sun, Y., The effect of oxygen vacancies on water wettability of a ZnO surface. *Phys Chem Chem Phys* **2013,** *15*, 16557-16565.

[275] Pan, Y.; Liu, Y.; Zeng, G.; Zhao, L.; Lai, Z., Rapid synthesis of zeolitic imidazolate framework-8 (ZIF-8) nanocrystals in an aqueous system. *Chem. Comm.* **2011,** *47*, 2071-2073.

[276] Leem, J. W.; Yu, J. S., Glancing angle deposited ITO films for efficiency enhancement of a-Si:H-μc-Si:H tandem thin film solar cells. *Opt. Express* **2011,** *19*, A258-A268.

[277] Li, Y.; Cai, X.; Chen, S.; Zhang, H.; Zhang, K. H. L.; Hong, J.; Chen, B.; Kuo, D.-H.; Wang, W., Highly Dispersed Metal Carbide on ZIF-Derived Pyridinic-N-Doped Carbon for CO_2 Enrichment and Selective Hydrogenation. *Chem. Sus. Chem.* **2018,** *11*, 1040-1047.

[278] Lu, Y.; Lin, Y.; Wang, D.; Wang, L.; Xie, T.; Jiang, T., A high performance cobalt-doped ZnO visible light photocatalyst and its photogenerated charge transfer properties. *Nano Res.* **2011,** *4*, 1144-1152.

[279] Wee, L. H.; Janssens, N.; Sree, S. P.; Wiktor, C.; Gobechiya, E.; Fischer, R. A.; Kirschhocka, C. E. A.; Martens, J. A., Local transformation of ZIF-8 powders and coatings into ZnO nanorods for photocatalytic application. *Nanoscale* **2014,** *6*, 2056-2060.

[280] Kegel, J.; Povey, I. M.; Pemble, M. E., Zinc oxide for solar water splitting: A brief review of the material's challenges and associated opportunities. *Nano Energy* **2018,** *54*, 409-428.

[281] May, J. W.; Ma, J.; Badaeva, E.; Li, X., Effect of Excited-State Structural Relaxation on Midgap Excitations in Co2+-Doped ZnO Quantum Dots. *J. Phys. Chem. C* **2014,** *118*, 13152-13156.

[282] Wilson, R. H., Observation and Analysis of Surface States on TiO2 Electrodes in Aqueous Electrolytes. *J. Electrochem. Soc.* **1980,** *127*, 228-234.

[283] Janotti, A.; Walle, C. G. V. d., Oxygen vacancies in ZnO. *Appl. Phys. Lett.* **2005,** *87*, 122102.

[284] Chen, C. K.; Shen, Y.-P.; Chen, H. M.; Chen, C.-J.; Chan, T.-S.; Lee, J.-F.; Liu, R.-S., Quantum-Dot-Sensitized Nitrogen-Doped ZnO for Efficient Photoelectrochemical Water Splitting. *Eur. J. Inorg. Chem.* **2013,** *2014*, 773-779.

References

[285] Wilson, R. H., Observation and Analysis of Surface States on TiO$_2$ Electrodes in Aqueous Electrolytes. *J. Electrochem. Soc.* **1980,** *127*, 228-234.

[286] May, J. W.; Ma, J.; Badaeva, E.; Li, X., Effect of Excited-State Structural Relaxation on Midgap Excitations in Co^{2+}-Doped ZnO Quantum Dots. *J. Phys. Chem. C* **2014,** *118*, 13152–13156.

[287] Kegel, J.; Povey, I. M.; Pemble, M. E., Zinc oxide for solar water splitting A brief review of the material's challenges and associated opportunities. *Nano Energy* **2018,** *55*, 409-428.

[288] Jing, H.-P.; Wang, C.-C.; Zhang, Y.-W.; Wang, P.; Li, R., Photocatalytic degradation of methylene blue in ZIF-8. *RSC Adv.* **2014,** *4*, 54454–54462.

[289] Yang, X.; Yan, D., Direct white-light-emitting and near-infrared phosphorescence of ZIF-8. *Chem. Comm.* **2017,** *53*, 1801-1804.

[290] Xie, S.; Lu, X.; Zhai, T.; Li, W.; Yu, M.; Liang, C.; Tong, Y., Enhanced photoactivity and stability of carbon and nitrogen co-treated ZnO nanorod arrays for photoelectrochemical water splitting. *J. Mater. Chem.* **2012,** *22*, 14272-14275.

[291] Fu, H.; Xu, T.; Zhu, S.; Zhu, Y., Photocorrosion Inhibition and Enhancement of Photocatalytic Activity for ZnO via Hybridization with C60. *Environ. Sci. Technol.* **2008,** *42*, 8064-8069.

[292] Zhang, H.; Zong, R.; Zhu, Y., Photocorrosion Inhibition and Photoactivity Enhancement for Zinc Oxide via Hybridization with Monolayer Polyaniline. *J. Phys. Chem. C* **2009,** *113*, 4605-4611.

[293] Tanaka, S.; Sakamoto, K.; Inada, H.; Kawata, M.; Takasaki, G.; Imawaka, K., Vapor-Phase Synthesis of ZIF-8 MOF Thick Film by Conversion of ZnO Nanorod Array. *Langmuir* **2018,** *34*, 7028–7033.

[294] Sutka, A.; Käämbre, T.; Pärna, R.; Juhnevica, I.; Maiorov, M.; Joost, U.; Kisand, V., Co doped ZnO nanowires as visible light photocatalysts. *Solid State Sci.* **2016,** *56*, 54-62.

[295] Chin, M.; Cisneros, C.; Araiza, S. M.; Vargas, K. M.; Ishihara, K. M.; Tian, F., Rhodamine B degradation by nanosized zeolitic imidazolate framework-8. *RSC Adv.* **2018,** *8*, 26987–26997.

[296] Grau-Crespo, R.; Aziz, A.; Collins, A. W.; Crespo-Otero, R.; Hernández, N. C.; Rodriguez-Albelo, L. M.; Ruiz-Salvador, A. R.; Calero, S.; Hamad, S., Modelling a Linker Mix-and-Match Approach for Controlling the Optical Excitation Gaps and Band Alignment of Zeolitic Imidazolate Frameworks. *Angew. Chem. Int. Ed. Engl.* **2016,** *55*, 16012 –16016.

271